NASA/CP—1999–209628

Fourth United States Microgravity Payload: One Year Report

Compiled by
E.C. Ethridge and P.A. Curreri
Marshall Space Flight Center, Marshall Space Flight Center, Alabama

D.E. McCauley
University of Alabama in Huntsville, Huntsville, Alabama

Proceedings of a conference held at
Marshall Space Flight Center
January 22, 1999

National Aeronautics and
Space Administration

Marshall Space Flight Center • MSFC, Alabama 35812

September 1999

Acknowledgments

The superb efforts and dedication of the STS–87 payload and orbiter crew, the mission and program managers, and mission operations personnel were critical to the completion of the mission's objectives and are sincerely appreciated. We wish to thank the Office of Life and Microgravity Science and Applications (OLMSA) and the Microgravity Research Division (MRD) at NASA Headquarters for their support; in particular, the USMP–4 Program Scientist, Dr. Michael J. Wargo, without whom the success of the mission would not have been possible. We also wish to thank the NASA Marshall Space Flight Center's Public Affairs Office for their help in publicizing the results of the USMP–4 mission as well as all of the authors for contributing to this document.

Available from:

NASA Center for AeroSpace Information
7121 Standard Drive
Hanover, MD 21076–1320
(301) 621–0390

National Technical Information Service
5285 Port Royal Road
Springfield, VA 22161
(703) 487–4650

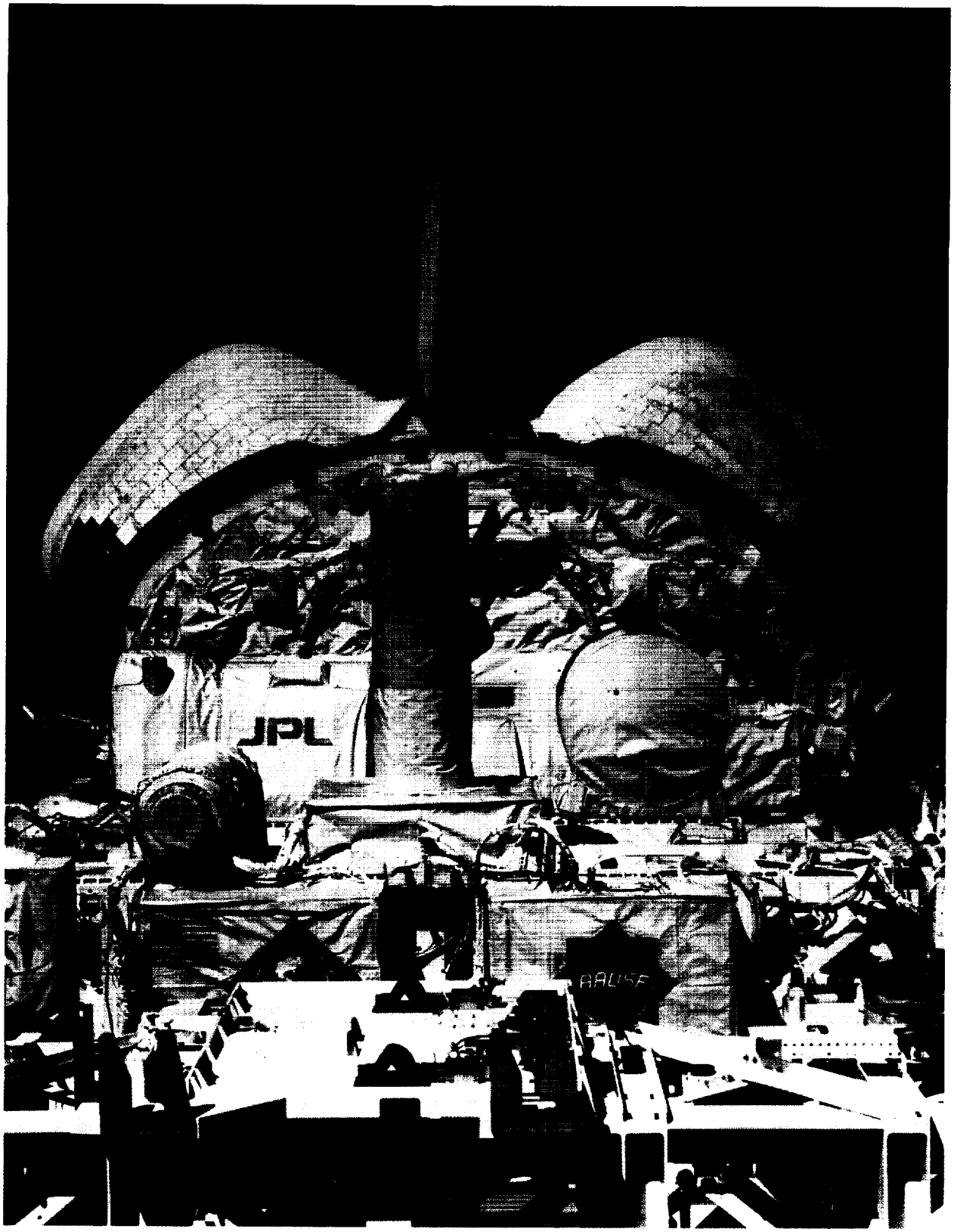
JPL

Table of Contents

FOURTH UNITED STATES MICROGRAVITY PAYLOAD: ONE YEAR REPORT

Edwin C. Ethridge and Peter A. Curreri
USMP-4 Mission Science
George C. Marshall Space Flight Center

Overview

The Fourth United States Microgravity Payload (USMP-4) Space Shuttle mission was launched November 19, 1997 and landed December 5, 1997. During the 15 day mission the Shuttle crew performed extensive microgravity science research. The Principal Investigators (PI's) for the mission presented their one year science results at the USMP-4 One Year Review held at Marshall Space Flight Center on January 22, 1999. This document includes the PI's written versions of their one year results. The purpose of this report is to inform the microgravity science community and the public of the results of the USMP-4 experiments flown on this Shuttle mission.

The USMP-4 One Year Report represents the culmination of many years of sustained effort on the part of the investigators, mission management, and support personnel and is intended not only for the scientific community, but also for general public awareness and education. This mission provided the microgravity science community outstanding research opportunities to verify results obtained from previous flights, and to perform new experiments which contribute substantially and uniquely to the scientific, technological, and commercial knowledge of the United States and its international partners. The results obtained and the lessons learned from this mission lead us into the next phase of microgravity research, the International Space Station.

The USMP-4 mission was launched on the Space Shuttle *Columbia*, STS-87. It consisted of four primary microgravity experiments, the middeck glovebox, and the SAMS and OARE acceleration systems. The primary USMP-4 experiments were the Advanced Automated Directional Solidification Furnace (AADSF), the Isothermal Dendritic Growth Experiment (IDGE), Material por l'Etude des Phenomenes Intéressent la Solidification sur Terre et en Orbite (Apparatus for the Study of Interesting Phenomena of Solidification on Earth and in Orbit), MEPHISTO, and the Confined Helium Experiment (CHEX). The USMP-4 experiments utilized microgravity to improve the fundamental understanding of materials processes. Four experiments studied the formation of solid from the melt and one studied confined helium near the superfluid transition temperature. The science payload also included three Middeck Glovebox investigations which studied combustion in microgravity, particle pushing during solidification, and surface energy induced segregation in immiscible liquids. The Glovebox investigations required significant crew involvement, while the primary USMP-4 experiments were almost completely controlled by the science team on Earth using telescience.

The AADSF furnace was used to gain new understanding of fundamental crystal growth by utilization of microgravity. The first AADSF experiment (Fripp et al.) was to solidify two ampoules with three samples each of lead tin telluride which is an infrared detector material. Samples in the first ampoule appeared to process as planned. However, a hardware problem was experienced during the exchange and insertion of the second ampoule. The second AADSF

experiment (Lehoczky et al.) was the solidification of mercury cadmium telluride, another electronic material used for infrared detection. The objective of these experiments was to produce new near perfect benchmark crystals or a basic understanding of crystal growth that may be used to improve detector technology on Earth.

IDGE studied the growth of dendrite crystals of a transparent metal model material. Dendritic solidification has an important role in determining the mechanical properties of cast metal alloys. The purpose of the first two flights of the IDGE on USMP-2 and USMP-3 was to test current theories for heat transfer from the interface by using microgravity. In the earlier experiments, succinonitrile (SCN) was used as the sample. For USMP-4, the science team chose pivalic acid (PVA), which is also a transparent analog for metals. It simulated a difference class of metals with a higher surface energy anisotropy at the interface of the dendrite and the melt. The comparison of the difference in behavior in microgravity of the PVA dendrites from that of SCN dendrites will help reveal important mechanisms for solidification. Some technical mile stones were that the experiment achieved the fastest dendrite growth rate measured for PVA and the highest level of undercooling obtained for pivalic acid.

MEPHISTO was used to study the solidification of a bismuth tin alloy. This alloy is a facet - forming material and solidifies in a multigranular manner. During solidification of the alloy at high enough growth rates, the interface between liquid and solid becomes unstable. Experiments previously conducted by Dr. Abbaschian on USMP-2 were to confirm theories that predict the onset of this instability and the resulting microstructural transition, but they also observed something surprising. In two crystals of bismuth tin solidified side-by-side in the furnace, the microstructural transition occurred at different times. For USMP-4 the cause of the time-dependent difference in the transition for the growing crystals was investigated.

CHEX studied the superfluid transition (Lamda Point) of liquid helium in microgravity to better understand the finite size theory, which predicts the effect of confinement on all materials. As materials are limited to smaller and smaller spaces, the effect of boundaries on the fundamental material's properties becomes more and more pronounced. As helium nears the superfluid point it is possible to measure, with greatly enhanced sensitivity, the changes caused by the effects of confinement on the heat capacity of the helium. During USMP-4, the experiment team was able to use telescience to measure the temperature of the experiment's sample with a resolution of one-tenth of a billionth of a degree Kelvin, the most precise temperature measurement made in space.

In addition to these five telescience experiments conducted in the payload bay of the shuttle, crew members conducted three Glovebox experiments inside the shuttle middeck: Engulfed Laminar Flames (ELF), Particle Engulfment and Pushing (PEP), and Wetting Characteristics of Immiscibles (WCI). ELF was designed to investigate the stability of laminar jet flames. These flames are common in practical combustion systems such as power plant combustors or jet engine afterburners. PEP was an investigation of the solidification of composite materials. As this substance solidifies, the solid particles are either pushed ahead of the liquid-solid interface or engulfed by it. WCI investigated the wetting of a container and the extent of the separation of immiscible liquids.

USMP-4 investigators required essential acceleration data that characterized the microgravity environment on the shuttle during the mission. Data from the accelerometers were downlinked during the mission and interpreted by analysts from the PI Microgravity Services (PIMS) team. Over the span of the USMP series, PIMS has identified vibrations caused by many types of shuttle events and activities, such as the dithering of the shuttle's Ku-band antenna, thruster firings, and water dumps, that can affect microgravity levels.

The fourth flight of the United States Microgravity Payload provided a combination of very high quality, highly interactive telescience and low cost, quickly developed Glovebox science. This combination provided a rich science return that fully utilized the Space Shuttle resources. USMP provides a model for the highly productive science that we eagerly anticipate on the International Space Station.

USMP-4 Key Personnel

Peter A. Curreri
NASA Marshall Space Flight Center
USMP-4 Mission Scientist

Edwin C. Ethridge
NASA Marshall Space Flight Center
USMP-4 Assistant Mission Scientist

Dr. Michael J. Wargo
NASA Headquarters
USMP-4 Program Scientist

Sherwood Anderson
NASA Marshall Space Flight Center
USMP-4 Mission Manager

Brian E. Blair
NASA Marshall Space Flight Center
USMP-4 Payload Operations Lead

USMP-4 Acronyms

AADSF	Advanced Automated Directional Solidification Furnace
BCC	Body Contoured Cubic
CFX	A commercial flow code
CHEX	Confined Helium Experiment
CGF	Crystal Growth Furnace
CT	Computed Tomography
DAP	Digital Auto Pilot
DAS	Data Acquisition System
EAC	Experiment Apparatus Container
EBSP	Electron Back Scatter Patterns
EDFT	Extravehicular Activity Demonstration Flight Test
EDS	Energy Dispersive/Dispersion Spectrometry
EDSE	Equiaxed Dendritic Solidification Experiment
ELF	Enclosed Laminar Flames
EVA	Extravehicular Activity
FCC	Face Centered Cubic
GCEL	Ground Control Experiment Laboratory
GMT	Greenwich Mean Time
HgCdTe	Mercury Cadmium Telluride
HgTe	Mercury Telluride
HRT	High Resolution Thermometer
IDGE	Isothermal Dendritic Growth Experiment
ISS	International Space Station
JPL	Jet Propulsion Laboratory
KSC	Kennedy Space Center
LeRC	Lewis Research Center
LPE	Lamda Point Experiment
LTT	Lead-Tin-Telluride
MAWS	Microgravity Analysis/Acceleration Workstation
MCT	Mercury Cadmium Telluride
MEPHISTO	Matérial por l'Etude des Phenomènes Intéressent la Solidification sur Terre et en Orbite
MET	Mission Elapsed Time
MEWS	Mission Evaluation Workstation
MGBX	Middeck Glovebox/Microgravity Glovebox
MPESS	Mission Peculiar Experiment Support Structures
MSFC	Marshall Space Flight Center
NMR	Nuclear Magnetic Resonance
NIST	National Institute of Standards and Technology
OARE	Orbital Acceleration Research Experiment
PAO	Public Affairs Office
PET	Pushing/Engulfment Transition
PbTe	Lead Telluride
PbSnTe	Lead Tin Telluride
PCIS	Passive Cycle Isolation System

PEP	Particle Pushing and Engulfment by Solidifying Interfaces
PGSC	A Laptop Computer
PIMS	Principal Investigator Microgravity Services
PRCS	Primary Reaction Control System
PSD	Power Spectral Density
PVA	Pivalic Acid
RMS	Root-Mean -Square
SACA	Sample Ampoule Cartridge Assembly
SAMS	Space Acceleration Measurement System
SCCS	Signal Conditioning and Control System
SCN	Succinonitrile
SEM	Scanning Electron Microscope
SEP	Société Européene de Propulsion
S/L	Solid/Liquid Interface
SnTe	Tin Telluride
SOLCON	An in-house code from the University of Florida
TC	Temperature of the moving interface
TCS	Thermal Control System
TD	Temperature of the stationary interface
TDRS	Tracking and Delay Relay Satellites
TDSE	Transient Dendritic Solidification Experiment
TSC	Telescience Support Center
TSH	Triaxial Sensor Head
URL	Uniform Resource Locator
USMP	United States Microgravity Payload
USRA	Universities Space Research Association
VCR	Video Cassette Recorder
VRCS	Vernier Reaction Control System
WA	Work Area
WCI	Wetting Characteristics of Immiscibles
WDS	Wavelength Dispersive Spectrometry
WWW	World Wide Web
ZAF	Atomic Number Absorption Fluorescence

Mission Information

Orbiter	Columbia
Mission Designation	STS-87
Dates of Flight	November 19, 1997 - December 5, 1997
Crew Size	Six
Number of Shifts	One
Accelerometers	OARE - measures low-level accelerations in the frequency range below one Hertz down to essentially steady state and is mounted near the center of gravity of the Orbiter. SAMS - measures low-level accelerations from about 0.01 Hertz up to 100 Hertz and is mounted in or near the science experiment equipment.

Crew:

Commander:	Kevin R. Kregel
Pilot:	Steven W. Lindsay
Mission Specialist:	Takao Doi
Mission Specialist	Winston E. Scott
Mission Specialist	Kalpana Chawla
Payload Specialist	Leonid Kadenyuk

The Isothermal Dendritic Growth Experiment (IDGE)
USMP-4 One-Year-Report

M.E. Glicksman	M.B. Koss	J.C. LaCombe	A.O. Lupulescu
glickm@rpi.edu	kossm@rpi.edu	lacomj@rpi.edu	lupula@rpi.edu
518/276-6721	518/276-2844	518/276-8068	518/276-2023

Materials Science and Engineering Department
Rensselaer Polytechnic Institute
Troy, NY, 12180-3590

And

D.C. Malarik
Diane.Malarik@lerc.nasa.gov
(216/433-3203)

Microgravity Science Division
MS 500-217
NASA Lewis Research Center
Cleveland, OH 44135

Introduction

Dendrites describe the tree-like crystal morphology commonly assumed in many material systems--particularly in metals and alloys that freeze from supercooled or supersaturated melts. There remains a high level of engineering interest in dendritic solidification because of the role of dendrites in the determination of cast alloy microstructures. Microstructure plays a key role in determining the physical properties of cast or welded products. In addition, dendritic solidification provides an example of non-equilibrium physics and is one of the simplest non-trivial examples of dynamic pattern formation, where an amorphous melt, under simple starting conditions, evolves into a complex ramified microstructure [1].

Although it is well-known that dendritic growth is controlled by the transport of latent heat from the moving solid-melt interface as the dendrite advances into a supercooled melt, an accurate, and predictive model has not been developed. Current theories consider: 1) the transfer of heat or solute from the solid-liquid interface into the melt, and 2) the interfacial crystal growth and growth selection physics for the interface. However, the effects of gravity-induced convection on the transfer of heat from the interface prevent either element from being adequately tested solely under terrestrial conditions [2].

The Isothermal Dendritic Growth Experiment (IDGE) constituted a series of three NASA-supported microgravity experiments, all of which flew aboard the space shuttle, *Columbia*. This experimental space flight series was designed and operated to grow and record dendrite solidification in the absence of gravity-induced convective heat transfer, and thereby produce a wealth of benchmark-quality data for testing solidification scaling laws [3,4].

The first flight of the IDGE flight, on STS-62, took place in March, 1994, on the second United States Microgravity Payload (USMP-2) [5], with a second flight on STS-75, in February/March, 1996, on USMP-3. Both flights used ultra-pure succinonitrile (SCN) as the test material. SCN is an organic crystal that forms dendrites similar to the BCC metals when it solidifies. Thus, SCN provides a nearly ideal physical model for ferrous metals. The third and final IDGE flight (USMP-4) launched on STS-87, in November of 1997, employed a different test material. This flight used pivalic acid (PVA)---an FCC organic crystal that solidifies like many non-ferrous metals. PVA, like SCN, has convenient properties for conducting benchmark experiments. However, unlike SCN, PVA exhibits a large anisotropy of its solid-melt interfacial energy, which is a key parameter in the selection of dendritic operating states.

Background

The main conclusions drawn from comparing the on-orbit SCN data to terrestrial dendritic growth data, obtained using the same apparatus and techniques, are that: 1) convective effects under terrestrial conditions cause growth speed increases up to a factor of 2 at the lower supercoolings ($\Delta T < 0.5$ K), and convection effects remain discernible under terrestrial conditions up to supercoolings as high as 1.7 K, far beyond what was thought. 2) In the supercooling range above 0.47 K, microgravity data remain virtually free of convective or chamber-wall effects, and may be used reliably for examining diffusion-limited dendritic growth theories. 3) The diffusion solution to the dendrite problem, combined with a unique scaling constant, σ^*, will not provide accurate prediction of the growth velocity and dendritic tip radii. 4) Growth Péclet numbers calculated from Ivantsov's solution deviate systematically from the IDGE data observed under diffusion-limited conditions. 5) The scaling parameter σ^* does not appear to be a constant, independent of supercooling. Finally, 6), the σ^* measurements from the terrestrial and microgravity data are in good agreement with each other, despite a difference of over six orders of magnitude in the quasi-static acceleration environment of low-earth orbit and terrestrial conditions [6,7].

The second IDGE flight on USMP-3/STS-75 mostly supported the above conclusions. However, there were some important modifications. With sufficient repeated observations [8], it now appears that the terrestrial and microgravity σ^* are distinguishable, with the microgravity σ^* larger than those measured under terrestrial conditions. However, even with the statistics of repeated experiment cycles, the functional dependence of σ^* with supercooling remains uncertain. Some of the

additional data supports the conclusion of USMP-2 that there is a functional dependence on supercooling, while some of the additional data argues against such a dependence.

The second flight also clarified some issues at the lower supercoolings as to the role of convection, wall proximity or other explanations by showing definitively that it is not convection [9,10] and argued as to what extent the low temperature features are due to wall proximity effects [11]. Finally, the second flight yielded sufficient data to make a three-dimensional reconstruction of the non-parabolic, non-body-of-revolution dendritic tip shape [12,13].

Results to date from USMP-4

The data and subsequent analysis from the final flight experiment are currently in a preliminary state, based on images received using telemetry from space. We compared the dendritic growth speed of PVA as a function of the supercooling to both terrestrially measured PVA data, and an estimate scaled from prior SCN microgravity data. The preliminary results of these tests indicate that the PVA data are in good agreement with the SCN data (Figure 1). This implies that dendritic growth in PVA is diffusion-limited with little, if any, kinetic response, just like SCN. This observation conflicts with the conclusion reached by other investigators that there are large interfacial kinetic effects in PVA. The film analysis from these photos (figure 2) confirms the results from the ccd and lends full credence to conclusions drawn from the ccd data alone at the higher supercoolings.

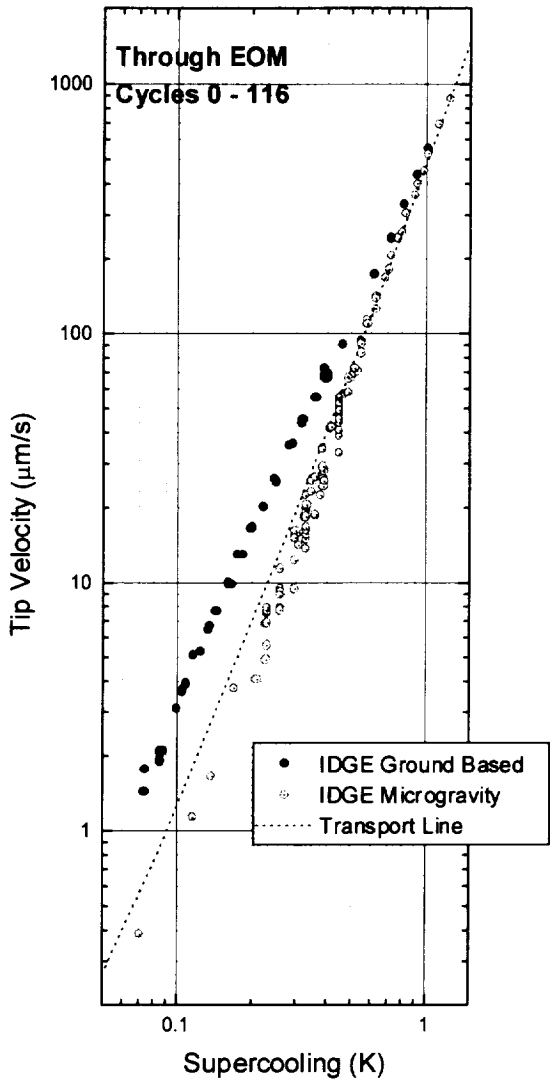

Figure 1

Figure 3 shows some preliminary data assessing the nature of these boundary layer interactions in PVA. We see that when the nearest neighbor distance exceeds about two thermal diffusion distances, λ, where the diffusion distance $\lambda=\alpha/V$ (α is the thermal diffusivity and V is the tip speed) the velocity levels off at

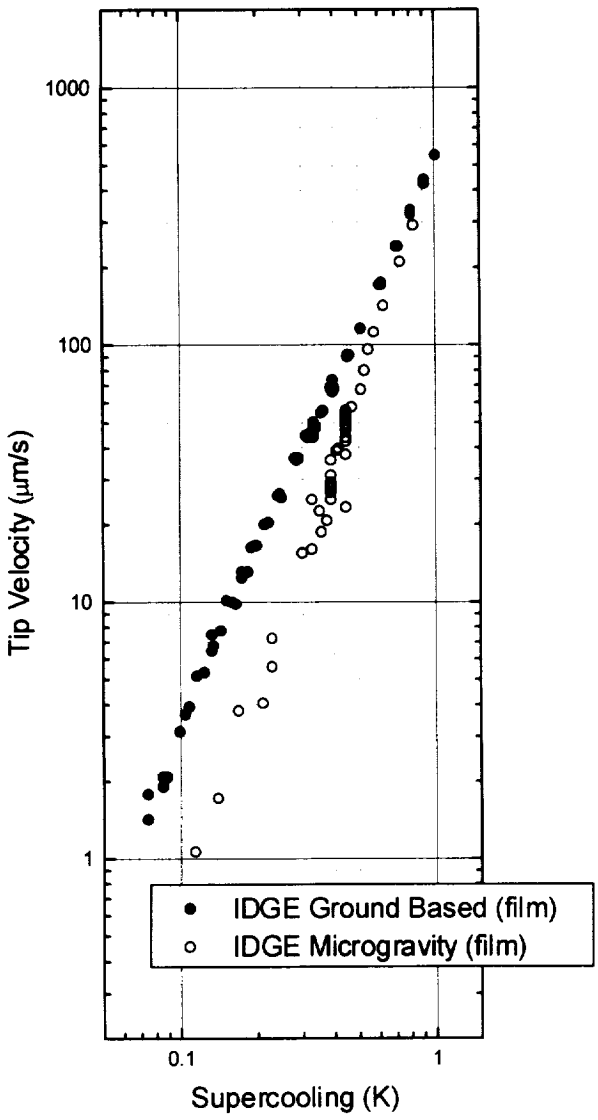

Figure 2

its maximum steady–state rate. When nearest neighbor spacings fall below about 2λ, the velocity is reduced due to thermal interactions of the boundary layers. This phenomenon of neighbor interactions has never been observed before, because microgravity conditions are needed to insure growth limited by thermal diffusion from the solid–melt interface.

As a consequence of this, we see that not all the dendrites obtained and measured for USMP-4 are appropriate for comparison with predictions that assume diffusion under isothermal conditions. We are performing measurements to determine for each growth cycle whether the primary tip in the field of view is separated enough from its next nearest neighbor dendrite to be considered isolated. If the primary tip in the field of view is not isolated, we will look for other dendrites in the field of view that are both visible and isolated. In this manner we will produce a data set of isothermal growths. At the same time, we will have several plots like figure 3 that show how the separation between tips influences the growth of the primary dendrite.

Once we have identified the isothermal dendrites for the flight, we will proceed to the radii analysis. Since the optical properties of PVA are slightly different than for SCN, and the apparatus and optics were configured somewhat differently, we will need to reexamine and further develop our techniques for edge location prior to calculating from that edge data the radius of curvature of the dendrite. This is further complicated by our qualitative estimate that PVA dendrites are different enough from SCN dendrites that new radius extraction techniques are necessary.

Analysis indicates that the methods used for characterizing the radius of curvature and shape of the tip region of SCN dendrites does not work for the USMP-4 pivalic acid dendrite tips. In short, it has been found that 4^{th}-order polynomials do not describe PVA

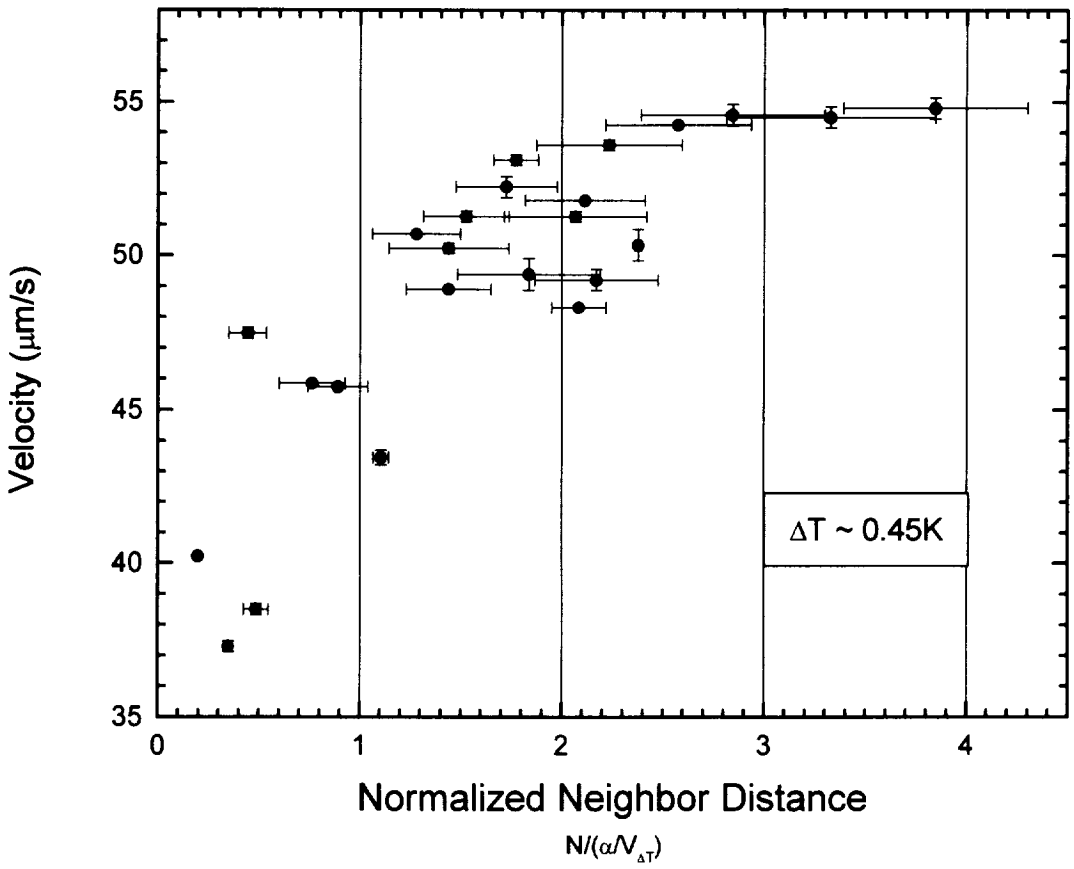

Figure 3

tip shapes very well, and cannot provide sufficient R and Q data that is necessary to evaluate various components of theory. The effort to obtain these data is focusing on characterizing the region closer to the tip using a simple paraboloid and extrapolating the derived shape information back to the tip itself to obtain R. At this point, it is not clear how a measure of the tip shape anisotropy, Q, will be obtained from PVA dendrites.

Currently we are extracting velocity and side-branching measurements from flight videos which provide 30 frames per second images at 256 gray-level for a 640 x 480 pixle field-of-view, at much lower spatial resolution then the film. The 30 frame per second video data are starting to be analyzed. Efforts have centered on developing analysis software tools and examination of ground-based data. Results so far indicate that there are several interesting transient aspects evident in the dendrite tip-displacement vs. time data. The first observation is that while the dendrites initially *appear* to grow at a constant rate (Figure 4), they actually do not, as evidenced by Figure 5, which shows the residuals from a straight line regressed through the displacement data. The systematic bowing of the residual plot is evidence of the fact that during the entire period of observation, a typical PVA dendrite tip is accelerating. The mechanism of this behavior is not yet clear. The spread in the residual data of Figure 5 illustrates the limiting resolution of approximately

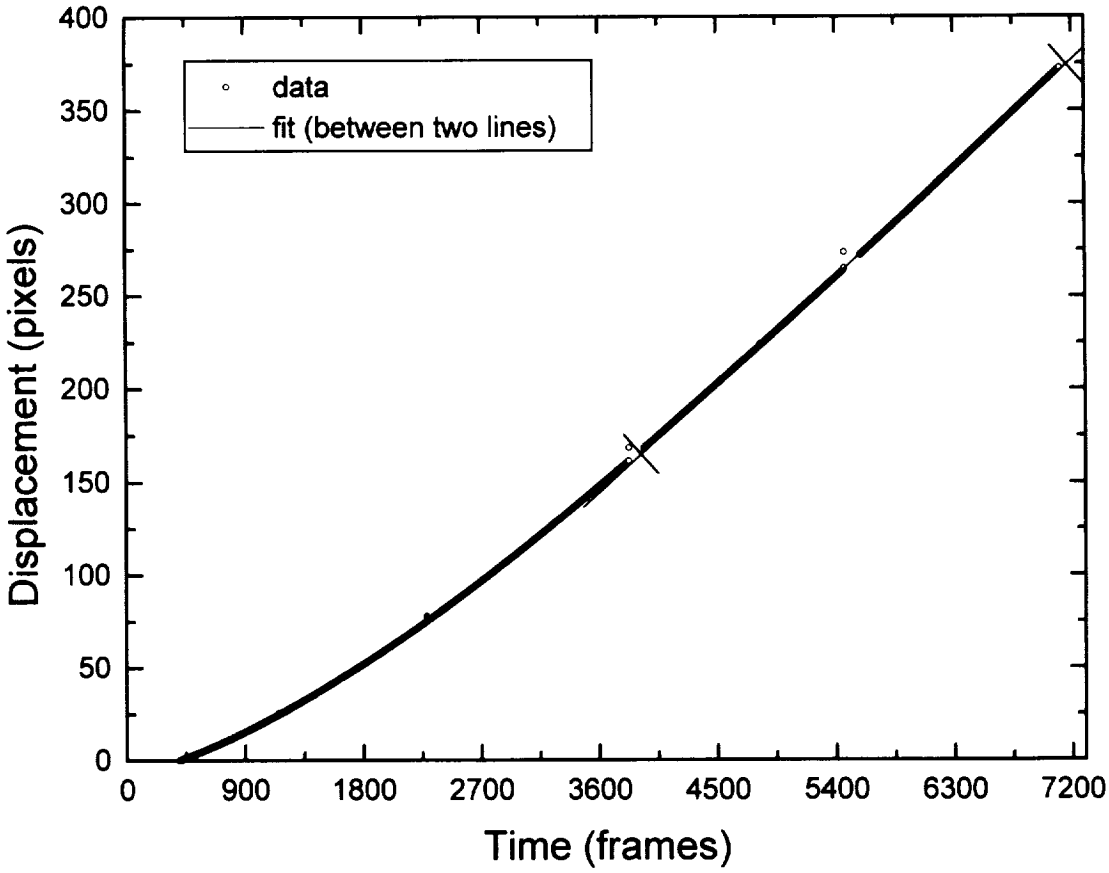

Figure 4

on) to meet this demand. Initial work suggests that the limiting resolution can be reduced 0.25 pixel's width. New image processing techniques are needed (and are being worked by a factor of 2 - 4 through additional sub-pixel interpolation tip-locating techniques.

Telescience

In addition to our investigation of dendritic solidification kinetics and morphology, the IDGE has been part of the development of remote, university-based teleoperations. These teleoperation tests point the way to the future of microgravity science operations on the International Space Station (ISS). NASA headquarters and the Telescience Support Center (TSC) at LeRC, set a goal for developing the experience and expertise to set up remote, non-NASA locations from which to control space station experiments. Recent IDGE space shuttle flights provide proof-of-concept and tests of remote space flight teleoperations [15].

Summary and Conclusions

The data collection from the on-orbit phase of the IDGE flight series is now complete. We are currently completing analyses and moving towards final data archiving. We have much more to do and to analyze from the IDGE data. In addition, we are gratified to see

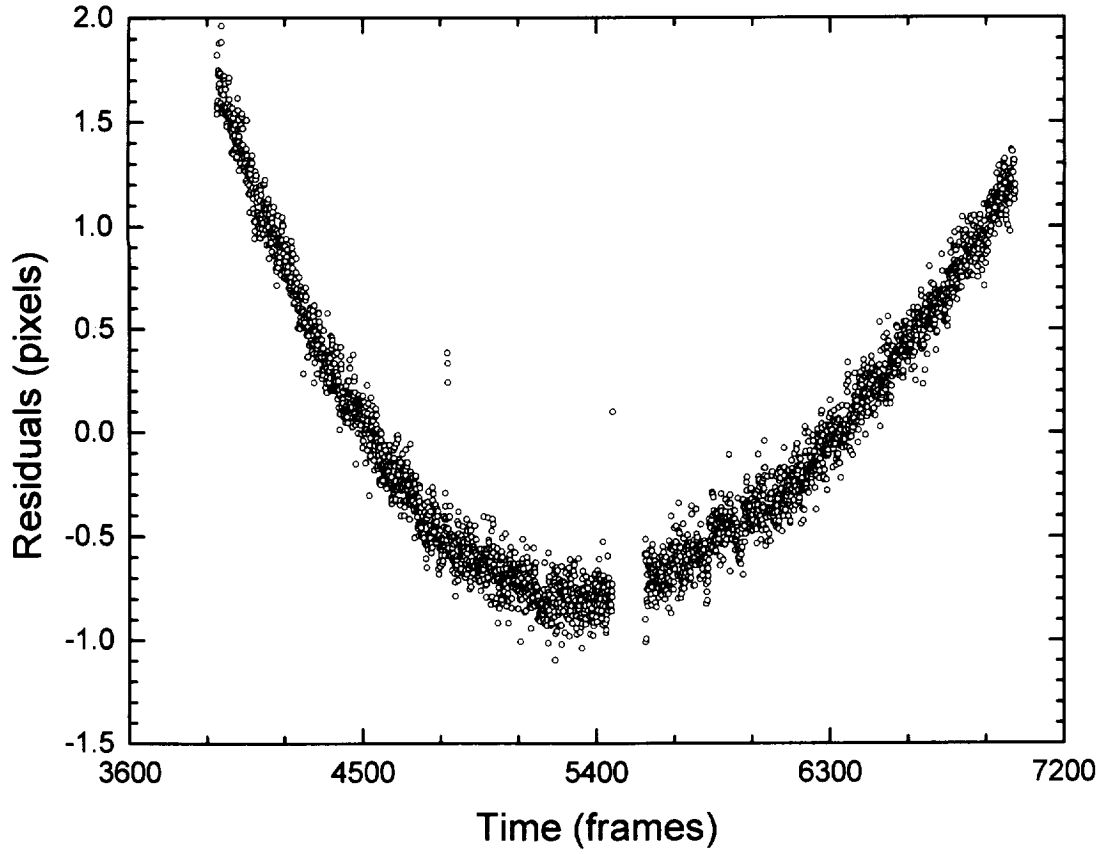

Figure 5

that the IDGE published results and archived data sets are being used actively by other scientists and engineers. In addition, we are also pleased to report that the techniques and IDGE hardware system that the authors developed with NASA, are being currently employed on both designated flight experiments, like EDSE, and on flight definition experiments, like TDSE.

References

1. M.E. Glicksman and S.P. Marsh, *The Dendrite*, Handbook of Crystal Growth, ed. D.J.T. Hurle, Vol 1b, p.1077, (Elsevier Science Publishers B.V., Amsterdam, 1993).
2. M.E. Glicksman and S.C. Huang, *Convective Heat Transfer During Dendritic Growth*, Convective Transport and Instability Phenomena, ed. Zierep and Ortel, Karlsruhe, 557, (1982).
3. M.E. Glicksman, E.A. Winsa, R.C. Hahn, T.A. LoGrasso, S.H. Tirmizi, and M.E. Selleck, Met. Trans. A, **19A**, 1945, (1988).
4. M.E. Glicksman, M.B. Koss, and E.A. Winsa, JOM, **47(8)**, 49, (1995).
5. M.E. Glicksman, M.B. Koss, and E.A. Winsa, Phys. Rev. Lett., **73**, 573, (1994).
6. M.E. Glicksman, M.B. Koss, L.T. Bushnell, J.C. LaCombe, and E.A. Winsa, ISIJ, **35(6)**, 604, (1995).

7. M.B. Koss, L.A. Tennenhouse, J.C. LaCombe, M.E. Glicksman, and E.A. Winsa, (Manuscript submitted to Metallurgical and Materials Transactions, 1998).
8. A.O. Lupulescu, M.B. Koss, J.C. LaCombe, M.E. Glicksman, and L.A. Tennenhouse, Rensselaer Polytechnic Institute, Troy, NY, unpublished research, (1998).
9. M.B. Koss, L.T. Bushnell, M.E. Glicksman, and J.C. LaCombe, Chem. Eng. Comm., **152-153**, 351, (1996).
10. L.A. Tennenhouse, M.B. Koss, J.C. LaCombe, and M.E. Glicksman, J. Crystal Growth, **174**, 82, (1997).
11. L.A. Tennenhouse, M.B. Koss, J.C. LaCombe, A.O. Lupulescu, and M.E. Glicksman, Rensselaer Polytechnic Institute, Troy, NY, unpublished research, (1998).
12. J.C. LaCombe, M.B. Koss, V.E. Fradkov, and M.E. Glicksman, Phys. Rev. E, **52**, 2278, (1995).
13. J.C. LaCombe, D.C Corrigan, M.B. Koss, L.A. Tennenhouse, A.O. Lupulescu, and M.E. Glicksman, Rensselaer Polytechnic Institute, Troy, NY, unpublished research, (1998).
14. R.J. Schaefer, J. Crystal Growth, **43,** 17, (1978).
15. M.B. Koss, M.E. Glicksman, L.T. Bushnell, J.C. LaCombe, and E.A. Winsa, 8th International Symposium on Experimental Methods for Microgravity Materials Science, ed. R.A. Schiffman, The TMS, Warrendale, PA, (1996).

PRELIMINARY RESULTS FROM THE CONFINED HELIUM EXPERIMENT

J.A. Lipa, D.R. Swanson, J.A. Nissen, P.R. Williamson, K. Geng and D.A. Stricker,
Stanford University, Stanford, California 94305

and

T.C.P. Chui, U.E. Israelsson and M. Larson,
Jet Propulsion Laboratory, California Institute of Technology, Pasadena, California 91109

We describe the preliminary results from an experiment to measure the heat capacity of helium confined within a stack of evenly spaced silicon plates at temperatures very close to the superfluid transition. The resolution of the heat capacity measurements was generally about 5×10^{-9} K, allowing the finite size peak to be mapped in detail. In addition, wide range data containing information on the behavior of the surface specific heat was collected. The preliminary analysis shows fair agreement with theory, but some discrepancies. The results can also be combined with related ground measurements on smaller length scales to perform additional tests of scaling predictions for cross-over to lower dimensional behavior. Some results in this area are also presented.

INTRODUCTION

When ordinary matter is confined by boundaries in one or more dimensions to the length scale over which its local properties are correlated, its global properties are found to change. In metals and insulators the length scale required is very small, but in superconductors, systems near critical points, superfluid ^{3}He and semiconductors, the scale can be tens of nanometers or more. For example, in $Ga_xAl_{1-x}As$, it can be as large as 0.1 microns[1]. With recent advances in nano-fabrication techniques, the behavior of materials at small length scales is becoming a topic of technological importance. Outside the quantum world, the effects of interest are commonly modeled using mean field theories, except near critical points, where renormalization methods are needed.

With these confinement effects occurring in very small systems, it is difficult to separate them experimentally from perturbations due to interactions with the confinement structure itself. Fortunately, there are a few situations where the intrinsic effects are greatly magnified, allowing detailed experimental measurements, free of artifact, that can be compared with theoretical models. At the lambda transition of helium the length scale of interest diverges due to critical effects, allowing the confinement behavior to be examined under nearly ideal conditions. Yet early results from helium showed clear departures from theoretical models.

The experiment described here was designed to give new, high precision heat capacity data for helium confined to a 2-dimensional geometry with a characteristic length scale of 57 microns. The maximum feasible length scale was chosen in an attempt to minimize extraneous effects that might have perturbed the early results. On this scale, surface effects related to Van der Waal's forces and other phenomena should be completely negligible, allowing a very clean measurement of the intrinsic behavior as the helium crosses over from the 3- to a 2-dimensional state. The results should therefore provide a high quality reference curve against which other experiments and detailed predictions can be compared.

The experiment was performed on the Space Shuttle to reduce the effect of gravity on the helium, which causes a rounding very similar to the finite size effect. The preliminary results from the experiment are discussed here.

In the field of critical phenomena, a correlation length, ξ, describes the characteristic length scale over which an order parameter can vary. Near the lambda point the measurable quantity related to the order parameter is the superfluid density, and the length scale of interest is the so-called healing length, over which boundary effects are appreciable. Asymptotically close to the transition temperature, T_λ, the healing length behaves as $\xi \approx \xi_o t^{-\nu}$ where $t = |T/T_\lambda - 1|$, $\nu = 0.671$, $\xi_o \approx 3.6$ Å below the transition, and ≈ 1.41 Å above[2]. Far from the transition, where $t \sim 1$, it can be seen that ξ is of order Ångstroms, making boundary effects difficult to observe. Very close to the transition it is clear that ξ can be much larger. To perform measurements with ξ in the range of tens of microns it is necessary to work with $t \sim 10^{-8}$. A high quality experiment spanning such a small temperature interval clearly puts severe demands on thermometry.

The theoretical predictions for cross-over behavior in the case of the lambda transition are not yet fully developed, due to computational difficulties below the transition. Nevertheless, significant progress has been made. Schmolke et al.[3] predict the effect of confinement in terms of a geometry-dependent function $f_1(x)$, calculated using renormalization group techniques. In this model, the heat capacity, C, can be written in the form:

$$C(t, L) - C(t_o, \infty) = L^{\alpha/\nu} f_1(x) \qquad (1)$$

where L is the confining dimension, $t_o = (1.41 \text{ Å} / L)^{1/\nu}$, α is the heat capacity exponent, and $x = t L^{1/\nu}$. In order to simplify the calculations, the curve has been calculated separately above and below T_λ. Data with $x > 100$ can be compared with the predictions of a bulk-plus-surface model, which treats the first order confinement effect as a simple surface effect. The predictions of Schmolke et al. for the whole region above T_λ are cast in terms of a function f_2 defined by:

$$C(t, L) - C(t, \infty) = -L^{\alpha/\nu} f_2(x) \qquad (2)$$

Similar behavior would be expected below the transition, but so far no quantitative predictions appear to exist. Knowledge of the surface specific heat term allows a straight-forward estimate of the free energy departure from bulk in the region where it is small. Through the transition region, the most detailed prediction is based on Monte-Carlo calculations[4]. These results are compared with the data below.

APPARATUS

The essential elements of the apparatus are the calorimeter, the high resolution thermometers (HRTs), the thermal control system (TCS), the helium cryostat and the electronics. The TCS was inherited from the Lambda Point Experiment (LPE) and modified slightly, and has been described in detail elsewhere[5]. The details of the other hardware specific to the present experiment have also been described[6]. Briefly, two HRTs are attached to the calorimeter and another pair to the inner stage of the TCS. The calorimeter is attached through a weak thermal link to the inner stage of the TCS which acts as a buffer from the outside world. This system attenuates thermal fluctuations through several isothermal stages controlled by germanium resistance thermometers and heaters configured in servo feedback loops. The helium cryostat[7], including monitoring and control electronics, is the major component of the Low

Temperature Research Facility developed by the Jet Propulsion Laboratory. It was first used on the SPACELAB-II mission and has now been successfully flown three times.

Thermometry

The construction of HRTs has been described in some detail elsewhere[8], however, some modifications[9] were made for the present experiment to improve the response time of the device. The paramagnetic salt is copper ammonium bromide, $Cu(NH_4)_2Br_4.2H_2O$, grown from aqueous solution onto a matrix of 76 high purity copper wires, which form a significant part of the thermal link to the calorimeter. The wires embedded in the salt are divided into seven bundles, each of which is soldered to a 1 mm copper rod. This rod is welded to a single 3 mm rod forming the main support of the assembly. All copper elements of the assembly are of very high purity and oxygen annealed to maximize their thermal conductivity at low temperatures. A schematic view of the arrangement is shown in figure 1. The 3 mm rod is welded to a copper cup which is indium-soldered to a sleeved post on the base of the calorimeter. All components of the thermal path are designed to minimize the thermal resistance between the salt and the helium.

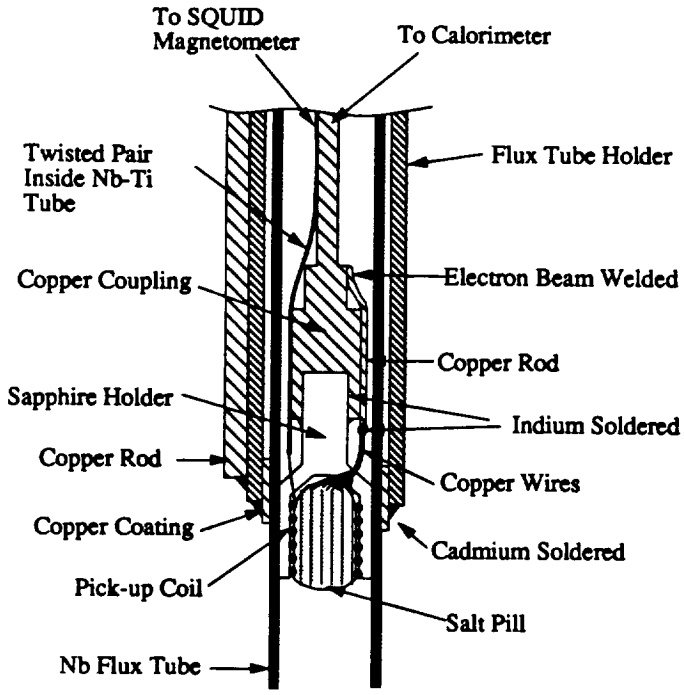

Figure 1: Schematic view of thermometer components.

Figure 2 shows a comparison of ground and flight data from one of the HRTs on the calorimeter. It can be seen that the ground data exhibits a peak-to-peak noise of about 0.5 nK whereas the flight data is slightly worse, with occasional large spikes. The excess noise appears to be due to the charged particle flux, with the large spikes generated by the more heavily ionizing components. The charged particle flux also introduces a temperature offset between the thermometer and the calorimeter estimated to be about 0.1 nK, due to heat dissipation in the salt, the Nb tube used to trap the applied magnetic field, and the sapphire holder surrounding the salt. To minimize these effects in the present experiment, the thermal link between

the salt and the calorimeter was improved as described above, and three annealed copper rods were soldered to the outside of the Nb tube holder. These rods helped transfer heat from the surroundings directly to the calorimeter instead of through the main thermal link between the salt and the calorimeter. Test results showed a response time of the HRT of about 0.12 sec as opposed to about 1 sec for the HRTs flown on LPE[10]. This implies an eightfold increase in the thermal conductivity of the assembly and a corresponding decrease in the temperature offset from the calorimeter. The low frequency noise from the thermometers was found to correspond to about 10^{-10} K/$\sqrt{\text{Hz}}$.

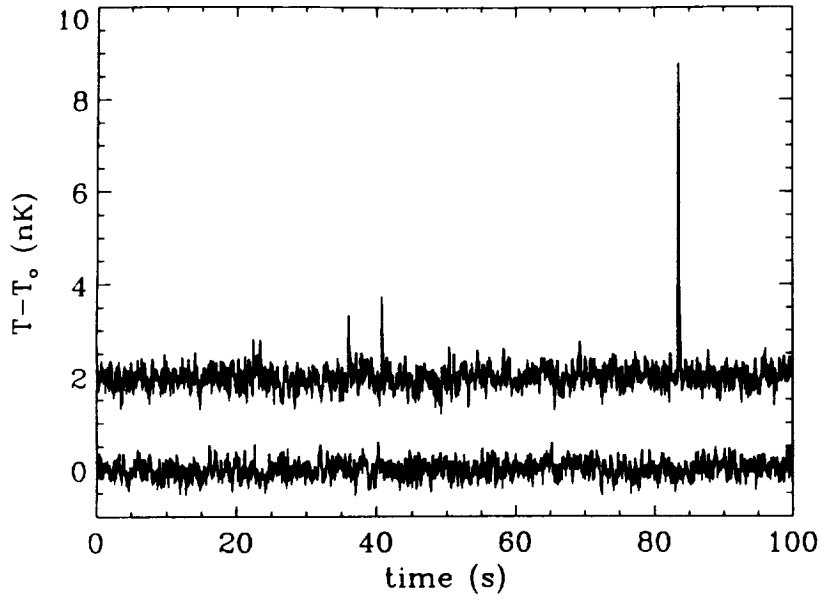

Figure 2: Comparison of the output from a thermometer on the calorimeter on the ground (lower trace) and in space (upper trace). Sampling rate was 25 Hz and bandwidth was 8 Hz.

Calorimeter

The calorimeter serves two main purposes: it maintains 60% of the sample in a confined state, and it provides the thermal coupling between the helium and the thermometers. The helium is confined in the gaps between uniformly etched (100) silicon wafers nominally 110 microns thick and 3.8 cm in diameter. One side of each wafer was chemically etched with potassium hydroxide to a depth of 57 microns, leaving 30 spacers in a grid-like pattern formed by photo-lithographic techniques. Most of the bumpers were nominally 500 microns in diameter, but three of them were 7 mm in diameter to support a 50 kg compression preload holding the stack of 408 wafers together. This preload was needed to avoid any slippage of the wafers during launch vibration, which could result in damage to the wafers due to collisions with the wall of the calorimeter. The wafers were epoxy bonded together into sub-stacks of eight to improve their structural rigidity. The large bumpers on one end of the sub-stacks and the corresponding regions on the mating substack were coated with a layer of indium 0.7 micron thick to increase friction between the sub-stacks. The sub-stacks were assembled within an invar cage which was used to apply the preload and hold the wafers away from the calorimeter wall. Invar was used because its

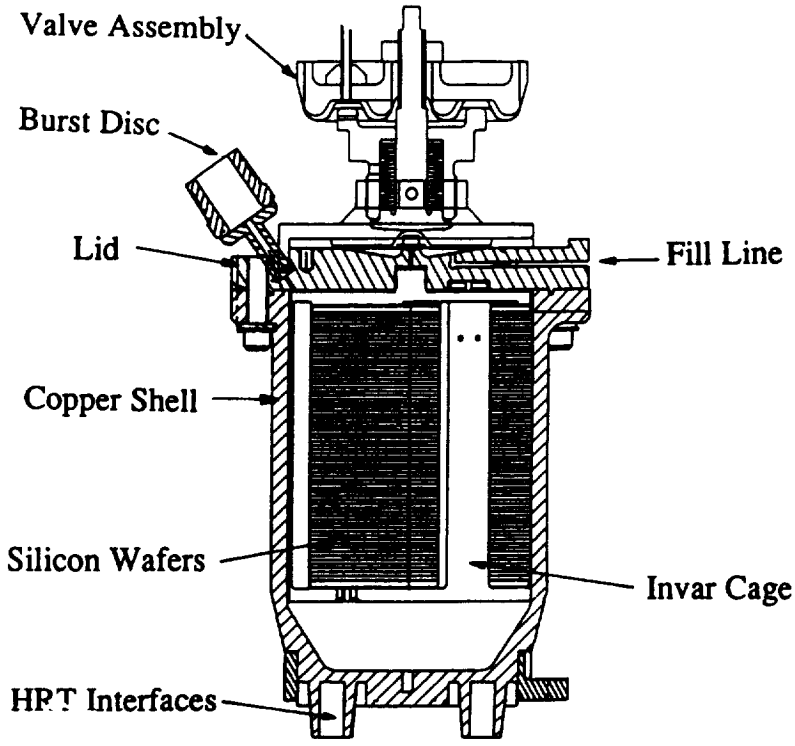

Figure 3: Cross-section of the calorimeter.

thermal expansion coefficient is a good match to that of the silicon-epoxy stack. The structure was then epoxied to a beryllium copper flange which served as the calorimeter lid, forming the interface to the fill line, a bubble chamber, a removable burst disc, a permanent burst disc, and a pressure actuated valve. The inside surface of this lid was electroplated with a thick layer of soft copper to decrease radial temperature gradients. The lid was attached to a calorimeter shell made of 99.9999% copper. Two HRTs were attached to the base of this shell. A cross-section of the calorimeter is shown in figure 3.

In contrast to the requirements of LPE[10], CHEX called for heat capacity measurements on both sides of the lambda transition, extending over a range of a few millidegrees. For this reason, internal thermal relaxation was a more significant issue than previously. Fortunately the high thermal conductivity of the single crystal silicon wafers reduced this problem to a manageable level. At 1 mK above the transition, the relaxation time of the whole assembly was found to be ~50 sec. On the other hand, very close to the transition, the thermal conductivity of the confined helium dominated, reducing the relaxation time to a few seconds.

PRELIMINARY RESULTS

The flight experiment passed through five main phases. After turn-on in orbit, the thermal control system was stabilized and the calorimeter was warmed to a point 20 mK below the transition temperature, where calibrations were performed. Then wide range heat capacity measurements were made below the transition, and the lambda point was located to within a few nano-Kelvins. Some high resolution data was then collected to map out the peak region. Next, data on the high temperature side was collected. The final

phase was to repeat the close-in scans for data averaging. Most of the measurements were made with temperature steps of 5 nanodegrees or larger to optimise the return from the experiment. However, some higher resolution measurements were attempted to explore the full capability of the apparatus. Figure 4 shows a heat capacity measurement with a temperature step of about $3x10^{-10}$ K. The step is well-resolved and the heat capacity was measured to about 10%. This measurement most likely represents the highest resolution heat capacity measurement ever. It would be useful in performing more advanced studies of the lambda transition in bulk helium.

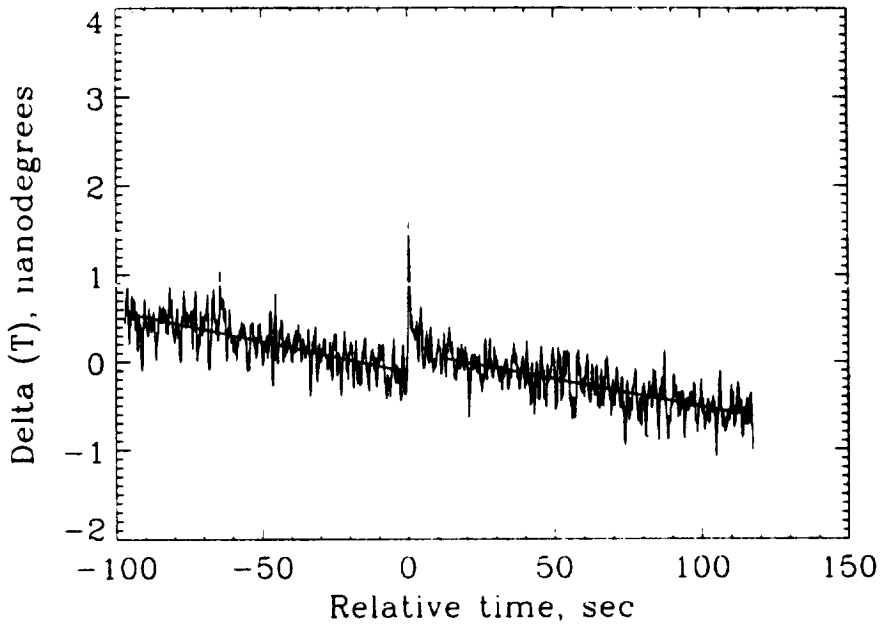

Figure 4: Temperature data vs time showing one of the smallest heat capacity steps performed during the CHEX mission. Temperature step: $3x10^{-10}$ K; heat capacity: 90 J/mole K.

Temperature calibration consisted of comparing the flux readings of the HRTs against the resistances of a pair of germanium thermometers over a 50 mK span. Heater calibration was accomplished by performing a set of heat capacity measurements at essentially constant temperature. The preliminary analysis shows that these sequences went well, with no significant changes from similar ground measurements. The main focus of the analysis has been the reduction of the noise on the heat capacity results. The primary noise source is thermometer noise, but other effects contribute to the overall uncertainty. A detailed evaluation taking into account the effects of thermal relaxation and cosmic ray heating is almost completed. So far, the cosmic ray effect appears to be fairly small, giving us confidence in the present level of analysis. The effect of vibration heating still needs to be looked at, but this is likely to be smaller than the cosmic ray effect, except at times of very large disturbances. Data over the full temperature range is shown in figure 5 on a semi-logarithmic scale, after subtracting the bulk contribution. In the figure, the results were bin-averaged at a density of 20 bins per decade of temperature difference from the bulk transition on the low temperature side, and 5 on the high side. Data from pulses that crossed the bulk transition were excluded. The finite size peak can clearly be seen in the figure. The dashed curve represents the bulk heat capacity, adjusted slightly to match the present data far from the transition.

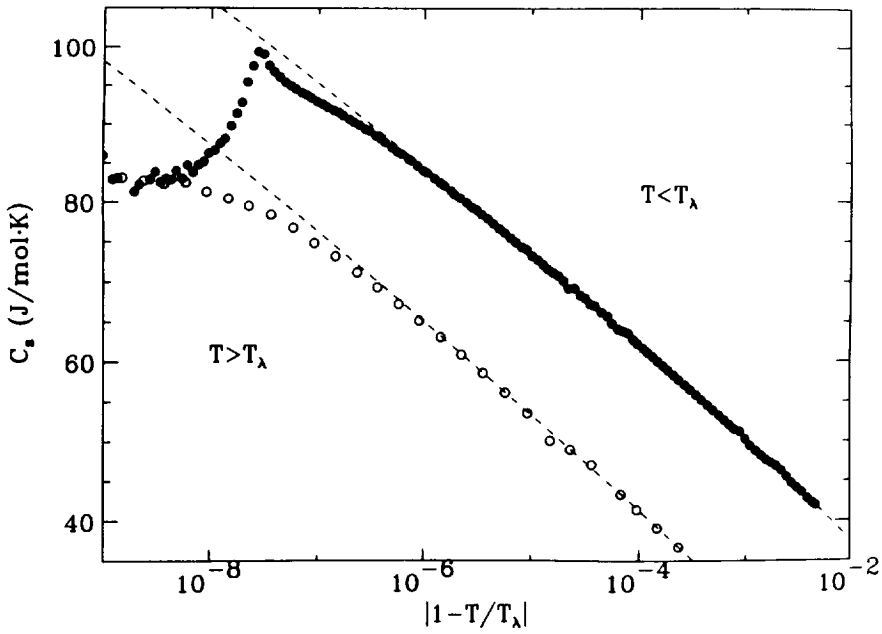

Figure 5: Heat capacity measurements over the full range measured on a semi-logarithmic scale. Each point represents the average of a number of measurements.

The heat capacity data close to the transition is shown on a linear scale in figure 6. Also shown are the results of Monte-Carlo simulations[4], and calculations by Schmolke et al[3]. It appears that the models are fairly representative of the measurements, but the effect of confinement is somewhat under-estimated. In figure 7a we show the surface specific heat data above the transition scaled as in eq. 2 for comparison with the theoretical function f_2. Over the range shown, the match is quite good. For x > 1000 or so, the scatter

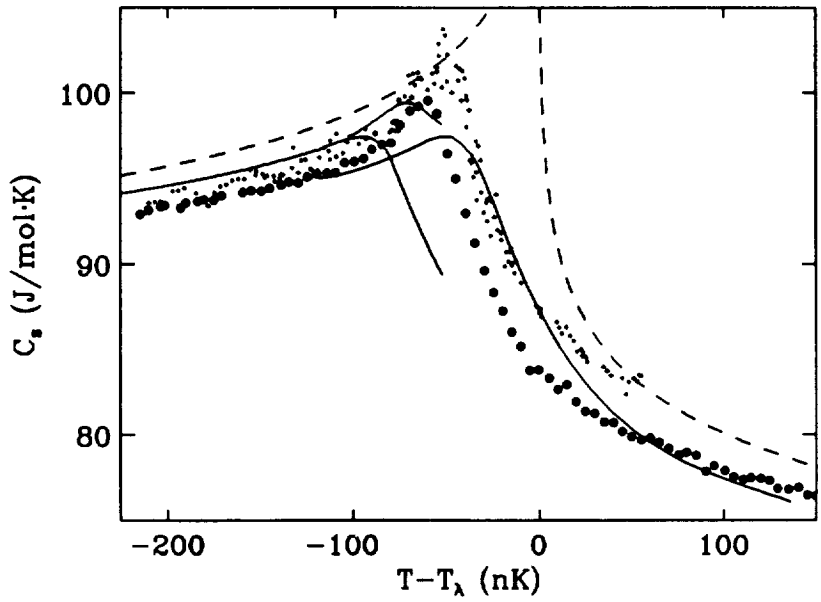

Figure 6: Heat capacity measurements close to the transition: • : present experiment; + : results of Monte-Carlo simulations; --- : bulk curve scaled to fit the data far from the transition; — : predictions of Schmolke et al.

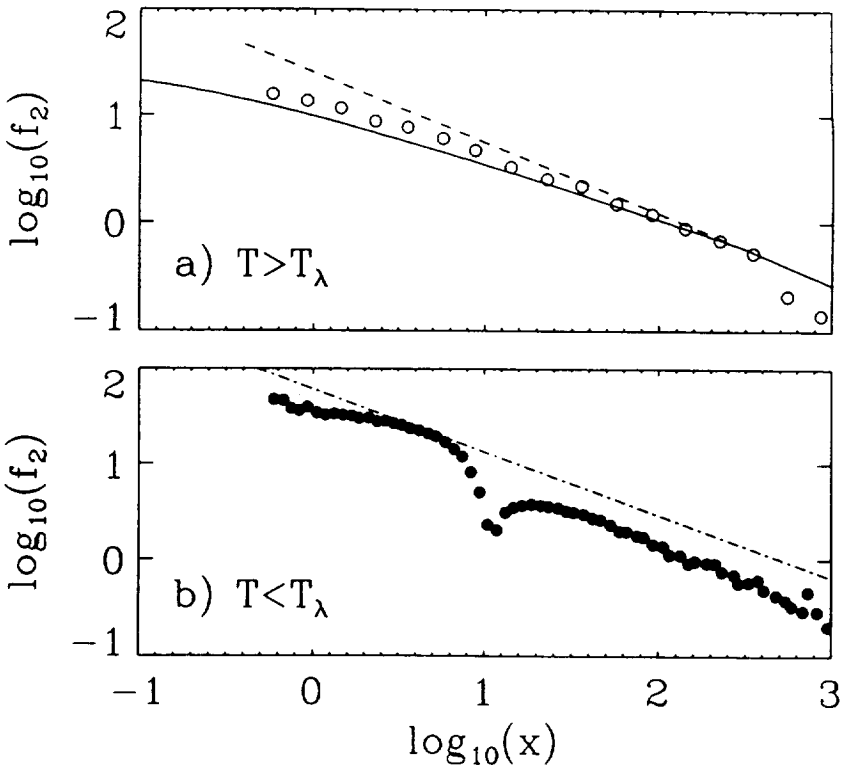

Figure 7a: Scaled surface specific heat results above the transition: lines: predictions of Ref. 3; b: Similar data below the transition: line: estimated surface specific heat.

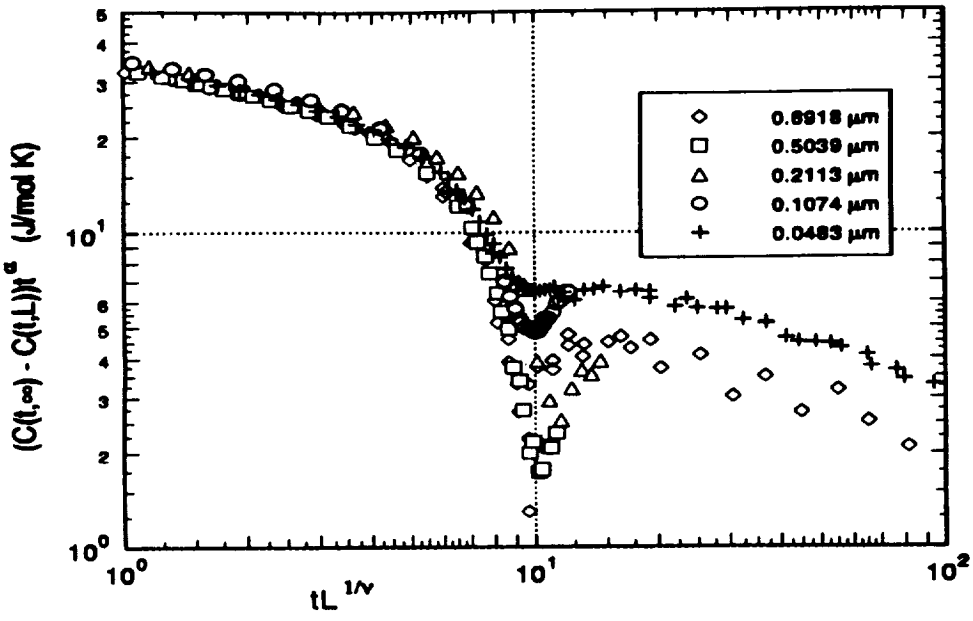

Figure 8: Comparison of scaled surface specific heat results below the transition obtained on various short length scales, from ref. 11.

in the data is still too large to say much. A substantial amount of processing is still needed for this region, including a better definition of the bulk heat capacity curve. In figure 7b we show similar results for below the transition. As yet, there is no firm theoretical prediction in this region, but we show as a broken line the estimated surface term, assuming that it has the same behavior as above T_λ, but scaled by the ratio ξ_o^+ / ξ_o^-. Figure 8 shows similar data as figure 7b obtained from ground experiments by Mehta and Gasparini[11] using much smaller length scales. It can be seen that there is a substantial amount of disagreement between the curves, indicating a possible breakdown of scaling over at least some of the temperature range. However, our results do not confirm the trend with length scale seen in their data, indicating a possible difficulty in their experiment. We are conducting additional ground measurements in an attempt to determine if this is a real effect.

Still to be included in the analysis is a substantial amount of data collected on the same sample before the flight. This data should contain some useful surface specific heat data after being corrected for the effect of gravity.

ACKNOWLEDGEMENTS

We wish to thank the Life Sciences and Microgravity division of NASA for its support with contract JPL 957448. We also thank the other members of CHEX team at Stanford and JPL for their many contributions to the development of the software and hardware, and the KSC and MSFC teams for their support with the launch activities and mission operations.

REFERENCES

1. J.F. Dobson, *Density Functional Theory* (Eds: E. Gross and R. Dreizler, NATO ASI Series B, #337), p. 397 (1995).
2. A. Singsaas and G. Ahlers, Phys. Rev. B, **30**, 5103 (1984).
3. R. Schmolke, A. Wacker, V. Dohm, and D. Frank, Physica B **165 & 166**, 575 (1990).
4. N. Schultka and E. Manousakis, Phys. Rev. Letts, **75**, 2710 (1995).
5. J. A. Lipa, T. C. P. Chui, J. A. Nissen and D. R. Swanson, Temp., its Meas. and Control in Sci. and Ind. **6**, 949 (1992).
6. D.R. Swanson, J.A Nissen, X. Qin, P.R. Williamson, J.A. Lipa, T.C.P. Chui, U.E. Israelsson, and F.M. Gasparini, J. Spacecraft and Rockets, **33**, 154 (1996).
7. T.S. Luchik, U.E. Israelsson, D. Petrac, and S. Elliott, Adv. Cryo. Eng. **41**, 1135 (1996).
8. J.A Lipa, B.C. Leslie and T.C. Wallstrom, Physica (Utrecht) **107B**, 331 (1981); M.J. Adriaans, T.C.P. Chui, M. Ndesandjo, D.R. Swanson, and J.A. Lipa, Physica B **169**, 455 (1991).
9. X. Qin, J.A Nissen, D.R. Swanson, P.R. Williamson, D.A. Stricker, J.A. Lipa, T.C.P. Chui, and U.E. Israelsson, Cryogenics **36**, 781 (1996).
10. J.A. Lipa, D.R. Swanson, J.A. Nissen and T.C.P. Chui, Cryogenics **34**, 341 (1994).
11. S. Mehta and F.M. Gasparini, Phys. Rev. Lett. **78**, 2596 (1997).

GROWTH OF SOLID SOLUTION SINGLE CRYSTALS

Sandor L. Lehoczky, F. R. Szofran, Donald C. Gillies, D. A. Watring

Space Sciences Laboratory
NASA Marshall Space Flight Center
Huntsville, AL 35812

1. ABSTRACT

The solidification of a solid solution semiconductor, having a wide separation between liquidus and solidus has been extensively studied in ground based, high magnetic field and Spacelab experiments. Two alloys of mercury cadmium telluride have been studied; mercury cadmium telluride with 80.0 mole percent of HgTe and 84.8 mole percent of HgTe respectively. These alloys are extremely difficult to grow by directional solidification on earth due to high solutal and thermal density differences that give rise to fluid flow and consequent loss of interface shape and composition. Diffusion controlled growth is therefore impossible to achieve in conventional directional solidification. The ground based experiments consisted of growing crystals in several different configurations of heat pipe furnaces, NASA's Advanced Automated Directional Solidification Furnace (AADSF), and a similar furnace incorporated in a superconducting magnet capable of operating at up to 5T. The first microgravity experiment took place during the flight of STS-62 in March 1994, with the AADSF installed on the second United States Microgravity Payload (USMP-2). The alloy was solidified at 3/4 inch per day over a 9 day period, and for the first time a detailed evaluation was performed of residual acceleration effects. The second flight experiment took place in the fourth United States Microgravity Payload Mission (USMP-4) in November 1997. Due to contamination of the furnace system by a previously processed sample, the sample was not received until May 1998, and the preliminary analysis shows that the conditions prevailing during the experiment were quite different from the requirements requested prior to the mission. Early results are indicating that the sample may not accomplish the desired objectives.

As with the USMP-2 mission, the results of the ground based experiments were compared with the crystal grown in orbit under microgravity conditions. On the earth, it has been demonstrated that the application of the magnetic field leads to a significant reduction in fluid flow, with improved homogeneity of composition. The field strength required to suppress flow increases with diameter of the material. The 8 mm diameter sample used here was less than the upper diameter limit for a 5T magnet. The configuration for USMP-4 was changed so that the material was seeded and other processing techniques were also modified. It was decided to examine the effects of a strong magnetic field under the modified configuration and parameters. A further change from USMP-2 was that a different composition of material was grown, namely with 0.152 mole fraction of cadmium telluride rather than the 0.200 of the USMP-2 experiment. The objective was to grow highly homogeneous, low defect density material of a composition at which the conduction band and the valence band of the material impinge against each other.

As indicated, the furnace was contaminated during the mission. As a result of solid debris remaining in the furnace bore, the cartridge in this experiment, denoted as SL1-417, was significantly bent during the insertion phase. During translation the cartridge scraped against the plate which isolates the hot and cold zones of the furnace. Thermocouples indicated that a thermal assymetry resulted. The scraping in the slow translation or crystal growth part of the processing was not smooth and it is probable that the jitter was sufficient to give rise to convection in the melt. Early measurements of composition from the surface of the sample have shown that the composition varies in an oscillatory manner.

2. INTRODUCTION

A major objective of this research is to establish the limitations imposed by gravity during growth on the quality of bulk solid solution semiconducting crystals having large separation between their liquidus and solidus temperatures. An important goal is to explore the possible advantages of growth in the absence of gravity, and to grow high quality material which will serve to provide fundamental electrical properties for the important $Hg_{1-x}Cd_xTe$ alloy system. The $Hg_{1-x}Cd_xTe$ system is extremely important in that x-values can be adjusted to be appropriate for infrared detector applications in the 8 to 14 μm region or the 3 to 5 μm range. The USMP-2 experiment concentrate on an x vaue of 0.200, while the USMP-4 experiment is targeted at the x = 0.152 composition. Both melt and Te-solvent growth methods as well as growth in magnetic fields are being considered. The study consists of flight experimentation and ground-based experimental and theoretical work needed to establish material properties and optimum experimental parameters for the on-going flight experiments, and to assist material evaluation. $Hg_{1-x}Cd_xTe$ is representative of several II-VI alloys which have electrical and optical properties that can be compositionally tuned to meet a wide range of technological applications in the areas of sensors and lasers with applications to optical computing and communications as well as the national defense.

The following specific objectives are deemed essential for accomplishing the primary objectives of the investigation:

1. By means of ground laboratory and flight experiments and concurrent theoretical analysis, establish quantitative correlation between growth parameters (translation rates, thermal fields, alloy compositions, and sample geometries) and growth interface shapes during the melt growth of $Hg_{1-x}Cd_xTe$ alloy crystals by unidirectional solidification.
2. Establish correlation between growth interface shapes and microstructural characteristics.
3. Develop theoretical models to delineate the effects of segregation, diffusion, and fluid flow in two dimensions on sample homogeneity and the solid-liquid interface shape during the melt growth of $Hg_{1-x}Cd_xTe$ alloy crystals and thus establish a fundamental understanding of the growth process.
4. Ascertain the relative effectiveness of ground-based stabilizing techniques (e.g., applied magnetic fields) for suppressing convective flow during melt growth of the crystals.
5. Establish ternary phase-equilibrium parameters for selected regions of the Hg-Cd-Te constitutional phase diagram required to model the Te-solvent growth process.
6. By means of growth experiments and theoretical analysis, establish quantitative correlation between growth parameters (growth rates, thermal fields, alloy compositions, and sample geometries), growth interface shapes, and microstructural characteristics for various Te-solvent growth processes.
7. Establish relationships between electrical characteristics and densities of charged and neutral defects for various growth conditions and thus correlate processing variables with the optical response of the processed alloy.
8. Evaluate the possible benefits of microgravity processing for device applications.

The investigation (Experiment No. MPS77F069) was originally selected based on the response to NASA OA-77-3 Announcement of Opportunity. The content of the current effort is based on an amended proposal submitted in response to Announcement of Opportunity OSTA-77-3 (formerly OA-77-3). Some of the initial work was done at McDonnell Douglas Research Laboratories under contract NAS8-33107.[1-7] The investigation is consistent with the committee recommendations resulting from the "Review of the Microgravity Science and Applications Flight Programs" conducted January - March of 1987. The majority of the ground-based studies are being performed in Space Sciences Laboratory of the George C. Marshall Space Flight Center.[8-57] In addition to crystal growth and characterization, this work has included thermophysical property determination, thermal modeling, phase diagram determination, fluid flow modeling, transient and diffusion analysis, and electronic property modeling. The flight portion of the investigation is being conducted using the Advanced Automatic Directional Solidification Furnace developed by the Marshall Space Flight Center and manifested for flights on the United States

Microgravity Payload series of missions.[71] The first flight of the instrument took place in March 1994 on STS-62.[58] The second flight took place on USMP-4 in November 1997 on STS–87.

3. STUDY RATIONALE

Segregation during solidification, high volatility of one of the components (Hg), and strain fields associated with large temperature gradients make the preparation of homogeneous, high-quality, bulk crystals of these alloys an extremely challenging problem. The usual melt or solvent growth methods tend to yield crystals with significant alloy compositional variations, many low angle boundaries, and second phase inclusions, e.g., Te-precipitates which we believe are at least partially caused by gravity-induced, thermosolutally-driven flows just ahead of the growth interface.

The reduction of the gravity-induced convection in a microgravity environment is expected to be advantageous for maintaining the crystal-melt interface shape required to minimize the densities of crystal defects while minimizing compositional variation transverse to the crystal growth direction. It is believed that CdTe, $Hg_{1-x}Cd_xTe$, etc. probably possess extremely small yield strengths near their growth temperatures. If this is the case, the high dislocation density ($\sim 10^5$ cm^{-2}) usually seen in these crystals could be due at least in part, to stresses induced by the sample's own weight, that is, self-induced stresses. Therefore, a second goal of these experiments is to assess the validity of this hypothesis.

4. ELECTRONIC PROPERTIES

4.1 Introduction

Over the duration of the investigation we have developed comprehensive theoretical models and computer codes specific to $Hg_{1-x}Cd_xTe$ for calculations of charge-carrier concentrations, Hall coefficients, Fermi energies, and electron mobilities as functions of x, temperature, and ionized-defect concentrations to establish correlations between electrical processing variables. [1, 6, 52-54, 77,78] The Kane three-band model [79] is used to describe the alloy band structure for the energy range of interest, i.e., the lowest-lying conduction band (Γ_6) and the two highest lying valence bands (Γ_8) for the normal band structure, as well as, the inverted band-structure, where the light-hole Γ_8 band becomes the conduction band and the heavy-hole Γ_8 band and the Γ_6 become the valence bands (Figure 4.1). The band transition is both composition and temperature dependent. The electron mobilities are calculated in terms of a microscopic theory of electrical conduction derived from the solution of the Boltzmann equation for the perturbed steady-state distribution function.

The secular equation describing the conduction, light-hole, and split-off-valence bands is

$$E^3 + (\Delta - Eg)\,E^2 - (Eg\,\Delta + P^2k^2)\,E - \Delta\,P^2k^2 = 0, \qquad 4.1$$

where E is the band energy in terms of the crystal momentum wave vector k, Δ is the Γ_{15} spin-orbit splitting, E_g is the Γ_6 - Γ_8 energy band-gap, and P is the momentum matrix element between the Γ_{15} valence-band and the Γ_1 conduction-wave functions defined by Kane.[79] The energies are referred to the top of the valence bands. The conduction, c, band and the light-hole, ℓh, band densities of states are given by

$$\rho_i(E) = \frac{k^2\,dk}{\Pi^2\,dE} = \frac{1}{2\Pi^2}\left(\frac{3}{2}\right)^{3/2}\frac{E^2_g}{P^3}\,\lambda_i \qquad (i = c, \ell h) \qquad 4.2$$

The crystal momentum as a function of energy is

$$k = \left(\frac{3}{2}\right)^{1/2} \frac{E_g}{P} s(\xi), \tag{4.3}$$

where

$$s(\xi) = \left[\frac{\xi(\xi - 1)(\delta\xi + 1)}{\left(\frac{3}{2}\delta\xi + 1\right)}\right]^{1/2}. \tag{4.4}$$

$$\xi = E/E_g, \tag{4.5}$$

and

$$\delta = E_g/\Delta. \tag{4.6}$$

The conduction-band wave functions are given by

$$|\vec{k},\ c,\ \pm\rangle = e^{i\vec{k}\cdot\vec{r}}\left[a\ |iS\alpha_{\mp}\rangle \pm b|(X \mp iY)\ \alpha_{\pm}\rangle + c|Z\alpha_{\mp}\rangle\right], \tag{4.7}$$

where x, y, and z are the basis set of Γ_{15} referred to a coordinate system with the x-axis along $\vec{k}$, S is the Γ_1 wave function, $\alpha_{\pm}$ are the Pauli spin functions for spin parallel (+) and anti-parallel (-) to k, and a, b, and c are functions defined by

$$a = [\xi(\delta\xi + 1)\ (\delta\xi + \tfrac{2}{3})]^{1/2}/N, \tag{4.8}$$

$$b = \sqrt{2}\ (\xi - 1)^{1/2}/3N \tag{4.9}$$

and

$$c = (\xi - 1)^{1/2}\ (\delta\xi + \tfrac{2}{3}))/N, \tag{4.10}$$

where

$$N = [\xi\ (\delta\xi + 1)\ (\delta\xi + \tfrac{2}{3}) + 2/9(\xi - 1) + (\xi - 1)\ (\delta\xi + 2/3)^2]^{2/3} \tag{4.11}$$

The heavy-hole, hh, band is represented by a simple parabolic band given by

$$E_{h\hbar} = \frac{h^2 k^2}{2m_o \mu_v}, \tag{4.12}$$

where μ_v is the effective-mass ratio.

4.2 Calculation of the Temperature Dependence of the Carrier Concentrations

The Fermi energy, E_F, electron concentration, n_e, light-hole concentration, $n_{\ell h}$, and the heavy-hole concentration n_{hh}, are calculated from the numerical solution of the charge neutrality equation,

$$n_e - n_{\ell h} - n_{hh} = N_D - N_A, \tag{4.13}$$

where

$$n_e = \frac{1}{2\pi^2}\left(\frac{3E_g k_B T}{2P^2}\right)^{3/2} \frac{1}{\beta^{1/2}} \int_{\beta^{-1}}^{\infty} dy\ \lambda_c(\beta y) f_o(y,z), \qquad 4.14$$

$$n_{\ell h} = \frac{1}{2\pi^2}\left(\frac{3E_g k_B T}{2P^2}\right)^{3/2} \frac{1}{\beta^{1/2}} \int_{o}^{\infty} dy\ \lambda_{\ell h}(\beta y) f_o(y,-z), \qquad 4.15$$

$$n_{hh} = \frac{1}{2\pi^2}\left(\frac{2\mu_v m_o k_B T}{h^2}\right)^{3/2} F_{1/2}(-z), \qquad 4.16$$

$$z = E_F/k_B T, \qquad 4.17$$

$$\beta = k_B T/E_g, \qquad 4.18$$

and

$$f_0(y,z) = (e^{y-z}+1)^{-1} \qquad 4.19$$

In equation 4.16, $F_{1/2}(-z)$ is the Fermi function of order ½, N_A and N_D are respectively the number of acceptors and donors per unit volume, k_B is the Boltzmann constant, T is the absolute temperature, m_0 is the free electron mass, and $y = E/k_B T$.

The electron mobility calculation includes the following scattering mechanisms: longitudinal-optical phonon (LO), longitudinal- and transverse- acoustical phonon (AC), heavy-hole (hh), and alloy disorder potential (dis.). The extrinsic scattering mechanisms include charged (ii) and neutral point defects (nd). The current densities, conductivities, and mobilities are calculated from the perturbed electron distribution function $f(\vec{k})$ given by

$$f(\vec{k}) = f_o - kc'(E)\ f_o' \cos\psi, \qquad 4.20$$

Where f_o is the unperturbed distribution function and $f_o' = df_o/dE$. The quantity ψ is the angle between the wavevector k and the applied electric field. The perturbation function c'(E) depends only on energy. The current density is given by

$$J_x = \frac{e}{3\pi^2\hbar} \int_{E_g}^{\infty} k^2 c'(E)\ f_o' dE, \qquad 4.21$$

where e is the electronic charge, $\hbar$ is Planck's constant, and c'(E) is given by the solution of the Boltzmann equation,

$$\frac{\partial f(\vec{k})}{\partial t} = \sum_i \left(\frac{\partial f}{\partial t}\right)_i + \left(\frac{\partial f}{\partial t}\right)_F \quad (i = LO,\ ac,\ eh,\ dis.,\ ii,\ nd). \qquad 4.22$$

the sum, $\sum_i \left(\frac{\partial f}{\partial t}\right)_i$, is the rate of change of the distribution function caused by the various scattering mechanisms, and $\left(\frac{\partial f}{\partial t}\right)_F$ is the rate of change of the distribution function caused by the application of a static electric field. For the steady-state,

$$\frac{\partial f(\vec{k})}{\partial t} = 0 \qquad 4.23$$

and

$$\sum_i \left(\frac{\partial f}{\partial t}\right)_i = -\left(\frac{\partial f}{\partial t}\right)_F . \qquad 4.24$$

The field term is given by

$$\left(\frac{\partial f}{\partial t}\right)_F = \frac{\mathscr{E} e}{\hbar} f_o' \cos\psi , \qquad 4.25$$

where $\mathscr{E}$ is the applied electric field. The scattering term is given by [80]

$$\sum_i \left(\frac{\partial f}{\partial t}\right)_i = -\frac{1}{k_B T} \sum_i \int V_i(k, k') \, [kc'(E) - k'c'(E')] \, d\underline{k}' \cos\psi , \qquad 4.26$$

where

$$V_i(k, k') = W_i(k',k) \, f_o(k') \, [1 - f_o(k)] = V_i(k',k). \qquad 4.27$$

$W_i(k',k)$ is the transition probability per unit time per unit volume and is given by

$$W_i(k',k) = \left| H_i(\underline{k}', \underline{k}) \right|^2 \left(\frac{1}{4\pi^3 \hbar^2}\right) \Omega \, (E_{\underline{k}'} - E_{\underline{k}} \pm E_S), \qquad 4.28$$

where $H_i(\underline{k}', \underline{k})$ is the matrix element for scattering from state $\underline{k}$ to $\underline{k}'$ for a given scattering process, Ω is a delta function, and E_s is the energy absorbed or emitted in the scattering process.

Equation 4.23 reduces to a linear finite-difference equation in c'(E), and the conductivity is determined from equation 4.20 by using the variational method of Kohler[77] as modified by Howarth and Sondheimer [78] and Ehrenreich.[79] the perturbation function is expanded in a complete set of trial functions,

$$c'(E) = \sum_{n=0}^{\infty} c_n \phi_n(E), \qquad 4.29$$

and the c_n are determined by the requirement that c'(E) be a stationary point [77] of a certain conserved integral.

The various scattering mechanisms and their contributions to the Boltzmann equation are summarized in Appendix A of reference 1.

4.1 Recent Calculations

Recent calculations of the composition dependence of the intrinsic electron concentration and electron mobilities at 25, 77 and 300 K are shown respectively in figures 4.2 and 4.3. Figure 4.4 shows the composition dependence of the electron effective mass. As seen in the figures, the electrical properties near the band cross-over show extreme sensitivity to compositional variations. This is primarily due to the large reduction of the effective mass as the band cross-over composition, x = 0.152, is approached. Figures 4.5 and 4.6 show the calculated results for the case of a donor (N_D) concentration 1 x 10^{15}cm^{-3} and an acceptor concentration (N_A) of 1 x 10^{13}cm^{-3}. A comparison of the results with the intrinsic case illustrates the strong influence of even small charged defect concentration near x = 0.152.

5. DRIVING FORCE FOR CONVECTION

As noted earlier, both melt and Se- and Te-solvent growth are subjects of the proposed investigation. Because of the relative maturity of the ground-based melt-growth method compared with solvent growth, the unseeded melt growth of HgCdTe alloys by Bridgman-Stockbarger-type directional solidification was the primary method selected for the initial USMP flight experiments. On Earth the Hg-rich component rejected during solidification is more dense then the original melt and the vertical Bridgman-Stockbarger growth process would appear to be both gravitationally and thermally stable against convection. However, this is not generally true. Due to the peculiar relationships between the thermal conductivities of the melt, solid, and ampule, it is not practicable to completely avoid radial temperature gradients in the growth region in these alloys. Because of the high Hg partial vapor pressures involved at the processing temperatures, the confinement of the alloys requires the use of very thick fused silica ampoules which have thermal conductivities comparable to those of the alloys. This, when combined with the large (a factor of 4 to 10) decrease in the thermal conductivities of Hg-alloys upon freezing, leads to isothermal surfaces near the melt/solid interface that are bowed into the solid. Although the interface under this condition is neither an isothermal nor an isocompositional surface, it is bowed in the same direction as the isotherms near it. We have developed a method that relies on a careful control of radiation heat transfer near the growth interface to minimize the effect for this type of growth system.[26] Nevertheless, the wide separation between the liquidus and solidus boundaries of each of the pseudobinary phase diagrams (by causing the growth interface temperature to undergo large changes during growth and yielding growth rate dependent thermophysical properties in the melt just ahead of the interface) makes a complete elimination of the radial temperature gradients in the vicinity of the interface nearly impossible. Thus, in spite of the stabilizing influence of the solutal density gradients, intense thermally-driven fluid flows will occur in a narrow region near the interface, that will control the extent of radial compositional-segregation in a gravitational environment.[59,62-64,68,69] An example of the flows induced during the terrestrial growth of HgCdTe is shown in Figure 5.1.[64] The second experiment, on USMP-4, took the lessons learned from USMP-2 and applied them to the growth of a different alloy, namely $Hg_{0.848}Cd_{0.152}Te$.

Frequently, the desirable surface geometry for crystal growth is planar or nearly so. Usually, however, the optimum interface shapes tend to be those that bow slightly into the melt, because such interface shapes favor grain selection and the outgrowth of extended line defects. These shapes are expected to produce ingots with better crystal perfection. While such shapes are difficult to obtain for these alloys, they may be achievable with judiciously chosen thermal boundary conditions. Under the influence of the stable flow conditions during fast growth, such interface geometries exacerbate lateral alloy segregation because of the tendency of the more dense Hg-rich liquid to settle at portions of the surface having the lowest gravitational potential. Due to the decrease of the alloy solidus temperatures with increased Hg-concentration, the interface temperature at this portion of the interface will be lowered, causing an increase in the interface curvature. Thus, a potential interface instability can result from the "settling" of the rejected Hg-rich solvent into the lowest-lying regions of the interface. Lateral diffusion and incomplete convective mixing will have the tendency to drive the interface melt compositions to some equilibrium value, but most ground-based melt-growth experiments involving the alloys show large radial compositional variations that are probably a direct consequence of such an interfacial fluid flow phenomenon. Although the growth at very slow rates, under the influence of reduced stabilizing composition gradients and thus non-steady flow conditions, tends to yield radially more homogeneous ingots, generally, no ingots could be obtained by the Bridgman-Stockbarger method that were simultaneously radially and axially homogeneous for any substantial length.

6. ADVANTAGES OF MICROGRAVITY GROWTH

In microgravity it is expected that the highly-desired, slightly-convex growth surfaces will be easier to maintain because of the reduced tendency for stratification of the denser (Hg-rich) fluid components at the higher growth rates that are usually needed to obtain solute conserving steady state growth and thus axial compositional uniformity. At the same time, the near-elimination of

transverse temperature gradient-driven incomplete mixing effects is expected to provide for a better control of the lateral compositional distribution in the melts, and stresses resulting from hydrostatic pressure will be nearly eliminated. We thus expect that by growing under the influence of low-gravity condition, crystals with significantly improved crystallinity and compositional homogeneity can be prepared as compared to the best crystals that can be produced on Earth. It is also reasonable to expect that careful characterization of both the space- and ground-growth materials will lead to better insights into the peculiarities of the various growth mechanisms, permitting improvements in Earth-based processing of semiconductor alloy systems.

7. ADVANCED AUTOMATED DIRECTIONAL SOLIDIFICATION FURNACE

The Advanced Automated Directional Solidification Furnace (AADSF) is a five zone tubular furnace module, with a total length of 381 mm. The tube diameter is 25.4 mm, and is restricted by an insert of 19.1 mm. This insert effectively separates two zones, which can be independently set at constant temperatures. A Bridgman-Stockbarger furnace configuration consisting of a "hot" and a "cold" zone, separated by a radiation barrier is thus readily achievable. The five heating zones are strategically sized to enable one to obtain uniform temperatures in the hot and cold zones. Short "guard" heaters are located at the top of the hot zone and the bottom of the cold zone to limit the thermal losses and consequent drop in temperatures at the ends of the furnace bore. Two of the other heating elements are the hot and cold main heaters respectively. Finally, there is a small "booster" heater (6.4 mm long), located at the cold end of the hot main heater. The purpose of this heater is to increase the temperature gradient at the boundary between the hot and cold zones. The hot and cold zones are respectively 254 and 127 mm in length. The furnace heater zones consist of beryllium oxide cores wrapped with platinum-rhodium (60/40) furnace wire. The heater element assembly is known as the Experiment Apparatus Container (EAC). The outside diameter of the EAC is 203 mm, with cooling loops which used freon for the flight experiment and water for the ground tests.

For materials science experiments involving solidification, the control of temperature and the position and shape of isotherms is most important at the boundary region between the hot and cold zones. In addition to the booster heater and the insert, this part of the furnace is reconfigurable. A heat extraction plate separates the two regions, while on each side of it, there are insulating layers. The thickness of these layers can be changed to modify the thermal characteristics. In general, thin layers will result in the highest temperature gradient, while thicker layers will produce a somewhat reduced gradient, but with flatter isotherms. For the USMP-4 experiment, medium thicknesses were used (8.6 mm for the hot plate, 3.2 mm for the heat extraction plate and 15.2 mm for the cold plate). Ground based testing had demonstrated that this configuration gave a flatter solid-liquid interface than the configuration used in USMP-2, while still maintaining the necessary temperature gradient. Thermal modeling of the furnace has been done by Rosch.[75] Schematic diagrams of the furnace configuration and the insulation or adiabatic region are shown in Figures 7.1 and 7.2.

In addition to the EAC, AADSF consists of two other components, namely the Data Acquisition System (DAS), and the Signal Conditioning and Control System (SCCS). The DAS consists of a 16-bit microprocessor which controls the command and data interfaces. It provides discrete inputs, analog inputs, serial/digital input/output ports and relay drivers. It is through the DAS that uplinked commands are received and processed. The DAS then transmits the commands to the SCCS. The SCCS controls the furnace parameters for the five zones, and can operate autonomously with pre-programmed parameters or can receive uplinked commands from the DAS to modify experimental parameters during the mission. The SCCS also transmits data to the DAS for downlink.

For USMP-4, the AADSF was modified to accommodate three samples. Each of the samples can be rotated in turn to the position of the furnace bore for processing. It is the sample which translates; speeds are nominally from 0.5-50 mm/hr. The AADSF, with the EAC housing removed is shown in Figure 7.3. The assembly has been described by Gillies et al.[71]

8. RESULTS FROM USMP-2

Previously explained in other references,[58,65,66] Figure 8.1 shows the effect of the steady state component of residual acceleration. Even thought the total level is well below $10^{-6}g_0$, there is a clear indication that the composition distribution tracks the direction of the residual acceleration vector. Following a change to the flight attitude of the orbiter (figure 8.1b), the homogeneity improved and is better than observed on the ground with comparable growth conditions. In this case the residual axial vector is pointed from liquid to solid and is hence stabilizing. The composition nevertheless aligns along the direction of the transverse vector. Results such as these demonstrated that the direction of any residual vector is of more consequence than its numerical value, and the requirements for USMP-4 were that there be a high positive ratio of axial to transverse vectors, with the axial directed from liquid to solid.

9. GROUND-BASED PREPARATIONS FOR USMP-4

9.1 Ampoule Load Preparation

As indicated, the USMP-2 experiment required ten days to complete the growth of the boule. For many reasons it is not possible to maintain the same attitude of the orbiter for this long a period, and so in order to decrease the time required for reaching steady state, the composition of the mercury cadmium telluride boule was arranged such that the starting solid material approximated the composition the boundary region of the solidifying liquid would attain while in the steady state growth regime. The final transient for a boule grown at 0.1 μm/s assumes a composition profile which is close to the diffusion boundary layer in a boule solidified at 0.2 μm/s, the desired growth rate for the USMP-4 experiment. This is illustrated in Figures 9.1 and 9.2. These curves are based on equations quoted by Smith et al [67] as evaluated by Clayton et al. [14]

Precursor boules were grown at 0.1μm/s in a single zone furnace containing a heat pipe furnace. At this translation rate the gradient achieved was sufficient to avoid constitutional supercooling. The temperature profile as recorded by thermocouples within the cartridge is shown in Figure 9.3, and demonstrates a gradient of 30 degrees C/cm at the freezing temperature. For precursor growth the solidification ampoules were fabricated from fused silica and were enclosed in Sample Ampoule Cartridge Assemblys (SACA), recovered from the Crystal Growth Furnace (CGF) program. The ampoule inner diameter was nominally 8 mm, but a selection was made to deliberately choose slightly undersized material from the fused silica stock. Similarly, the crystal growth ampoules were chosen to be slightly oversized. Figure 9.4 shows a typical composition profile for the boule after the slow growth. The composition has been determined by energy dispersive spectrometry (EDS) from electron beam excited x-ray generation in a scanning electron microscope (SEM), and by computed tomography (CT) using a radioactive cobalt source.[73] The EDS data represent the surface composition, while the CT results are determined by high energy gamma ray absorption. They are equivalent to density measurements as done by precision weighing. The CT technique is non-destructive in that no cutting of the sample is necessary to produce the readings. To prepare the boules for crystal growth, the data such as are obtained from Figure 9.4 were used to determine locations at which to cut these boules to provide the boundary region of the desired compositional profile. The desired composition has a CdTe mole fraction (x) of 0.152, which is in equilibrium with a liquid of x = 0.05. The positions on the boule at which cuts were made are shown in Figure 9.5. The first cut corresponds to the region on the boule where the material is at the end of the initial transient region. As the desire was to obtain as much material from the flight experiment as possible, it was decided not to use the initial transient composition, but to use quenched material from another boule which would serve as a reservoir of material of constant x = 0.152 material. Thus the boules were loaded to give 10 cm of material, of which 5 are of "steady state liquid" material and 5 cm are of constant composition produced by rapid solidification. A complete set of these precursor boules is shown in Table 9.1. During the early part of the program, attempts were made to coat the inside of the ampoule with boron nitride. While the process seemed to work, the resulting castings were no better than carbon coated ampoules used previously. For the

precursor work, it was found that careful cleaning procedures produced clean, non-sticking boules. For the final loading and crystal growth the ampoules were "graphitized."

It can be seen that several different lengths of boule were used for the precursor boules. It was found that the 12 cm boule furnished only the bare minimum amount of final transient material, and so a change was made to grow 15 cm lengths. Growth of 18 cm lengths was also attempted, but the length of the sample was longer than the uniform temperature region of the furnace, and these boules could only be used as quenched material. In an attempt to reduce the convection and produce radially uniform material in the final transient region, one boule was grown in the magnetic field. Analysis of this boule had not yet been completed.

Two compositions were prepared. For the primary experiment, the cadmium telluride mole fraction was 0.152, and the boules identified as MCT-152-XX. The secondary experiment used a composition of x = 0.200 to complement the UMSP-2 flight. As can be seen, far less of the 0.200 composition was prepared.

9.2 Ampoule/Cartridge Design

The ampoule design was changed from the USMP-2 configuration. As has been mentioned, in the USMP-4 mission the idea was to melt back the sample onto precursor material of a composition simulating the liquid region. When back melting in space it was felt that the composition in the liquid would be retained, although on the ground considerable mixing would take place. It was also felt important that the samples be seeded with a single, oriented crystal of cadmium telluride. The melting point of CdTe is more than 300 degrees C higher that the melt back material, and so successful seeding of the material could be done with little melt back or dissolution of the seed material. To accommodate the seed, the ampoule design was as shown in Figure 9.6. The bottom of the ampoule was then closed with a flat 1 cm fused silica plug. First a graphite cylinder was loaded to improve thermal conduction properties, followed by the seed crystal. The seed was <111> oriented and placed such that the B (Te) face was the growth direction. The precursor boules were then loaded, with at least two and occasionally three pieces necessary to create the entire load. At the top of the ampoule, fused silica wool was added to cushion the material during the stress of launch. Vibration tests of both the ampoule and the assembled cartridge demonstrated that the design was satisfactory. Following the sealing of the fused silica with a hydrogen/oxygen flame, the ampoules were each heated to 625°C for 12 hours to proof test and stress relieve the seal.

The cartridges were fabricated mainly by Teledyne Brown Engineering with two also made internally at Marshall Space Flight Center. The external design was similar to that of USMP-2, but internally changes were made for two reasons. Firstly, the sealing weld to close the tube was difficult to reach with a welding torch, and trials with O-rings demonstrated that the assembly would hold the applied pressure. More importantly, the design was changed to accommodate six thermocouples which were strategically located along the length of the sample ampoule. With respect to the ampoule, two were at the cold end, two were alongside the center of the CdTe seed crystal, one was a cm above the seed and one was two cm above the seed. In this way the progress of the melt back interface could be monitored as the sample was brought into the furnace, and the thermocouples also assisted in the thermal profiling of the assembly to provide data for future experiments. A radiograph of a typical cartridge/ampoule assembly before growth is shown in two magnifications in Figure 9.7. In the higher magnification view of SL1-420, all six thermocouples are visible. This is not often the case as the objective of the design is to distribute the thermocouples radially such that the four longer ones are at 90° from each other. The loading procedure does not permit exact positioning, but this is not an operational problem; x-radiographs such as these are used to determine the exact positions. Also visible is the shoulder at the top of the seed. Thus it is possible to measure precisely the distance of all the thermocouples relative to the seed and to the end of the cartridge. The latter measurement enables an exact correlation to be made between the entire sample and the furnace reference frame.

9.3 Timeline for Ground Experiments

As indicated, the ampoule preparation design involved a slow growth of 12-18 cm of material to prepare the precursor or starting material for the crystal growth. Typically this took a month or more. Preliminary tests with a calibration sample of a set of four thermocouples within alumina tubes, and experience gained from the USMP-2 mission were used to set the furnace set points. The furnace had been re-configured since USMP-2 and included a longer adiabatic region (2 cm). While this reduced the temperature gradient, the added insulation had the advantage of reducing the radial heat loss in the solidification region, and hence led to a flatter interface.

The objectives of the ground experiments were:

1. To establish the optimal set points for the five zones within the furnace. This entails determining the position of the liquid-solid interface relative to the furnace frame, the shape of the interface and the temperature gradient within the liquid region adjacent to the interface.
2. To determine favorable melt back conditions such that the precursor material melts back completely to the seed without dissolving any excess cadmium telluride from the seed. These conditions should also accentuate the chances of producing epitaxial growth and an oriented single crystal from the seed. There are two possible end points for this determination. The first of these is the use of the translation position on the furnace, assuming that the isotherm positions are well known. The other method is to make use of the thermocouple readings within the cartridge itself. As the calibration samples were quite different in properties from the mercury cadmium telluride assembly, it was felt that there would be a clear difference between these two techniques.
3. To establish the optimal time for holding the melt after back melting and prior to starting the slow crystal growth. These conditions are desirable to ensure that all the material is molten, and that any radial segregation remaining in the precursor material is removed.
4. To establish a safe, but rapid translation rate for removing the sample from the furnace at the end of the crystal growth period of the timeline, and hence obtain the most representative indication of the liquid close to the solidifying interface.
5. To establish the techniques for fully characterizing the material such that the science objectives of the mission could be obtained. The amount of material is limited to 3.5 cm. In ground based experiments it was felt that there would be sufficient convection during the melt back that the pre-arranged "boundary layer " composition would be removed and so even less material would be available for characterization. The analysis required includes compositional mapping at a high degree of accuracy, precision and spatial resolution. A need for examining the interface is important so that some of the material needs to be sectioned through the interface region. For electrical property measurement, the need is for the most homogeneous material; this would come from the last to freeze of the slow growth material and would require a wafer cut across the crystal. Another important issue in crystal growth in microgravity is the potential for the elimination of defects. Thus a study of the defect density is also important. Ideally this would be done on oriented planes for etch pit density and triple axis x-ray diffractometry measurement. These needs are not always compatible with each other.

Of these five issues, the first four basically define the time line for the flight experiment. The experiments with the cartridges listed in table 9.2 were designed to fulfill the objectives, while the characterization tools were optimized with the products from the crystal growth experiments. The timeline which evolved is shown below:

1. From the phase diagram of HgTe-CdTe determined by Szofran and Lehoczky[3], the liquidus for the x=0.152 material is at 763°C, and the solidus at 698°C. For the x=0.200 alloy these temperatures are 795°C and 705°C respectively. The cartridge is initially positioned in the furnace such that the top of the solid is 1 cm beyond the estimated liquidus isotherm.

2. While the length of the MCT charge after melting is not known exactly, the solid charge was generally within a mm of 10 cm. The melt back was done by moving at 10 mm per hour for 10 hours so that the material is liquid down to within 1 cm of the seed. The translation is then slowed to 2 mm/hr, and stopped when the end point is reached. This end point is generally estimated from the furnace position, and finally determined from the thermocouple readings adjacent to and just above the seed. It should be noted that during this entire melt back procedure, thermocouple readings give a temperature profile of the furnace.
3. After a predetermined time, crystal growth is initiated by reversing the translation direction and removing the sample at 0.2 μm/s (or 0.72 mm/hr). The actual nominal growth time, which was limited by anticipated flight constraints, was 48 hours.
4. After the nominal time the sample was translated from the furnace. This rate was 10 mm/hr in the first experiments, but was increased to 5 cm/hr in later tests and in the flight sample itself. Some crystals were solidified at 0.72 mm/hr to completion.

During the test no adjustments to the furnace zone temperatures were made, but from run to run changes were made to ensure that the cold end furnace elements were drawing power and hence controlling the temperature. The hot zone temperatures and booster heaters were also adjusted to move the interface position lower in the furnace and hence flatter. In general, the interface curvature was of the order of 1mm displacement across the 8 mm diameter, with the material concave looking form liquid to solid. The temperature gradient, as measured with thermocouples alongside the sample was approximately 60 degreesC/cm.

9.4 Preliminary Growth Results

Unlike the USMP-2 experiments, with the exception of the magnetic field growth, all ground experiments were made in either the flight unit or the Ground Control Experimental Laboratory (GCEL). The first test run was made from February 28 - March 1, 1997 and was run in the GCEL. The sample cartridge assembly, SL1-415, had previously been through a vibration test to simulate the loads anticipated during the mission, and was thoroughly tested prior to running in the furnace. This included a test of the integrity of the seal, and radiography. A radiograph of the sample after the vibration testing is seen in Figure 9.8. The test for the seal integrity was successful during a helium leak test. The radiography showed that the sample integrity was maintained and that the fused silica wool evidently was preventing any movement of the sample. Some powdering of the boron nitride and the sample material has taken place. The longest of the thermocouples, which was open-bead, unfortunately broke. As this is not a safety issue it was decided to proceed with the test. Following the test, the cartridge assembly was opened, and a small chip which had broken from the lower ampoule support was found together with associated boron nitride dust. The broken bead from the thermocouple was also found. These small mishaps were not believed to be significant as the vibration test loads are in excess of the real flight loads. As will be reported later, all thermocouples maintained their integrity and behaved perfectly during the mission.

The thermocouple readings during the running of a parallel test with sample SL1-413 are shown in Figure 9.9. The thermocouples positions have been normalized to the furnace frame using measurement taken from the radiographs, and so represent a temperature profile of the sample within the furnace itself as a reference. This became general practice for all the growth tests. The test constituted the thermal verification test for the flight furnace in the new configuration which includes a sample exchange mechanism to accommodate three samples. The procedure was designed to test the exact flight line but with continuity from the first sample (A. Fripp, NASA Langley Research Center). In the real flight, the furnace avionics were switched off during the mission, and this had a small, but insignificant effect on the processing of the flight sample. This will be described later.

The sample was removed by dissolving the silica glass in hydrofluoric acid. A series of back reflection Laues x-ray photographs was taken of the sample including the seed and at 5 mm intervals along the slow growth region. This was done to confirm that epitaxial growth from the seed had occurred. The Laue technique was later superseded by the use of electron back scatter patterns (EBSP) within the SEM. Normal practice was to take EDS readings to determine the

composition of the surface layers. Often the surface was irregular or covered with vapor grown or other deposits and it was necessary to etch in bromine-methanol to produce meaningful EDS results. Later with careful experimentation it became possible to take precise WDS readings on these curved surfaces. These techniques have been described by Carpenter et al.[76]

Some typical results are shown in Figures 9.10 and 9.11. A cross section was cut of the sample from the seed through the entire slow grown region, and carefully chemo-mechanically polished in a 2% bromine/ethylene glycol solution. This region was analyzed using an electron microprobe analyzer. Quantitative WDS data were made in an axial direction at the center line and 1 mm in from each edge. The results are shown in Figure 9.10, and clearly demonstrate that the pre-processed layer is not maintained during the back melting on earth. Nevertheless, close to steady state conditions have been obtained in a short sample and there is no lag during translation while nucleation takes place. In comparison to the USMP-2 configuration, this experimental design saves 2-3 days of processing to reach this stage. There is also some evidence of radial inhomogeneity, but less than has been seen on the previous configuration. A two dimensional view of this sample as represented by raw cadmium count data is shown in Figure 9.11. Superimposed are some radial profiles with the full quantitative corrections of atomic number, absorption, and fluorescence (ZAF) applied. The degree of homogeneity is better than achieved with the conventional Bridgman growth and in the flight experiment in USMP-2. The dendrites resulting from the rapid translation are also visible. Of significance is that they are not parallel to the direction of withdrawal from the furnace and the simple explanation is that there is a large radial cooling component. This was the reason for increasing the quench rate in the later experiments and the flight experiment.

9.5 Ground Truth Results

After the mission, three ground truth samples were processed. These were different from the preliminary experiments reported above in that the experimental parameters were identical to those in the flight sample. The real mission permitted 50 hours 43 minutes of processing at slow translation rate, with a real hold time of 1 minute 25 seconds after melt back and prior to growth. None of the earlier test had used exactly these parameters, and so the tests were run. All three tests were run in the GCEL due to the non-availability (see later) of the flight furnace.

The first test with SL1-418 was initiated, but abandoned due to a failure of the ground data collection system. Rather than run with no live monitoring data and with no possibility of recovering any furnace data or sample thermocouple data after the run, the test was terminated early on. Growth had been initiated in the sample, and it will be examined when time permits. The sample will provide some useful experimental results in that the interface shape during the period of the initial transient will be observed.

Two samples were run with the profiles and timelines identical to the flight sample. These were SL1-420 and SLNF-423. The reason for running two was so that adequate material was available for characterization, and especially the ability to cut one sample completely into wafers, and the other longitudinally to examine the "melt-back" and "quench" interfaces."

The thermal and translation profiles recorded during the processing of SLNF-423 are shown in Figure 9.12 and 9.13. Figure 9.12 is a representation of the behavior of the six sample thermocouples during a typical timeline for the experiment. The initial rise in temperature is due to the furnace heating up, followed by the insertion of the sample cartridge into the furnace once temperature stabilization has been completed. During crystal growth the temperatures recorded by all thermocouples drops slowly. The corresponding SACA position as a function of time is shown in figure 9.13. The position is the furnace parameter TPM. In this case the data are prolonged to show the rapid removal of the cartridge from the furnace at the conclusion of the crystal growth portion of the time line. This is in contrast with the data shown in figure 9.9, where each sample thermocouple was adjusted in position to correspond to its location within the furnace frame. Figure 9.12 and 9.13 demonstrate the complete experimental procedure developed for the USMP-4 mission.

Analysis of these two samples is in progress. So far an extensive effort has been made to examine and fully characterize the surface features. The sample differs from the completely molten sample used in USMP-2. There is a gap beside the seed, and in the ground test molten

material can flow down to some extent. Both liquid material and vapor penetrated the space beside the seed and the graphite. This issue will be further addressed with regard to the microgravity sample. It was also found that there was much deposition of elemental tellurium and mercury telluride on the surface, making chemical analysis for mercury cadmium telluride impossible. A typical result is shown in Figure 9.14. After several attempts to dissolve these materials without disturbing the underlying material (bromine solutions would not be suitable), a 50% solution of nitric acid for one hour was found to be ideal. However, it was found that this treatment severely etched the cadmium telluride seed material. Thus sample SLNF-423 has no clear representation for the end of the seed and its position cannot be well defined. For this reason, this sample was chosen to be used for wafers, and SL1-420 for the longitudinal cut. It was found that application of a varnish to cover the seed permitted the seed to be retained while the crystal surface was cleaned. The results of the analysis along the surface at four different locations following removal of the extraneous material are shown in Figure 9.15. These reading were first taken with EDS, but later experimentation demonstrated that it was possible to obtain better quality data in terms of totals even with the more stringent geometrical requirements of WDS. It is the WDS results that are shown in figure 9.15. These readings incorporate the ZAF correction. Much compositional data can be observed and it is clear that convection has taken place. The pre-processed composition has been destroyed and a conventional initial transient is present. The seed region of 10 mm is influenced by the presence of mercury-rich vapor and liquid present in the gap between the seed and the wall of the ampoule; the resulting HgCdTe alloy has been formed on the seed surface. In the quenched region there is as a lot of scatter in the data as the small (50 μm x 50 μm) incident beam is hitting dendritic features of varying composition.

The sample SLNF-423 was cut axially down the center line and polished mechanically with a final chemo-mechanical polish with 2%bromine dissolved in ethylene glycol. Initial WDS results are available at the time of writing, and are shown in figure 9.16. Four views are shown, namely secondary electron imaging, CdL, TeL and HgM. Of these, the Cd and Te are WDS while the Hg is EDS, and consequently noisy. It should be noted that these readings represent raw count data and are not corrected for the physics effects as in WDS. Several important points can be made. First of all, the narrowing of the CdTe seed can be seen. It had been dissolved in the acid. Secondly, the interface shape is much improved over earlier tests. In this case the deflection across the boule is about 0.3 mm, compared with 1.3 mm in sample SL1-424 (see figure 9.11). There is confirmation of the surface results in that there is an obvious initial transient. The dendritic region clearly shows up. Further work is progressing, on this sample, including ZAF corrected WDS readings along the complete area of the slow growth region.

At the time of writing the sample SL1-420 has been cut into 2 mm wafers through the entire slow-growth region. Half of these have been polished, but none have been analyzed yet. This work will be continued, and much characterization, including electrical property measurements is planned. The other advantage of the "wafer" cuts is that, provided the growth is epitaxial, the orientation of the wafers will be <111> and hence will be ideal for etch pit density measurements.

9.6 Growth in Magnetic Field

The application of a magnetic field has been shown to reduce the fluid flow which affects compositional homogeneity in HgCdTe and HgZnTe alloys.[61,70] Because of the changes to the geometry and type of sample involved here as compared with USMP-2, it was felt valuable to repeat a complete end to end growth of a sample with the USMP-4 configuration. The furnace within the magnet facility was set up to get as close as possible to the thermal conditions existing in the GCEL and AADSF flight unit. The magnet was run at 5 Tesla during the melt back of the preconditioned material. The sample, SL1-416, was sectioned completely down the center; Figure 9.17 represents EDS compositional values for the centerline for the material. The magnet was operating during the melt back stage of the experiment, but there is still an initial transient region present indicating that either the precursor composition was not close enough or there was still convective mixing taking place. The axial composition profile closely fits modeled one dimension diffusion control.

WDS readings were also taken across the sample at several locations. These are shown in Figure 9.18. These show there is good compositional uniformity across the material and an improvement over previous AADSF experiments. To complete this part of the experiment it is necessary to run an identical experiment in the magnet furnace, but without the magnet switched on. This is planned for the near future.

10. FLIGHT RESULTS

10.1 Flight Timeline

The flight timeline was based on the availability of time with the optimal residual or DC acceleration, and was negotiated to 72 hours total processing with 48 hours of actual slow translation. The microgravity criteria are that there are no perturbations caused by re-alignment of the orbiter attitude during the period when any part of the sample is molten. During the mission, several factors associated with other experiments resulted in modifications to the timeline and the availability of the optimized microgravity conditions. In particular, the deployment of a retrievable satellite led to a delay of one day to the microgravity portion of the mission and to an increased need to conserve propellant on the orbiter. The ground based experiments had revealed that there was no advantage to be gained by holding the sample at the end of the melt back region; instead slow growth was initiated as soon as the appropriate commands could be sent up. This in fact took 1 minute and 25 seconds. The result of this change and other mission related activities, such as when the orbiter was moved away from the growth attitude, was to extend the time of the slow growth portion of the timeline to almost 51 hours. These modifications to the nominal timelines were incorporated into the ground truth experiments (SL1-418, SL1-420 and SLNF-423). Another slight change was a time lag of 3½ minutes between the 10 mm/hr insertion and the 2 mm/hr insertion rates. This was believed to be of no consequence and was not included in the ground truth experiments. The actual events relative to Mission Elapsed Time (MET) are shown in Table 10.1.

While the growth of bench mark quality material by diffusion control was the main objective, knowledge of the compositional distribution in the liquid of the boundary layer close to the solidifying interface was also important. During the experiment the slow growth was terminated by an immediate change of translation velocity. The intent here was to freeze the liquid axially and preserve the composition for characterization. The first samples run, SL1-413/4/5, were all quenched at 10 mm/hr. As mentioned in section 9.3 for the flight and ground truth sample the faster rate of 50 mm/hr was determined more likely to succeed.

10.2 Residual Acceleration Results

As became obvious from the USMP-2 results and from modeling calculations, there is overwhelming evidence that to optimize quality, any residual steady state accelerations present during crystal growth in the HgTe-CdTe system should be directed from the liquid to the solid with the smallest component possible directed across the interface. The requirements were that there be a ratio of the axial/radial components of the vector of at least 4:1, that the axial vector not be more than 1 μg, and that it be directed from liquid to solid. The attitudes considered for the mission are shown in Table 10.2. As mentioned before, the extra maneuvers required to retrieve a satellite left the orbiter low on propellant. This became a factor in choosing option 2. While the nominal ratio and values for residual acceleration look good, in fact there was a strong requirement to maintain a tight orientation or dead band within this attitude to keep the stabilizing vernier jets firing frequently and hence prevent icing. This led to a periodic drift followed by a movement back to attitude as the orbiter reached the edge of the orientation control or dead band. Such motion was regular and every 8 minutes and produced a saw tooth effect in the z-component of the residual acceleration at the AADSF position. These data were available during the mission from the Orbital Acceleration Research Equipment (OARE) experiment. The OARE data are downlinked and after transformation processing give the low frequency accelerations at

the AADSF position. In addition, calculations of the presumed residual accelerations were made by the Microgravity Acceleration Work Station (MAWS) team during the mission, but before this experiment was started. These simulations ahead of time use data from the ongoing mission to test predictions based on assumed values for the solar flux and drag on the orbiter to calculate the residual acceleration vectors.

OARE data taken during the time segment of slow growth are shown in Figure 10.2. This represents a three hour time slot, but is typical of the entire slow growth period. The effect of the vernier firing clearly shows as the spiking or saw tooth seen in the lowest (Z-axis) component. Other features which are prominent are the data drop out 9/16:00 due to the orbiter being out of reach of tracking and data relay satellites (TDRS), and the spikes at 9/16:47 and 9/17:40. These spikes are the result of "dead band collapse" where the vernier temperatures get so low that the normal dead band adjustments will not ensure that all the jets are firing. Certain verniers are therefore fired manually; this operation is known as "dead band collapse." As can be seen the result may temporarily alter the ratio of axial to radial acceleration to unacceptable values. The amount and effect of the pulse depends on where in the cycle the collapse firing takes place. The dead band collapses took place at approximately 45 minute intervals from MET 8/00 onwards. Some of them hardly registered, while others such as the one at 9/16:54 (see Figure 10.1) were of sufficient force as to reverse the axial vector. Close attention will be paid to the sample to determine if any effects can be detected. The X component of the vector generally varies between 0.4 and 0.25 μg, while the y component varies between 0.05 and 0.1. These readings are the result of gravity gradient and drag in the X- and Z-components, while the y-component is cloe to zero because the furnace is on the centerline. The average vector runs at approximately 0.3 μg, while the Z component averages to approximately 0.9 μg. The axial/radial ratio therefore close to 3. While not ideal this is considerably better than the conditions prevailing on USMP-2.

10.3 Mission Thermocouple and Furnace Readings

As reported in another section of this review, the first sample, AF-1, experienced difficulties; the problems affected the processing of this, the SL-1 sample. During the mission itself, furnace parameters and cartridge thermocouple data were downlinked. Some anomalies were noted, and were not explained during the mission itself, but were understood after the sample was retrieved. The first anomaly was that the sample thermocouples all read considerably lower than the furnace readings during the first stage of fast translation of the cartridge into the furnace. The problem cured itself as can be shown in Figure 10.3. The cause was that the thermocouple compensating junction updates continuously and then takes the average of the fifty most recent readings. As the furnace was switched off following the end of the AF-1 experiment, the readings were retained from high temperature processing and thus were giving incorrect compensation for the SL-1 sample. Once the "old" readings had been superseded for the compensating junction, the thermocouple readings became normal, and continued to be of value throughout the remainder of the processing.

Other anomalies were soon noted, however. Figure 10.4 shows typical irregularities which occurred during the heating stage (GMT 331:10:40:00). As can be seen, the anomalies disappear and the heat up looks normal after GMT 331:11:40:00. The most significant issue here is that thermocouples TC 3 and TC4, which are positioned exactly opposite one another within the cartridge, and should exhibit identical temperatures. In fact from this point on they were always some 20 degrees apart with TC3 reading lower. After the mission all thermocouples were tested and found to within calibration, and so there is no reason to doubt the recorded temperatures. During this period of the cartridge insertion, all thermocouples lag behind the projected temperatures, and then suddenly catch up. This behavior corresponded to the anomalous translation behavior noted on Figure 10.5.

As mentioned, the end point for inserting the sample into the furnace is judged from the thermocouples. In this case, with TC3 and TC4 unreliable, it was decided to use TC5 (just above the seed) as the end point. The history of the melt back is shown in Figure 10.6, which was obtained post mission. The downlinked data were also noisy. There is therefore considerable doubt that the initiation point was correctly chosen. Either excessive melt back would have occurred, or the material was no melted back far enough to grow epitaxially. Later, the analysis

made after the mission supplied the answers. The temperatures from 19:00 to 21:00 are also anomalous; they do not exhibit the anticipated steady drop. The cartridge was bent and shorting against the inside of the furnace. While the furnace itself provided a uniform thermal environment, excessive thermal conduction where the cartridge touched the furnace dictated that the sample was subjected to a non-uniform field.

10.4 Cartridge post mission qualities

Upon opening the furnace post mission, it became obvious that there had been a major escape of material from the first sample processed, namely AF-1. As the temperature used for SL-1 is substantially lower than for AF-1, the residual material within the furnace remained as a solid. Some of the anomalies seen in the thermocouple readings were obviously caused by the cartridge having to overcome the force need to remove the extraneous material within the furnace. The cartridge was bent considerably as can be seen from Figure 10.7. The sample position was defined with zero degrees in the direction of the front of the orbiter. The deviation from thermal assymetry exhibited by the thermocouples TC3 and TC4, was caused by the cartridge rubbing against the Haynes alloy insert within the bore of the furnace designed to separate the hot and cold zones of the furnace. One side was thus thermally short circuited and so the readings are lower. It was also found that there was a visible ring of material round the cartridge. Examination of the material revealed crystalline material of lead telluride. The ring was not evenly placed round the cartridge, and was related to the location of the mark caused by the cartridge scraping the insert. These deposits are shown in Figure 10.8.

Two scratches were clearly visible along the length of the cartridge. A narrow one close to the zero degree can be seen in Figure 10.7, and there is a longer, wider one at close to the 90^{o} position. The 90^{o} mark also shows considerable rubbing against a large piece of debris, which may have initiated the bending of the cartridge and the slowing of the translation into the furnace. This hypothesis would also explain the anomalous thermocouple readings seen in Figure 10.4. The second scratch at 0^{0} was presumably made during the crystal growth phase. The cartridge at this time was able to scrape away the crystalline material previously grown there.

An explanation of the behavior of the thermocouple and translation behavior is that the cartridge encountered resistance to insertion during the period 11:00 to 11:45 on 11/27/98. At this time we believe the liquid would have been stirred considerably. Similarly the scraping during growth will have induced considerable vibration into the sample.

10.5 Radiographic results

Computed tomography was not used immediately to examine the flight sample, nor the ground truths. It was felt that the high energy of the cobalt source (over 1 MeV) had the potential to cause damage to the electronic structure of the material, and hence mask the very property of major interest. Post mission, microfocus x-radiography was done at Kennedy Space Center. This was done with an image intensifier and so it was possible to translate and rotate the sample and record the image on VCR tape. By this means the exact positions of the sample and all the thermocouples were verified before opening the cartridge.

High-resolution radiographs were also taken to examine fully the nature of the ampoule prior to opening the cartridge. Using the photographs as guides for depth, the cartridge was slit with a diamond blade through the inconel, the fused silica and just into the mercury cadmium telluride at the last to freeze end. This practice had been perfected with ground samples. The objective was to preserve the orientation of the sample relative to the flight direction of the orbiter, and hence relative to any residual acceleration vector. The microfocus x-ray results were vital to establishing the thermal environment within the furnace by measuring the circumferential positions of TC3 and TC4.

A selection of these photographs is shown in Figures 10.9 and 10.10. The cartridge is bent at the end, but the ampoule has also been forced sideways during the processing. The boron nitride piece at the first to freeze end was not recovered and was completely broken. It did, however, protect the ampoule during launch and the extra force during the processing. A helium test was done on the cartridge and, not surprisingly, several large leaks were found. No mercury

had been found in the furnace, and it has been presumed that the ampoule survived the mission intact. As mentioned above, the ampoule was cut in such a way as to identify the direction of flight, and so its integrity could not be tested.

10.6 Optical Photography

After slotting the cartridge with an outside diameter diamond blade, the cartridge screws were removed and the ampoule was extracted. The region where the blade had passed had a crack in the quartz, but the material itself survived and had a neat scratch mark to identify the direction.

The crystalline material was removed from the cartridge by etching the glass away with hydrofluoric acid. Photographs were taken along the four prominent positions; these photographs are shown in Figures 10.11. The seed is at the top in each photograph, and the identifying orientation slit can be seen at the bottom of the left hand photograph. As can be seen there is a considerable amount of residual material left on the surface. This had to be removed prior to meaningful characterization of the surface could be resumed.

10.7 Scanning Electron Microscopy (SEM)

Prior to the removal of the residual material shown in figure 10.11 surface photographs were made, using the SEM, of the flight sample on four surfaces at 0, 90, 180, and 270° to the direction of flight. The collection was made at low magnification to capture the entire length of the sample. Some equivalent photographs were made on the two ground truth samples. Additionally, higher magnification photographs were made of the areas of the sample which had significant and typical characteristics. Individual locations were also analyzed by EDS.

A set of photographs for one surface is shown in figures 10.12. The four orientations have certain features in common. The seed covered region, for instance, is generally coated with material which at high magnification was shown to be mercury cadmium telluride. Often the material manifested itself as well developed crystals as shown in Figure 10.13. These are believed to be crystals formed by vapor transport. As one progresses further along the sample, the vapor phase material gives way to more featureless material with occasional large deposits being present. The majority of the surfaces were fibrous looking at the low magnification, but with larger clumps of material attached. The fibrous material seemed to be dendritic and analysis showed that it was mainly mercury telluride within a tellurium matrix (see Figure 10.14). These patterns were repeated on all four surfaces.

10.8 Energy Dispersion Spectrometry (EDS)

Energy dispersive spectrometry readings for Hg, Cd and Te were made on four surfaces of the flight sample, identified with respect to the flight direction (0°). The data were difficult to interpret because of the roughness of the surface and the extraneous matter deposited. Small quantities were dissolved away and the analysis was tried several times as recounted in section 9.5. Success was achieved with a solution of 50% nitric acid for 1 hour. Reasonable totals (close to 100% weight) with 50 atomic % tellurium were found. The results are not reproduced here as a technique evolved which enabled us to make use of the more accurate and precise wavelength dispersive spectrometry (WDS).

10.9 Wavelength Dispersive Spectrometry (WDS) – surface

As previously mentioned WDS results were successfully produced from the curved surface of the flight sample following suitable acid treatment. The complete set of results are shown in figure 10.15. Here it can be seen that the surface composition passes through an initial transient region, and never really reaches "steady state." Comparison with figure 9.15, the ground truth equivalent sample, SLNF-423, demonstrates similarities and differences. SLNF-423 also has an initial transient region, and there is a predicted change in composition at the location of the start of the rapid removal from the furnace. In each sample, there is still residual mercury-rich material remaining on the seed. There are two significant differences, however. The surface of the

ground sample is very consistent in composition from surface to surface, while the flight sample shows considerable fluctuations. The behavior of the material during the rapid removal from the furnace is quite difference. The flight sample demonstrates a distinct fan-shape of composition with CdTe mole fractions between 0.04 and 0.3. Bearing in mind that the material is dendritic and the WDS analysis would be selective, the overall shape of the curve is consistent with a typical boundary layer. The ground material shows a steady band of composition with no obvious average change in composition from the beginning of the rapid cooling to the end of the sample. Convection has clearly played a role in this

Each surface of the flight sample was grown with different compositional characteristics. The four surfaces are separately plotted on figures 10.16-10.19. The 0° and 270° positions (figures 10.16 and 10.19) demonstrate an almost periodic oscillation of composition which is not regular nor in phase with the other surface. In contrast, the compositions of the 90° and 180° surfaces demonstrate erratic fluctuations at times. In contrast, the behavior of all four surfaces during the rapid removal stage is more regular. Our initial hypothesis is that the fluctuations during the slow growth region are caused by the rubbing and consequent periodic sticking and releasing of the cartridge within the furnace. By the time the rapid removal part of the experiment was reached the cartridge was free and so the "quench" part of the boule exhibited closer to the predicted behavior.

10.10 Wavelength Dispersive Spectrometry – polished sections

At the time of writing the flight sample had not been sectioned. The plan is to examine the surface WDS data and the thermocouple readings to determine the direction of longitudinal sectioning that can demonstrate the maximum deflection of the interface. The melt back interface will also be sectioned. The region between the two "interface' cuts, which will comprise over 2 cm of material will be cut into wafers and prepared for compositional analysis. The wafers will be characterized in a similar way to the ground truth SL1-420 samples. The cutting will be done as in figure 10.20. This figure is not to scale, nor will the real number of wafers produced correspond to the cuts indicated.

10.11 Computed Tomography

As mentioned in section 10.5, the initial presumption was that computed tomography (CT), which involves the use of 1.33 MeV radiation could damage the crystal. However it soon became clear that the material was not of the anticipated or desired quality, and so CT evaluation was done. The actual scanning was done after the material had been removed from the glass, and indeed after the etching and subsequent WDS analysis. Using the technique described by Gillies and Engel,[73] the density was determined, and converted to CdTe mole fraction assuming stoichiometric HgCdTe. The resulting compositional profile is shown in figure 10.21. The data correspond to average compositions across cross sections 1 mm high, and are equivalent to density measurements of composition, as first elucidated by Bowman et al,[74] and used by Lehoczky et al for HgCdTe. [1] The data exhibit more spread than the WDS surface readings. Both the accuracy and the precision of the technique are still being evaluated, and are not high. Better standards, particularly of mercury telluride are needed. The HgTe is very prone to porosity. The next generation of CT scanners will improve matters, both statistically and spatially. The main benefits for CT are to examine a sample prior to cutting, and this was done with the second ground truth sample, SL1-420. In the case of the flight sample we are getting averaged composition values in the rapidly frozen, or dendritic region. Thus the composition from 45 mm and higher is a reasonable representation of the true averaged value, and the spread is much less than the results shown in figure 10.16. Further work on the methods to interpret CT data for this application are in progress.

10.12 Optical Microscopy – polished sections

Polished sections of the flight sample had not been prepared at the time of writing. The plan is to use these sections for compositional mapping, defect evaluation using etch pit density,

synchrotron topography, and electrical property measurements.

10.13 Synchrotron Radiation Studies

White beam synchrotron topography has been done at Brookhaven National Laboratory using a white beam reflection technique. The samples, both for the ground based (SLNF-423) and the flight, were examined in their original condition with much extraneous material deposited on the surface. The beam was not able to hit sufficient single crystal material for any worthwhile topographs to be obtained. The technique will be used again when the samples have been polished.

11. SUMMARY AND PRELIMINARY CONCLUSIONS

Results of ground based experiments have demonstrated that the modified configuration of using seeded growth with a compositionally-tuned pre-fabricated boule represents a significant improvement over the unseeded conventional Bridgman Stockbarger design for USMP-2. In particular improvements in interface shape, radial composition and the ability to produce large single crystals have been noted.

There are no data available with regard to the actual flight to indicate that good results would not have been obtained had the experiment proceeded nominally. The ratio of axial to radial residual accelerations was generally favorable and almost always higher than 3. The AADSF performed admirably, and the design of the cartridge and ampoule was sufficiently robust to withstand forces well above the anticipated level.

The single sample run in the magnetic field with the USMP-4 configuration gave excellent results, although the melt back was clearly under a convective regime. Homogeneity was higher than in the conventional ground truth samples. An equivalent experiment in the same furnace under identical conditions, but without the magnetic field will be shortly be made.

New, important electronic property calculations have been made, and will be reported on later.

All indications are that this would have been a successful experiment had it not been made in a contaminated furnace. The data collected so far give positive reinforcement of the design of the experiment. The PI and his team are continuing to collect and analyze data, and there is a distinct probability that a re-flight will be requested based on the adverse conditions existing in the furnace prior to the start of this experiment.

12. REFERENCES

1. Lehoczky, S. L., F. R. Szofran and B. G. Martin, "Advanced Methods for Preparation and Characterization of Infrared Detector Materials," McDonnell Douglas Report No. MDC QO717, July 5, 1980, (Final Report for the period December 5, 1978-July 5, 1980, for the George C. Marshall Space Flight Center, Contract No. NAS8-33107), pp. 1-151 (1980) (also NASA CR-161598, July 5, 1980).
2. Lehoczky, S. L. and F. R. Szofran, "Advanced Methods for Preparation and Characterization of Infrared Detector Materials," McDonnell Douglas Report No. MDC Q0744, September 30, 1981 (Interim Report for the period July 5, 1980-September 30, 1981, for the George C. Marshall Space Flight Center, Contract No. NAS8-33107), pp. 1-33 (1981) (also NASA CR-161949, September 30,1981).
3. Szofran, F. R. and S. L. Lehoczky, "The Pseudobinary HgTe-CdTe Phase Diagram," J. Electronic Materials, 10, 1131-1150 (1981).
4. Kelley, J. D., B. G. Martin, F. R. Szofran, and S. L. Lehoczky, "Applications of the Regular-Associated-Solution Model to the Cd-Te and Hg-Te Binary Systems," J. Electrochem. Soc., 129, 2360-2365 (1982).
5. Lehoczky, S. L. and F. R. Szofran, "Directional Solidification and Characterization of $Hg_{1-x}Cd_xTe$ Alloys," in Materials Research Society Proceedings, Materials Processing in the Reduced Gravity Environment of Space, ed., G. E. Rindone (Elsevier: New York), 9, 409-420 (1982).
6. Lehoczky, S. L., C. J. Summers, F. R. Szofran, and B. G. Martin, "Electrical Characterization of $Hg_{1-x}Cd_xTe$ Alloys," in Materials Research Society Proceedings, Materials Processing in the Reduced Gravity Environment of Space, ed., G. E. Rindone (Elsevier: New York), 9, 421-431 (1982).
7. Szofran, F. R. and S. L. Lehoczky, "Liquidus Temperatures of Hg-Rich Hg-Cd-Te Alloys," J. Electronic Matls., 12(4), 713-717 (1983).
8. Holland, L.R., "A Thermal Transmission Function for Fused Silica Ampoules," J. Cryst. Growth 49, 246 (1980).
9. Holland, L.R., "Radiant Heating of Ampoule Contents," NASA Tech Briefs 349 (Fall/Winter 1981).
10. Naumann, R. J., "An Analytical Approach to Thermal Modeling of Bridgman-Type Crystal Growth I. One-Dimensional Analysis," J. Cryst. Growth 58, 554-568 (1982).
11. Naumann, R. J., "An Analytical Approact to Thermal Modeling of Bridgman-Type Crystal Growth II. Two-Dimensional Analysis," J. Cryst. Growth 59, 569-584 (1982).
12. Clayton, J. C., "Transient and Diffusion Analysis of HgCdTe," NASA CR162049, 1982.
13. Cothran, E. K., "An Analytical Approach to Thermal Modeling of Bridgman-type Crystal Growth: One Dimensional Analysis, Computer Program Users Manual," NASA TM82487, May 1982.
14. Clayton, J. C., M. C. Davidson, D. C. Gillies, and S. L. Lehoczky, "One Dimensional of Segregation in Directionally Solidified HgCdTe," J.Cryst. Growth, 60, 374 (1982).
15. Gillies, D. C., "Analysis of Mercury Cadmium Telluride by Energy Dispersive Analysis," J. Electronic Mat. 11, 689 (1982).
16. Lehoczky, S. L., F. R. Szofran, and R. J. Naumann, "Crystal Growth of Homogeneous $Hg_{1-x}Cd_xTe$ Crystals from Pseudobinary Melts," Bull. Am. Phys. Soc. 28, 294 (1982).
17. Naumann, R. J. and S. L. Lehoczky, "Effect of Variable Thermal Conductivity on Isotherms in Bridgman Growth," J. Cryst. Growth, 61, 707-710 (1983).
18. Holland, L. R., R. P. Harris, and R. Smith, "High Temperature, High Pressure Optical Cells," Review of Scientific Instruments, 54, 993 (9183).
19. Holland, L. R. and R. E. Taylor, "Measured Thermal Diffusivity of $Hg_{1-x}Cd_xTe$ Solids and Melts," Journal of Vacuum Science Technology, A1, 1615 (1983).
20. Chandra, D. and L. R. Holland, "Density of Liquid $Hg_{1-x}Cd_xTe$," Journal of Vacuum Science and Technology, A1, 1620 (1983).

21. Lehoczky, S. L., F. R. Szofran, D. Chandra, and J. C. Wang, "Growth Rate Dependence of the Axial Compositional Variations in Bridgman-Grown $Hg_{1-x}Cd_xTe$ Crystals," Fall Meeting of the American Physical Society, San Francisco, CA, November 20-23, 1983 (Bull. APS, 28, 1313 (1983)).
22. Szofran, F. R. and S. L. Lehoczky, "High Temperature Electrical Properties of HgTe," ibid (Bull. APS, 28, 1313 (1983)).
23. Lehoczky, S. L., and F. R. Szofran, "Growing Crystals for Infrared Detectors," NASA Tech Briefs 8, 136 (1983).
24. Jasinski, T. and R. J. Naumann, "One-Dimensional Modeling of Vertical Bridgman-Type Crystal Growth", J. Cryst. Growth 66, 469 (1984).
25. Holland, L. R., "Sealed Silica Pressure Ampules for Crystal Growth", J. Cryst. Growth 66, 501 (1984).
26. Szofran, F. R. and S. L. Lehoczky, "A Method for Interface Shape Control During Bridgman Type Crystal Growth of HgCdTe Alloys," J. Cryst. Growth,70(1/2), 349-355 (1984).
27. Szofran, F. R., D. Chandra, J. C. Wang, E. K. Cothran, and S. L. Lehoczky, "Effect of Growth Parameters on Compositional Variations in Directionally Solidified HgCdTe Alloys," J. Cryst. Growth, 70(1/2), 343-348 (1984).
28. Holland, L. R., "VLS Growth to Purify Elements of Groups II and VI", J. Cryst. Growth 70, (1984).
29. Lehoczky, S. L. and F. R. Szofran, "Further Comments on Segregation During Bridgman Growth of $Hg_{1-x}Cd_xTe$," J. Cryst. Growth (Lett.), 69, 201-203 (1984).
30. Lehoczky, S. L. and F. R. Szofran, "Solidification and Crystal Growth of Solid Solution Semiconducting Alloys," in NASA CP-2313, edited by Camille M. Jernigan, p. 320 (1984) (Proceedings of the Second Symposium on Space Industrialization, Huntsville, AL, February 13-15, 1984)
31. Szofran, F. R. and P. N. Espy, "Automated ac Galvanomagnetic Measurement System," Review of Scientific Instruments 56, 1363 (1985).
32. Chandra, D., "Anomalous Volume Expansion in $Hg_{1-x}Cd_xTe$ Melts: An Analysis Employing the Inhomogeneous Structure Model," Phys. Rev. 331, 7706 (1985).
33. Lehoczky, S. L., and Frank R. Szofran, "HCT Crystal Growth Method," U.S. Patent No. 4,545,848, October 1985.
34. Su, C.-H., S. L. Lehoczky, and F. R. Szofran, "A Method to Eliminate Wetting During the Homogenization of HgCdTe," J. Appl. Phys., 60(10), 3777-3778 (1986).
35. Su, Ching-Hua, "Heat Capacity, Entalphy of Mixing and Thermal Conductivity of $Hg_{1-x}Cd_xTe$ Pseudobinary Melts", J. Cryst. Growth 78, 51 (1986).
36. Lehoczky, S. L. and F. R. Szofran, "Growth of Solid Solution Single Crystals," NASA TP-2787, December 1987.
37. Szofran, F. R. and S. L. Lehoczky, "Bridgman Growth of Mercury Cadmium Telluride Alloys," in Processing of Electronic Materials, eds., C. G. Law, Jr. and R. Pollard (American Institute of Chemical Engineers: New York), pp. 342-348 (1987) (proceedings of First International Conference on Processing of Electronic Materials, held Santa Barbara, CA, February 23-28, 1986).
38. Lehoczky, S. L. and F. R. Szofran, "Growth of Solid Solution Single Crystals," in The Nation's Future Materials Needs, International SAMPE Technical Conference Series, eds., T. Lynch, J. Persh, T. Wolf, and N. Rupert (SAMPE: Covina, CA), Vol. 19, p. 332 (1987 (proceedings 19th International SAMPE Technical Conference, Arlington, VA, October 13-15, 1987).
39. Lehoczky, S. L., F. R. Szofran, C.-H. Su, S. D. Cobb, and R. N. Andrews, "Crystal Growth of Solid Solution Systems by Directional Solidification," Proceeding of ASM International '87 Materials Congress (held Cincinnati, Ohio, October 12-15, 1987).
40. Naumann, Robert J., S. L. Lehoczky, and Donald O. Frazier, "Growing Single Crystals of Compound Semiconductors," in NASA Tech Briefs, Vol. 11, No. 6, pp. 47-48, June 1987.
41. Naumann, Robert J., Donald O. Frazier, Sandor Lehoczky, Marcus Vlasse, and Barbara

Facemire, "Crystal Growth in Liquid-Encapsulated Float Zone," in NASA Tech Briefs, Vol. 11, No. 8, pp. 44-45, September 1987.
42. Su, C.-H., S. L. Lehoczky, and F. R. Szofran, "Growth of HgZnTe Alloy Crystals by Directional Solidification," J. Cryst. Growth, 86, 87-92 (1988).
43. Szofran, F. R., Gretchen L. E. Perry, and S. L. Lehoczky, "Highly Automated Transmission-Edge Mapping," J. Cryst. Growth, 86, 650-655 (1988).
44. Dakhoul, Y. M., R. Farmer, S. L. Lehoczky, and F. R. Szofran, "Numerical Simulation of Heat Transfer During the Crystal Growth of HgCdTe Alloys," J. Cryst. Growth, 86, 49-55 (1988).
45. Andrews, R. N., F. R. Szofran, and S. L. Lehoczky, "Growth and Characterization of $Hg_{1-x}Cd_xSe$ Alloys," J. Cryst. Growth, 92(3/4), 445-453 (1988).
46. Andrews, R. N., F. R. Szofran, and S. L. Lehoczky, "Internal Temperature Gradient of Alloy Semiconductor Melts from Interrupted Growth Experiments," J. Cryst. Growth, 86(1-4), 100-105 (1988).
47. Su, C.-H., G.L.E. Perry, F. R. Szofran, and S. L. Lehoczky, "Compositional Redistribution During Casting of $Hg_{0.8}Cd_{0.2}Te$ Alloys," J. Cryst. Growth, 91, 20-26 (1988).
48. Patterson, J. D., and S. L. Lehoczky, "The Second Born Approximation and the Friedel Sum Rule," Physics Lett. A, 137(3), 137-138 (1989).
49. Lehoczky, S. L. and F. R. Szofran, "Method of Preparing Radially Homogeneous Mercury Cadmium Telluride Crystals," U.S. Patent No. 4,863,553, September 1989.
50. Andrews, R. N., S. D. Walck, M. W. Price, F. R. Szofran, C.-H. Su, and S. L. Lehoczky, "Microhardness Variations in II-VI Semiconducting Compounds as a Function of Composition," J. Cryst. Growth, 99, 717-721 (1990).
51. Su, C.-H., S. L. Lehoczky, and F. R. Szofran, "Directional Solidification of HgCdTe and HgZnTe in a Transverse Magnetic Field," J. Cryst. Growth, 109, 392-400 (1991).
52. Abdelhakiem, W., J. D. Patterson, and S. L. Lehoczky, "A Comparison Between Electron Mobility in N-Type $Hg_{1-x}Cd_xTe$ and $Hg_{1-x}Zn_xTe$," Materials Letters, 11(1,2), 47-51 (1991).
53. Patterson, J. D., W. A. Gobba, and S. L. Lehoczky, "Electron Mobility in n-Type $Hg_{1-x}Cd_xTe$ and $Hg_{1-x}Zn_xTe$ Alloys," J. of Materials Research, 7(8), 2211-2218 (1992).
54. Gobba, W. A., J. D. Patterson, and S. L. Lehoczky, "A Comparison Between Electron Mobilities in $Hg_{1-x}Mn_xTe$ and $Hg_{1-x}Cd_xTe$," Infrared Phys., 34(3), 311 (1993).
55. Mazuruk, K., C.-H. Su, S. L. Lehoczky, and F. Rosenberger, "Novel oscillating cup viscometer - application to molten HgTe and $Hg_{0.8}Cd_{0.2}Te$," J. Appl. Phys., 77 (10), 5098-5102 (1995).
56. Palosz, W., F. R. Szofran, and S. L. Lehoczky, "The Effect of Heat Treatment in the Magnitude and Composition of Residual Gas in Sealed Silica Glass Ampoules," J. Cryst. Growth, 169, 20, (1996).
57. Price, M. W., R. N. Andrews, C.-H. Su, S. L. Lehoczky, and F. R. Szofran, "Effect of Transverse Magnetic Field on the Microstructure of Directionally Solidified CdTe," J. Cryst. Growth, 137, 201-207 (1994).
58. Lehoczky, S. L., D. C. Gillies, F. R. Szofran, F. A. Reevees, J. D. Sledd, T. K. Pendergrass, D. A. Watring, C. R. Coppens, J. E. LeCroy and D. Popok, "Crystal Growth of HgCdTe in the AADSF on the USMP-2 Mission," Paper AIAA 95-0609, 33rd Aerospace Sciences Meeting and Exhibit, Reno, NV, 1995.
59. Kim, D. H. and R. A. Brown, "Modeling of the dynamics of HgCdTe growth by the vertical Bridgman method," J. Cryst Growth, 114, 411 (1991).
60. Kim, D. H. and R. A. Brown, "Models for convection and segregation in the growth of HgCdTe by the vertical Bridgman method," J. Cryst. Growth, 96, 609 (1989).
61. Watring, D. A., and S. L. Lehoczky, "Magneto-hydrodynamic damping of convection during vertical Bridgman-Stockbarger growth of HgCdTe," J. Cryst. Growth, 167, 478 (1996).

62. Bune, A.V., D.C.Gillies and S.L.Lehoczky, "Optimization of Bulk HgCdTe Growth in a Directional Solidification Furnace by Numerical Simulation," Mat. Res. Symp. Proc., 398, 139, (1996).
63. Bune, Andris.V., Donald. C. Gillies and Sandor.L.Lehoczky, " Numerical modeling of HgCdTe; effects of phase diagram, double-diffusion and microgravity level, "SPIE 3123, Materials Research in Low Gravity, 241, (1997).
64. Motakef, Shariar, Cape Simulations, Inc., private communication (1997).
65. Gillies, Donald C., Sandor L. Lehoczky, F. R. Szofran, Dale A. Watring, Helga A. Alexander and Gregory A. Jerman, "Effect of residual accelerations during microgravity directional solidification of mercury cadmium telluride on the USMP-2 mission," J. Cryst. Growth, 174, 101 (1997).
66. Lehoczky, Sandor L., Donald C. Gillies, Frank R. Szofran, and Dale A. Watring, "Directional Solidification of Mercury Cadmium Telluride in Microgravity," 10th International Symposium on Experimental Methods for Microgravity Science, San Antonio, TMS, (1998).
67. Smith, V. G., W. A. Tiller and J. W. Ritter, "A Mathematical Analysis of Solute Redistribution During Solidification," Can. J. Physics, 33, 723, (1955).
68. Bune, Andris.V., Donald C. Gillies and Sandor L. Lehoczky, "3-D Modeling of Directional Solidification of a non-Dilute Alloy with Temperature and Concentration fields Coupling via Material Properties Dependence and via Double-Diffusive Convection," presented at MRS Meeting, April 1998.
69. Bune, A. V., D. C. Gillies and S. L. Lehoczky, "3-D Modeling of Double-Diffusive Convection During Directional Solidification of a Non-Dilute Alloy with Application to the HgCdTe Growth in Microgravity Conditions," 12th International Conference on Crystal Growth, Jerusalem, 1998 to be published in J. Cryst Growth.
70. Sha, Yi-Gao, Ch-H. Su and S. L. Lehoczky, "Growth of HgZnTe by directional solidification in a magnetic field," J. Cryst. Growth, 173, 88 (1997).
71. Gillies, D. C., F. A. Reeves, L. B. Jeter, J. D. Sledd, J. M. Cole and S. L. Lehoczky, "The Advanced Automated Directional Solidification Furnace," SPIE 3123, Materials Research in Low Gravity, 329, (1997).
72. Lehoczky, Sandor L., Frank R. Szofran and Donald C. Gillies, "Growth of Solid Solution Single Crystals," Second United States Microgravity Payload: One Year Report, P. A. Curreri and D. E. McCauley, editors, NASA Technical Memorandum 4737, April 1996.
73. Gillies, Donald C. and H. Peter Engel, "Quantitative Computed Tomography for Determining Composition of Microgravity and Ground Based Solid Solutions," 11th International Symposium on Experimental Methods for Microgravity Materials Science, 128th TMS Annual Meeting and Exhibition, San Diego, March 1999.
74. Bowman, Horace A., Randall M. Schoonover and Mildred W. Jones, "Procedure for High Precision Density Determination by Hydrostatic Weighing," J. Research of the National Bureau of Standards, 71C, 179-198, July-August 1967.
75. Rosch, William Rogers, "Furnace Temperatures and Their Effect on Vertical Bridgman Crystal Growth," Ph. D. Thesis, U. Virginia, 1995.
76. Carpenter Paul K., J. C. Cochrane and D. C. Gillies, "Characterization by Scanning Electron Microscopy (SEM) and Energy Dispersive X-Ray Spectroscopy (EDS) of Solid Solution Single Crystals Grown on Earth and in Microgravity," Microscopy and Microanalysis '99, Portland, OR, August 1-5, 1999.
77. Patterson, J. D., W. A. Gobba and S. L. Lehoczky, "Electron Mobility in n-Type $Hg_{1-x}Cd_xTe$ and $Hg_{1-x}Zn_xTe$ Alloys," J. Materials Research, 7(8),2211, (1992).
78. Madarasz, F. and S. L. Lehoczky, work in progress.
79. Kane, E. O., "Band Structure of Indium Antimonide," J. Phys. Chem. Solids, 1, 249, (1957).
80. Kohler, M., "Transportsheinringen Mim Electronengas," Z. Phys.", 125, 679, (1949).
81. Howarth, D. J. and E> M. Sondheimer, "The Theory of Electronic Conduction in Polar Semiconductors," Proc. Roy. Soc., A219, 53, (1953).
82. Ehrenreich, E. "Electron Scattering in InSb," J. Phys. Chem. Solids, 2, 131, (1957).

Acknowledgements

We are indebted to many people over the course of this project. On the Project side, Fred Reeves and Linda Jeter managed the program, with Fred Kroeger and Jim Sledd as Project Engineers. Kent Pendergrass, Mike Cole, Wayne Gandy, Ron Cantrell and Fred Flack were the Test Engineers. The cartridge and ampoule design was by Chris Coppens. The furnace was built by Teledyne Brown Engineering with Rick Howard as Manager, Jerry LeCroy as Engineer, and Mark Shelton as Software Engineer. Sample characterization was done by Helga Alexander, Chris Cochrane, Dayna Boxx, Greg Jerman, and Paul Carpenter. Expert glassblowing was provided by Gene Nelson and Mark Jones. Technical support, including the building of the ground furnaces came from LeRoy Mullaley, Curtis Bahr, Jeff Quick and Don Lovell. Radiography and Computed Tomography were done by Dexter Strong and Pete Engel respectively. The modeling was done by Andris Bune and Shari Motakef. The electron band modeling was done by Frank Madarasz. Support during the mission came from Brian Blair, Marcus Vlasse, Peter Curreri, Sherwood Anderson, Larry French, and Brian Matisak. The support of numerous others is gratefully acknowledged. Finally, the continued, enthusiastic support of the Microgravity Research Division of NASA Headquarters made this project possible.

Table 9.1 Precursor Boule History

ID	Composition	Quality	length	coating	crystal growth	End Use
MCT-152-1-BN	0.152		12 cm	BN	quench cast	SLNF-401
MCT-152-2-BN	0.152		12	BN	slow grow	uniformity test
MCT-152-3-C	0.152		12	C	slow grow	SLNF-401
MCT-152-4-C	0.152		12	C	slow grow	
MCT-152-5-C	0.152		12	C	disassembled	
MCT-152-7-C	0.152		12	C	slow grow	
MCT-152-8-C	0.152		12	C	quench cast	SLNF-424
MCT-152-9-C	0.152		12	C	slow grow	SLNF-402
MCT-152-10-C	0.152		12	C	slow grow	SLNF-427
MCT-152-11-C	0.152	yes	12	C	slow grow	SL1-416
MCT-152-12-C	0.152	yes	12	C	slow grow	SL1-412,15
MCT-152-13-C	0.152	yes	12	C	slow grow	SL1-414
MCT-152-14-C	0.152	yes	12	C	quench cast	SL1-416
MCT-152-15-C	0.152	yes	12	C	quench cast	SL1-414
MCT-152-16	0.152	yes	12		slow grow	SL1-413
MCT-152-17-C	0.152	yes	12	C	slow grow	SL1-413
MCT-152-18-C	0.152	yes	12	C	slow grow	SLNF-424
MCT-152-19	0.152	yes	12	C	quench cast	SL1-415, 420
MCT-152-20	0.152	yes	15		slow grow	SL1-417
MCT-152-21	0.152	yes	15		slow grow	SL1-418
MCT-152-22	0.152	yes	15		slow grow	
MCT-152-23	0.152	yes	15		slow grow	
MCT-152-24	0.152	yes	15		slow grow	SL1-418,420
MCT-152-25	0.152	yes	15		slow grow	SL1-419
MCT-152-26	0.152	yes	18		slow grow	
MCT-152-27	0.152	yes	18		slow grow magnet fnce	
MCT-152-28	0.152	yes	18		quench cast	SL1-417,418,419
MCT-152-29	0.152	yes	18		slow grow	
MCT-152-30	0.152	yes	18		slow grow	
MCT-152-31	0.152	yes	15		quench cast	SLNF-423
MCT-152-32	0.152	yes	15		slow grow	SLNF-427
MCT-152-33	0.152	yes	15		devitrified during slow growth	
MCT-152-34	0.152	yes	15		slow grow	SLNF-423
MCT-200-1	0.200	yes	12		slow grow	
MCT-200-2-C	0.200	yes	12	C	slow grow	SLNF-426
MCT-200-3-C	0.200	yes	12	C	quench cast	SL2-421,422
MCT-200-4-C	0.200	yes	12	C	bad casting	
MCT-200-5	0.200	yes	15		slow grow	SL2-422
MCT-200-6	0.200	yes	15		slow grow	SL2-421
MCT-200-7	0.200	yes	15		quench cast	SLNF-425,426
MCT-200-8	0.200	yes	15		slow grow	SLNF-425

Table 9.2 Cartridge Inventory

ID	x-value	Quality grade	Precursor material	History
SLNF-401	0.152	non	MCT-152-1,3	
SLNF-402	0.152	non	MCT-152-9	
SL1-413	0.152	non	MCT-152-16,17	grown in flight unit (thermal test)
SL1-414	0.152	yes	MCT-152-13,15	grown in GCEL
SL1-415	0.152	yes	MCT-152-12,19	grown in GCEL (vibration sample)
SL1-416	0.152	yes	MCT-152-11,14	grown in magnet furnace
SL1-417	0.152	yes	MCT-152-20,28	FLIGHT SAMPLE
SL1-418	0.152	yes	MCT-152-21,28	first ground truth (test discontinued)
SL1-419	0.152	yes	MCT-152-25,28	
SL1-420	0.152	yes	MCT-152-19,24	third ground truth (for radial cuts)
SL1-421	0.200	yes	MCT-200-3,6	grown in GCEL
SL1-422	0.200	yes	MCT-200-3,5	
SLNF-423	0.152	non	MCT-152-31,34	second ground truth (for longitudinal cuts)
SLNF-424	0.152	non	MCT-152-8,18	grown in GCEL
SLNF-425	0.200	non	MCT-200-7,8	grown in GCEL
SLNF-426	0.200	non	MCT-200-2,7	
SLNF-427	0.152	non	MCT-152-10,32	to be grown in magnet furnace with field off

Table 10.1 **USMP-4 AADSF SL1 Sample Mission Events**

MET (day/hour:minute:second)	EVENT
7/02:24:45	Furnace heat up start
7/05:25 (?)	Orbiter attitude established as 190-0-0
7/05:51	Sample fast translate to start position
7/06:48	Sample translate to 10 mm/hr
7/16:48:00	Terminate translation
7/16:51:30	Start translate at 2 mm/hr
7/22:15:35	Stop translation
7/22/17:00	Start crystal growth (0.72 mm/hr)
10/03:00:01	End of slow growth; start of 50 mm/hr
10/05:10	End of 190-0-0 attitude

Table 10.2 **Proposed Attitudes for SL1 Sample**

	Nominal Attitude	acc_x	acc_y	acc_z	axial/radial
1	10 – 0 – 180	-0.052	0.001	-0.725	14.4
2	190 – 0 – 0	0.040	0.002	-0.759	18.9
3	170 – 0 – 180	0.041	0.001	-0.760	18.5
4	170 – 0 – 180	-0.389	0.002	-0.658	1.7

The attitude is described in terms of angles relative to the three axes of the orbiter in terms of pitch, roll and yaw. The first indication is the x-axis of the orbiter, where 0 indicates flying forward, 180 backward, and 10 with the nose up. Thus 190 indicates a mode of flying backwards with the engine pointing slightly upwards. Similar arguments apply to the y- and z-axes.

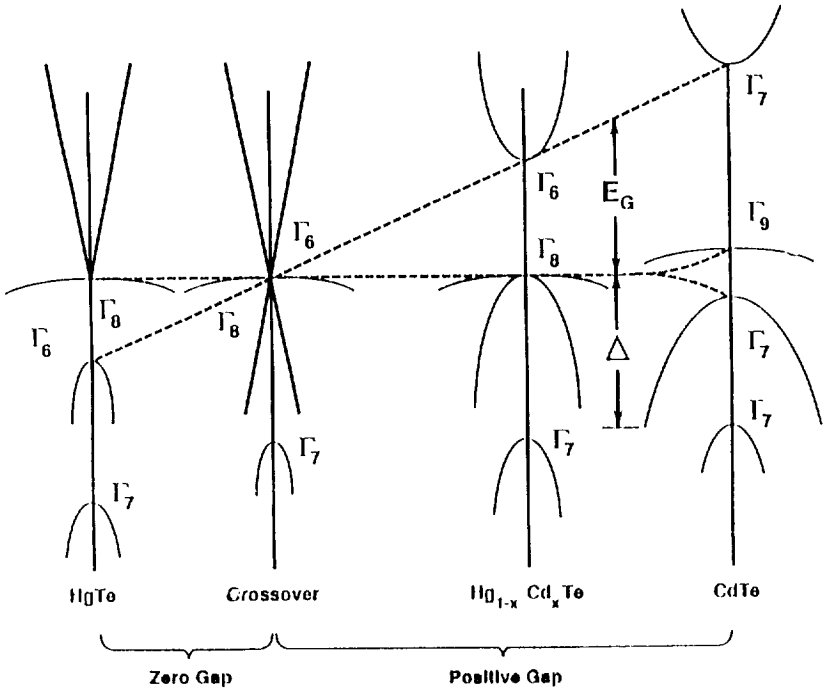

Figure 4.1 $Hg_{1-x}Cd_xTe$ Band Structure

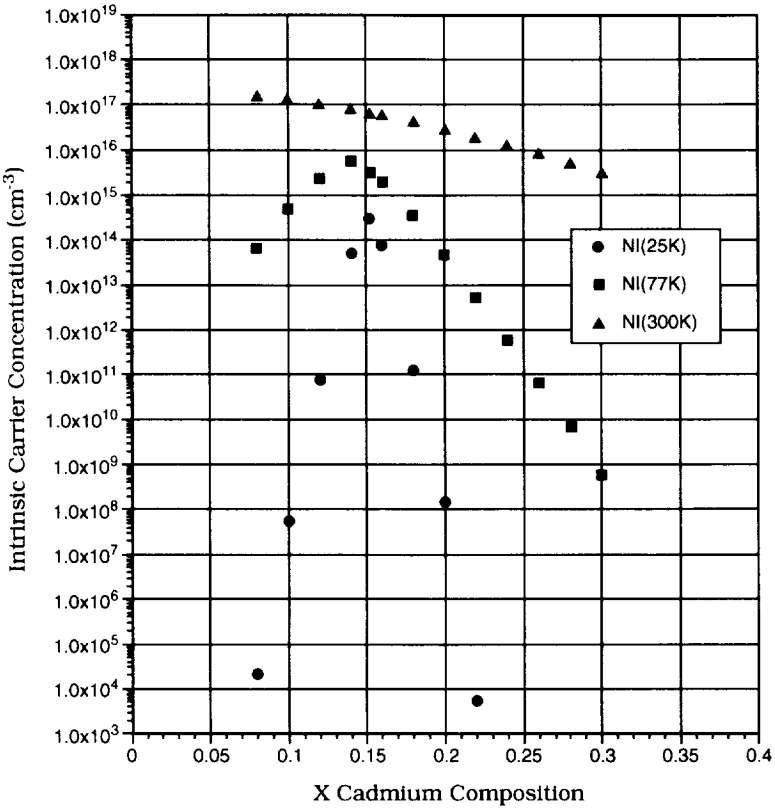

Figure 4.2 Intrinsic $Hg_{1-x}Cd_xTe$ - Carrier Concentration vs. Cadmium Composition

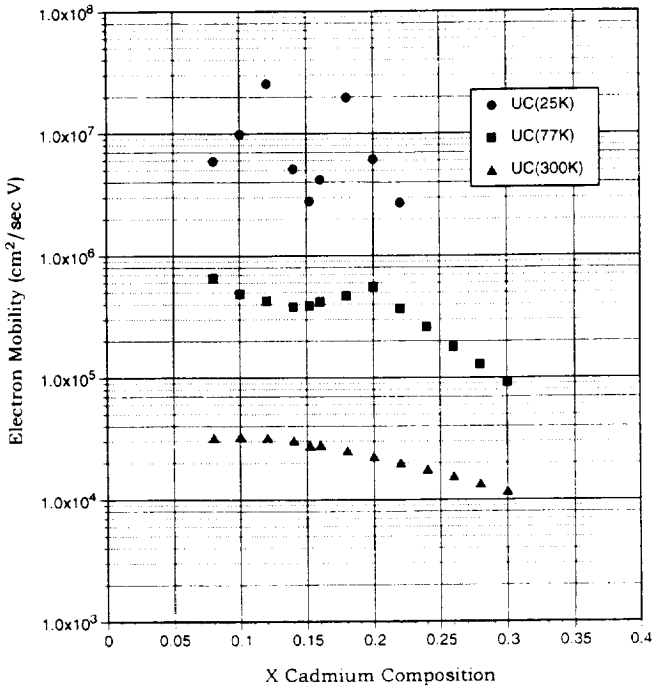

Figure 4.3 Intrinsic $Hg_{1-x}Cd_xTe$ - Electron Mobility vs. Cadmium Composition

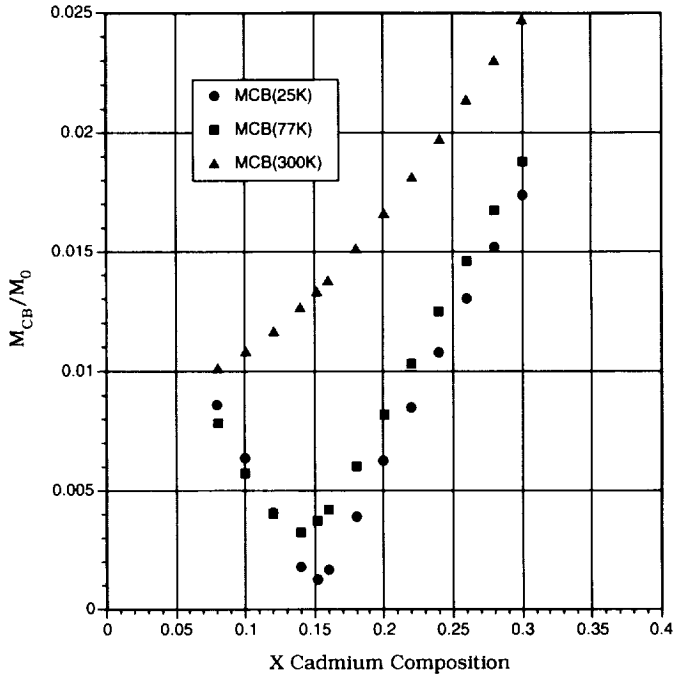

Figure 4.4 Intrinsic $Hg_{1-x}Cd_xTe$ - Carrier Concentration Effective Mass vs. Cadmium Composition

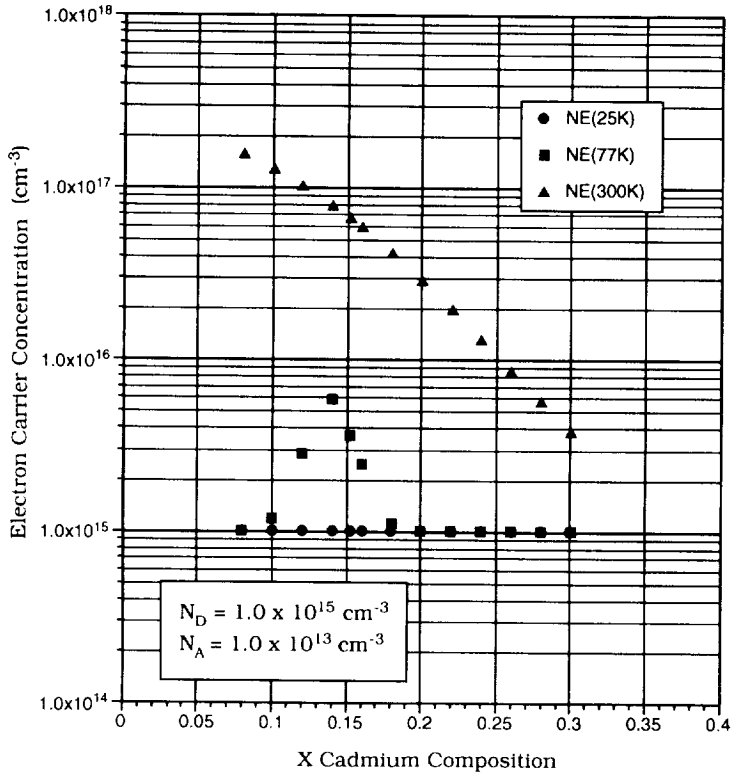

Figure 4.5 Extrinsic $Hg_{1-x}Cd_xTe$ - Electron Carrier Concentration vs. Cadmium Composition

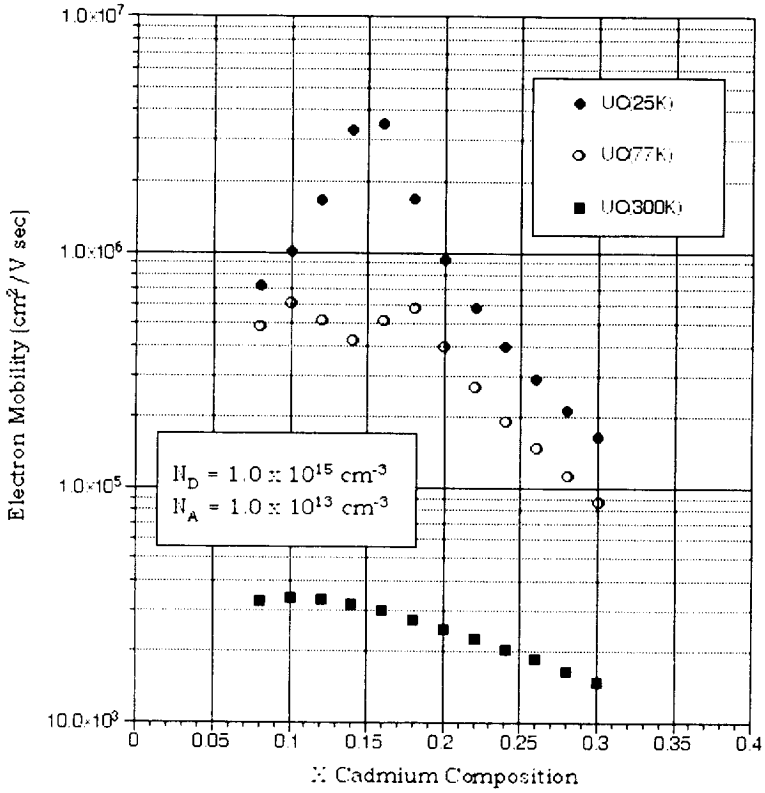

Figure 4.6 Extrinsic $Hg_{1-x}Cd_xTe$ - Electron Mobility vs. Cadmium Composition

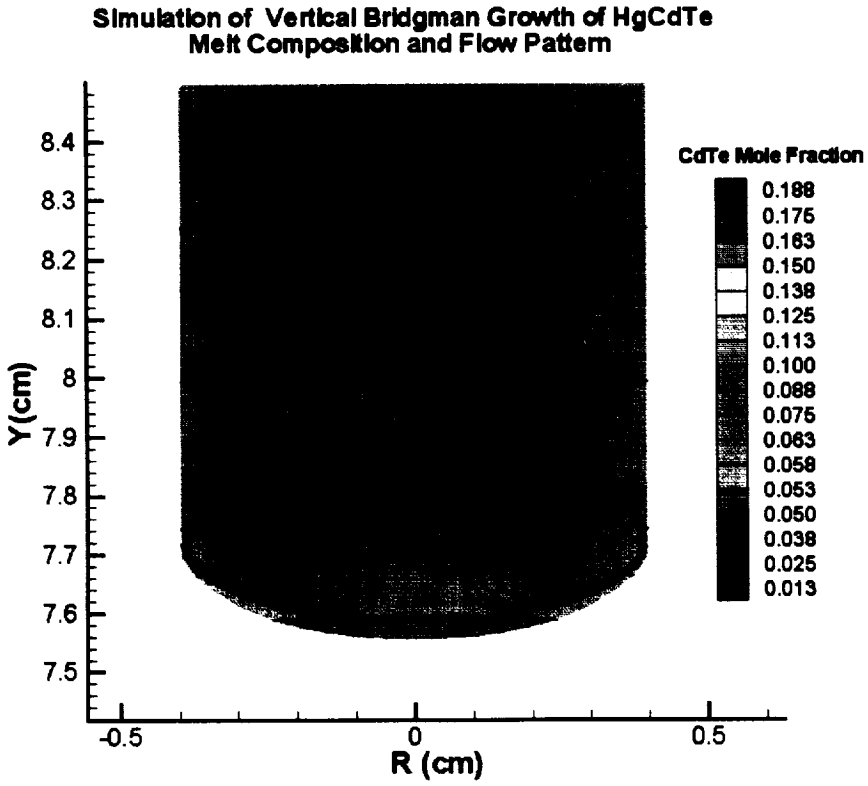

Figure 5.1 Liquid compositional Distribution and fluid flow during directional solidifciation of mercury cadmium telluride (after Motakef[64])

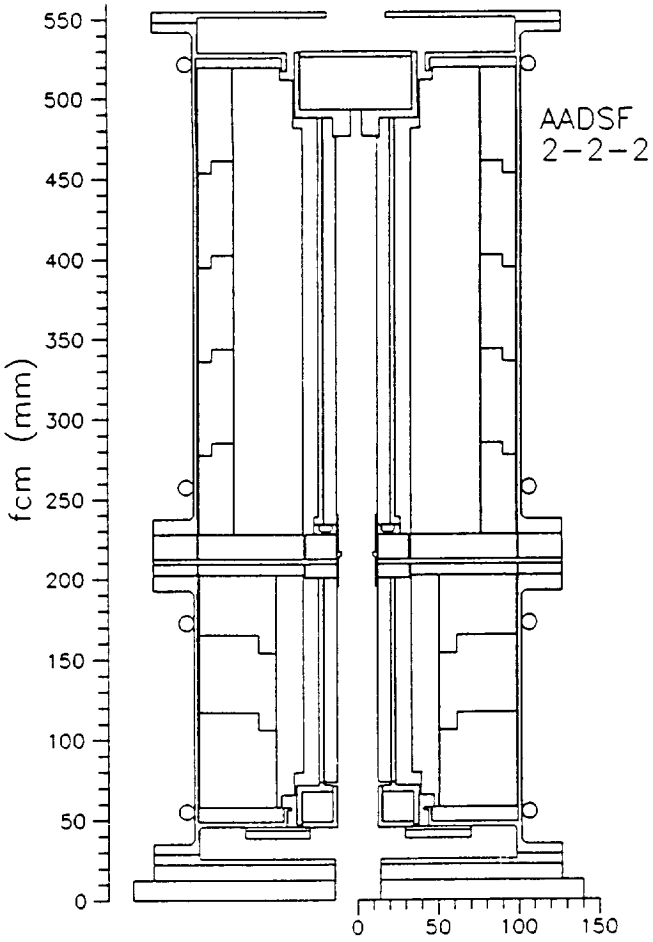

Figure 7.1 Schematic View of AADSF

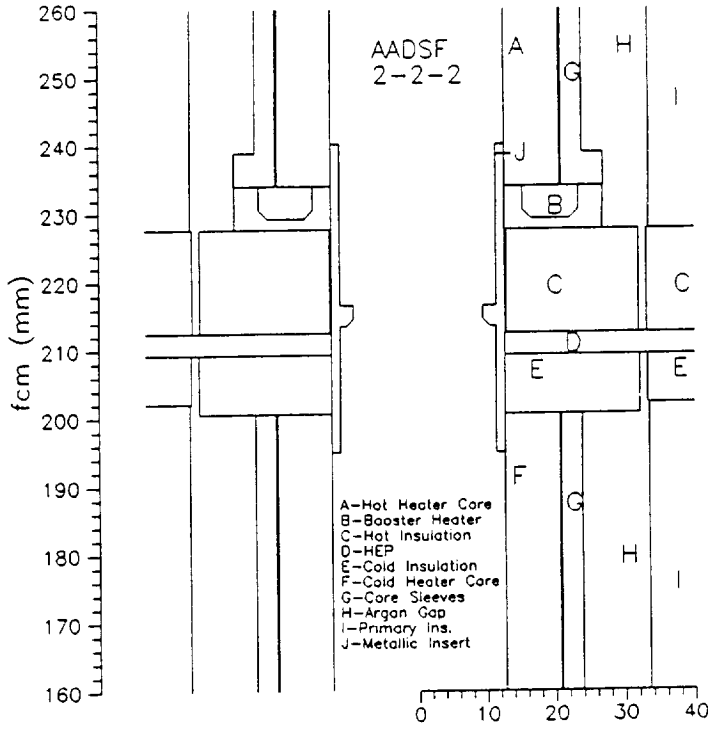

Figure 7.2 Adiabatic Region of AADSF

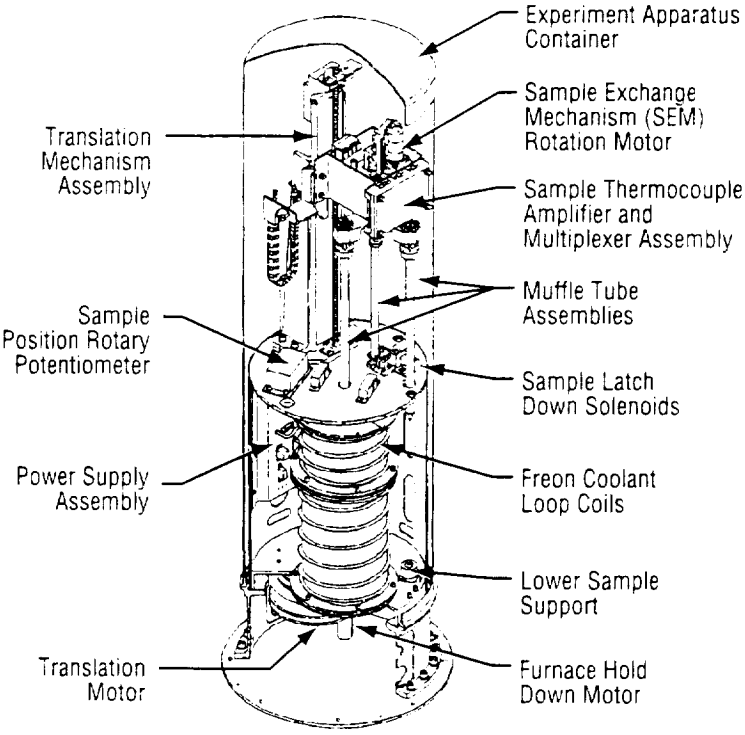

Figure 7.3 Advanced Automated Directional Solidification Furnace with Sample Exchange Mechanism (SEM)

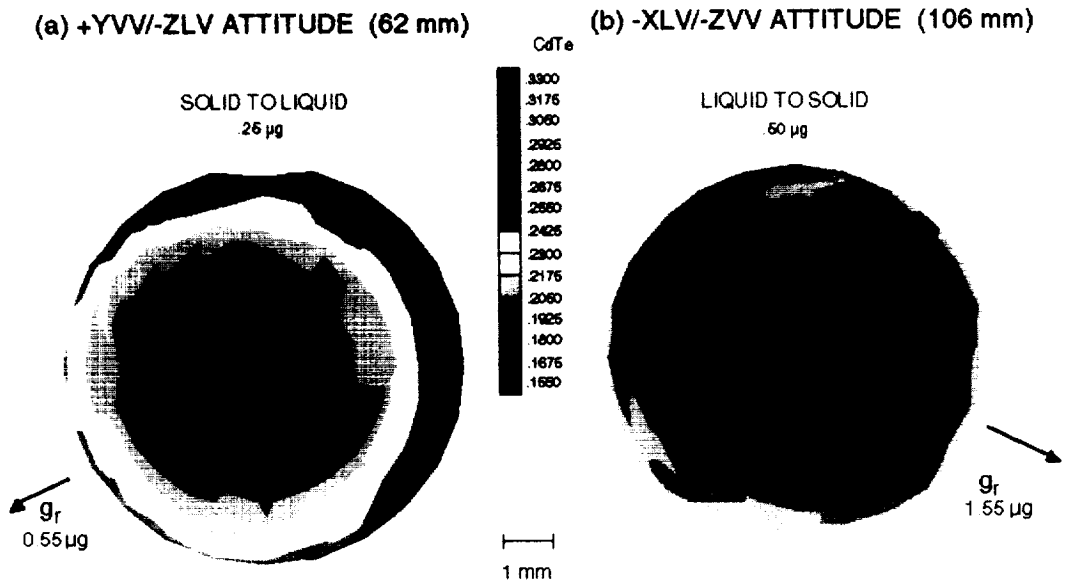

Figure 8.1 Compositional variation in USMP-2 Sample caused by different residual steady state accelerations

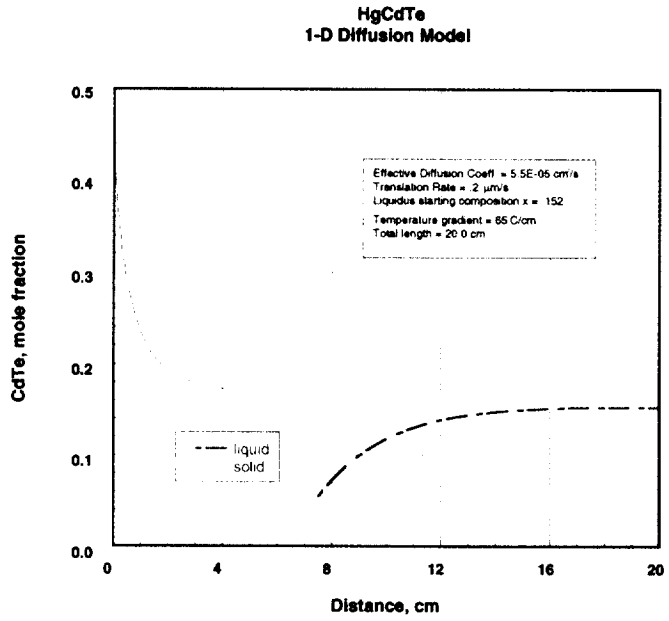

Figure 9.1 Modeled Composition profiles for growth of $Hg_{0.848}Cd_{0.152}Te$ at 0.2 µm/s with liquid composition at steady state region

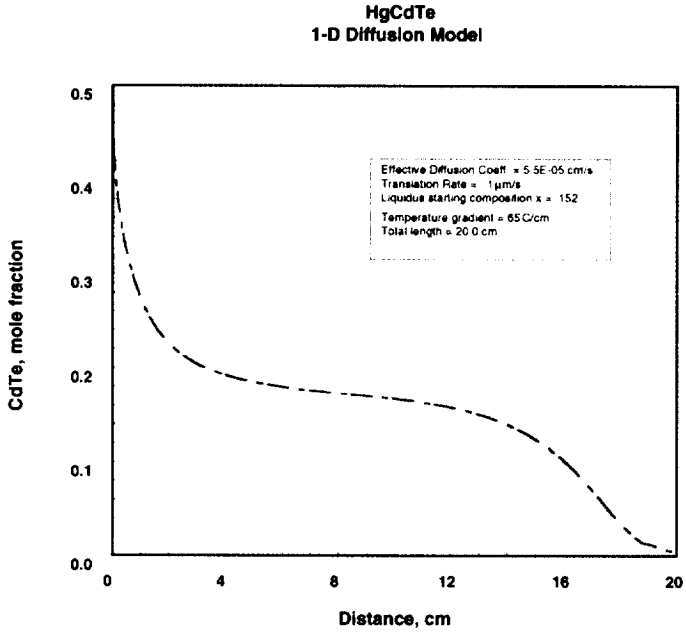

Figure 9.2 Modeled Composition profile for growth of $Hg_{0.848}Cd_{0.152}Te$ at 0.1 µm/s

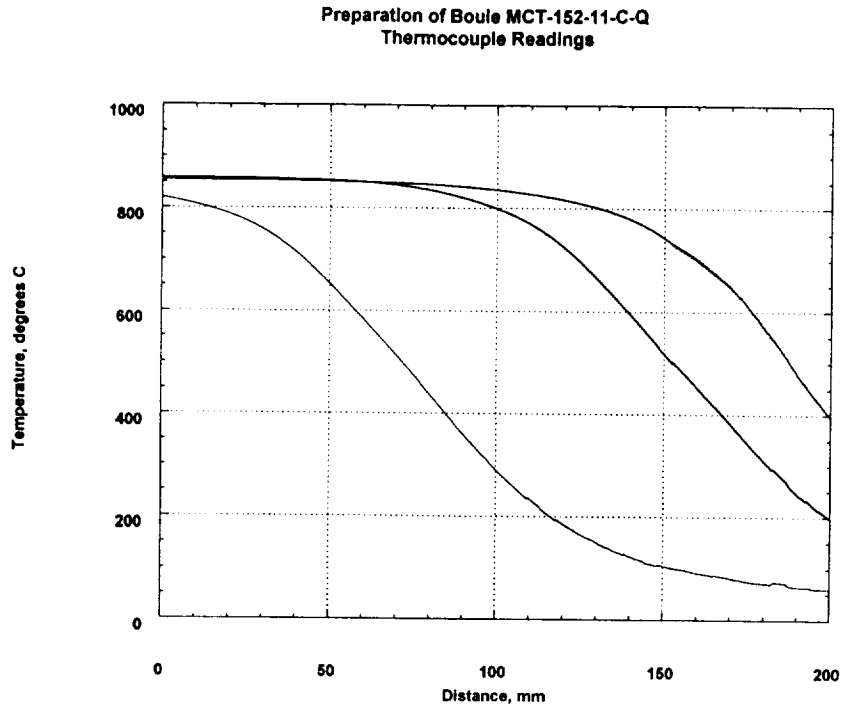

Figure 9.3 Thermocouple data obtained during processing of precursor material
Gradient at solidification temperature is 30 degree/cm

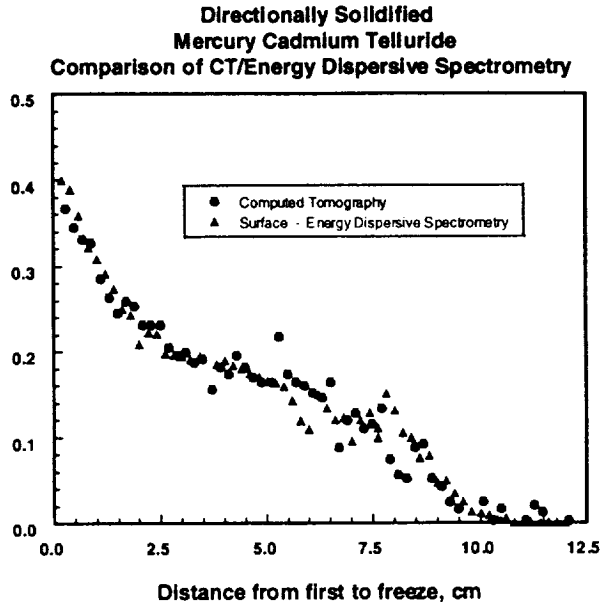

Figure 9.4 Composition of precursor boule as determined by surface EDS and
Computed x-ray Tomography (CT)

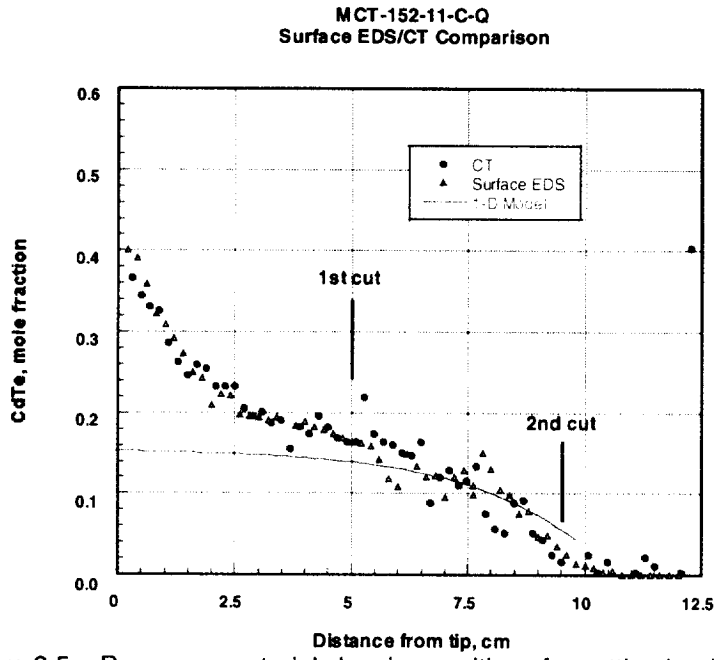

Figure 9.5 Precursor material showing positions for cutting boule
Composition determined by surface EDS and computed tomography

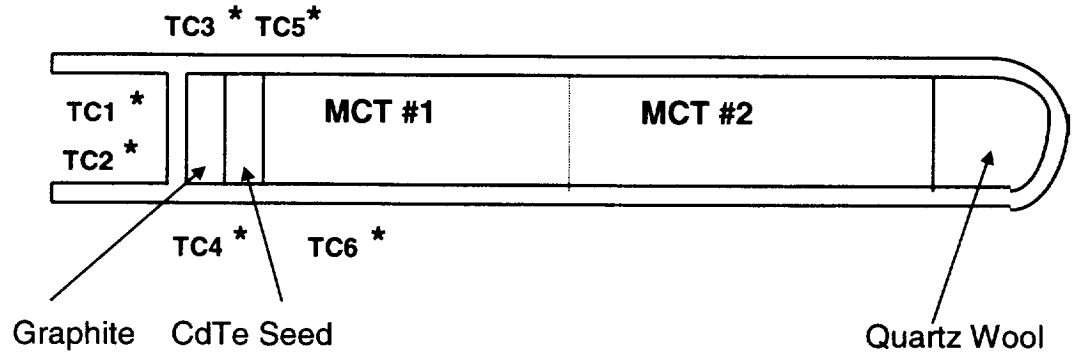

MCT #1 - Mercury cadmium telluride alloy with grown in "diffusion profile"
MCT #2 - Uniform composition mercury cadmium telluride alloy
TC1-TC6 - Type K thermocouples

Figure 9.6 Ampoule Design for USMP-4 (Not to scale)

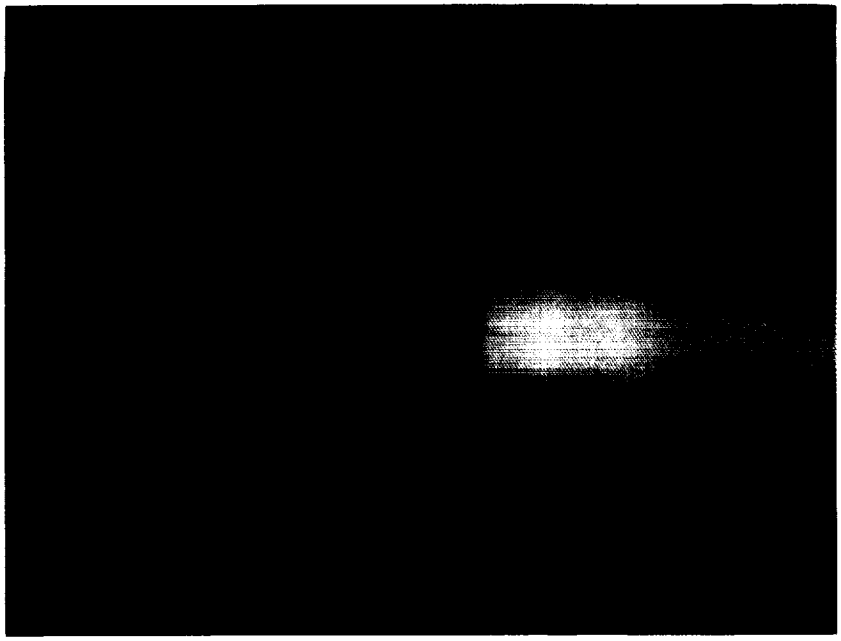

Figure 9.7 Radiograph of Cartridge showing position of thermocouples
Positions of thermocouples move during assembly

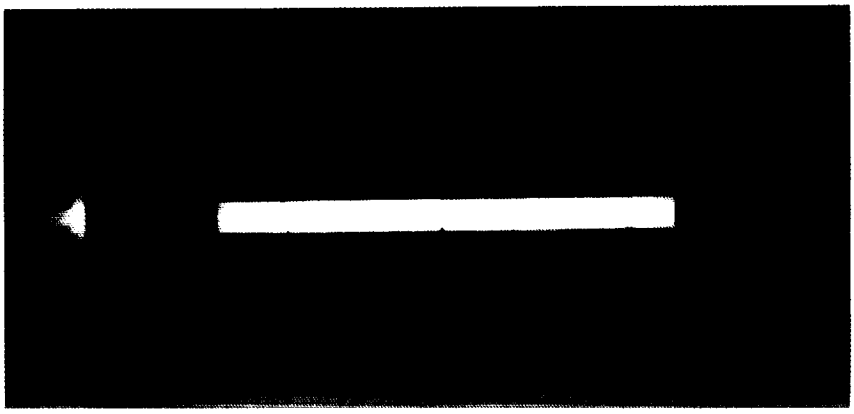

Figure 9.8 Sample SL1-415 Radiograph following vibration test

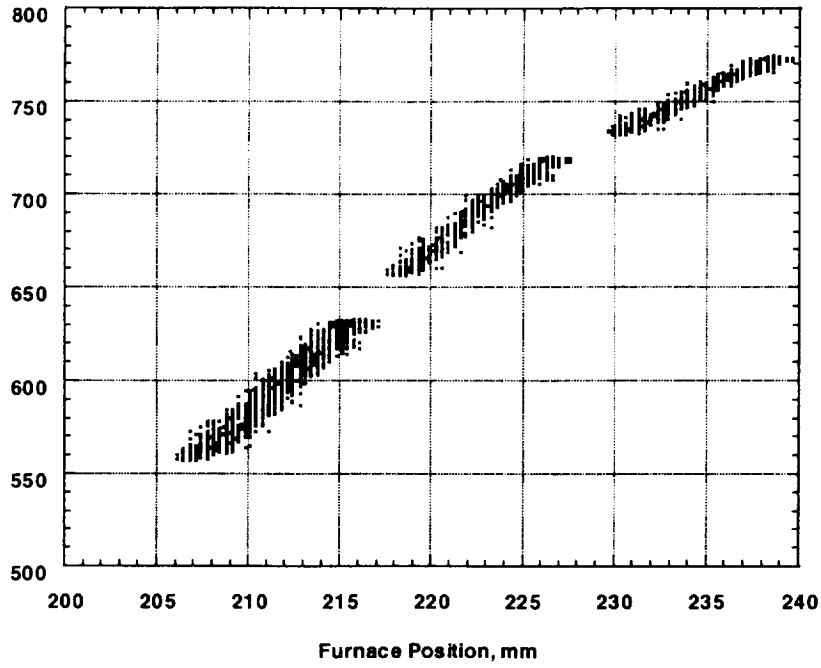

Figure 9.9 Temperatures recorded during processing of SL1-413. Normalized to furnace position

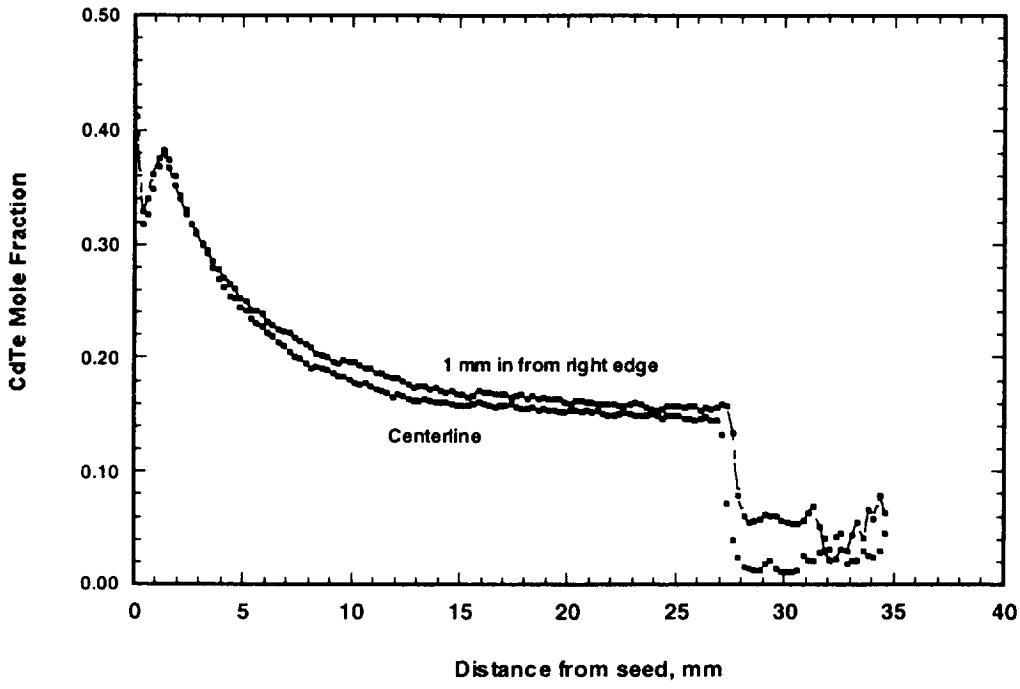

Figure 9.10 WDS ZAF corrected compositions for SL1-424

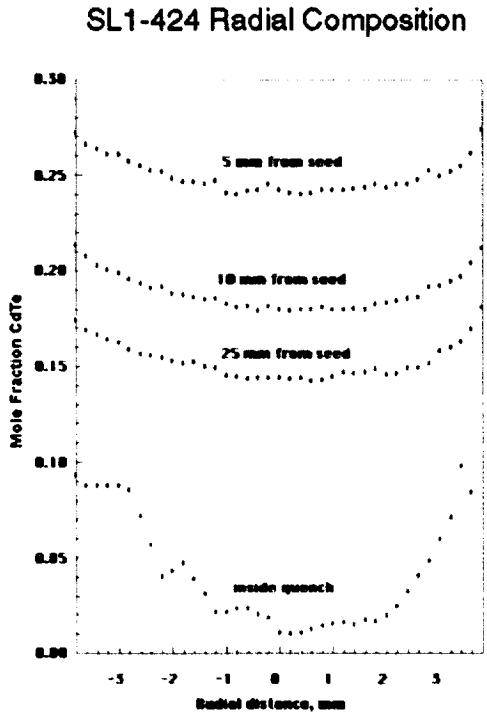

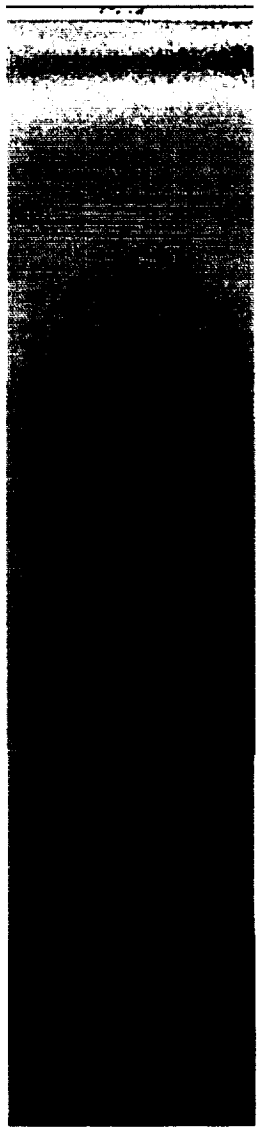

Figure 9.11 2-D Chemical Analysis for sample SL1-424. Electron microprobe counts of Cd L lines

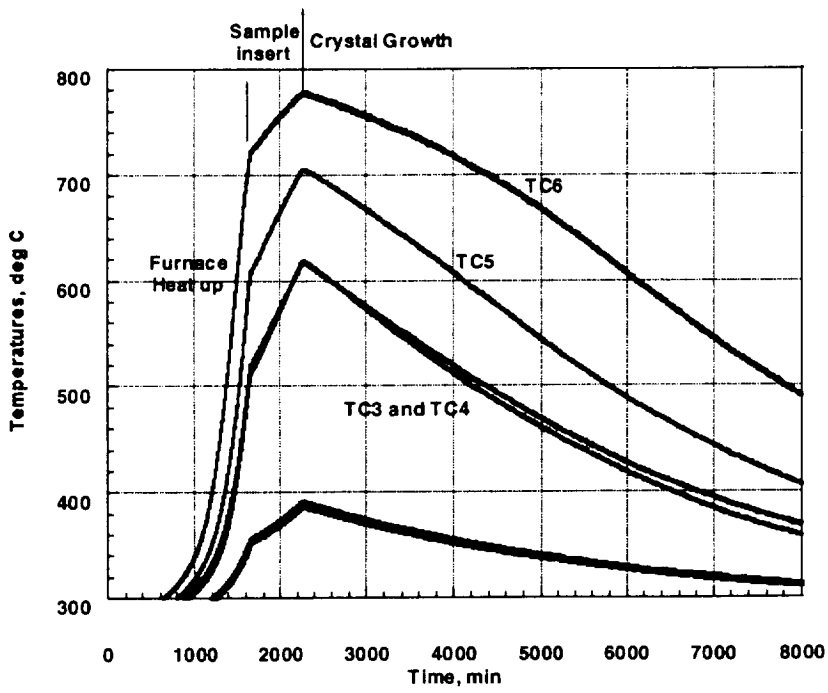

Figure 9.12 Sample Temperatures during Processing of SLNF-423

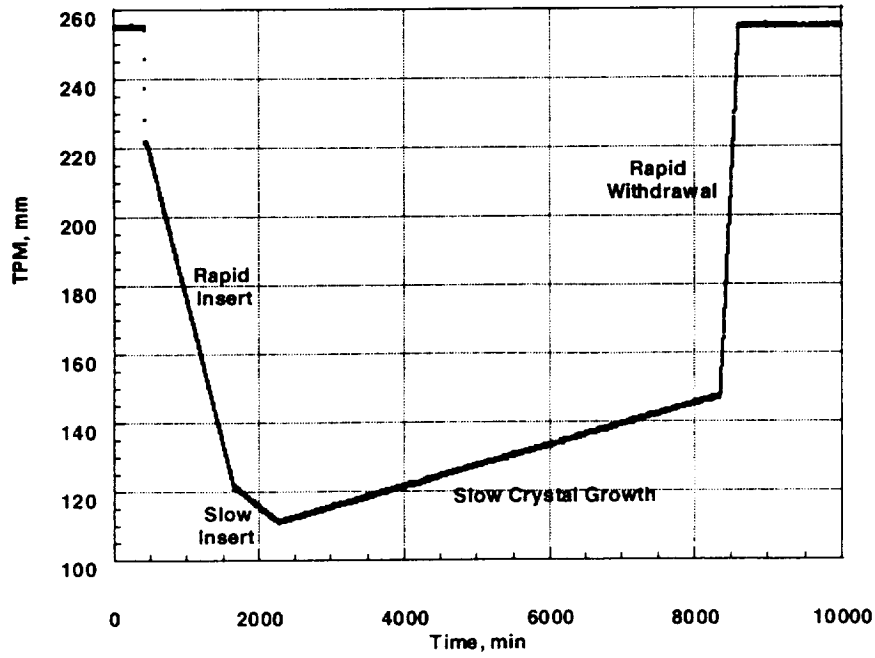

Figure 9.13 Sample Position during Processing of SLNF-423

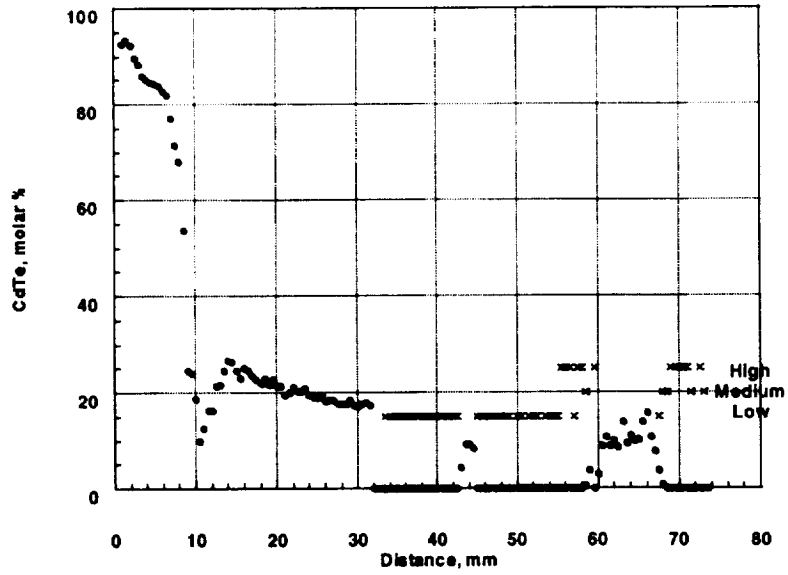

Figure 9.14 Surface EDS Analysis of Sample SLNF-423 showing excess tellurium and mercury telluride

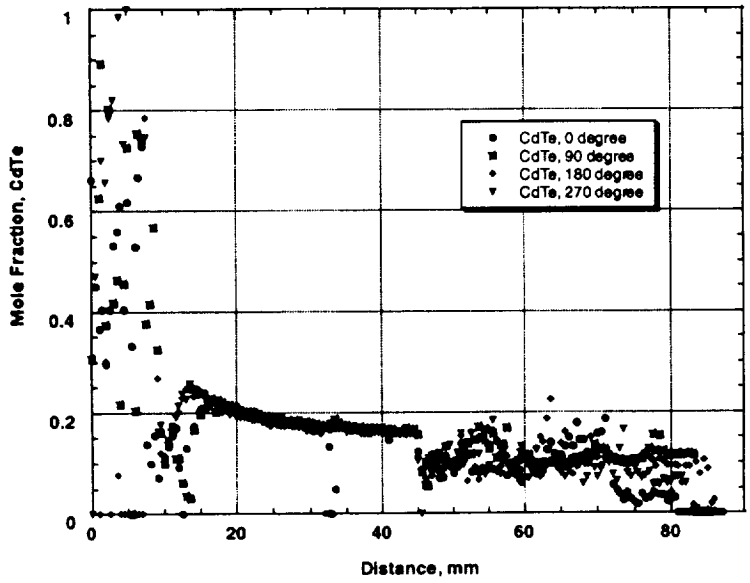

Figure 9.15 WDS readings of all four surfaces of SLNF-423 following "cleaning" with nitric acid

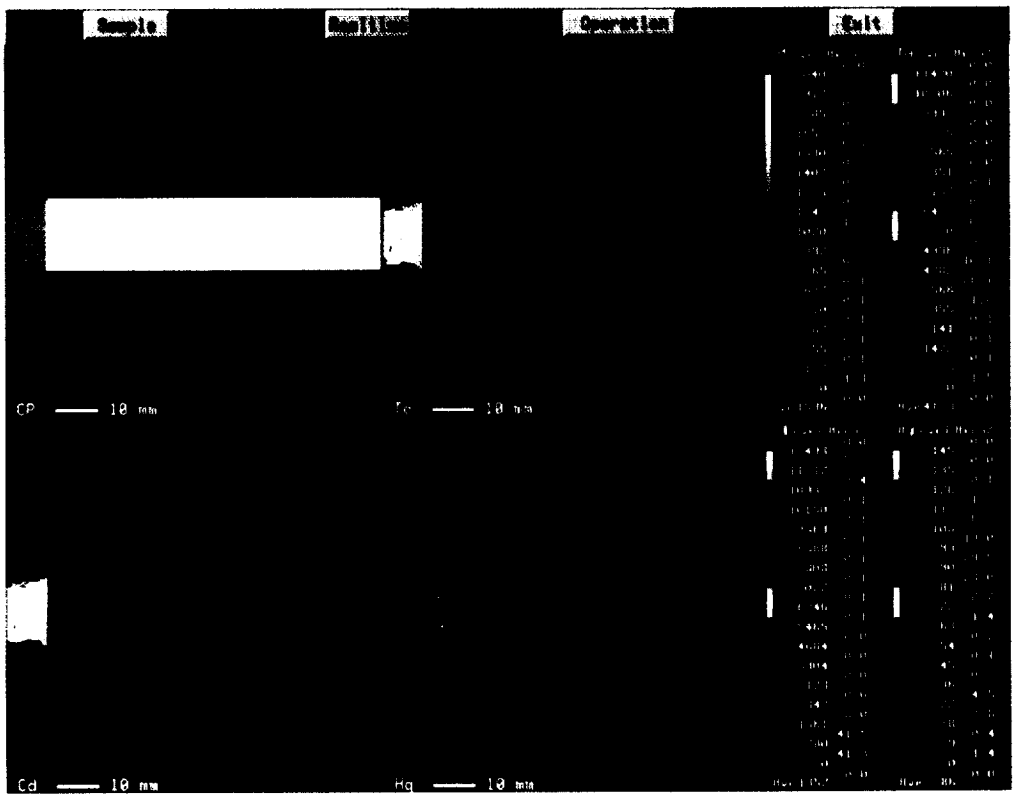

Figure 9.16 Analysis of the polished surface of SLNF-423
Showing secondary electron image, Cd (WDS), Te (WDS) and Hg (EDS

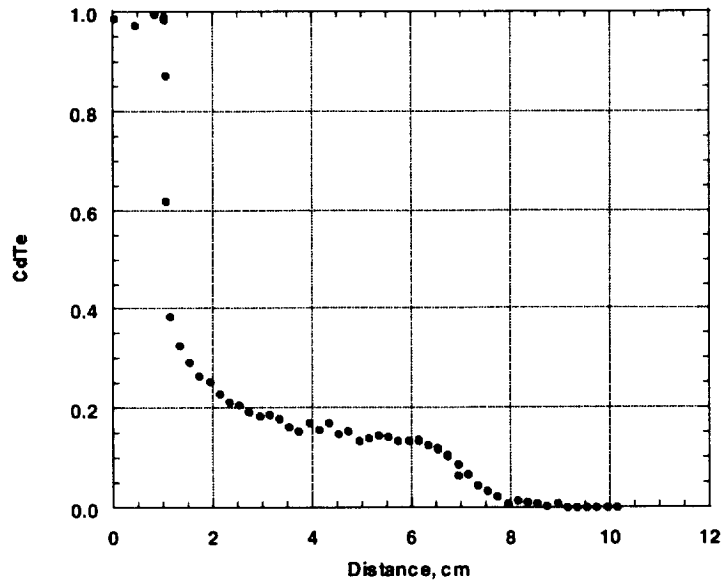

Figure 9.17 Centerline Composition for SL1-416, Grown in 5T Static Magnetic Field

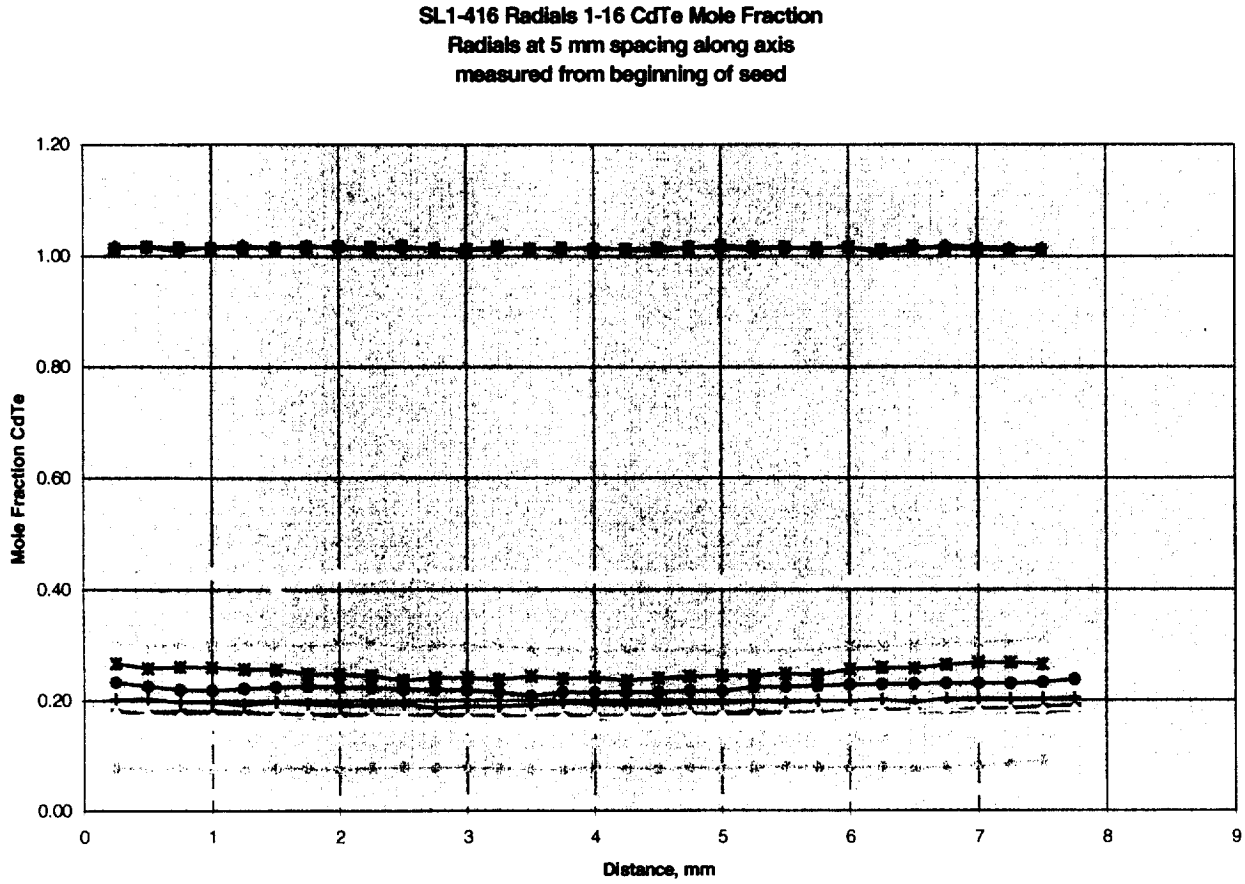

Figure 9.18 WDS radial compositions for sample grown in a 5 tesla static magnetic field

Figure 10.1 **Orbiter Attitude during the SL1 Sample Processing**

The orbiter is flying from left to right with the earth at the bottom. The AADSF is mounted along the center line of the orbiter with the hot zone towards the cargo bay.

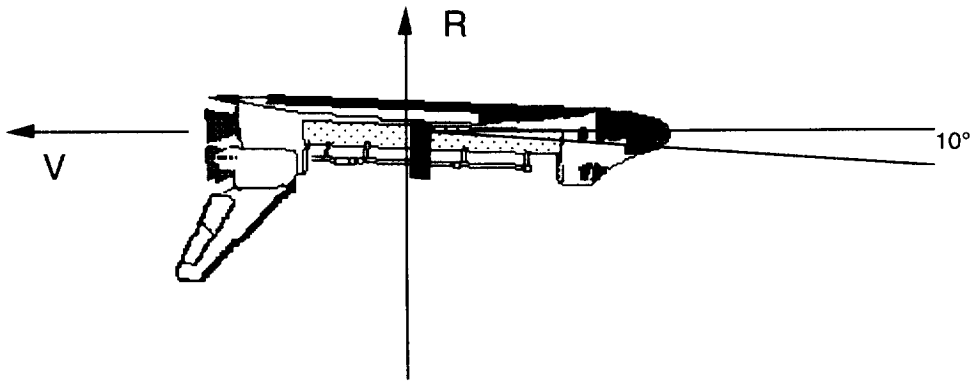

Figure 10.2 **Three Hours of OARE Data During the SL1 Processing Segment**

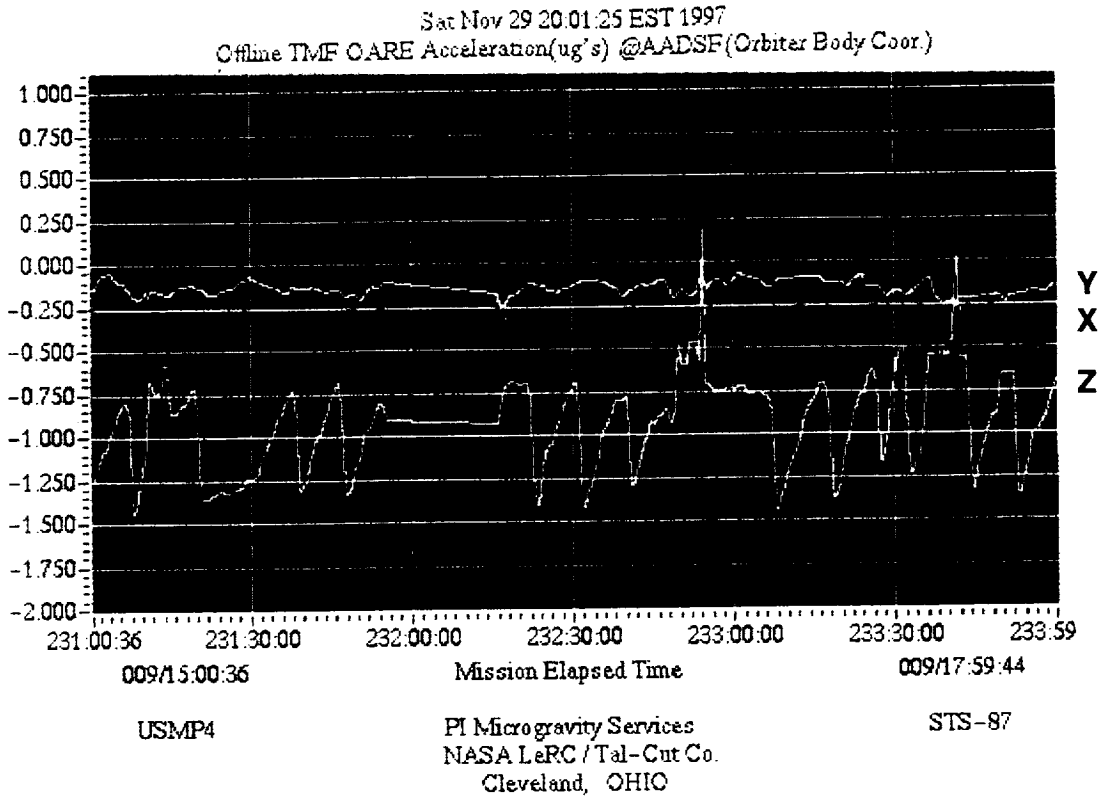

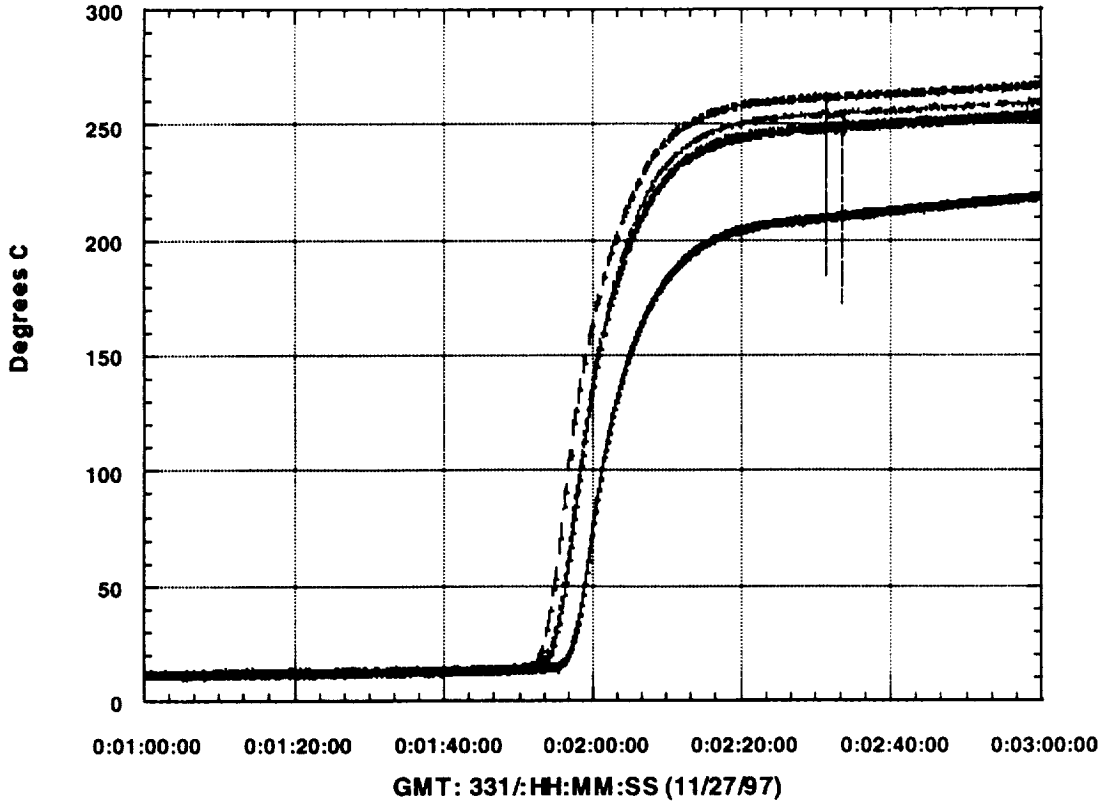

Figure 10.3 Heat up anomaly caused by erroneous compensating junction temperatures

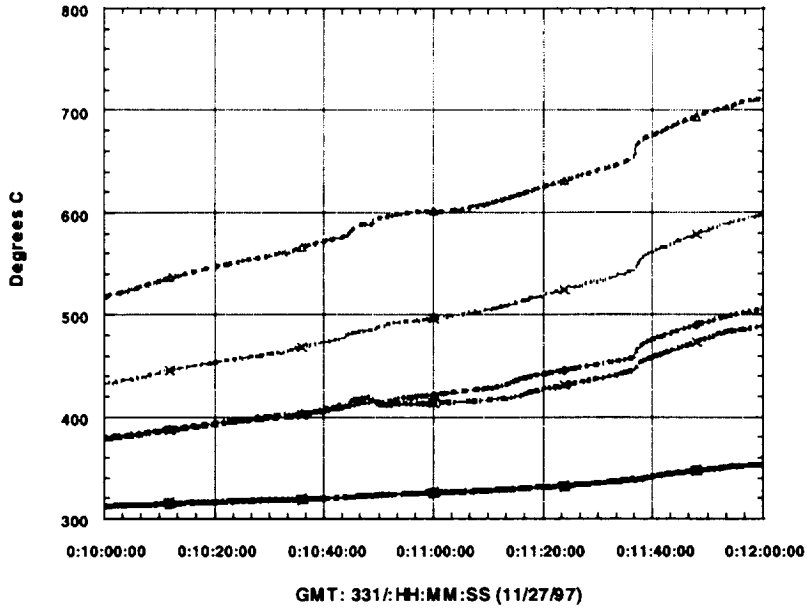

Figure 10.4 Anomalous Heating of Flight Sample –Thermocouple Readings

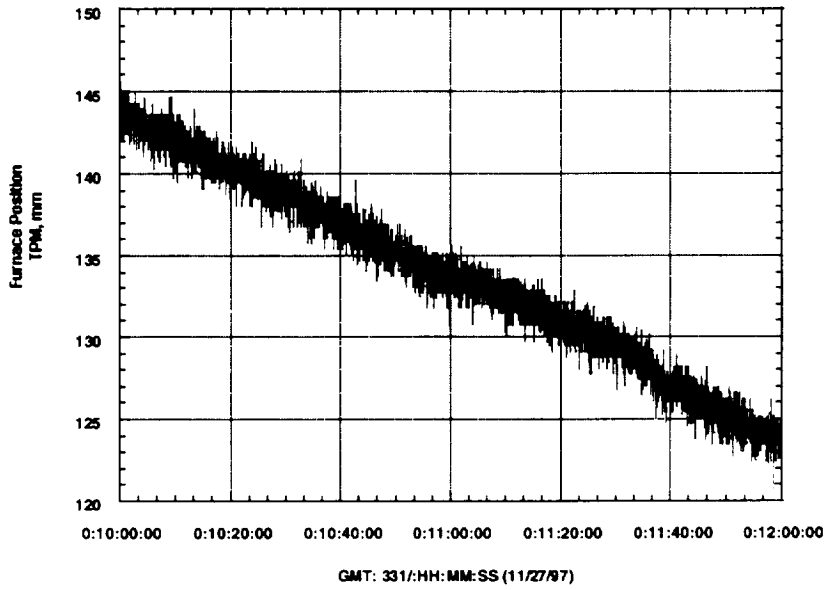

Figure 10.5 Anomalous Behavior during Heating – Cartridge Position

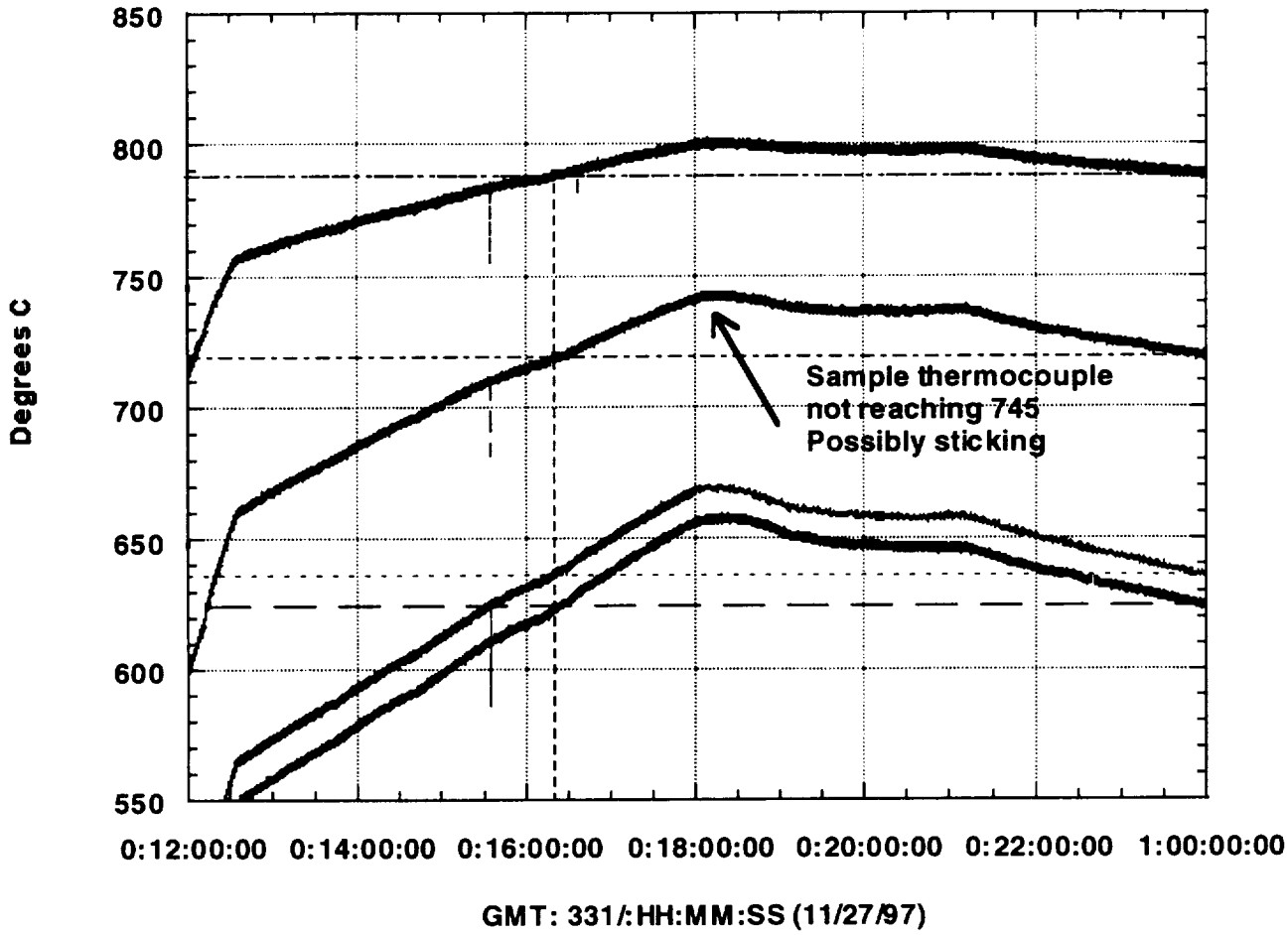

Figure 10.6 Thermocouple readings during end of melt back and start of crystal growth
Note the slowing of the thermocouple as it moves towards 745°C.
The melt back was stopped at 18:00:31, and the growth cycle started at 18:02:56

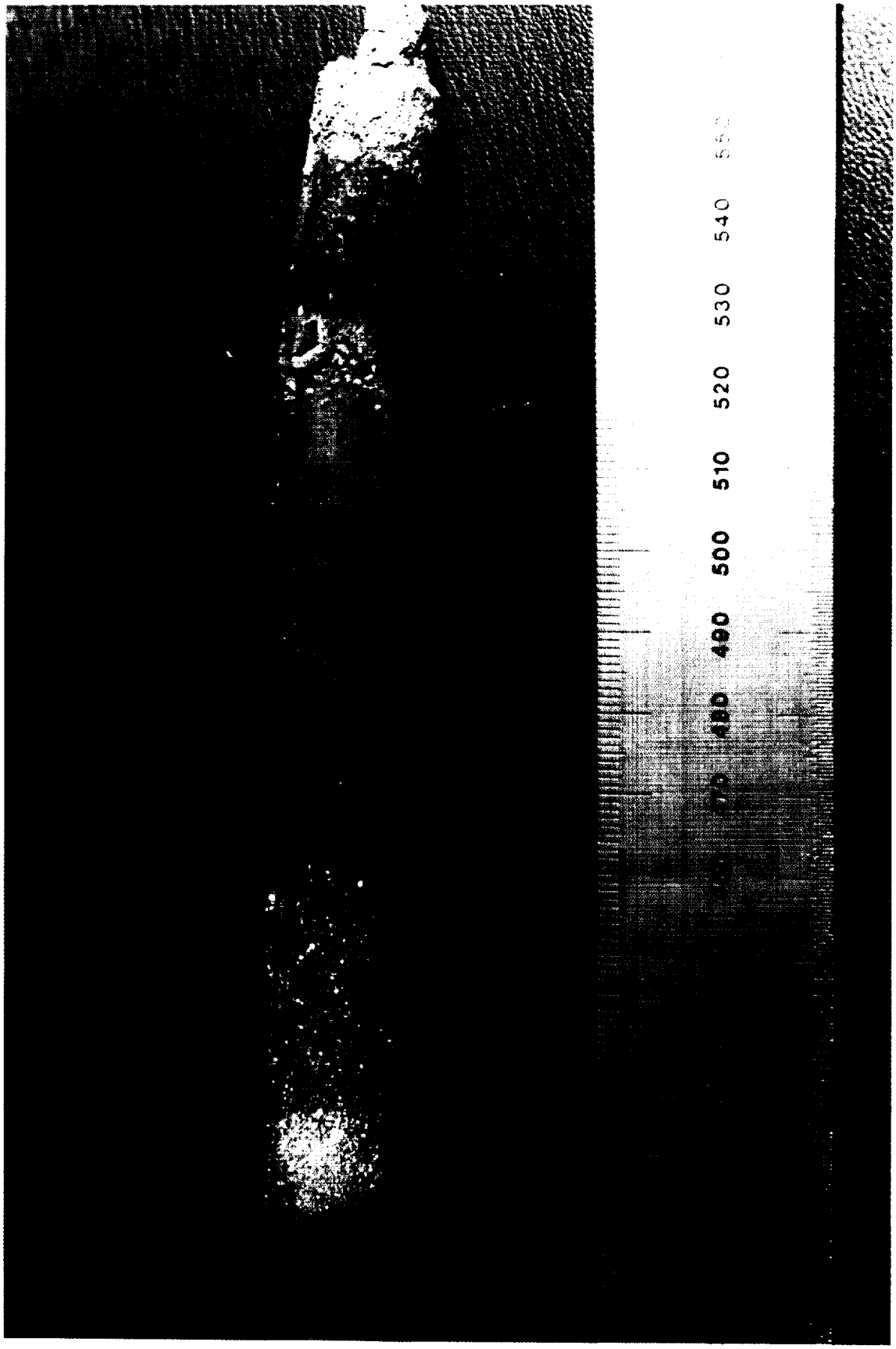

Figure 10.7 Flight cartridge, post-mission showing severe bending Scale is in cm.

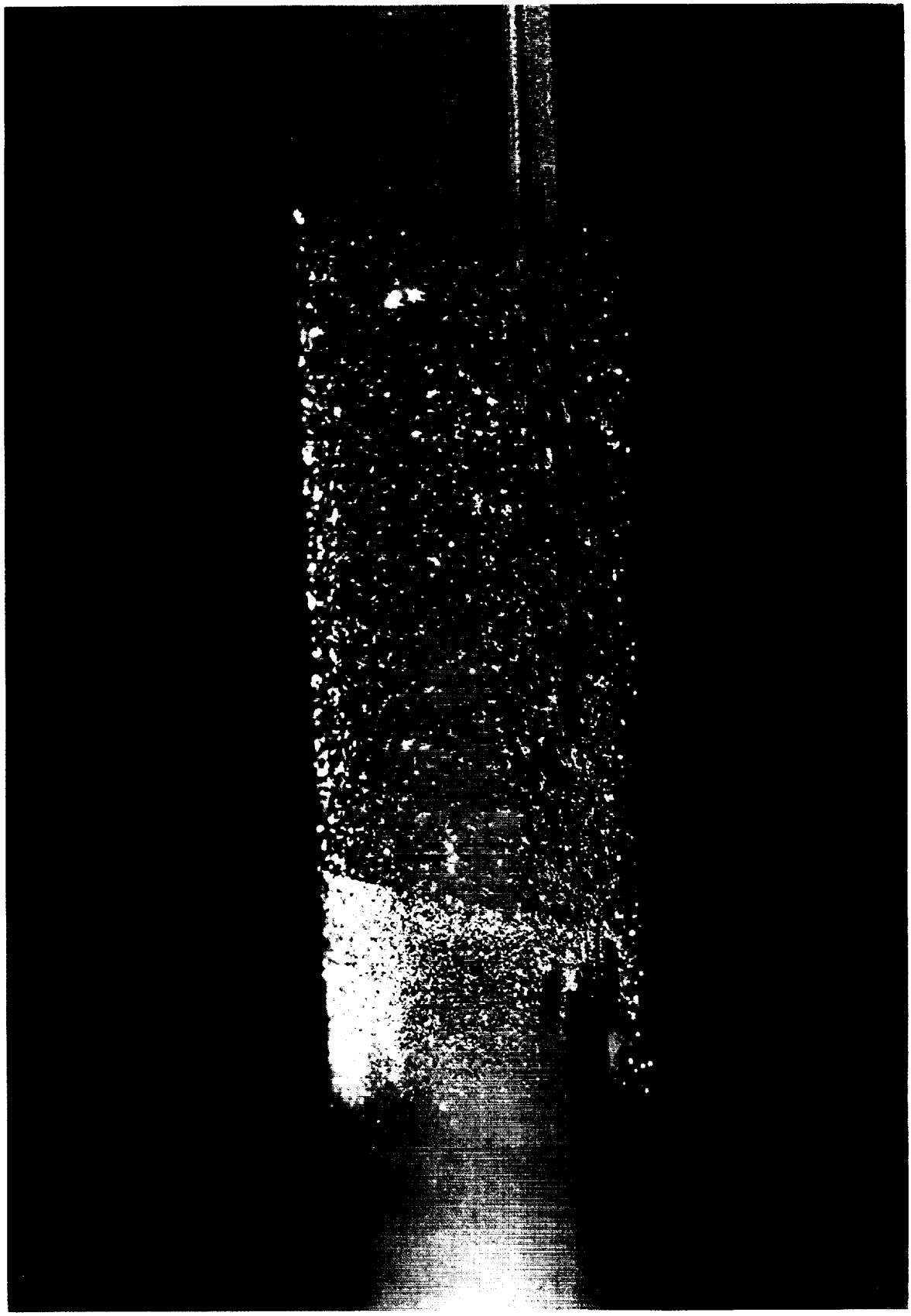

Figure 10.8 Close up of crystalline deposits on surface of cartridge SL1-417

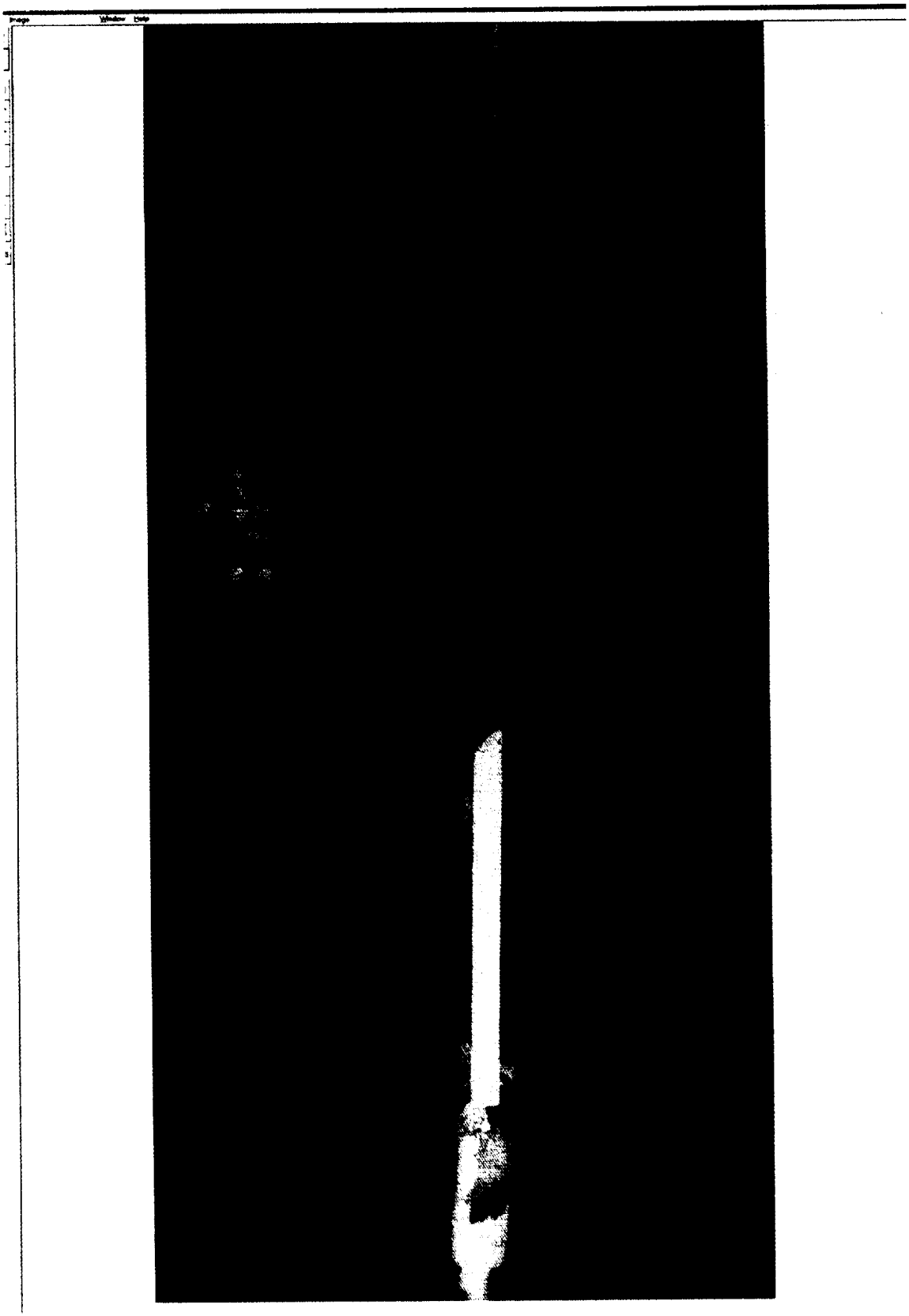

Figure 10.9 Radiograph of Cartridge SL1 showing HgCdTe intact, and surrounding debris
0° view – Parallel to direction of flight

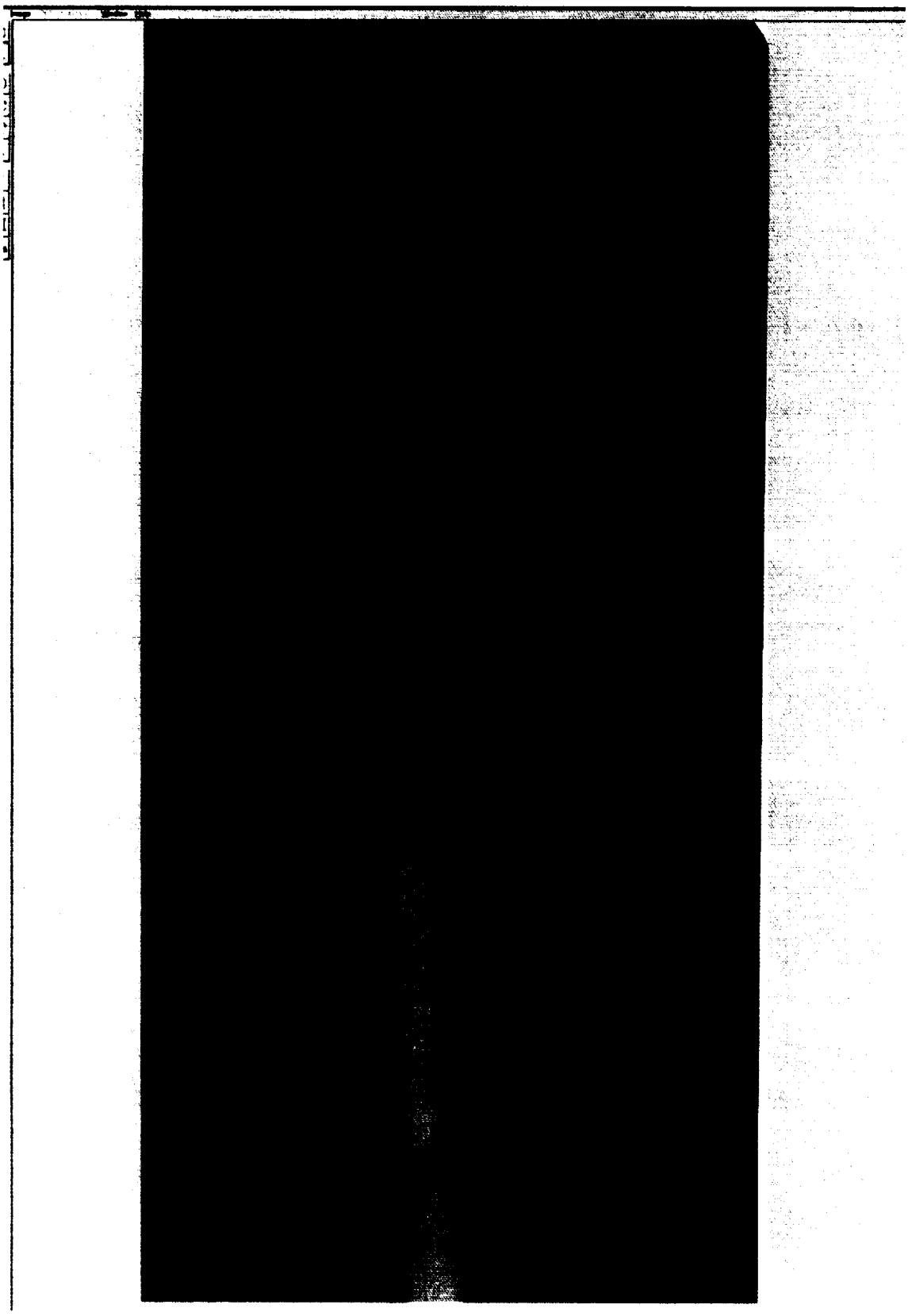

Figure 10.10 Radiograph of Cartridge SL1 showing HgCdTe intact, and surrounding debris
90^{o} view – Perpendicular to direction of flight

Figure 10.11 Macro photographs of flight sample SL1-417 taken at four different orientations relative to the flight direction..The seeds is at the top. Note the slit on the 0° surface (bottom left)

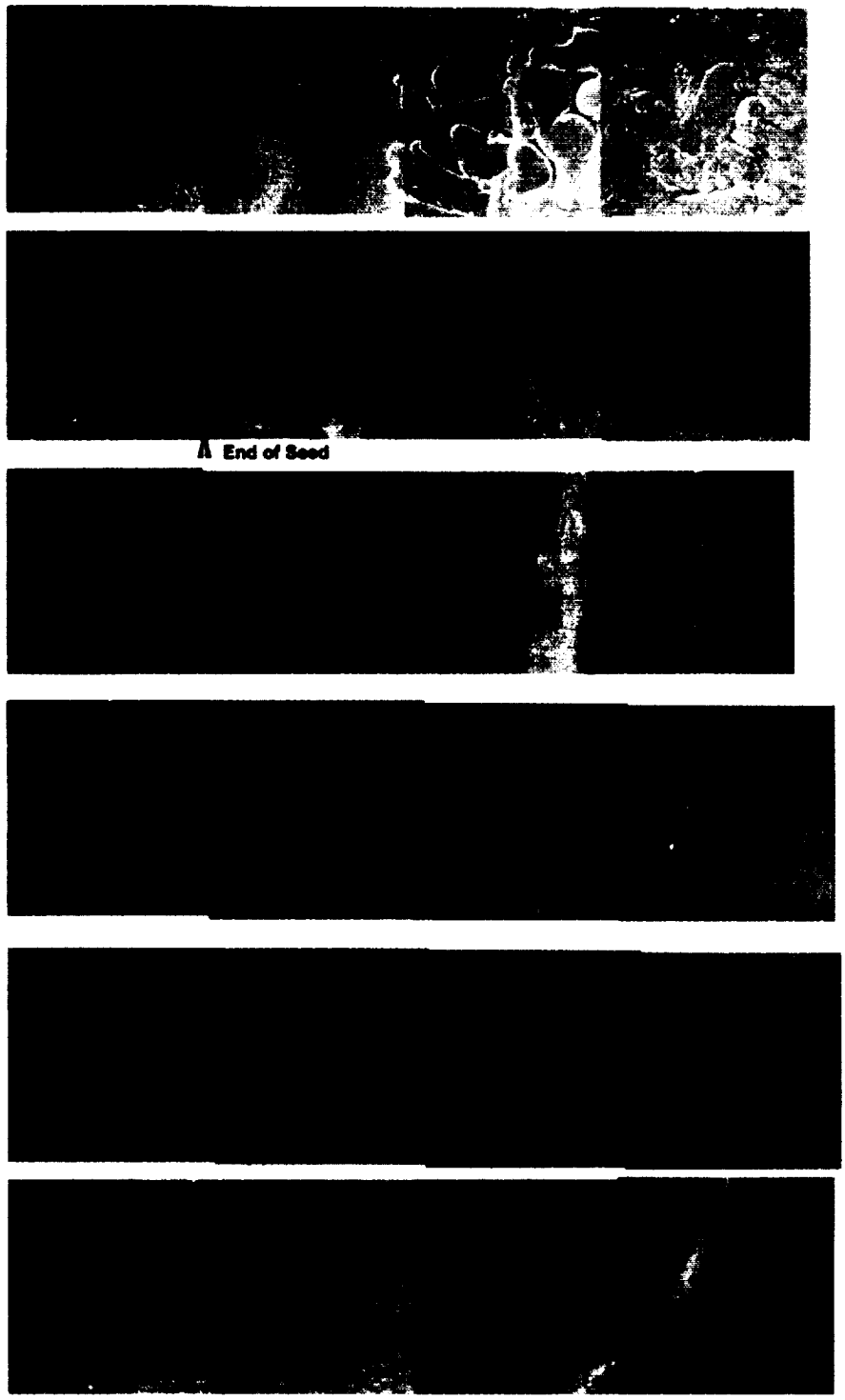

Figure 10.12 SEM photographs of surface of flight sample.
Start of seed is at top right – Series continues with the first to freeze at the right hand edge on each line. About three quarters of the total length is shown, and goes beyond the end of the slow grown region and into the rapidly withdrawn part of the sample.

Figure 10.13 SEM Photographs of crystals grown on seed surface
All were shown by EDS to be HgCdTe of very similar compositions

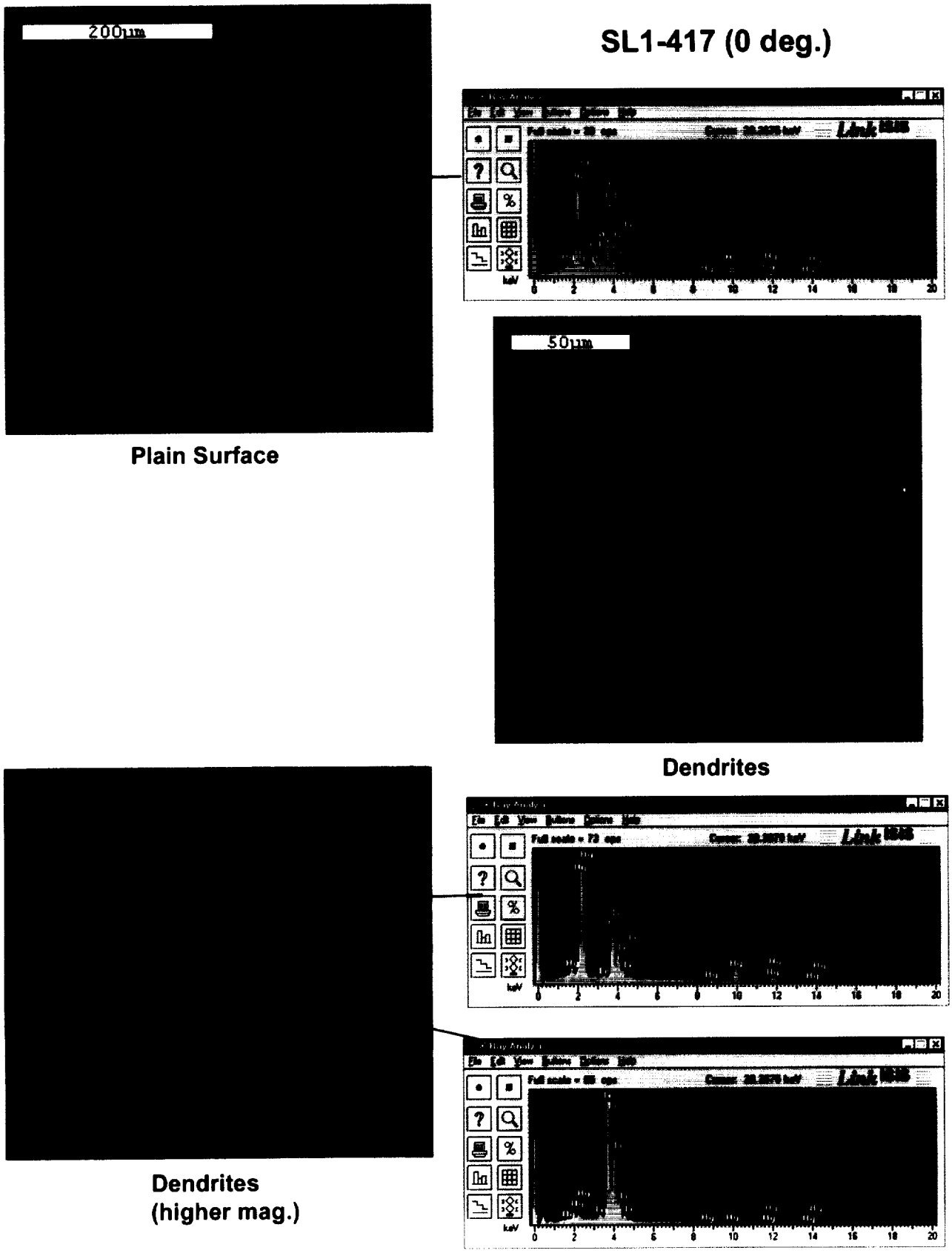

Figure 10.14 Typical surface regions from the flight sample with accompanying EDS spectra

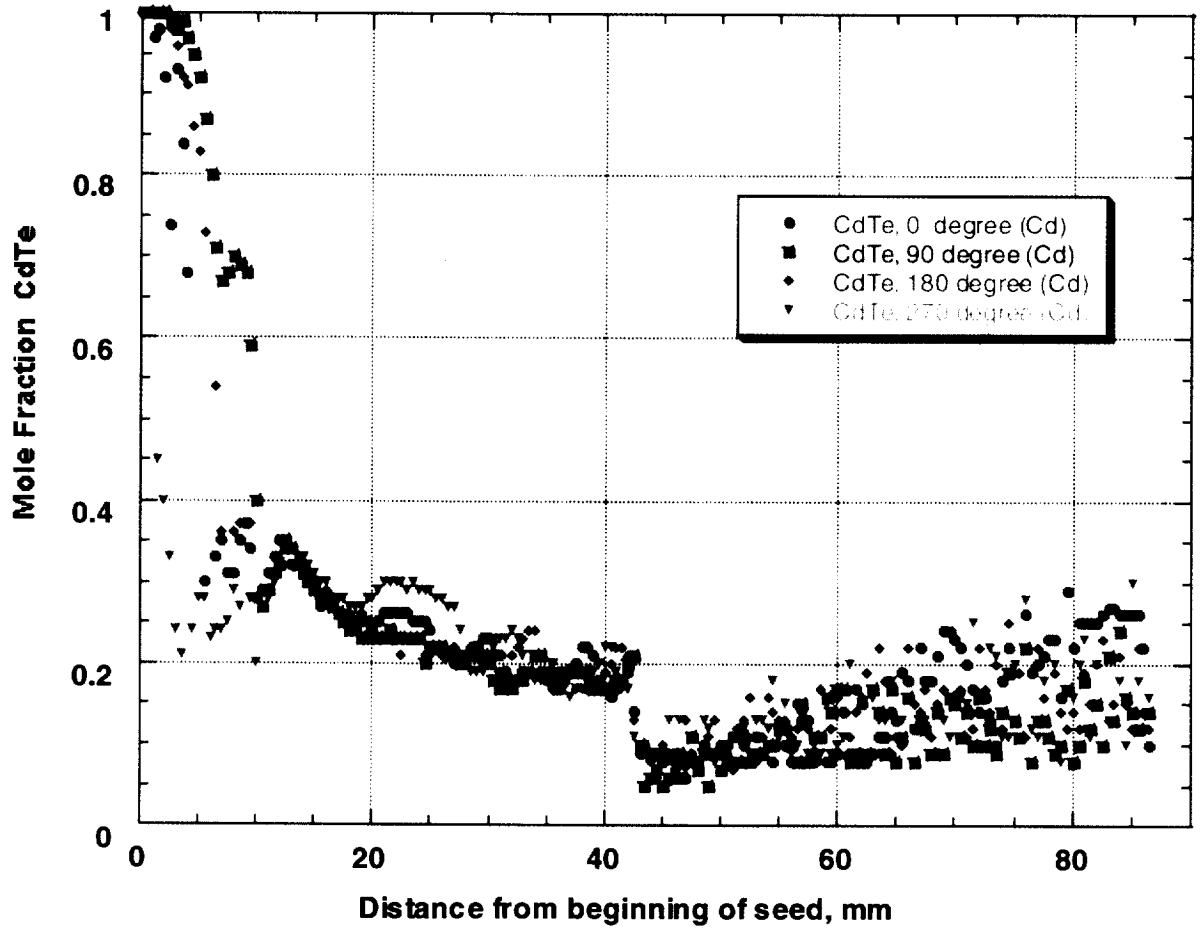

Figure 10.15 WDS results from four surfaces of the flight sample

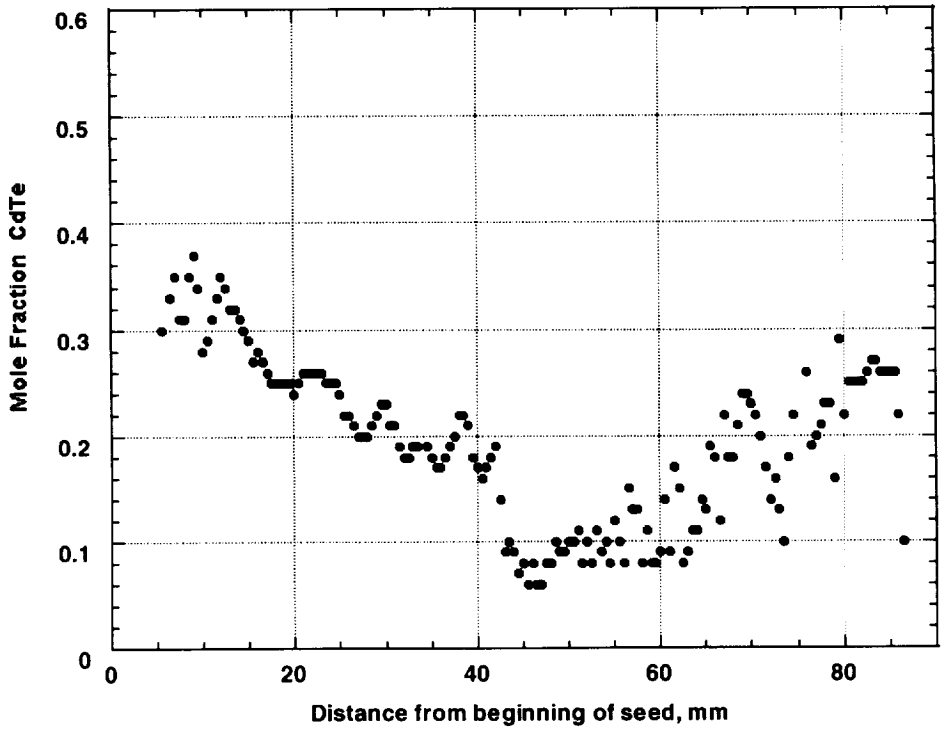

Figure 10.16 WDS Compositional readings from the 0° surface

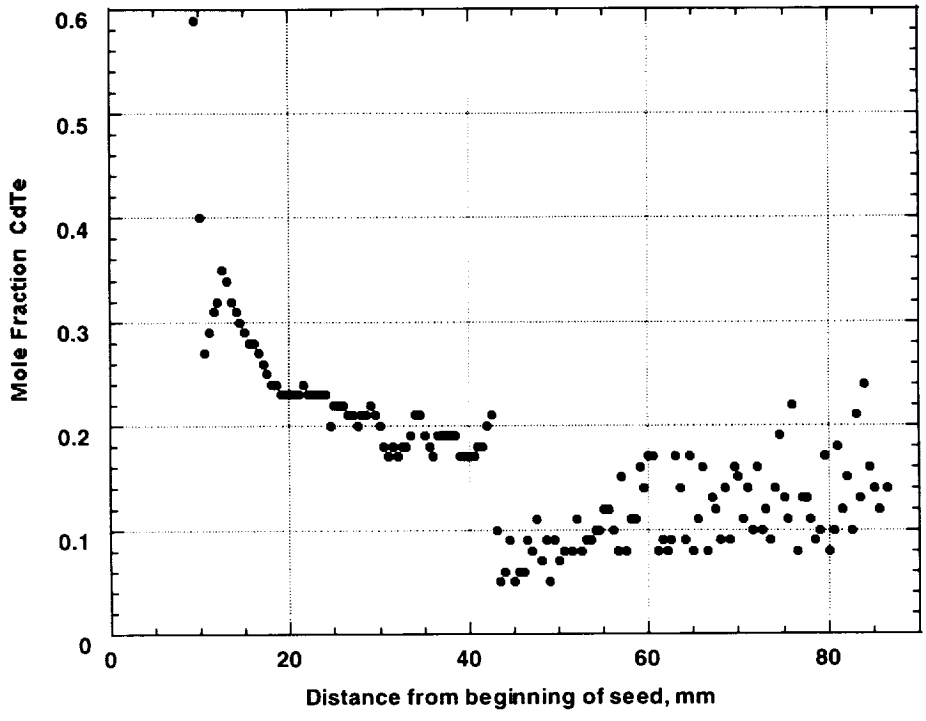

Figure 10.17 WDS Compositional readings from the 90° surface

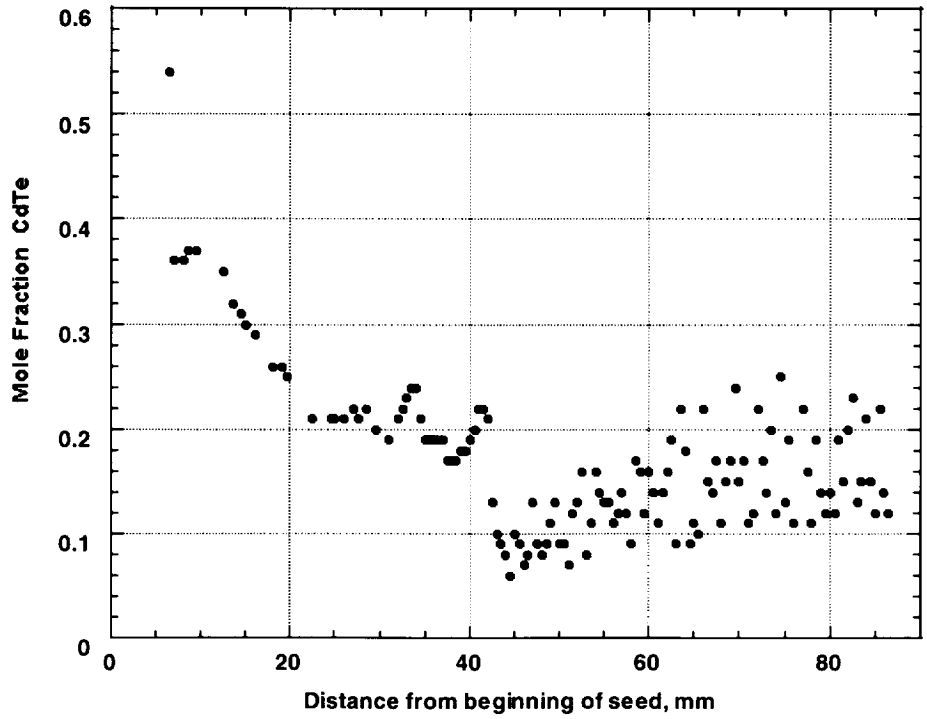

Figure 10.18 WDS Compositional readings from the 180° surface

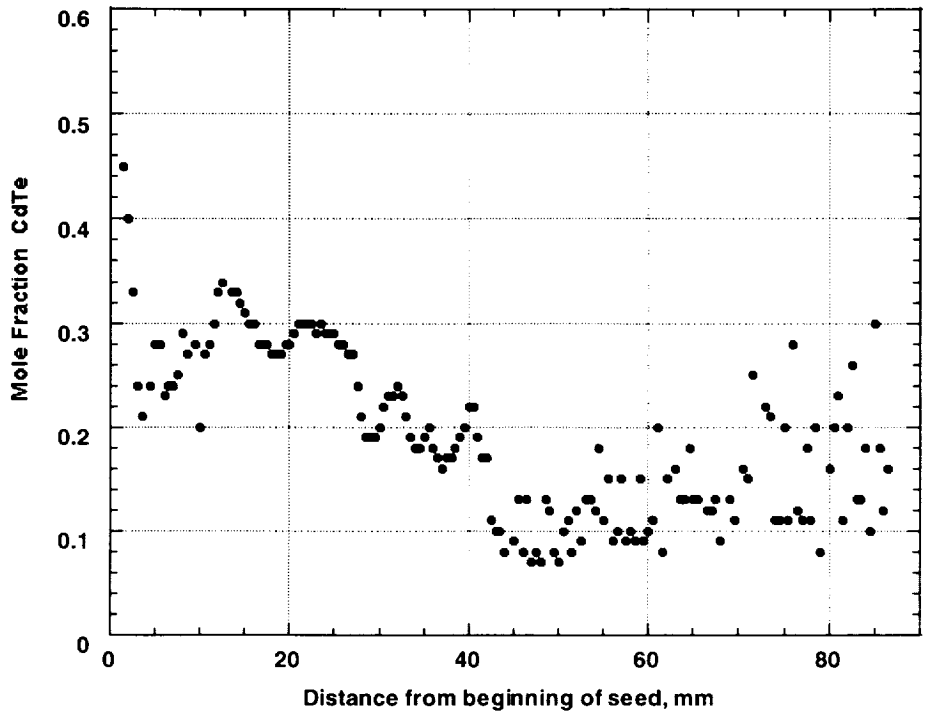

Figure 10.19 WDS Compositional readings from the 270° surface

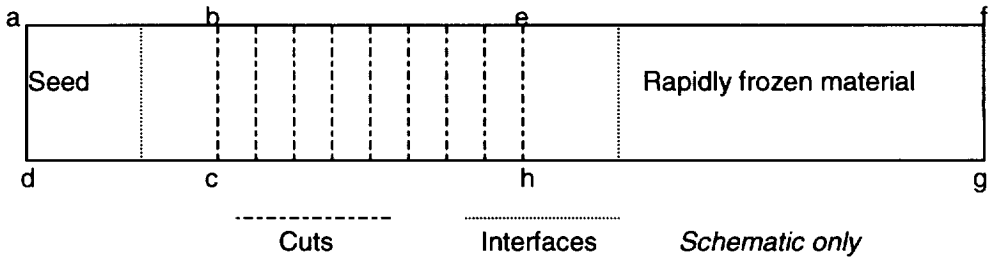

Figure 10.20 Strategy for Cutting Flight Sample, SL1-417.
Sections abcd and efgh will each be half cylinders
Wafers will be cut between bc and eh

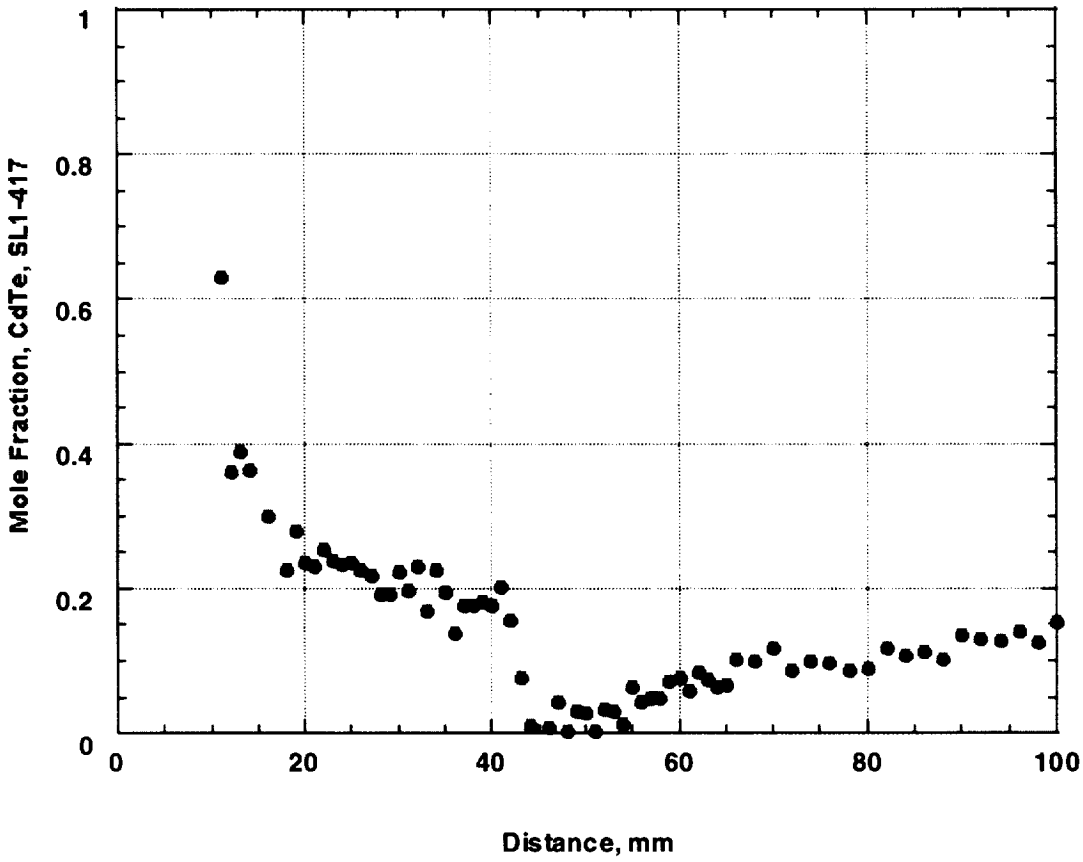

Figure 10.21 Composition of the flight sample as determined following conversion from density readings obtained by CT scanning

GROWTH OF COMPOUND SEMICONDUCTORS IN A LOW GRAVITY ENVIRONMENT: MICROGRAVITY GROWTH OF PbSnTe

A.L. Fripp[a], W.J. Debnam[a], W.R. Rosch[b], N.R. Baker[c], and R. Narayanan[d]

Introduction

The growth of the alloy compound semiconductor lead tin telluride (PbSnTe) was chosen for a microgravity flight experiment in the Advanced Automated Directional Solidification Furnace (AADSF), on the United States Microgravity Payload-3 (USMP-3) in February, 1996 and on USMP-4 in November, 1997.

The objective of these experiments was to determine the effect of the reduction in convection, during the growth process, brought about by the microgravity environment. The properties of devices made from PbSnTe, an alloy of PbTe and SnTe, are dependent on the ratio of the elemental components in the starting crystal. Compositional uniformity in the crystal is only obtained if there is no significant mixing in the liquid during growth. The technological importance of PbSnTe lies in its band gap versus composition diagram which has a zero energy crossing at approximately 40% SnTe. This facilitates the construction of long wavelength (>6 μm) infrared detectors and lasers. The properties and utilization of PbSnTe are the subject of other papers.[1,2]

PbSnTe is also interesting from a purely scientific point of view. It is, potentially, both solutally and thermally unstable due to the temperature and density gradients present during growth. Density gradients, through thermal expansion, are imposed in directional solidification because temperature gradients are required to extract heat. Solutal gradients occur in directional solidification of alloys due to segregation at the interface. Usually the gradients vary with both experiment design and inherent materials properties.

In a simplified one dimensional analysis with the growth axis parallel to the gravity vector, only one of the two instabilities work at a time. During growth, the temperature in the liquid increases ahead of the interface. Therefore the density, due to thermal expansion, is decreasing in that direction. However, the phase diagram shows that the lighter SnTe is preferentially rejected at the interface. This causes the liquid density to increase with distance away from the interface.

---

[a]. NASA, Langley Research Center, Hampton, VA 23681 (retired)

[b]. NRC, Langley Research Center, Present address: Northrop Grumman STC, Pittsburgh, Pa 15235

[c]. Lockheed Martin Engineering and Sciences Co., Hampton, VA 23681

[d]. Department of Chemical Engineering, University of Florida, Gainesville, FL 32611

The Experiments

The PbSnTe growth experiment on USMP-3 consisted of three separate crystals grown in a single segmented ampoule. The crystals were grown in series, one in each of the three primary orientations with respect to the residual gravity vector. The growths on USMP-3 were roughly analogous to hot-on-top, cold-on-top, and horizontal growth.

The work on USMP-4 was to grow two sets of three crystals, again in segmented ampoules. The hot on top orientation was chosen for all growths. The variables, this time, were to be ampoule translation rate, thermal gradient, internal pressure, and nucleation procedure. The growth rate, which is related to the translation rate, is a key growth parameter under control of the experimenter. Higher growth rates produce steeper solutal gradients but less penetration of this vital diffusion zone into the convecting fluid flow. Thus, the growth rate presents a dichotomy of effects; a high growth rate produces a steeper concentration gradient while a low growth rate allows the diffusion tail to extend into the thermal convection cells. A change in thermal gradient has the obvious effect of changing the temperature dilatation contribution to the convective driving force. The internal pressure, at elevated temperatures, was adjusted by the amount of excess tellurium in the compound, and it was thought that it may affect pore formation in the crystals. The nucleation procedure was studied by using both seeded and unseeded growths and tests the influence of the evolution of latent heat on initial growth.

For the combined two flights we designed a set of nine experiments in three different ampoules to measure the effect of the gravitational body force on the convective properties of alloy compound crystal growth as modified by reduced gravity and other crystal growth parameters. As is often the case, especially in new and difficult experimental arenas such as found when using the microgravity laboratory, nature may have her way with even the best laid plans of human endeavor and can wreck total havoc with strategies such as ours.

Results

Ampoule #1 processed without any problems that were telemetered to the ground. Recalescence was observed in cells 1 and 2, and due to failure of the uppermost thermocouples (not a surprising event due the operating limits of the 20 mil diameter sheaths) it was not expected to be observed in cell 3.

The observations, as seen on the ground, for our second ampoule (the third ampoule on the USMP-4 flight) were not so gratifying. On this part of the experiment, anomalies were observed in the sample thermocouples during the initial melting of the samples. When control thermocouples failed on the furnace booster heater, a cell (ampoule) failure and leakage from one of the lead tin telluride samples was suspected. To protect the two experiments already processed, the furnace drive was sent to the store position (full insertion), and growth was started in a gradient freeze manner by selectively powering down the different furnace zones. The experiment was terminated when the main heater control thermocouples failed.

The actual anomalies were only identified during sample retrieval at the Kennedy Space Center in February 1998. Clearly, the anomaly first occurred in ampoule #,1 not our second ampoule as was

suspected. Cell 1, of ampoule #1, was intact and cell 2 was broken with approximately one third the length of the crystal still in the broken ampoule. The Inconel cartridge, or muffle tube, was swollen along its length starting near the cold end of cell 1, which was heated to 1000 C; the swelling increased at the beginning of cell 2, where the temperature had increased to 1150 C; and then the cartridge appeared ripped apart in the vicinity of the ampoule breakage. The remainder of the cartridge and ampoule were deposited in the furnace and caused the observed problems during the space processing of ampoule #2.

The experimental ampoules, that is, what is left of them, were impounded by the Marshall Space Flight Center for action of the Anomaly Resolution Team and were only released to the investigators in November 1998. Therefore the remainder of this paper will only discuss the observations made to date and attempts to duplicate, on Earth, the cartridge swelling that apparently caused the anomaly.

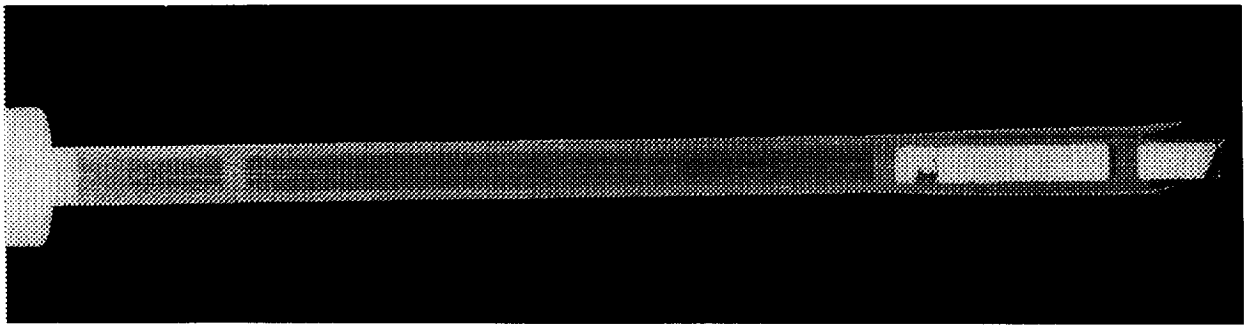

Figure 1. X-ray of sample AF-1 showing intact cell1, broken crystal in cell 2, and the swollen and torn Inconel cartridge.

Figure 1 is an x-ray of the ruptured sample showing the completed cell 1 and the broken sample in cell 2 along with swelling of the cartridge. Figure 2 is a photograph of the broken end on cell 2. The metal cartridge appears forcibly torn and not corroded by PbSnTe vapors, and the remaining crystal in cell 2 appears to be broken and not just decanted from spilled liquid.

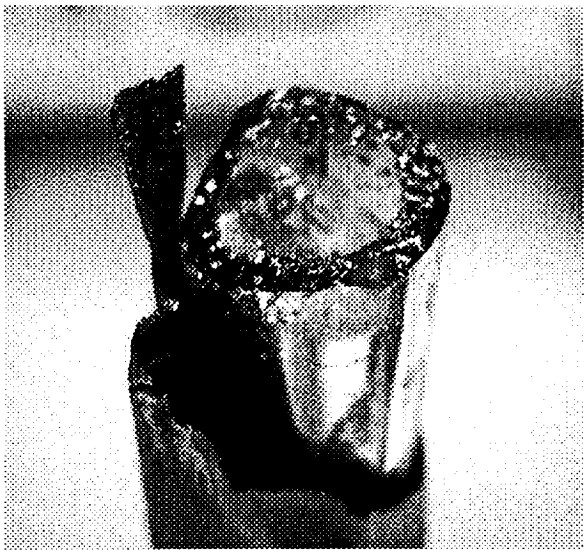

Figure 2. Photograph on the broken crystal and torn cartridge of AF-1.

A set of experiments was conducted at the Langley Research Center to determine if excess pressure within the cartridge (that is, the space between the sealed quartz ampoule and the Inconel cartridge) could have caused the cartridge to swell to a diameter greater than the 0.75 inch diameter of the radiation shield insert in the insulation zone of the furnace. The maximum excess pressure within the cartridge during growth in the AADSF is approximately 10 psi if the cartridges are sealed at 12 psia. In these post- flight tests the argon pressure was actively controlled at pressures up to 100 psig to simulate the possibility that the flight

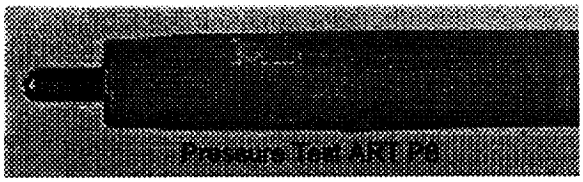

Figure 3. Result of pressure test where cartridge was pressurized to 75 psig.

sample was over pressurized during sample preparation. Table 1 summarizes these tests and figure 3 shows one of the tubes after failure where the maximum bulge reached 0.70 inches only in the area of the failure. Three separate Inconel tubes were taken to failure (that is, an observation of pressure drop in the cartridge), but none produced sufficient swelling to have caught on the radiation shield and caused the tearing of the cartridge as observed on the flight sample.

Another set of tests (see Table 2) looked at the hypothesis that one of the cells developed a crack and the leaking PbSnTe vapor weakened the Inconel to allow the concomitant swelling. (Note: had the quartz containing the PbSnTe broken and liquid come in contact with the Inconel then the metal would have lost its integrity within seconds relieving any pressure differential.)

As a cracked ampoule is difficult to simulate, we used an open ended ampoule that was maintained vertical to prevent any contact of the liquid PbSnTe with the Inconel. Figure 4 shows the open

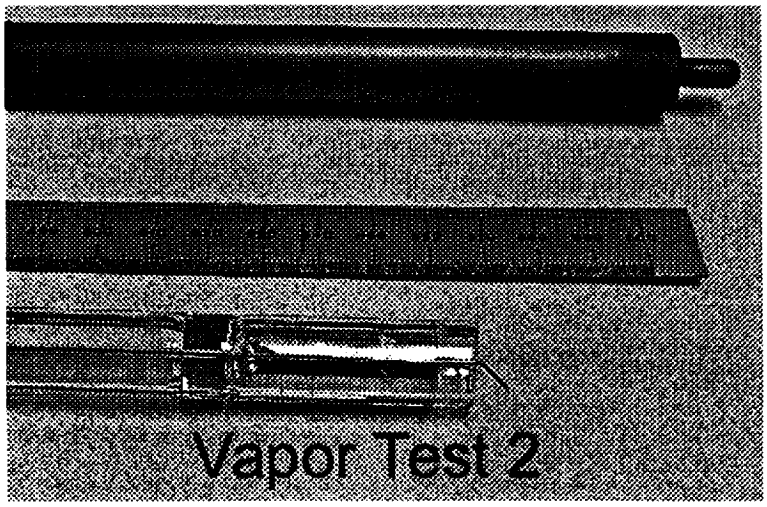

Figure 4. Setup for a PbSnTe vapor test on the integrity of the Inconel cartridge. The PbSnTe resides in the open ended quartz ampoule.

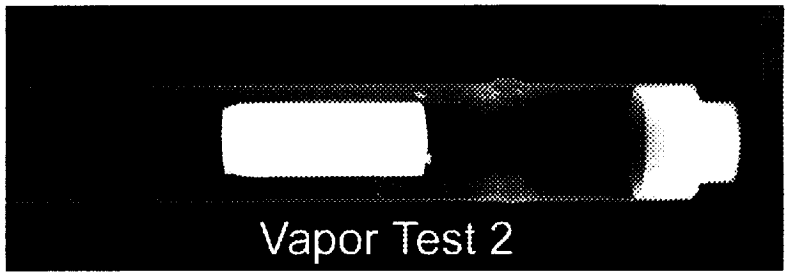

Figure 5. X-ray of loaded test cartridge after failure. Note that the only appreciable swelling (~0.66 inch) is immediately ahead of the open end of the ampoule.

ended ampoule with the PbSnTe and the Inconel muffle tube which will surround it and contain the vapor. Figure 5 is an x-ray of the sample after the failure as demonstrated by a pressure drop. Note that the only appreciable swelling occurred at the end of the open ampoule but even that was insufficient to bind on the AADSF insert.

The ampoules now reside at the Langley Research Center. Analysis of both the space grown crystals and the ruptured cartridge is still in a preliminary status, and a completed report will be released in the near future.

REFERENCES:

1. T.C. Harman; "Control and Imperfections in Crystals of PbSnTe, PbSnSe and PbSSe"; J.Nonmetals 1 (1973) 183.

2. S.G. Parker and R.W. Johnson; "Preparation and Properties of PbSnTe"; in Preparation and Properties of Solid State Materials vol 6, Ed. W.R. Wilcox, Marcel Dekker, Inc., New York 1981, p 1.

Table 1: Effect of Pressure, Temperature, and Time on Muffle Tube Expansion

This series of experiments examine the combined effect of temperature, pressure and duration on the expansion of the Inconel muffle tubes. All tubes used were from the same batch as the flight (AF1-105) tube, and the tests were conducted in the Bridgman furnace at Langley. ART-P1 through P6 involved heating the muffle tubes during the day, cooling overnight, and measuring the tube diameter, before proceeding to the next heat/cool/measure cycle. ART-P9 is a variation of the P7 and P8 tests, but without cooling and measuring the tube diameter after the 24 hours at 1000 C and 75 psig.

Number	Date	psig	Temp °C	Time hr	Post Test Tube Dia	Increase inches	Notes
ART-P1	3/18/98	15	1000	7:00	0.624	0.0	Muffle Tube # N25
ART-P2	3/19/98	15	1150	6:30	0.627	0.003	Followed ART-P1, same tube (N25)
ART-P3	3/20/98	25	1150	6:20	0.629	0.002	Followed ART-P2, same tube (N25)
ART-P4	3/23/98	45	1150	6:46	0.638	0.009	Followed ART-P3, same tube (N25)
ART-P5	3/24/98	75	1150	6:53	0.665	0.027	Followed ART-P4, same tube (N25)
ART-P6	3/25/98	100	1150	0:44	0.687	0.022	Leak developed in N25, test terminated.
ART-P7	4/02/98	75	1000	24:00	0.645	0.021	Muffle Tube # N27
ART-P8	4/06/98	75	1150	0:36	0.685 0.70 at split	0.040	Leak developed in N27, test terminated Tube split 2" from tip.
ART-P9	4/09/98	75	1000	24:00	NA	NA	Muffle Tube # N28 Straight to 1150C
ART-P9#2	4/09/98	75	1150	0:47	0.674	0.050	Leak developed in N28, test terminated

Table 2: The Effect of Lead-Tin-Telluride Contamination On Muffle Tube Expansion

Because the experiments employing pressure only did not achieve muffle tube expansions of the same order as the AF1 flight sample, the below series of tests examined the effect of lead-tin-telluride (LTT) contamination on the Inconel muffle tubes. All tubes used were from the same batch as the flight (AF1-105) tube, and the tests were conducted in the Bridgman furnace at Langley. The goal of all tests was to duplicate the flight conditions for Cell 1 of AF1-105: 24 hours at 1000 C, and ~10 psig pressure of argon (the expected maximum internal pressure during its processing in the AADSF).

Tests LTT VAP-1 through -4 examined the effect of exposure of the interior of the muffle tube by LTT vapor from solid material: The difference between the tests was in how the vapor should have distributed within the tube. The LTT VAP-5 through -7 tests employed fine LTT powder adhering to or in direct contact with the muffle tube interior wall, prior to heating the tube.

The muffle tubes ruptured in the first four tests; Their maximum expansions, while significant, were very localized and generally in the area where the LTT vapor first came in contact with the Inconel tube. Test results for the 5th and 6th tests showed that the LTT dusting had no measurable effect, and the LTT VAP-7 results are very similar to those of the ART-P7 pressure test, which was conducted at the same temperature and pressure but without any LTT present. Thus, it appears that although the combination of flight-like internal pressures and the presence of LTT vapor can cause local expansion of the tube wall, none of these results can be used to explain the near-uniform expansion of the AF1-105 muffle tube from the base of Cell 1 onward.

Test Number	Test Description	Duration (time at pressure)	Max. Diameter, inches	Region of measurable expansion (> .005")	Description of maximum expansion region
LTT VAP-1	Melt-in-Place	11 hrs	0.640	60 mm	Localized bump
LTT VAP-2	Directionally Melt	16 hrs	0.669	60 mm	Ring-like bulge, 3 mm wide
LTT VAP-3	Hot-on-Bottom Furnace	10 hrs	0.649	60 mm	Ring-like bulge, 4 mm wide
LTT VAP-4	Horizontal Furnace	<9 hrs	0.714	<5 mm	Localized bumps & corrosion
LTT VAP-5	LTT Dusting of Tube ID only, 37 mg	24 hrs	0.625	None	No expansion detected
LTT VAP-6	LTT Dust (< 40 mesh), 1.4 gms	24 hrs	0.625	None	No expansion detected
LTT VAP-7	Resumption of above test at 75 psig	24 hrs	0.641	230 mm	OD > 0.635" over 100 mm

IN SITU MONITORING OF CRYSTAL GROWTH USING MEPHISTO
Mission STS 87- Program USMP-4
Experimental Analysis

Reza Abbaschian, F. Chen, and J. R. Mileham
Materials Science and Engineering
University of Florida, Gainesville, FL 32611

H. de Groh III
NASA/Lewis Research Center
Cleveland, OH 44135

V. Timchenko, E. Leonardi, and G.de Vahl Davis
University of New South Wales, Sydney, Australia 2052

S. Coriell
NIST, Gaithersburg, MD 20899

G. Cambon
Centre National d'Etudes Spatiales
Toulouse, France 31055

SECTION I. Overview

This report summarizes the results of the In situ Monitoring of Crystal Growth Using MEPHISTO (Material por l'Etude des Phenomenes Intéressant de la Solidification sur Terre et en Orbite) experiment on USMP-4. The report includes microstructural and compositional data obtained during the first year of the post flight analysis, as well as numerical simulation of the flight experiment. Additional analyses are being continued and will be reported in the near future.

The experiments utilized MEPHISTO hardware to study the solidification and melting behavior of bismuth alloyed with 1 at% tin. The experiments involved repeated melting and solidification of three samples, each approximately 90 cm long and 6mm in diameter. Half of each sample also included a 2 mm diameter growth capillary, to assist in the formation of single grain inside. One sample provided the Seebeck voltage generated during melting and freezing processes. Another one provided temperature data and Peltier pulsed demarcation of the interface shape for post flight analysis. The third sample provided resistance and velocity measurements, as well as additional thermal data. The third sample was also quenched at the end of the mission to preserve the interface composition for post flight determination. A total of more than 45cm of directionally solidified alloy were directionally solidified at the end of the flight for post mission structural and compositional characterization.. Metallurgical analysis of the samples has shown that the interfacial kinetics play a key role in controlling the morphological stability of faceted alloys. Substantial differences were observed in the Seebeck signal

between the ground-based experiments and the space-based experiments. The temperature gradient in the liquid for the ground-based experiments was also significantly lower than the temperature gradient in the liquid for the space-based experiments. Both of these observations indicate significant influence of liquid convection for the ground-based experiments.

SECTION II. Background

The formation of dendrites generally follows morphological instability of a planar solid/liquid interface [1]. The morphological stability criterion of Mullins and Sekerka [2] can be utilized to predict the onset of instability in planar interfaces. The criterion determines the conditions for the growth or decay of a perturbation on a planar interface under a given steady state condition. More recent theoretical models indicate that anisotropic interfacial properties play a role in the morphological stability of planar interfaces, as well as the evolution of cellular and dendritic structures; this has been predicted theoretically by Coriell and Sekerka [3] and Coriell *et al.* [4] by extending the linear stability analysis of Mullins and Sekerka [2], and by Young *et al.* [5] in the weakly nonlinear regime. These treatments indicate that such anisotropies tend to stabilize the growth of a planar interface. Experimental observations reported by Tiller and Rutter [6] for lead-tin alloys and by Trivedi [7] and Trivedi *et al.* [8] for transparent organic systems have been found to be generally consistent with the theoretical predictions.

The influence of anisotropic interfacial kinetics on the morphological stability threshold was recently demonstrated by the present investigators for solidification of Bismuth alloyed with 0.1% Sn [9,10]. The experiments were conducted under microgravity conditions during STS-62 flight of the space shuttle Columbia, using the MEPHISTO directional solidification facility. Similar to the USMP-4 experiments, the experiments yielded 15 cm of three parallel-processed samples, each grown directionally at six velocities ranging from 1.85 to 40 μm/s. The microstructural evaluation of the space grown samples indicated that for 1.85, 3.4 and 6.7 μm/s interface velocities, the growth occurred in a planar mode. The microstrutural evolution at a higher velocity of 13.3 μm/s appeared to be cellular in one grain, and planar in another, whereas for 26.9 and 40 μm/s velocities, cellular/dendritic porphologies were observed in both grains. The most interesting aspect of the planar-cellular transition at 26.9μm/s velocity was the existence of distinct preferential breakdown in one grain versus the other. The upper grain became cellular approximately 0.6 mm after the initiation of growth, forming cells which were tilted about 6.5° with respect to the heat flow and growth directions. The neighboring grain on the other hand, continued with planar growth about 12.2 mm until it became cellular, with cells parallel to the growth direction. The cell spacing within the two grains were approximately the same; 265 and 276 μm, respectively.

The USMP-4 flight experiments were intended to build on the findings of USMP-2 flight. In particular to provide additional data on the dominant role of interfacial kinetics on the morphological instability of facet forming materials. Since the interfacial kinetics and morphological instabilities also depends on the solute concentration, obtaining additional data at a higher solute concentration was also another aim of the experiment. As such, the Sn concentration for the USMP-4 flight was selected as 1 at% Sn instead of the 0.1 at% used for the USMP-2 flight.

SECTION III. USMP-4 Mission Description

Experimental Facility and Techniques

The MEPHISTO hardware is shown schematically in Figure 1 [9,11]. The apparatus is capable of simultaneous processing of three rod shaped samples, each of which is approximately 900 mm in length and 6mm in diameter. The central part of MEPHISTO consists of two furnaces each with a neighboring heat sink, which is cooled by a refrigerant. One of the furnace-heat sink structures is stationary, while the other is on a moving platform. Between these heaters special reflectors and insulation are used to maintain a nearly uniform temperature. In the experiments to be described the furnaces were heated to 750° C, while the cold zones were kept near 50° C, resulting in a molten zone in the middle of each as illustrated in Figure 1. When the movable furnace-heat sink structure is translated away from the fixed furnace, the extent of the hot zone is lengthened, increasing the extent of the molten zone in the sample. Near the solid-liquid interfaces, which are located between each furnace and its accompanying heat sink, a temperature gradient on the order of 200° C/cm is established. The furnace heaters are in contact with cylindrical thermal diffusers made of graphite and are regulated using thermocouples within the diffusers. The graphite diffusers have three holes to accommodate the samples. The uniform temperature field produces a very similar thermal profile for the three samples. In order for the heat sinks to efficiently remove the heat from the samples, a metal seal of a low melting point (45° C) alloy was utilized. When the heat sink reached its operating temperature, the liquid alloy made a direct contact between the heat sink and the outer quartz wall of the samples.

The alloy used for the experiments was Bi with 1 atomic %Sn. As shown in Figure 2, Bi and Sn form a simple eutectic diagram, with a maximum solubility of 1.63 atomic %Sn at the eutectic temperature of 140° C. The distribution coefficient for Sn in Bi is measured to be around 0.03. Schematics of the three samples inserted into the MEPHISTO apparatus and their dimensions are shown in Figure 3. Each of the three samples, which will be referred to as the "Quenching", "Peltier", and "Seebeck", has a special purpose in the study of alloy solidification. A 2mm ID, 3 mm OD quartz capillary is located on the moving furnace side, which extends about 250 mm into the sample. Thin capillaries (approximately 0.6 mm OD) for the thermocouples were also inserted for the thermocouples in the Peltier and Quenching samples. The 3mm OD were filled with the alloy during sample preparation. The samples used in the ground-based processing were similar except the capillaries were about 40 mm shorter.

The Quenching sample is used to measure the rate of solidification using the resistance change across the sample during processing and to produce a short section of quenched interface at the end of the experiments. To achieve the latter, the sample is attached to a mechanism which quickly pulls the sample about 2 cm towards the cold zone and freezes the sample. The Quenching sample was electrically connected for the resistance measurements. The contact for the Quenching sample on the capillary side is with the alloy outside the capillary, insulated from the alloy in the center by quartz. The change in the resistance of the sample was used to calculate the solidification rate as will be explained later in the report.

The Peltier sample has connections to allow marking the sample with short electrical pulses which cause heating or cooling at the solid-liquid interface according to the equation:

$$Q_p = -(\pi_s - \pi_L)J\Delta t$$

Q_p is the heat generated at the solid-liquid interface, π_S and π_L are the Peltier coefficients of the solid and liquid alloy, respectively, J is the current (positive for flow from solid to liquid), and Δt is the pulse duration. As shown in Figure 3, a small slit was put in the capillary to allow current pulses to pass through the entire sample during Peltier pulsing. If the current direction results in cooling at the interface, the rate of solidification will momentarily increase and there will be a build up of solute at the interface.

The Seebeck sample is used to measure the difference between the temperature of the stationary and moving solid-liquid interfaces. The relationship between the measured Seebeck signal and the temperature of the moving interface, TC, and the temperature of the stationary interface, TD, will be discussed together with the experimental results. Details of Seebeck interface temperature measurement can be found elsewhere [12].

Experiments and Growth Conditions

The flight experiments were performed with the help of Société Européene de Propulsion (SEP) by telecommanding. The experiments were initiated by heating the movable and stationary furnaces to 750°C. This established a liquid zone approximately 340 mm long as depicted in Figure 1. Melting and solidification experiments were performed by commanding the apparatus to move the mobile furnace/heat sink structure. The fully open position was referenced as 1mm and the fully closed 150mm. Increasing the furnace position corresponded to freezing and decreasing the furnace position to melting. Figure 4 is a plot of the MEPHISTO movable furnace position during the USMP-4 mission. More detailed timeline can be found in Table 1. Many of the experiments consisted of a freezing period where the furnace was moved forward, a hold period where the furnace was kept stationary, and a melt period where the furnace was moved back to the original position for the cycle with the opposite velocity of the freezing period. Figure 5 is an example with a start position of 115 mm, freezing for 15 mm at 13.5 μm/s, and a hold period of 30 minutes, and then melting back to the 115 mm position at 13.5 μm/s. The detailed analysis of the Seebeck, resistance and thermocouple measurements benefited from the large number of experiments performed aboard USMP-4. As shown in Figure 4, the experiments included thirty-five freeze-hold-melt cycles during the mission and eleven periods of final directional solidification. The experiments were performed over a range of solidification rates from 0.74 to 40 μm/s.

The MEPHISTO apparatus monitored many of the conditions of alloy growth using the furnace position, thermocouples, change of sample resistance, Peltier interface demarcation, and Seebeck measurements. In the following section, the use of these measurements/techniques to determine the temperature gradients (in the solid and liquid), growth velocity, and interface undercoolings will be explained and applied to both the ground- and space-based experiments.

Flight Summary

The entire flight experiments were commanded and controlled via telemetry from the NASA-Marshall Payload Operational Control Center. The performance of the hardware and samples, and the

quality of telemetric data received were superb throughout the entire mission. We gathered approximately 0.5 Gb of data for 35 Seebeck solidification and melting cycles. The experiment covered a range of velocities as low as 2.67 millimeters per hour (mm/hr) to as high as 144 mm/hr (0.1-55 inches per hour). Thirteen of these Seebeck cycles were as planned in the original timeline. The productivity and quality of the science and engineering teams and hardware performance provided the opportunity for the additional 22 cycles. It should be noted that the lowest design velocity specification for MEPHISTO performance by a factor of more than two beyond its specifications clearly indicates the outstanding design and workmanship of the hardware. In addition, 150 mm of each sample was directionally solidified at the end of the mission, with different velocities from 6.6 through 144 mm/hr. The last has provided 450mm of directionally grown samples under microgravity environment. Peltier pulses were successfully performed in five regions of the Peltier sample, as planned in the timeline. The resistance sample was quenched at the end of the mission.

SECTION IV. Microstructural and Data Analysis

Microstructural Analysis

Overview of Microstructural Evolution- Figure 6 shows a general view of the flight samples processed. An overview of the microstructural evolution of the samples grown in space was obtained from the low magnification composite of a microsection of all three samples. Figure 7 shows the location and orientation of the microsection with respect to the furnace graphite diffuser center. Note that the microsection orientations of all the samples were cut so that they are thermally equivalent. The growth conditions during final solidification steps and velocity values are summarized in Table 2. The micrographs in Figures 8(a)-(b) show the successive development of the microstructure as a function of the distance and the growth velocity for the Seebeck sample. Figure 9 shows schematically a summary of processing lengths and velocities as well as the microstructure in each section. Also shown is the successive development of the microstructure as a function the growth velocity. As detailed later, for solidification at velocities below V2 the growth occurs in a planer mode, while cellular morphology is seen at V3 through V6 velocities. The planar to cellular transition reveal many important aspects of the solidification of faceted materials in microgravity as discussed in more detail in the following section.

The initial (Earth grown) microstructure of the samples is shown in Figure 10. The samples were produced from a homogeneous liquid through quenching. The optical micrograph in Figure 10 shows relatively uniform microstructure with a faceted cellular/dendritic morphology.

Plane Front Solidification- The development of a plane-front microstructure is illustrated in Figures 11(a)-(c) which show the transition from a facet cellular/dendritic structure of the Earth-grown portion of the samples to a plane-front morphology at the moving furnace interface. At all three interfaces, the initial cellular to plane-front transition interface was sharply delineated. The optical micrographs show that only a few dominant orientations emerge from the initial microstructure, which was found to be a common feature of all three samples. The microstructure is characterized by a complete absence of the Sn-rich second phase indicating plane-front solidification. It was found that the interface was associated with a sharp compositional change, detected via electron microprobe analysis as presented later.

S/L Interface Shape- When an interface was revealed, for example during the interface breakdown, it was found that the interface was nearly flat, with a slight curvature near the s/l/crucible triple junction.

Upon closer examination, the boundary across each grain appears to be fairly flat, with the small angles between them giving the appearance of an overall slight curvature of the interface, as shown by the micrograph of the interface where the sample was quenched in Figure 12.

Transition to a Cellular Growth Mode- Microstructural examination of the microgravity-processed sections indicated that those regions of samples grown at V3 through V6 velocities exhibited a morphological transition to a cellular growth mode. The microstructural appearance of the cellular breakdown of event 15, V5 (Peltier sample) is shown in Figure 13. A much narrower planar to cellular transition zone was seen at a higher growth velocity (V5, V6) than that at lower growth velocity V3.

Kinetics Data Analysis

Temperature Profile- The thermal profile in the MEPHISTO apparatus were monitored using nine thermocouples located in each of the furnace diffusers and heat sinks. Four thermocouples were also placed inside the small quartz capillaries within the Quenching and Peltier samples. The thermocouples in the heater and heat sink diffusers were used to control the overall thermal conditions of the furnace. The thermal profile of the samples, however, is not fully determined by the temperatures imposed by the diffusers, but also by the properties of the sample to be processed. Therefore, the temperature field in the samples was monitored using the four experimental thermocouples located within the samples. A typical thermal measurement by three of the thermal couples is shown in Figure 14. Also shown in the figure is the corresponding furnace position and the melting temperature. The temperature gradients in the solid and liquid near the interface were measured as 260 and 204 K/cm for growth within the 6mm quartz tube.

Figure 15 gives the temperature profile for ground- and space-based experiments within the Peltier sample using thermocouple T4 in the ground-based experiment, and T4 and T6 in the space-based experiments. (The positions of these thermocouples are marked in Figure 3.) Note the temperature gradient for the space-based experiments within and outside the capillary for the space-based experiments are both about 260° C/cm. The thermal profile in the solid (below about 270° C) for the ground-based experiments is very similar to the space-based measurements. However, the average temperature gradient in the liquid for the ground-based mission is only about 100 °C/cm.

Growth Rate Measurement- In the MEPHISTO apparatus there are two complementary techniques for ascertaining the solidification rate during an experiment. The simplest method is to use the translation rate of the MEPHISTO Moving Furnace. Since the temperature gradient in the MEPHISTO apparatus is fairly steep, it is anticipated that the moving interface would follow the movement of the moving furnace very closely. However, the interface movement may not exactly correlate with the furnace translation because of the thermal lag between the temperature imposed on the exterior of the ampoule and the temperature within the sample. The decrease in the melting temperature of the solid-liquid interface because of the build up of solute at the moving interface would also cause the interface to lag the furnace. In addition to this chemical undercooling, there is also a kinetic undercooling associated with a finite growth rate for faceted interfaces.

A more accurate determination of the interface migration was made from the change in resistance of the Quenching sample. The resistance change as a function of the processing time during a typical cycle is shown in Figure 16, together with the furnace position. While the two data sets correlate

nicely, more detailed analysis show that there is a slight lag in the resistance change at the beginning of solidification. The resistance of the sample is the sum of the contributions from the solid and the liquid. When a section of liquid is replaced by solid the change in resistance is:

$$\Delta R = \frac{\Delta L_1 \rho_1}{A_1} + \frac{\Delta L_2 \rho_2}{A_2}$$

where ΔR is the change in resistance, ΔL is the change in length, ρ is the resistivity, and A is the cross-sectional area. The subscripts 1 and 2 refer to the solid and the liquid respectively. Figure 17 is a plot of the Quenching sample resistance as a function of the movable furnace position. Two different lines are used to fit the data. The line to the left is for resistance measurements within the capillary, while the line to the right is to fit data outside the capillary. The steeper slope within the growth capillary is due to the smaller cross-sectional area for *A1* and *A2*.

Interfacial Undercooling- A non-intrusive technique for studying interfacial undercooling is to measure the Seebeck signal generated by a solid-liquid-solid structure [13,14,15]. The technique enables a quantitative investigation of interfacial undercooling including compositional and kinetic terms. For the current loop pictured in Figure 1, the Seebeck Voltage will be given by:

$$E_s = \int_A^F \eta(\phi(w), c(w), \theta(\vec{w}), T(w)) \nabla T \bullet d\vec{w}$$

where w is the path, η is the Seebeck coefficient, and ∇T is the temperature gradient. Here we have assumed the Seebeck coefficient depends only on the phase of material, ϕ, the composition, c, and the crystallographic orientation, θ. For the equation to be valid, a necessary condition is that the integral does not depend on the path taken within the material. This could be violated, for example, if there are alternate paths through materials with different Seebeck coefficients. For the present setup, $T_A = T_F$ (where T refers to temperature, and the subscript the position), $T_B = T_E$, and the wires from A to B and F to E are the same material. (The MEPHISTO apparatus can monitor and control the end temperatures of the sample to within 0.01°C.) If it is assumed that the Seebeck coefficients for the solid and liquid do not vary with concentration, temperature or structure, the resulting signal for the simplified conditions will be:

$$E_s = \eta_s(T_c - T_B) + \eta_L(T_E - T_D) + \eta_s(T_E - T_D)$$

where η_S is the Seebeck coefficient for the solid, and η_L is the Seebeck coefficient for the liquid. Since $T_B = T_E$, this simplifies to $E_S = -(\eta_S - \eta_L)(T_D - T_C)$. If the Seebeck coefficient of the liquid and solid are known, then one can determine the difference in temperatures of the two solid-liquid interfaces. The temperature at the stationary interface, T_D, is given by the phase diagram in Figure 2. The equation simplifies to:

$$T_c = T_D + \frac{E_s}{\eta_s - \eta_L} = T_D + \frac{E_s}{\eta_{S/L}}$$

where $\eta_{S/L}$ is the difference in the Seebeck coefficient of the solid and liquid near the melting temperature.

Figure 5 gives the Seebeck signals acquired for a ground- and a space-based experiment. Each consisted of solidification, hold, and melt period as previously described. The Seebeck signal for the ground-based experiment rose during freezing, fluctuated around an average value for the hold, then decreased during melting. The fluctuations in the signal are due to hydrodynamic mixing in the liquid. It was observed that the magnitude of the fluctuations strongly depended on the maximum temperature of the melt. The signal for the space-based experiment had an initial increase, then decreased during freezing. After the furnace stopped, the signal increased due to the interface temperature increase caused by the exponential decay of solute at the interface. During melting the signal decreased, then increased back to near its initial value before the freeze-hold-melt cycle was began. The differing behavior of the ground- and space-based Seebeck results may be due to the differences in the amount of solute build-up at the interfaces as well as structural changes in the solid. As such, the results can not be explained by the above mentioned simplified equation that is based on the assumption that structure and composition do not affect the Seebeck coefficient of the solid or the liquid. More accurate analysis of the Seebeck data await the microstructural determination of the samples. Analysis of the flight samples should help discern the origin of the Seebeck signal. This will include composition and microstructure of the solidified space-processed samples.

As indicated earlier, the temperature gradient in the liquid, G_L, for the ground-based mission was significantly smaller than G_L for the space-based experiments. This is evidence of hydrodynamic mixing on the ground-based experiments, as well as the differences in the heat transfer coefficient between the metals, the quartz tube, and the surrounding graphite diffuser. The existence of hydrodynamic mixing during the ground-based experiments with a maximum liquid temperature of about 750°C is further supported by fluctuations in the Seebeck signal while the mobile furnace/ heat sink structure was at rest. Figure 18 shows the moving and fixed furnace diffuser temperatures and Seebeck signal during part of the heat-up of the MEPHISTO furnaces. When the fixed furnace diffuser temperature was held at 400°C, fluctuations in the Seebeck signal are not noticeable. However, as the temperature of the fixed furnace diffuser rose above 550°C, strong fluctuations in the Seebeck signal become apparent, presumably from the onset of strong hydrodynamic mixing in the liquid. Fluctuations in the Seebeck signal were not observed for the space-based experiments.

Section V. Numerical Modeling

Introduction

In this section a review is presented of the modeling work of the flight experiment performed by the Computational Fluid Dynamics Research Group at the University of New South Wales, Sydney, Australia. The results of the calculations are being compared with those of the experiments for the propose of better interpretation of the data, as well as the determination of the property values for bismuth.

A mathematical model of heat, momentum and solute transfer during directional solidification of binary alloys in a Bridgman furnace has been developed. A fixed grid single domain approach (enthalpy method) is used. The effects of coupling with the phase diagram (a concentration-dependent melting temperature) and of thermal and solutal convection on segregation of solute, shape and position of the

solid/liquid interface are investigated.

Two numerical approaches are being employed. In the first, the primitive variable equations are solved by a finite volume discretization, using a commercial flow code CFX 4.1. In the second, a finite difference/finite volume discretization of the vorticity-stream function formulation of the equations is solved by an in-house code SOLCON.

Validation of the codes has been obtained by a comparison of CFX calculations with an experiment in earth gravity using the material succinonitrile, and by comparison of SOLCON with CFX.

A computational study of the transient directional solidification for Bi-1at% Sn with different pulling velocities corresponding to events of the MEPHISTO-4 experiment was undertaken. Results were compared with analytical solutions and at present comparisons with experimental results are being performed.

Mathematical formulation

We consider a Bridgman furnace in which a moving temperature profile, consisting of a cold zone (T_c), a nominally adiabatic zone (which is simulated by a linear temperature profile) and a hot zone (T_h) is imposed on the boundary of the ampoule. This boundary temperature profile is translated with a constant pulling velocity as a result of the furnace movement, causing the s/l interface to move along the ampoule. The material in the ampoule is thus divided into two sub-regions: solid and liquid.

Although the ampoule is three-dimensional, a two-dimensional model is used. This simplification is valid because, under the microgravity conditions being considered, convection is weak and the solidification process remains largely (but not solely) diffusion-controlled. A Newtonian fluid and laminar flow are assumed in the liquid phase, and the Boussinesq approximation has been used, in which the liquid density is assumed to be constant except in the buoyancy term of the equation of motion.

The governing time dependant equations describing heat, mass and momentum transport can be written

$$\nabla.\tilde{V} = 0 \tag{1}$$

$$\rho\left(\frac{\partial \tilde{V}}{\partial t} + \tilde{V}.\nabla\tilde{V}\right) = -\nabla P + \nabla.\left\{\mu\left[\nabla\tilde{V} + (\nabla\tilde{V})^T\right]\right\} + \rho\tilde{g} \tag{2}$$

$$\rho\left(\frac{\partial h}{\partial t} + \nabla.\left(\tilde{V}h\right)\right) = \lambda\nabla^2 T \tag{3}$$

$$\frac{\partial C}{\partial t} + \nabla.\left(\tilde{V}C\right) = D\nabla^2 C \tag{4}$$

where ρ, μ, λ, D and $\tilde{g}$ are respectively the density, viscosity and thermal conductivity of the alloy, the diffusivity of the solute and the gravitational acceleration vector; P, h, T, $\tilde{V}$ and C are respectively the pressure, enthalpy, temperature, velocity vector and solute concentration. The density in the buoyancy term of equation (2) is assumed to be a linear function of temperature and solute concentration:

$$\rho = \rho_r\left[1 - \beta_T(T - T_r) + \beta_C(C - C_r)\right] \tag{5}$$

where β_C and β_T are the thermal and solutal expansion coefficients, defined by

$$\beta_T = -\frac{1}{\rho_r}\frac{\partial \rho}{\partial T} \text{ and } \beta_C = \frac{1}{\rho_r}\frac{\partial \rho}{\partial C} \tag{6}$$

and assumed to be constant, and ρ_r, T_r and C_r are the reference density, temperature and concentration.

Latent heat evolution during phase change is incorporated in the energy equation through the use of an appropriate source term. For each phase ϕ, and for a constant specific heat, the enthalpy h is given by

$$h = C_{p\phi}\, T + f_\ell L = h_{sens} + f_\ell L \tag{7}$$

where L is the latent heat of fusion, $C_{p\phi}$ is the specific heat, h_{sens} is the sensible heat and f_ℓ is the local liquid volume fraction. For isothermal phase change, the liquid fraction is determined by the melting temperature T_m:

$$\begin{aligned} &\text{for } T > T_m \quad f_\ell = 1 \\ &\text{for } T < T_m \quad f_\ell = 0 \end{aligned} \tag{8}$$

Substituting (7) into the energy equation (3), we obtain

$$\rho\left(\frac{\partial h_{sens}}{\partial t} + \nabla.\left(\vec{V}\, h_{sens}\right)\right) = \lambda \nabla^2 T + S_h \tag{9}$$

where

$$S_h = -\frac{\partial}{\partial t}(\rho\, f_\ell L) \tag{10}$$

The source term (10) is used to account for latent heat release during phase change.

Solute transport with phase change The most difficult problem in modeling solute transport during solidification is associated with the discontinuity of solute concentration at the interface. Additional difficulties occur due to the presence of a thin solute boundary layer in the liquid in which large solute gradients, induced by the low partition coefficient, develop. Unlike front-tracking techniques with deforming grids in which the interface position is calculated explicitly and interface boundary conditions may be applied at the grid points, the enthalpy method avoids direct tracking of the interface. The position of the interface is not known *a priori* and has to be recovered from the temperature field. It can and generally does lie between, rather than at mesh points, and hence solutal and thermal boundary conditions cannot be applied directly at the interface. To satisfy mass balance and handle solute redistribution at the moving solidification front, a source term is introduced into (4).

The following assumptions are made:

- thermodynamic equilibrium exists at the solid-liquid interface: $T_m = T_s = T_\ell$ and $C_s = kC_\ell$, where k is the partition coefficient, and the subscripts ℓ and s refer to the liquid and solid phases;
- solute diffusion in the solid phase is negligible;
- the solid phase is stationary and a distinct separation of the phases exists at the interface;
- the densities of the liquid and solid phases are constant and equal.

A source term accounting for the release of solute into the liquid during solidification can be derived by considering an average solute concentration in an arbitrary control volume which is undergoing phase change (Voller *et al.* [16]). This control volume can be treated as partially solidified with an average concentration

$$C = f_s C_s + f_\ell C_\ell \tag{11}$$

where $f_s = 1 - f_\ell$ is the local solid volume fraction. Since diffusion in the solid is neglected, the concentration in the solid at any point is constant with time, although it changes with position as new solid is formed at the solid-liquid interface. Noting that $C_s = kC_\ell$, we can thus write

$$\frac{\partial C}{\partial t} = -\frac{\partial f_s}{\partial t}(1-k)C_\ell + (1-f_s)\frac{\partial C_\ell}{\partial t} \tag{12}$$

When (12) is used in the solute transport equation (4), we obtain the solute conservation equation in the form

$$\frac{\partial C_\ell}{\partial t} + \nabla.\left(\tilde{V} C_\ell\right) = D\,\nabla^2 C_\ell + S_c \tag{13}$$

in which

$$S_c = \frac{\partial f_s}{\partial t}(1-k)C_\ell + f_s\frac{\partial C_\ell}{\partial t} \tag{14}$$

Calculation of liquid fraction As the s/l interface moves from one control volume to the next, the average liquid fraction in a control volume undergoes a step change. This abrupt change in the liquid fraction, defined by the step function (8), can cause serious numerical instabilities. To overcome this problem, (8) is replaced by a linear approximation

$$\begin{aligned} &\text{for } T_{i,j} > T_m + \Delta T && f_\ell = 1 \\ &\text{for } T_m - \Delta T \le T_{i,j} \le T_m + \Delta T && f_\ell = (T_{i,j} - T_m + \Delta T)/2\Delta T \\ &\text{for } T_{i,j} < T_m - \Delta T && f_\ell = 0 \end{aligned} \tag{15}$$

in which 2ΔT is a temperature interval over which phase change is supposed to occur, chosen so that the time taken for the control volume to change temperature by 2ΔT due to the boundary temperature profile translation is approximately the same as the time necessary for the liquid in it to change phase completely.

If the cell boundary temperatures in the direction of crystal growth are T_1 and T_2 respectively, and the melting point is T_m, the liquid fraction f_ℓ is given by

$$f_\ell = \frac{T_2 - T_m}{T_2 - T_1} \tag{16}$$

During solidification, the melting temperature varies due to changes in solute concentration. With the assumption that phase change takes place under local thermodynamic equilibrium, the temperature at the interface, *i.e.*, the melting temperature $T_m(C)$, can be expressed

$$T_m(C) = T_{m0} - mC_l \tag{17}$$

where T_{m0} is the melting temperature of pure solvent (bismuth, in the case of MEPHISTO-4), m is slope of the liquidus, assumed to be constant and obtained from the phase diagram and C_I is the interface concentration in the liquid. It is worth noting that due to the radial segregation which develops, T_m is not uniform over the interface.

During melting, we have assumed that the interface solute concentration on the liquid side is equal to that on the solid side (Abbaschian [17]). The equilibrium condition $C_s = kC_\ell$ is supposed to be satisfied by the creation of a thin layer of molecular scale in the solid which we have not attempted to model.

The computed solute concentration is known to oscillate when the phase change front moves from one cell into the next. The reason is that in a finite volume formulation, the computed values of C are cell averaged values. As the interface moves from one cell to the next, C suddenly drops from one value to a lower value. The concentration in the new cell then increases due to progressive solute rejection at the interface which occurs at a rate faster than diffusion out of the interface control volume.

The interface concentration can be calculated from the cell-averaged values in the neighbouring liquid, taking into account the fraction of the first cell which remains liquid. The concentration near the interface may be approximated by (Chen *et al.* [18])

$$C(x) = (C_I - C_O)e^{-\gamma x} + C_O \tag{18}$$

where x is the distance from the interface, C_O =1 at% and both C_I and γ can be determined from two adjacent cell averaged concentrations. For numerical reasons and in order to achieve a smooth transition from one solidifying cell to the next, we use a weighted extrapolation formula for C_I:

$$C_I = (f_\ell C_I)_i + (1 - f_\ell)_i (C_I)_{i+1} \tag{19}$$

where the subscript i refers to the grid point.

Solution Methods

Two different solution methods are being used. One uses a finite volume, primitive variable formulation in the commercial code CFX[1]; the other is a finite difference vorticity-stream function formulation implemented in an in-house code called SOLCON[2]. CFX is a general purpose code designed so that complex three-dimensional geometries may be readily handled. Although it can be used for two-dimensional problems (by selecting a mesh size of three in the 'third' direction), it tends to be more demanding in CPU time than a purpose written 2-D code. SOLCON is available in 2-D and 3-D versions.

CFX A sequential solution algorithm using the commercial flow code CFX with a primitive variable formulation is used. In order to simulate the solid region in which the velocity is zero, a resistive force R is introduced into the momentum equation (2). R is set to zero in the liquid and is given a very large value in the solid (typically 10^6).

[1] Available from AEA Technology plc, CFDS, 8.19 Harwell, Didcot, Oxfordshire OX11 0RA, U.K. CFX is a trade mark; mention of it here is for completeness and is not an endorsement of this product by NASA

[2] SOLidification and CONvection

The set of transport equations (1), (2), (9) and (13) was discretized using a finite volume method. The SIMPLEC algorithm was used for pressure-velocity coupling with the Rhie-Chow interpolation method to prevent oscillations of pressure on the non-staggered grid. A fully implicit scheme was used for marching in time. Discretization of convection fluxes was performed using a hybrid scheme and the diffusion fluxes were discretized using central differences. The full field Stone's method was used to solve the complete system of equations.

SOLCON The time-dependant primitive variables equations were converted into the vorticity-stream function formulation in the conventional way. For the evolution of latent heat during phase change, an apparent heat capacity method (Morgan *et al.* [19]) has been used in which an effective specific heat is defined by

$$C^*(T) = \frac{\partial h}{\partial T} = C_{p\phi} + L\frac{\partial f_\ell}{\partial T} \tag{20}$$

Using (20), the energy equation (3) can be written:

$$\rho\left[C^*(T)\frac{\partial T}{\partial t} + C_{p\phi}\nabla.(\tilde{V}T)\right] = \lambda\nabla^2 T \tag{21}$$

To solve (21), an effective heat capacity coefficient $\partial f_\ell / \partial T$ has to be calculated. We define

$$\frac{\partial f_\ell}{\partial T} = \frac{\partial f_\ell / \partial n}{\partial T / \partial n} = \frac{(f_\ell)_n T_n}{T_n^2} = \frac{(f_\ell)_x T_x + (f_\ell)_y T_y}{T_x^2 + T_y^2} \tag{22}$$

where subscripts n (denotes the normal direction), x and y denote differentiation.

A modified Samarskii–Andreyev (ADI) scheme was used to solve iteratively the vorticity, stream function, energy and solute equations at each time step. The modification was designed to ensure accurate coupling between the solution of the transient equations and the thermal boundary conditions and to achieve true transient "simultaneous" solution of the equations. The coupling between equations and boundary conditions becomes especially important because of the movement of the temperature boundary profile. Moreover, the use of iterations becomes necessary because of the strong non-linearity of all governing equations. To ensure stability of the computational process, all source terms and non-linear coefficients depending on liquid fraction are linearized based on the value of the liquid fraction obtained from the previous iteration.

In the solid, the vorticity, stream function and velocities are set to zero.

The vorticity, stream function and energy equations were discretized using central differences and solved by this modified ADI scheme. Interface boundary conditions for vorticity and stream function were applied at the mesh points in the solid sub-region nearest to the s/l interface. For the calculation of vorticity boundary conditions, the definition of vorticity was used: $\tilde{\zeta} = \nabla \times \tilde{V}$. The boundary condition $\tilde{\psi} = 0$ was used for the stream function. The concentration equation (13) was discretized using a

control volume approach to ensure mass balance during phase change in the partially solidified control volume. A second order upwind scheme (SOU) was used for the convection fluxes with central differences for the diffusion terms.

Model and Code Validations

The mathematical model and codes were validated by (a) a comparison of the two codes with each other and with the theory of Smith *et al.* [20] for the solidification of an alloy of bismuth with 1 at% tin in a microgravity environment of 10μg and (b) a comparison with earth based succinonitrile solidification experiments performed at NASA Lewis Research Center [21,22].

The results of these comparisons have been published elsewhere (case(a) in [23] and case (b) in [24]) and will only be summaries here.

Case (a): solidification of Bi-1at% Sn Figure 19 shows the solute concentration distribution at the mid-height of the ampoule. The first 0.01m of sample had been solidified in this time, creating a solute rich boundary layer in front of the interface. This decayed, nominally exponentially, to C_0. The peak value of concentration at the interface caused by solute rejection into the liquid reached almost 11 at%. The results from SOLCON and CFX are almost identical. Maximum and minimum values of concentration at the interface are shown in Table 3.

Solute concentration in the solid at the mid-height of the ampoule is shown in Figure 20. An analytical solution for one-dimensional, diffusion-controlled plane front solidification (Smith *et al.* [20]) is also shown since under microgravity conditions convection is very weak.

It can be seen from Figure 20 that the computed concentrations at the mid-height of the ampoule are close to the analytical, diffusion controlled value. The actual computed values of C_s at the mid-height of the ampoule are 0.328 at% (SOLCON) and 0.309 at% (CFX), whereas the analytical value is 0.335 at%.

Case (b): earth based succinonitrile experiments In this case comparison was made with earth based experiments of solidification, melting and no-growth (the imposed temperature conditions did not vary with time) of succinonitrile contained in a glass ampoule of square cross-section (6 mm inside dimension and 150 mm long) in a horizontal Bridgman furnace.

The interface shapes observed in various planes during the experiment were compared with the numerical calculations. The agreement in almost every case was well within the expected experimental error of 0.5 mm (which is due mainly to the finite size - about 1 mm - of the thermocouples).

Analysis of rehomogenization times

Attention was then turned to the analysis of a complete solidification/hold/melt cycle. During the solidification stage, a solute-rich layer is formed immediately in front of the interface. The peak concentration decays by diffusion and weak convection during the hold stage; this continues during the subsequent melt stage. During the solidification stage, solute movement across the interface and solute build-up in the liquid must be correctly computed. A linear dependency of the melting temperature on

the solute concentration based on the liquidus line of the Bi-Sn phase diagram was used. Thus interface movement will occur in the hold stages due to solidification or melting as the liquid solute concentration at the interface changes, as well as during the solidification stage itself. In the melting stages, solute movement across the solid/liquid interface was assumed to be zero.

The calculations are based on the following scenario, which is illustrated in Figure 21. As a result of previous furnace operations, the solid/liquid interface is initially located at a nominal position of 5 mm, and sufficient time is assumed to have elapsed to ensure that the liquid solute concentration is uniform. Thus the initial condition is that the solid and liquid each have a uniform concentration of C_0 = 1 at% Sn.

Furnace movement at a speed of V_1 for a distance of 5 mm then causes approximately 5 mm of solid[3] to be formed (and the associated solute boundary layer in the liquid is created). The apparatus is held stationary for 30 minutes, and that 5 mm is then melted, using a pulling velocity of $-V_1$. A second hold period of 30 minutes is imposed, following which an additional 5 mm is melted at a pulling velocity of $-V_2$, so that the interface has moved to a nominal position of 0 mm.

The question is: how long would now be required for the solute concentration in the liquid to return to being within $\pm\ 1/e$ of C_o?

In these calculations, g = 1 μg and a single orientation of 45° to the ampoule axis (directed away from the solid) was employed. The solution domain was taken to be a two-dimensional ampoule which is 6 mm high by 30 mm long, and the calculations were performed for two sets of pulling velocities:
(i) V_1 = 3.34 μm/s, V_2 = 6.6 μm/s and (ii) V_1 = 1.85 μm/s, V_2 = 6.6 μm/s.

At these pulling velocities, the durations of the solidification stage and the two melt stages are 24.95, 24.95 and 12.63 minutes respectively for (i), and 45.05, 45.05 and 12.63 minutes for (ii). Thus the two melt stages require a total of approximately 38 minutes for (i), and 58 minutes for (ii).

Figures 22-26 show the longitudinal concentration profiles at the mid-height of the ampoule for case (i) at the various stages as indicated in the figure captions. The progressive decay of the non-uniformities in concentration can be seen. Figure 27 shows the transverse ("radial") concentration profiles at the end of the second melt stage. It can be seen that some radial segregation exists, especially at about 1 cm from the interface. The maximum velocity at this stage is of the order of 0.2 μm/s.

Figure 26 shows that C_{max} = 1.22 at% Sn and C_{min} = 0.67 at% Sn at this time, *i.e.*, before any additional hold occurs. In other words, the rehomogenization is complete, in the sense that C lies within $\pm(1/e)$ of C_0, at the end of the V_2 melt, without the need for a further hold period. The reason is that the two 30 minute waiting periods within the cycle and the two melt stages provide sufficient time for rehomogenization to occur.

The results for case (ii), in which V_1 = 1.85 μm/s and V_2 = 6.6 μm/s, are similar and need not be displayed in figures. Again, rehomogenization is complete at the end of the V_2 melt, without the need for a further hold period: C_{max} = 1.18 at% Sn and C_{min} = 0.69 at% Sn.

---

[3] It is not exactly 5 mm of solid because of the "drag" of the interface caused by the depression of the melting temperature as a result of variations in solute concentration.

Allowance was made for the change of the melting temperature due to a change of the interface solute concentration as a result of rehomogenization. These changes cause a small movement of the interface during the hold periods. In Figure 23 it can be seen that there has been a small forward movement (about 0.4 mm) of the interface compared with its position in Figure 22 as a result of the decay in the peak value of C and the consequent rise in T_m during the 30 minutes between these two figures. Similarly, a comparison of the results underlying Figures 24 and 25 shows that during the second 30 minute hold period, the interface has receded by a very small amount as a result of the increase in C and decrease in T_m at the interface.

MEPHISTO (Event 9W)

Modeling of the MEPHISTO events and comparison of the numerical and experimental results are presently being undertaken. We present here one of typical events, 9W, performed at a time when the solid/liquid interface was located inside the capillary.

A solution domain 2 mm high and 30 mm long was used. The value of g was 1 μg, and a 10×200 mesh was used (uniform 0.2 mm across the ampoule; 100×0.1 mm followed by 100×0.2 mm along the ampoule). At such a low value of g, the velocities are extremely small, and although a finer mesh was tested, it was not needed for the production runs.

As shown in Figure 28, the simulation started after the solid/liquid interface had reached a certain position and had remained there for sufficient time for the liquid in front of the interface to have become homogeneous (Chen *et al.* [18]). Solidification at a pulling speed of 5.185 μm/s then occurred for 965 s (from A to B, Figure 28). The furnace was stopped for 1800 s (B to C), during which time partial rehomogenization of the liquid occurred. Melting at the same speed followed for 965 s (C to D), and then a further rehomogenization stage (D to E) for another 1800 s. The melting temperature was calculated according to (17) with T_{m0} = 271.3 °C and m = 2.32 K/at%. The interpolation scheme given by equation (18) was used.

The distributions of solute concentration along the center line at the end of each stage of the process (*i.e.*, at B, C, D and E) are shown in Figure 29. The peak solute concentration at the end of solidification is about 8 at%. The solute distribution in the liquid becomes increasingly homogeneous during the subsequent stages of the process. Note the shift in the position of the interface between stages B and C, and the accompanying drop in C_s. This is due to the additional solidification following the decay in interface C_l by diffusion and the consequent rise in melting temperature T_m: the temperature in the thin layer of liquid in front of the interface is thereby lower than the new T_m and this layer therefore freezes.

The history of the solute build-up and decay on the liquid side of the interface is shown in Figure 30, as well as the corresponding melting temperature. C_l rises during solidification (A-B), and decays due to diffusion during the rehomogenization stage B-C.

When melting begins (at C), the interface concentration drops to a value (C′) which reflects the additional solidification described above. After this thin layer of solid has melted (C′-C″), the liquid is

then exposed to solid which had formed during A-B and which has a solute concentration which gradually diminishes as it melts (C″-D).

The interface solute concentration again rises due to diffusion during the final rehomogenization (D-E). The variation in C_ℓ has a significant effect on T_m. From the large range of values of melting temperature which results, it is clear that the effect of concentration on T_m cannot be ignored. The velocities at the lower value of g and in the smaller diameter ampoule are much lower – of the order of 0.01 μm/s.

Nevertheless, the flow pattern is of interest. Figure 31 shows the velocity vectors at three stages of the process: (a) early in the solidification; (b) at the end of solidification; and (c) part way through the first rehomogenization stage. In 13(a) a thermally-driven counterclockwise circulation can be seen, the result of which is a slight variation in interface solute concentration, of the order of about ½ % across the ampoule. In 13(b) there is a reverse, solutal-driven clockwise cell which has formed in front of the interface due to the lower density accompanying the higher concentration. Finally, in 13(c), the reverse cell has almost disappeared as the concentration peak decays and the liquid becomes more homogeneous. The interface movement during rehomogenization can again be seen.

Seebeck Signal (Events 11A, 11B, 8A)

The total Seebeck signal ΔV_T can be calculated from [9]:

$$\Delta V_T = \eta_{s/l}\Delta T_I + \int \nabla T(x)\eta_{st}dx \qquad (23)$$

in which $\eta_{s/l}$ is the difference in the Seebeck coefficients of the solid and liquid and ΔT_I is the interfacial undercooling which is in general made up from chemical (constitutional), kinetic and capillary undercooling. The second term in equation (23) is the structural component of the Seebeck signal which comes from differences in the microstructure of crystal during solidification.

Since in our calculations only the constitutional component was taken into account it is convenient to rewrite equation (23) as

$$\Delta V_T = \Delta V_C + \Delta V \qquad (24)$$

in which ΔV_C is the constitutional component of the Seebeck signal and ΔV is the remainder of the signal comprising of structural and kinetic components.

Thus we can determine ΔV , since we have ΔV_T (from the experiments) and we can calculate ΔV_C using,

$$\Delta V_c = \eta_{s/l}m(C_I - C_0) \qquad (25)$$

where C_I is the computed concentration of solute at the interface, C_0 is the initial alloy concentration equal to 1 at% , m=-2.32 K/at% and $\eta_{s/l}$ = 45 μV/K.

Calculations were made for an ampoule 42 mm long. For this study the conductivity was taken to be equal in the solid and liquid. A moving temperature profile consisting of a cold zone (T_c = 50 ^{0}C), a linear temperature profile with gradient 20 K/mm and a hot zone (T_h = 700 ^{0}C) was imposed on the boundary of the ampoule. The ampoule wall was not included in the computational domain. Solidification of the alloy for three events 11A, 11B and 8A has been modeled. The histories of the interface solute concentration and corresponding values of melting temperature were computed. These values taken at the mid-height of the ampoule were used to calculate the component of the Seebeck signal ΔV_c.

Then the sum of the structural and kinetic components was estimated as the difference between experimental Seebeck signal and computed Seebeck voltage due to constitutional undercooling. Results for events for 11A and 11B are shown in Figures (32) and (33).

Effects of g-jitter on directional solidification

We have investigated numerically the effects of sinusoidal disturbances of the form,

$$g(t) = g_0 + A\sin(2\pi\omega t) \qquad (25)$$

in which the amplitude, A, vary from 10^{-5} g to 10^{-2} g and the frequency, ω, vary from 10^{-2} to 1 Hz, on the solute redistribution and segregation at the interface during directional solidification of Bi-1at% Sn alloy. g_0 is the steady component of the acceleration and is taken to be 10^{-6}g.

These results are summarized in Table 4.

It was found that for large frequencies a higher amplitude of the gravitational acceleration is required to produce an effect on the segregation. For example, disturbances with frequencies from 0.5 to 1 Hz and amplitudes less then 10^{-2}g produce very little effect on the segregation. For this frequency range an amplitude of 10^{-2}g resulted in 20.2% and 10.9% segregation compared with a segregation of 1.8% for the steady 1μg case. For frequencies from 0.05 Hz to 0.1 Hz, an amplitude of 10^{-3} g results in the segregation changing to 11.3% and 8.9% respectively. The largest effect on the segregation was produced by disturbances with a frequency of 0.01 Hz, where the maximum segregation was equal to 4.9% for an amplitude of 10^{-4} g, 38.2% for an amplitude of 10^{-3}g and 188.7% for an amplitude of 10^{-2}g. In the last case complete mixing of the solute in the cavity was observed.

Figure 34 shows the effect of g-jitter on the average concentration at the interface for an amplitude of 10^{-2}g and a range of frequencies.

Radial Segregation

Our numerical results showed strong dependence of the radial segregation on the interface curvature. Computations have been done for the solidification with a pulling velocity of 3.34 μm/s and different conductivities in the solid and liquid. In the case when conduction through the wall was not included interface deflection from the flat was about 26% after 1000 sec. of solidification with the corresponding segregation equal to 22%. Including the wall decreased deflection to 11% and radial segregation to 10%. Kaddeche *et al.* [25] suggest that segregation as function of the deflection is given by,

$$\gamma = 0.8 * Pe * (1-k) * \eta \qquad (26)$$

where γ is the segregation of the solute at the interface, η is the deflection of the interface and Pe is the Peclet number. This formula is valid for small curvature (deflection).

To check our results computations were performed with physical parameters taken from [25], they showed good agreement with results obtained in the [25]. It can be concluded that computations without the ampoule wall could introduce unrealistic curvature and as a consequence unrealistic segregation. This is particularly important in the case of concentration dependent melting temperature in which the increased concentration in the centre of the interface will decrease the speed of solidification and hence cause the interface curvature to increase further. As the interface deflection strongly depends on the temperature solutions, implementation of the proper temperature boundary conditions will determine the accuracy of the radial segregation calculated.

SECTION VI. Summary

Many of the parameters important for studying morphological instabilities were successfully measured during directional solidification of Bi 1 at% Sn. The Seebeck signals and calculated temperature gradient in the liquid for the ground- and space-based sets of experiments were significantly different. The differences are consistent with strong hydrodynamic mixing in the liquid during the ground-based experiments. The analysis of the Seebeck measurements indicate that for bismuth-based alloys, the structure and composition of the solid alloy have strong influences on the Seebeck signal generated. The microstructural examination of the directionally solidified samples reveals strong influences of interfacial kinetics and anisotropy on the morphological instability of the solid-liquid interface.

Acknowledgments

The authors would like to thank CEA and the Société Européene de Propulsion, France for their support during ground-based experiments and flight preparations. We would also like to acknowledge the entire USMP-4 team, especially Philippe Beaugrand, Kirk Beatty, P. Y. P. Chen, Vincent Gounot, Philippe Le, Regis Rieu, Bill Foster, Gil Santoro, Mingwu Yao, Nick Barbosa, Jeff Clancy, Gordon Seuell and the superb support of the NASA Marshall USMP-4 team. The financial support of the program by the NASA is gratefully acknowledged.

SECTION VII. References

1. As reviewed in "Morphological Stability," S. R. Coriell and G. B. McFadden, Handbook of Crystal Growth, Vol.1, ed. D. T. J. Hurle, (Elsevier) 785.

2. W.W. Mullins and R.F. Sekerka, "Stability of a planar Interface During Solidification of a Dilute Binary Alloy," *J. Appl. Phys.*, (1964) 444.

3. S. R. Coriell and R. F. Sekerka, "The Effect of Anisotropy of Surface Tension and Interface Kinetics on Morphological Stability," *J. Crystal Growth*, 3 (1976) 157.

4. S. R. Coriell, B. T. Murray, and A. A. Chernov, "Kinetic Self-Stabilization of a Stepped Interface: Binary Alloy Solidification," *J. Cryst. Growth*, 141 (1994) 219.

5. G. W. Young, S. H. Davis and K. Brattkus, "Anisotropic Interface Kinetics and Tilted Cell Unidirectional Solidification," *J. Cryst. Growth*, 83 (1987) 560.

6. W. A. Tiller and J. W. Rutter, "The Effect of Growth Conditions Upon the Solidification of a Binary Alloy," *Can. J. Phys.*, 34, (1956) 96.

7. R. Trivedi, "Effects of Anisotropy Properties on Interface Pattern Formation," *Appl. Mech. Rev.*, 43 (5) Part 2, (1990) S79.

8. R. Trivedi, V. Seetharaman and M. A. Eshelman, "The Effects of Interface Kinetics Anisotropy on the Growth of Cellular Microstructures," *Met. Trans. A*, 22A (1991) 585.

9. R. Abbaschian, A. B. Gokhale, J. J. Favier, G. Combon, S. R. Coriell, H. C. de Groh III, and R. L. DeWitt, "A Study of Directional Solidification of Faceted Bi-Sn Alloys in Microgravity," (American Institute of Aeronautics and Astronautics, January 1995) AIAA 95-0608.

10. R. Abbaschian, A. B. Gokhale, and D. B. Allen, " A Study of Directional Solidification of Faceted Bi-Sn Alloys in Microgravity", *Solidification Science and Processing*, Edited by I. Ohnaka and D. M. Stefanescu, 1996, pp.73-84

11. A.Rouzard, J. J. Favier and D Thevenard, *Adv. Space*. Res. 8, (1988) p 49

12. S. D. Peteves, Ph.D. Dissertation, University of Florida, (1985)

13. S.D. Peteves and R. Abbaschian, *Met. Trans.* A 22A (1991), 1259

14. S.D. Peteves and R. Abbaschian, *Met. Trans.* A 22A (1991), 1271

15. B.Sixou, A. Rouzaud J.J. Favier, *J. Crstal Growth* 137 (1994) p. 605

16. R. Voller, A.D. Brent, and C. Prakash, "The Modeling of Heat, Mass and Solute Transport in Solidification Systems", *Int. J. Heat Mass Transfer*, Vol. 32, pp 1719-1731, 1989.

17. Abbaschian, Private Communication, 1997.

18. P.Y.P. Chen, G. de Vahl Davis, J. Kaenton, E. Leonardi, S.S. Leong, V. Timchenko, H.C. de Groh III and R. Abbaschian, "Rehomogenization: Diffusion and Convection in Microgravity", AIAA Paper 98-0740, 36th Aerospace Sciences Meeting, Reno NV, Jan 12-15, 1998.

19. K. Morgan, R.W. Lewis and O.C. Zienkiewicz, "An Improved Algorithm for Heat Conduction Problems with Phase Change", *Int. J. Numer. Meth. Eng.*, Vol.12, pp. 1191-1195, 1978.

20. V.G. Smith, W.A. Tiller and J.W. Rutter, "A Mathematical Analysis of Solute Redistribution during Solidification", *Canadian J. of Physics*, Vol.33, pp. 723-743, 1955.

21. H.C. de Groh III and T. Lindstrom, NASA TM 106487, 1994.

22. M. Yao and H.C. de Groh III, "Three-Dimensional Finite Element Method Simulation of Bridgman Crystal Growth and Comparison with Experiments", *Num. Heat Transfer*, Part A, Vol. 24, pp 393-412, 1993.

23. Timchenko, P.Y.P. Chen, G. de Vahl Davis and E. Leonardi, "Directional Solidification in Microgravity", *Heat Transfer 1998*, J.S. Lee (ed), Taylor & Francis, pp. 241-246, 1998.

24. P.Y.P. Chen, V. Timchenko, E. Leonardi, G. de Vahl Davis and H.C. de Groh III, "A Numerical Study of Directional Solidification and Melting in Microgravity", HTD-Vol.361-3/PID-Vol.3, Proc. of the ASME Heat Transfer Division - Volume 3, R.A. Nelson Jr., L.W. Swanson, M.V.A. Bianchi, C. Camci (eds), ASME, New York, pp.75-83, 1998.

25. S. Kaddeche, J. Garandet, C. Barat, H. Ben Hadid, D. Henry, "Interface Curvature and Convection Related Macrosegregation in the Vertical Bridgman Configuration", *J. Crystal Growth*, Vol. 158, pp.144-152, 1996.

Publications Related to the Project

1. R. Abbaschian, A. B. Gokhale, J. J. Favier, G. Cambon, S. R. Coriell, H. C. de Groh III, and R.L. DeWitt, "A Study of Directional Solidification of Faceted Bi-Sn Alloys in Microgravity", *American Institute of Aeronautics and Astronautics*, January 1995, AIAA 95-0608.

2. R. Abbaschian, A.B. Gokhale, S.R. Coriell, J.J. Favier, "In-Situ Monitoring of Crystal Growth Using MEPHISTO", in *Microgravity Science & Applications*, NASA Technical Memorandum 4677, March 1995, p. II-112-II-114.

3. R. Abbaschian, "In Situ Monitoring of Crystal Growth Using Mephisto", NASA Technical Memorandum 4737, April 1996, pp. 47-87.

4. R. Abbaschian, A. B. Gokhale, and D. B. Allen, "A Study of Directional Solidification of Faceted Bi-Sn Alloys in Microgravity", *Solidification Science and Processing*, Edited by I. Ohnaka and D. M. Stefanescu, 1996, pp. 73-84.

5. M. Yao, H. C. de Groh III, and R. Abbaschian, "Numerical Modeling of Solidification in Space with MEPHISTO-4 (Part 1)", *American Institute of Aeronautics and Astronautics*, January 1997, AIAA 97-0449.

6. P. Chen, G. deVahl Davis, J. Kaenton, E. Leonardi, S. Leong, V. Timchenko, H.C. de Groh III and R. Abbaschian, "Rehomogenization: Diffusion and Convection in Microgravity", *American Institute of Aeronautics and Astronautics*, January 1998, A1AA98-0740

7. J. E. Simpson, S. V. Garimella, H. C. de Groh III and R. Abbaschian, "Melt Convection Effects in the Bridgman Crystal Growth of an Alloy under Microgravity Conditions", 7th AAIA/ASME Joint Thermophysics and Heat Transfer Conference, June 1998, HTD-Vol. 357-4, pp. 123-132.

8. G. Cambon, G Hieu, R. Abbaschian, K. Beatty, H. DeGroh, N. Kernevez, E. Rolland, V. Gounot, Ph. Beaugrand, "In-Situ Monitoring of Crystal Growth Using MEPHISTO", 49th International Astronautical Congress, September 28-October 2, 1998, Melbourne, Australia.

9. R. Abbaschian, K.M. Beatty, F. Chen, T. Lenzi, H. de Groh III, G. Cambon, G. de Vahl Davis, E. Leonardi, "Directional Solidification of Bi-Sn Alloys", Proceedings of 10th International Symposium on Experimental Methods for Microgravity Materials Science, San Antonio, Texas, 16-19 February 1998.

10. V. Timchenko, P.Y. P. Chen, G. de Vahl Davis and E. Leonardi, "Directional solidification in microgravity", *Heat Transfer 1998*, J.S. Lee (ed), Taylor & Francis, pp. 241-246, 1998.

11. P. Y. P. Chen, V. Timchenko, E. Leonardi, G. de Vahl Davis and H.C. de Groh III, "A Numerical Study of Directional Solidification and Melting in Microgravity", HTD-Vol.361-3/PID-Vol.3, Proc. of the ASME Heat Transfer Division - Volume 3, R. A. Nelson Jr., L.W. Swanson, M.V.A. Bianchi, C. Camci (eds), ASME, New York, pp.75-83, 1998.

12. P.Y. P. Chen, G. de Vahl Davis, J. Kaenton, E. Leonardi, S.S. Leong, V. Timchenko, H.C. de Groh III and R. Abbaschian, "Rehomogenisation: Diffusion and Convection in Microgravity", Paper No. AIAA 98-0740, AIAA 36th Aerospace Science Meeting and Exhibit, Reno NV, Jan. 12-15, 1998.

13. G. de Vahl Davis: "Crystal Growth by the Bridgman Process in Microgravity". In *Advanced Computational Methods in Heat Transfer V*, A.J. Nowak, C. A. Brebbia, R. Bialecki and M. Zerroukat (eds), Computational Mechanics Publications, Southampton, pp. 567-581, 1998.

14. C. Benjapiyaporn, V. Timchenko, G. de Vahl Davis, E. Leonardi and H. C. de Groh III, "Effects of g-jitter on Directional Solidification of a Binary Alloy", Paper No. IAF-98-J.2.01, 49th International Astronautical Congress, Melbourne, Australia, Sept 28 - Oct 2, 1998.

15. V. Timchenko, P.Y.P. Chen, E. Leonardi, G. de Vahl Davis and R. Abbaschian, "A Computational Study of Transient Plane Front Solidification of Alloys in a Bridgman Apparatus under Microgravity Conditions", Accepted for publication in *Int. J. Heat and Mass Transfer*, 1999.

16. R. Abbaschian, S. Coriell and A. Chernov, "Morphological Stability of Bismuth-Tin Alloys", to be published in Solidification 1999, TMS.

Table 1. Timeline for MEPHISTO experiment of USMP-4 mission

Stage	Step	TYPE	V	Velocity [mm/hr]	Initial [mm]	Final [mm]	Duration [hr]	MET [hr]	(INITIAL FOR STAGE) [days]	D	H	M
1		CD		0.00	149	149	3.000	0.00	0.00	0	0	0.0
2		OH		0.00	149	149	5.000	3.000	0.13	0	3	0.0
3	A	HFF		0.00	149	149	1.500	8.000	0.33	0	8	0.0
		H		0.00	149	149	0.500	9.500	0.40	0	9	30.0
3	B	HFF		0.00	149	149	0.500	10.000	0.42	0	10	0.0
		H		0.00	149	149	0.500	10.500	0.44	0	10	30.0
3	C	HFF		0.00	149	149	0.500	11.000	0.46	0	11	0.0
		H		0.00	149	149	0.500	11.500	0.48	0	11	30.0
3	D	HFF		0.00	149	149	0.500	12.000	0.50	0	12	0.0
		H		0.00	149	149	0.500	12.500	0.52	0	12	30.0
3	E	HFF		0.00	149	149	3.500	13.000	0.54	0	13	0.0
		H		0.00	149	149	0.500	16.500	0.69	0	16	30.0
3	F	HMF		0.00	149	149	1.500	17.000	0.71	0	17	0.0
		H		0.00	149	149	0.500	18.500	0.77	0	18	30.0
3	G	HMF		0.00	149	149	0.500	19.000	0.79	0	19	0.0
		H		0.00	149	149	0.500	19.500	0.81	0	19	30.0
3	H	HMF		0.00	149	149	0.500	20.000	0.83	0	20	0.0
		H		0.00	149	149	0.500	20.500	0.85	0	20	30.0
3	I	HMF		0.00	149	149	4.000	21.000	0.88	0	21	0.0
		EH		0.00	149	149	1.783	25.000	1.04	1	1	0.0
7	A	PM	V3	-23.99	149	144	0.208	26.783	1.12	1	2	47.0
		EH		0.00	144	144	6.420	26.992	1.12	1	2	59.5
9	A	F	V1	6.67	144	149	0.750	36.500	1.52	1	12	30.0
		H		0.00	149	149	0.500	37.250	1.55	1	13	15.0
		M	V1	-6.67	149	144	0.750	37.750	1.57	1	13	45.0
		H		0.00	144	144	0.500	38.500	1.60	1	14	30.0
7	B	PM	V3	-23.99	144	139	0.208	39.000	1.63	1	15	0.0
		EH		0.00	139	139	0.500	39.209	1.63	1	15	12.5
9	B	F	V2	12.00	139	144	0.417	39.709	1.65	1	15	42.5
		H		0.00	144	144	0.500	40.126	1.67	1	16	7.5
		M	V2	-12.00	144	139	0.417	40.626	1.69	1	16	37.5
		H		0.00	139	139	0.500	41.042	1.71	1	17	2.5
10	A	F	V4	47.99	139	144	0.104	41.542	1.73	1	17	32.5
		H		0.00	144	144	1.000	41.646	1.74	1	17	38.8
		M	V4	-47.99	144	139	0.104	42.646	1.78	1	18	38.8
		H		0.00	139	139	1.000	42.751	1.78	1	18	45.0
		EH		0.00	139	139	3.907	43.751	1.82	1	19	45.0
10	B	F	V1	6.67	139	144	0.750	47.658	1.99	1	23	39.5
		H		0.00	144	144	1.000	48.408	2.02	2	0	24.5
		M	V1	-6.67	144	139	0.750	49.408	2.06	2	1	24.5
		H		0.00	139	139	1.000	50.158	2.09	2	2	9.5
		EH		0.00	139	139	2.175	51.158	2.13	2	3	9.5
7	C1	F	V3	23.99	139	148	0.375	53.333	2.22	2	5	20.0
		H		0.00	148	148	1.000	53.708	2.24	2	5	42.5
		M	V3	-23.99	148	139	0.375	54.708	2.28	2	6	42.5
		H		0.00	139	139	1.000	55.083	2.30	2	7	5.0
7	C2	PM	V3	-23.99	139	130	0.375	56.083	2.34	2	8	5.0
		EH		0.00	130	130	4.042	56.459	2.35	2	8	27.5

Stage	Step	TYPE	V	Velocity [mm/hr]	Initial [mm]	Final [mm]	Duration [hr]	MET [hr]	(INITIAL FOR STAGE) [days]	D	H	M
9	C	F	V3	23.99	130	140	0.417	60.501	2.52	2	12	30.0
		H		0.00	140	140	0.500	60.917	2.54	2	12	55.0
		M	V3	-23.99	140	130	0.417	61.417	2.56	2	13	25.0
		H		0.00	130	130	0.500	61.834	2.58	2	13	50.0
7	D	PM	V3	-23.99	130	115	0.625	62.334	2.60	2	14	20.0
		EH		0.00	115	115	2.000	62.959	2.62	2	14	57.6
9	D	F	V4	47.99	115	130	0.313	64.959	2.71	2	16	57.6
		H		0.00	130	130	0.500	65.272	2.72	2	17	16.3
		M	V4	-47.99	130	115	0.313	65.772	2.74	2	17	46.3
		H		0.00	115	115	0.500	66.084	2.75	2	18	5.1
7	E	F	V3	23.99	115	135	0.834	66.584	2.77	2	18	35.1
		H		0.00	135	135	0.050	67.418	2.81	2	19	25.1
7	E1	PM	V3	-23.99	135	95	1.667	67.468	2.81	2	19	28.1
		EH		0.00	95	95	1.000	69.135	2.88	2	21	8.1
9	E	F	V5	95.98	95	115	0.208	70.135	2.92	2	22	8.1
		H		0.00	115	115	0.500	70.343	2.93	2	22	20.6
		M	V5	-95.98	115	95	0.208	70.843	2.95	2	22	50.6
		H		0.00	95	95	0.500	71.052	2.96	2	23	3.1
7	F	PM	V3	-23.99	95	75	0.834	71.552	2.98	2	23	33.1
		EH		0.00	75	75	0.865	72.385	3.02	3	0	23.1
7	G	PM	V3	-23.99	75	70	0.208	73.250	3.05	3	1	15.0
		EH		0.00	70	70	0.566	73.459	3.06	3	1	27.5
9	F	F	V3	23.99	70	90	0.834	74.025	3.08	3	2	1.5
		H		0.00	90	90	0.500	74.858	3.12	3	2	51.5
		M	V3	-23.99	90	70	0.834	75.358	3.14	3	3	21.5
		H		0.00	70	70	0.500	76.192	3.17	3	4	11.5
		EH		0.00	70	70	9.675	76.692	3.20	3	4	41.5
9	G	F	V1	6.67	70	75	0.750	86.367	3.60	3	14	22.0
		H		0.00	75	75	0.500	87.117	3.63	3	15	7.0
		M	V1	-6.67	75	70	0.750	87.617	3.65	3	15	37.0
		H		0.00	70	70	0.333	88.367	3.68	3	16	22.0
7	H	PM	V3	-23.99	70	65	0.208	88.701	3.70	3	16	42.0
		EH		0.00	65	65	2.000	88.909	3.70	3	16	54.5
9	H	F	V2	12.00	65	70	0.417	90.909	3.79	3	18	54.5
		H		0.00	70	70	0.500	91.326	3.81	3	19	19.5
		M	V2	-12.00	70	65	0.417	91.826	3.83	3	19	49.5
		H		0.00	65	65	0.500	92.242	3.84	3	20	14.5
7	I	PM	V3	-23.99	65	55	0.417	92.742	3.86	3	20	44.5
		EH		0.00	55	55	1.190	93.159	3.88	3	21	9.6
9	M	F	V5	95.98	55	75	0.208	94.349	3.93	3	22	21.0
		H		0.00	75	75	0.500	94.558	3.94	3	22	33.5
		M	V5	-95.98	75	55	0.208	95.058	3.96	3	23	3.5
		H		0.00	55	55	0.500	95.266	3.97	3	23	16.0
		EH		0.00	55	55	4.065	95.766	3.99	3	23	46.0
9	O	F	V6	144.04	55	75	0.139	99.831	4.16	4	3	49.9
		H		0.00	75	75	0.500	99.970	4.17	4	3	58.2
		M	V6	-144.04	75	55	0.139	100.470	4.19	4	4	28.2
		H		0.00	55	55	0.500	100.609	4.19	4	4	36.5
		EH		0.00	55	55	8.200	101.109	4.21	4	5	6.5

Stage	Step	TYPE	V	Velocity [mm/hr]	Initial [mm]	Final [mm]	Duration [hr]	MET [hr]	(INITIAL FOR STAGE) [days]	D	H	M
9	N	F	V3	23.99	55	75	0.834	109.309	4.55	4	13	18.5
		H		0.00	75	75	0.500	110.142	4.59	4	14	8.5
		M	V3	-23.99	75	55	0.834	110.642	4.61	4	14	38.5
		H		0.00	55	55	0.500	111.476	4.64	4	15	28.5
		EH		0.00	55	55	3.700	111.976	4.67	4	15	58.5
9	P	F	V2	12.00	55	75	1.667	115.676	4.82	4	19	40.5
		H		0.00	75	75	0.500	117.343	4.89	4	21	20.6
		M	V2	-12.00	75	55	1.667	117.843	4.91	4	21	50.6
		H		0.00	55	55	0.500	119.510	4.98	4	23	30.6
		EH		0.00	55	55	5.860	120.010	5.00	5	0	0.6
11	Q1	F	V2	12.00	55	60	0.417	125.870	5.24	5	5	52.2
		H		0.00	60	60	0.500	126.287	5.26	5	6	17.2
11	Q2	F	V2	12.00	60	65	0.417	126.787	5.28	5	6	47.2
		H		0.00	65	65	0.500	127.204	5.30	5	7	12.2
7	Q	M	V3	-23.99	65	55	0.417	127.704	5.32	5	7	42.2
		EH		0.00	55	55	7.880	128.120	5.34	5	8	7.2
9	I	F	V1	6.67	55	70	2.251	136.000	5.67	5	16	0.0
		H		0.00	70	70	0.500	138.251	5.76	5	18	15.1
		M	V1	-6.67	70	55	2.251	138.751	5.78	5	18	45.1
		H		0.00	55	55	0.500	141.001	5.88	5	21	0.1
7	J	PM	V3	-23.99	55	45	0.417	141.501	5.90	5	21	30.1
		EH		0.00	45	45	3.180	141.918	5.91	5	21	55.1
9	J	F	V1.5	10.66	45	55	0.938	145.098	6.05	6	1	5.9
		H		0.00	55	55	0.500	146.036	6.08	6	2	2.2
		M	V1.5	-10.66	55	45	0.938	146.536	6.11	6	2	32.2
		H		0.00	45	45	0.500	147.474	6.14	6	3	28.4
7	K	PM	V3	-23.99	45	20	1.042	147.974	6.17	6	3	58.4
		EH		0.00	20	20	0.985	149.016	6.21	6	5	0.9
9	K	F	V5	95.98	20	55	0.365	150.001	6.25	6	6	0.0
		H		0.00	55	55	0.500	150.365	6.27	6	6	21.9
		M	V5	-95.98	55	20	0.365	150.865	6.29	6	6	51.9
		H		0.00	20	20	0.500	151.230	6.30	6	7	13.8
		EH		0.00	20	20	1.271	151.730	6.32	6	7	43.8
9	L	F	V6	144.04	20	55	0.243	153.000	6.38	6	9	0.0
		H		0.00	55	55	0.500	153.243	6.39	6	9	14.6
		M	V6	-144.04	55	20	0.243	153.743	6.41	6	9	44.6
		H		0.00	20	20	0.500	153.986	6.42	6	9	59.2
		EH		0.00	20	20	5.700	154.486	6.44	6	10	29.2
11	R	F	V1	6.67	20	25	0.750	160.186	6.67	6	16	11.2
		H		0.00	25	25	2.500	160.937	6.71	6	16	56.2
9	R	F	V1	6.67	25	35	1.500	163.437	6.81	6	19	26.2
		H		0.00	35	35	0.500	164.937	6.87	6	20	56.2
		M	V1	-6.67	35	25	1.500	165.437	6.89	6	21	26.2
		H		0.00	25	25	0.090	166.937	6.96	6	22	56.2
7	R	PM	V3	-23.99	25	1	1.000	167.027	6.96	6	23	1.6
		EH		0.00	1	1	0.600	168.028	7.00	7	0	1.7
11	A	F	V1	6.67	1	5	0.600	168.628	7.03	7	0	37.7
		EH		0.00	5	5	6.000	169.228	7.05	7	1	13.7
11	B	F	V2	12.00	5	10	0.417	175.228	7.30	7	7	13.7
		EH		0.00	10	10	9.359	175.645	7.32	7	7	38.7

Stage	Step	TYPE	V	Velocity [mm/hr]	Initial [mm]	Final [mm]	Duration [hr]	MET [hr]	(INITIAL FOR STAGE) [days]	D	H	M
9	S	F	V4	47.99	10	25	0.313	185.004	7.71	7	17	0.2
		H		0.00	25	25	0.500	185.316	7.72	7	17	19.0
		M	V4	-47.99	25	10	0.313	185.816	7.74	7	17	49.0
		H		0.00	10	10	0.500	186.129	7.76	7	18	7.7
		EH		0.00	10	10	3.000	186.629	7.78	7	18	37.7
8	A	F	V0.5	2.67	10	15	1.875	189.629	7.90	7	21	37.7
		H		0.00	15	15	1.000	191.504	7.98	7	23	30.2
		M	V0.5	-2.67	15	10	1.875	192.504	8.02	8	0	30.2
		H		0.00	10	10	1.000	194.380	8.10	8	2	22.8
		EH		0.00	10	10	13.878	195.380	8.14	8	3	22.8
9	T	F	V3	23.99	10	35	1.042	209.258	8.72	8	17	15.5
		H		0.00	35	35	0.500	210.300	8.76	8	18	18.0
		M	V3	-23.99	35	10	1.042	210.800	8.78	8	18	48.0
		H		0.00	10	10	0.500	211.841	8.83	8	19	50.5
		EH		0.00	10	10	5.758	212.341	8.85	8	20	20.5
9	U	F	V3.5	35.99	10	35	0.695	218.099	9.09	9	2	6.0
		H		0.00	35	35	0.500	218.794	9.12	9	2	47.6
		M	V3.5	-35.99	35	10	0.695	219.294	9.14	9	3	17.6
		H		0.00	10	10	0.500	219.989	9.17	9	3	59.3
		EH		0.00	10	10	5.794	220.489	9.19	9	4	29.3
9	V	F	V2.5	18.67	10	20	0.536	226.283	9.43	9	10	17.0
		H		0.00	20	20	0.500	226.818	9.45	9	10	49.1
		M	V2.5	-18.67	20	10	0.536	227.318	9.47	9	11	19.1
		H		0.00	10	10	0.500	227.854	9.49	9	11	51.2
		EH		0.00	10	10	6.207	228.354	9.51	9	12	21.2
9	W	F	V2.5	18.67	10	15	0.268	234.561	9.77	9	18	33.7
		H		0.00	15	15	0.500	234.829	9.78	9	18	49.7
		M	V2.5	-18.67	15	10	0.268	235.329	9.81	9	19	19.7
		H		0.00	10	10	0.500	235.597	9.82	9	19	35.8
		EH		0.00	10	10	7.610	236.097	9.84	9	20	5.8
12		F	V3	23.99	10	25	0.625	243.707	10.15	10	3	42.4
		EH		0.00	25	25	1.668	244.332	10.18	10	4	19.9
9	X	F	V3	23.99	25	40	0.625	246.000	10.25	10	5	60.0
		H		0.00	40	40	0.500	246.625	10.28	10	6	37.5
		M	V3	-23.99	40	25	0.625	247.125	10.30	10	7	7.5
		H		0.00	25	25	0.025	247.750	10.32	10	7	45.0
9	Y	F	V1	6.67	25	30	0.750	247.775	10.32	10	7	46.5
		H		0.00	30	30	0.500	248.525	10.36	10	8	31.5
		M	V1	-6.67	30	25	0.750	249.025	10.38	10	9	1.5
		H		0.00	25	25	0.019	249.776	10.41	10	9	46.5
9	Z	F	V5	95.98	25	45	0.208	249.795	10.41	10	9	47.7
		H		0.00	45	45	0.500	250.003	10.42	10	10	0.2
		M	V5	-95.98	45	25	0.208	250.503	10.44	10	10	30.2
		H		0.00	25	25	0.500	250.711	10.45	10	10	42.7
		EH		0.00	25	25	1.500	251.211	10.47	10	11	12.7
9	AA	F	V5	95.98	25	45	0.208	252.711	10.53	10	12	42.7
		H		0.00	45	45	0.500	252.920	10.54	10	12	55.2
		M	V5	-95.98	45	25	0.208	253.420	10.56	10	13	25.2
		H		0.00	25	25	0.500	253.628	10.57	10	13	37.7
		EH		0.00	25	25	6.872	254.128	10.59	10	14	7.7

Stage	Step	TYPE	V	Velocity [mm/hr]	Initial [mm]	Final [mm]	Duration [hr]	MET [hr]	(INITIAL FOR STAGE) [days]	D	H	M
13		F	V5	95.98	25	45	0.208	261.000	10.88	10	21	0.0
		EH		0.00	45	45	2.500	261.209	10.88	10	21	12.5
11	C	F	V4	47.99	45	60	0.313	263.709	10.99	10	23	42.5
		EH		0.00	60	60	3.729	264.021	11.00	11	0	1.3
14		F	V3	23.99	60	90	1.250	267.750	11.16	11	3	45.0
		EH		0.00	90	90	6.000	269.000	11.21	11	5	0.0
11	D	F	V6	144.04	90	105	0.104	275.000	11.46	11	11	0.0
		EH		0.00	105	105	4.896	275.105	11.46	11	11	6.3
15		F	V5	95.98	105	125	0.208	280.001	11.67	11	16	0.0
		EH		0.00	125	125	5.791	280.209	11.68	11	16	12.5
8	D	F	V0.6	4.00	125	130	1.250	286.000	11.92	11	22	0.0
		H		0.00	130	130	1.000	287.250	11.97	11	23	15.0
		M	V0.6	-4.00	130	125	1.250	288.250	12.01	12	0	15.0
		H		0.00	125	125	1.000	289.500	12.06	12	1	30.0
		EH		0.00	125	125	1.500	290.500	12.10	12	2	30.0
8	E	F	V0.8	5.33	125	130	0.938	292.000	12.17	12	4	0.0
		H		0.00	130	130	1.000	292.938	12.21	12	4	56.3
		M	V0.8	-5.33	130	125	0.938	293.938	12.25	12	5	56.3
		H		0.00	125	125	1.000	294.875	12.29	12	6	52.5
		EH		0.00	125	125	2.000	295.875	12.33	12	7	52.5
9	AB	F	V3	23.99	125	140	0.625	297.875	12.41	12	9	52.5
		H		0.00	140	140	0.500	298.500	12.44	12	10	30.0
		M	V3	-23.99	140	125	0.625	299.000	12.46	12	11	0.0
		H		0.00	125	125	0.500	299.625	12.48	12	11	37.5
		EH		0.00	125	125	9.875	300.125	12.51	12	12	7.5
16		F	V3	23.99	125	140	0.625	310.000	12.92	12	22	0.0
		EH		0.00	140	140	2.000	310.625	12.94	12	22	37.5
11	E	F	V2	12.00	140	144	0.333	312.625	13.03	13	0	37.5
		EH		0.00	144	144	3.700	312.959	13.04	13	0	57.5
11	F	F	V1	6.67	144	148	0.600	316.659	13.19	13	4	39.5
17		Q			148	148	0.017	317.259	13.22	13	5	15.5
18		CF			148	148	7.000	317.276	13.22	13	5	16.5
19		DE			148	148	0.083	324.276	13.51	13	12	16.5

Time line Information Sheet

V0.5	2.666	mm/hr
V0.6	4	mm/hr
V0.8	5.3333	mm/hr
V1	6.665	mm/hr
V1.5	10.664	mm/hr
V2	11.997	mm/hr
V2.5	18.667	mm/hr
V3	23.994	mm/hr
V3.5	35.991	mm/hr
V4	47.988	mm/hr
V5	95.976	mm/hr
V6	144.04	mm/hr

M	Melt
F	Freeze
PM	Primary Melt
EH	Extended hold
H	Hold
CD	Cold Degassing
OH	Overall heat
HFF	Heat Fixed Furnace
HMF	Heat Movable Furnace
Q	Quench
CF	Cool Furnace
DE	Deactivate

Table 2. Growth Conditions and Velocity Values During Final Solidification Steps

Name	MET TIME (Day/Hr.)	Velocity (μm/Sec.)	Start Position (mm)	End Position (mm)
11A (V1)	7/1	1.869	1	5
11B (V2)	7/9	3.426	5	10
12 (V3)	10/4	6.763	10	25
13 (V5)	10/21	26.86	25	45
11C (V4)	11/0	13.47	45	60
14 (V3)	11/4	6.743	60	90
11D (V6)	11/11	40.29	90	105
14 (V3)	11/16	27.01	105	125
16 (V3)	12/23	6.737	125	140
11E (V2)	13/0	3.322	140	144
11F (V1)	13/5	1.823	144	148

Notes:
Start and End Positions in MEPHISTO Coordinates
MET: Mission Elapsed Time

Table 3. Comparison of Two Methods

Method	C_{min}(at%)	C_{max}(at%)	$\|U_{max}\|$(m/s)	V_{max}(m/s)	V_{min}(m/s)	CPU time(s)
SOLCON	10.04	11.54	2.282×10^{-6}	5.943×10^{-7}	-1.224×10^{-6}	80296
CFX	9.98	11.28	2.311×10^{-6}	5.977×10^{-7}	-1.217×10^{-6}	841800

Table 4. Summary of Results

Amplitude (m/s^2)	Frequency (Hz)	Maximum velocity (mm/s)		Maximum segregation (%)	Segregation at 500s (%)
		U_{max}	V_{max}		
$10^{-2}g$	0.01	2.50	0.89	188.7	90.0
	0.05	1.26	0.78	192.4	188.0
	0.1	0.75	0.32	39.9	39.9
	0.5	0.19	9.66×10^{-2}	20.2	20.2
	1.0	9.78×10^{-2}	4.81×10^{-2}	10.9	10.9
$10^{-3}g$	0.01	0.22	0.11	38.2	33.0
	0.05	0.12	6.75×10^{-2}	11.3	10.3
	0.1	7.49×10^{-2}	4.13×10^{-2}	8.9	8.9
	0.5	1.90×10^{-2}	9.78×10^{-3}	3.1	3.1
	1.0	9.95×10^{-3}	4.94×10^{-3}	2.5	2.5
$10^{-4}g$	0.01	2.15×10^{-2}	1.15×10^{-2}	4.9	4.3
	0.05	1.27×10^{-2}	6.86×10^{-3}	2.7	2.7
	0.1	7.68×10^{-3}	4.23×10^{-3}	2.3	2.3
	0.5	2.06×10^{-3}	1.08×10^{-3}	1.8	1.8
	1.0	1.14×10^{-3}	6.02×10^{-4}	1.8	1.8
$10^{-5}g$	0.01	2.41×10^{-3}	1.27×10^{-3}	2.0	2.0
	0.05	1.47×10^{-3}	7.96×10^{-4}	1.8	1.8
	0.1	9.66×10^{-4}	5.29×10^{-4}	1.8	1.8
	0.5	3.85×10^{-4}	2.12×10^{-4}	1.8	1.8
	1.0	2.97×10^{-4}	1.65×10^{-4}	1.8	1.8
Steady at $g = 10^{-6}g$		2.28×10^{-4}	1.20×10^{-4}	1.8	1.8

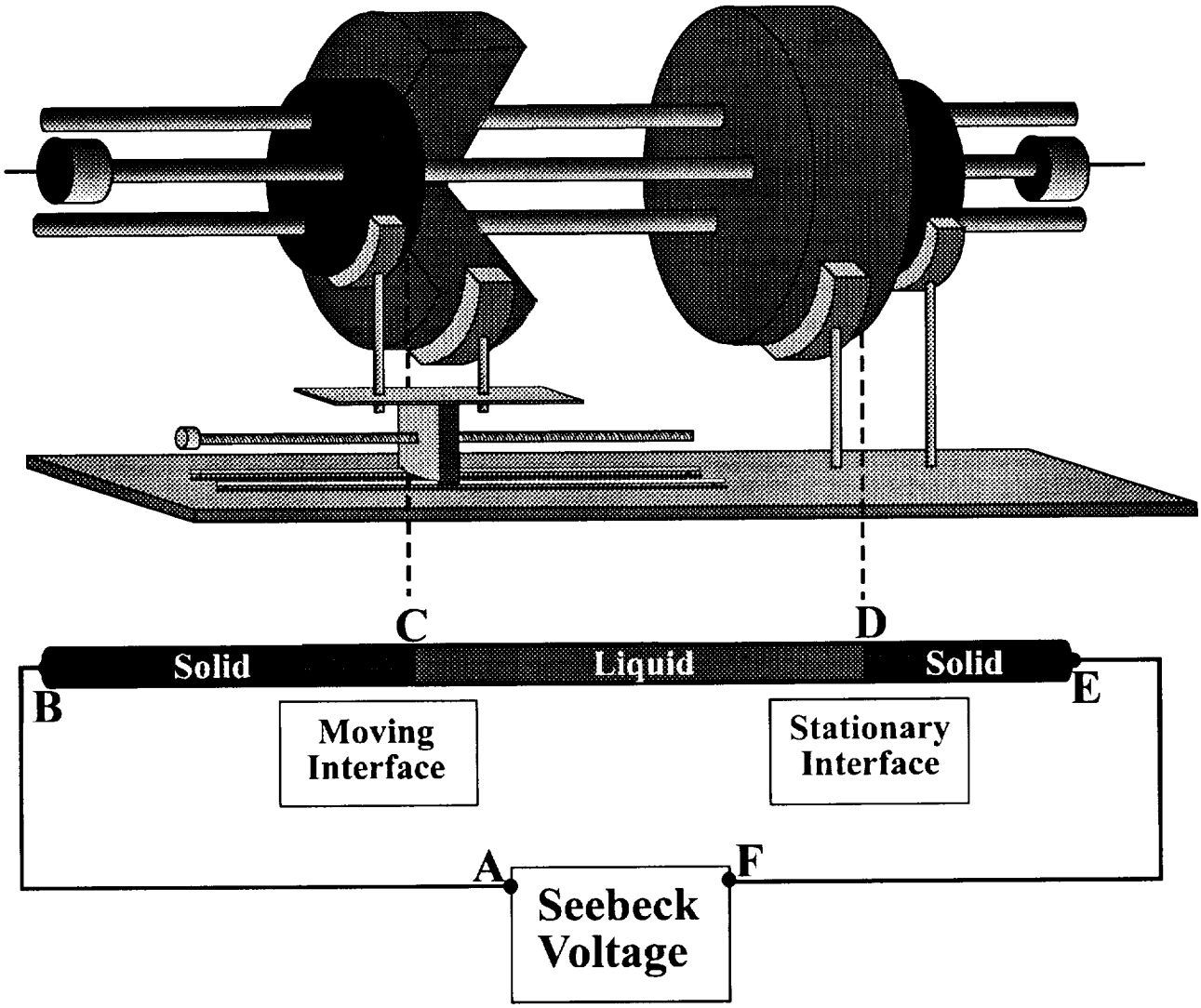

Figure 1. MEPHISTO Apparatus is shown with two furnace/heat sink structures. The three long cylinders going through the two furnace/heat sink structures are the Quenching, Peltier, and Seebeck Samples. The three samples are subjected to the same temperature field, except the Seebeck sample has additional temperature regulation to match the temperature at its ends. The furnace/heat sink structure on the left can move, causing melting or solidification at the moving solid-liquid interface. In the schematic of the Seebeck sample the ends marked B and E while the sold-liquid interfaces are marked C and D. When solidifying/melting at the moving interface, the temperatures at C and D will not be the same due to compositional and kinetic undercooling/superheating.

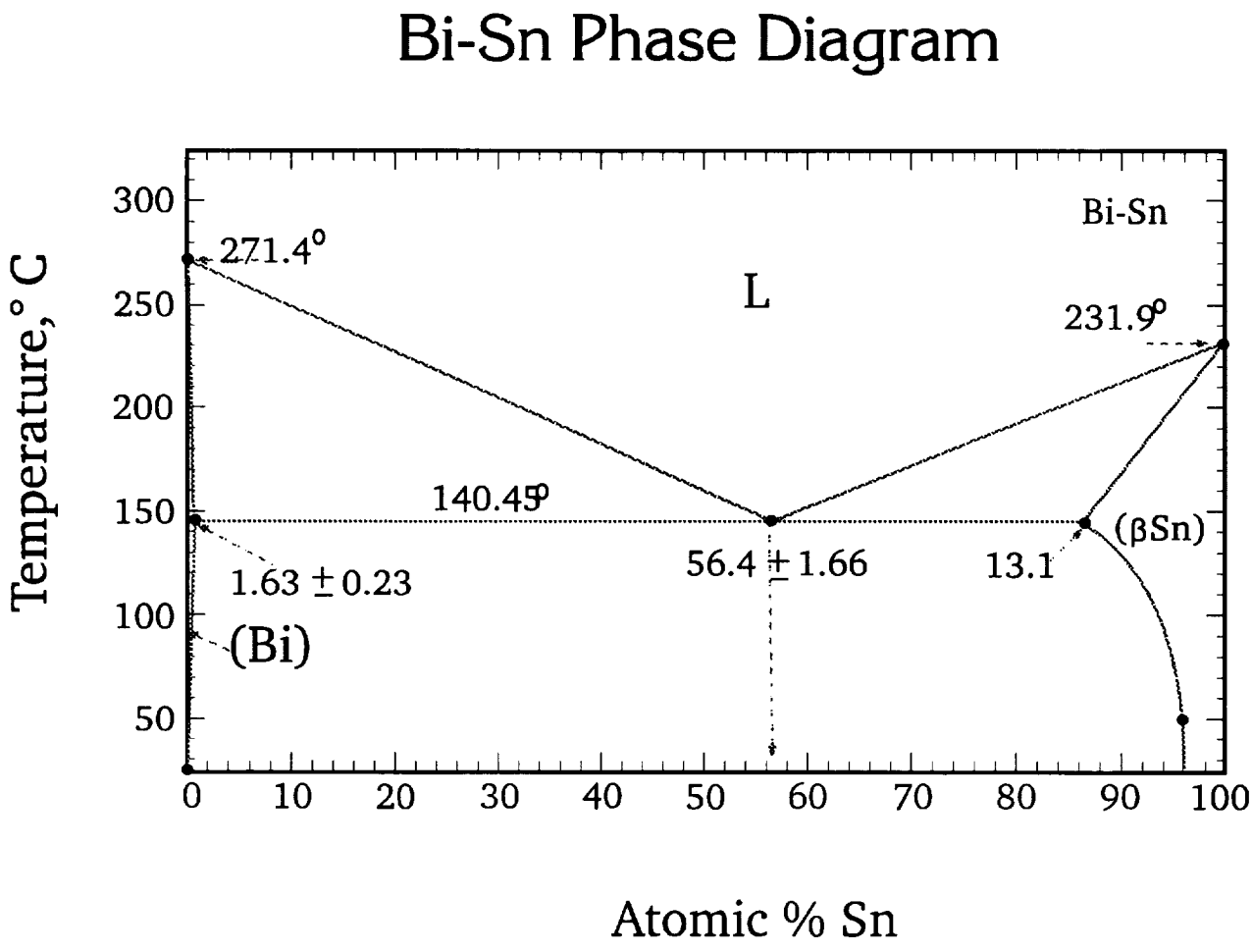

Figure 2. Phase Diagram for the bismuth-tin system.

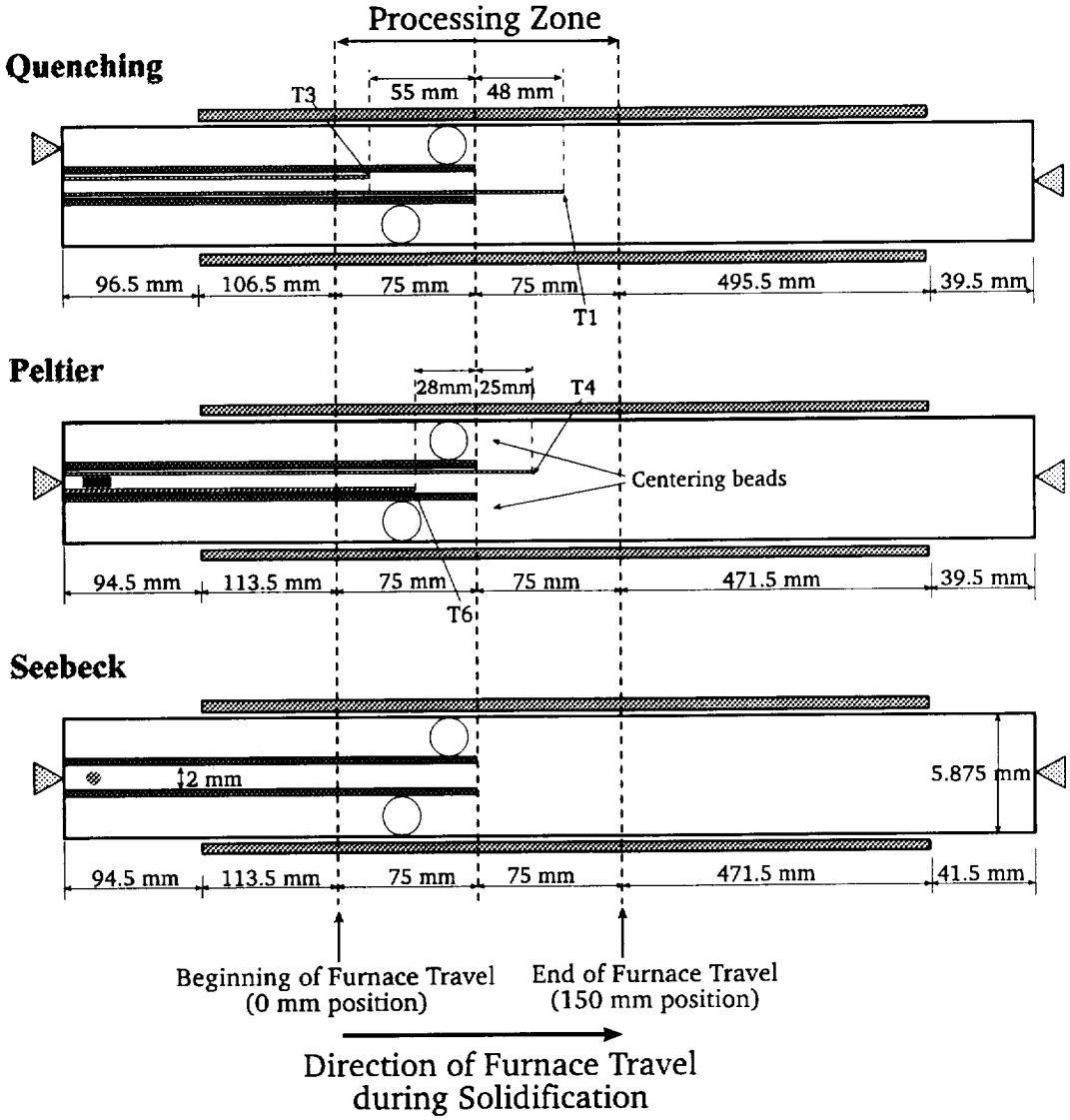

Figure 3. Configurations for the Quenching, Peltier, and Seebeck samples. The samples consist of 5.87 mm diameter cylinders of Bi- 1 atomic % Sn alloy which are contained in quartz tubing. The four thermocouples (the Quenching and Peltier each has two) are labeled T1, T3, T4 and T6. The Seebeck capillary is a 2 mm i.d. quartz tube on the left of each sample. The triangles indicate position of electrical contacts. A small cut in the capillary tube for the Peltier sample alloys current to flow in the alloy inside and outside the capillary.

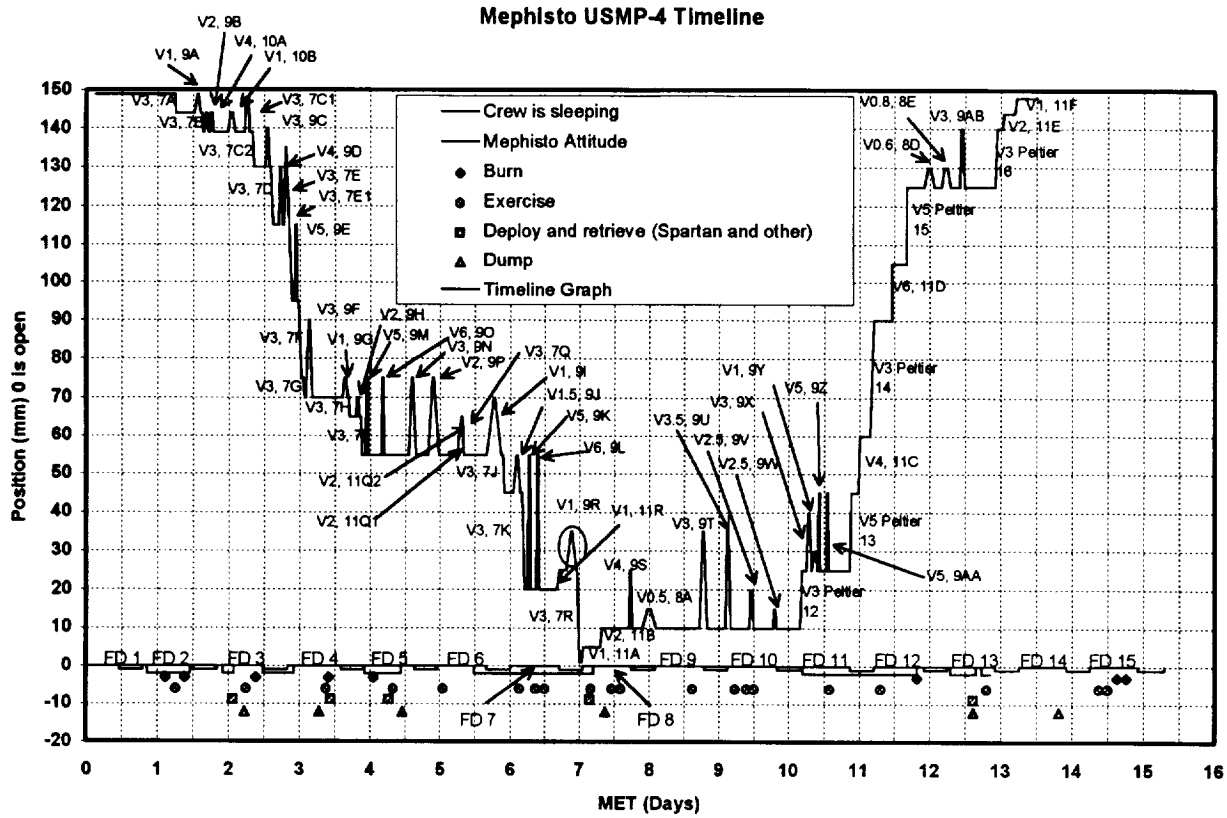

Figure 4. The MEPHISTO moving furnace position as a function of days into USMP-4 mission. The velocities for V0.5, V0.6, V0.8, V1, V1.5, V2, V2.5, V3, V3.5, V4, V5, V6 are 0.74, 1.11, 1.48, 1.85, 2.59, 3.7, 5.2, 6.7, 10, 13.3, 26.7 and 40 μm/s respectively.

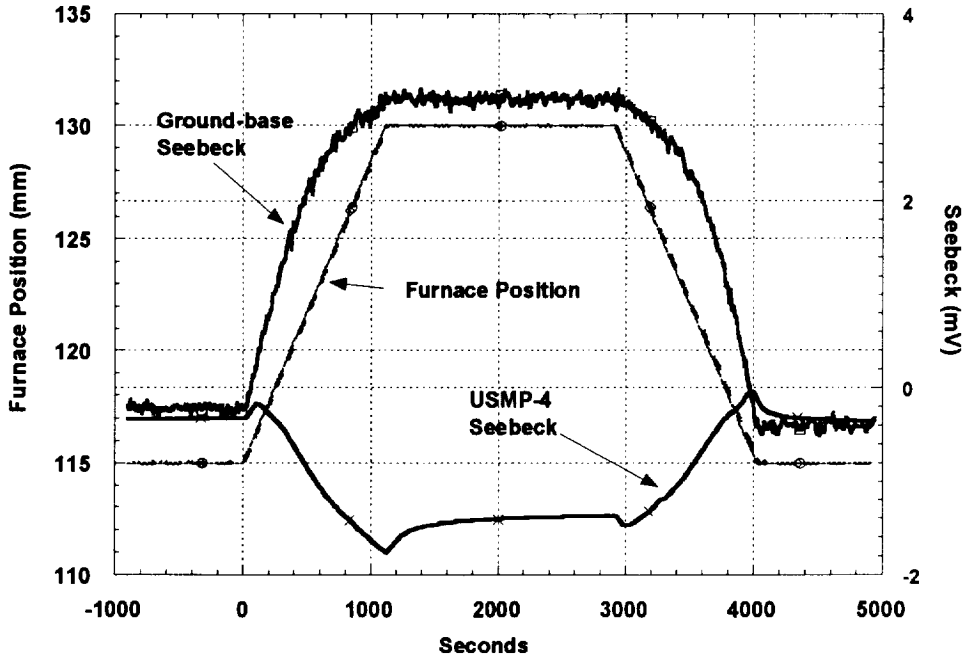

Figure 5. Seebeck signal and position for ground- and space-based experiments for solidification at 13.5 μm/s. The moving furnace position as a function of time into the experiment is very similar for the two experiments. The ground-based experiments have noticeable fluctuations in the Seebeck signal, presumably from hydrodynamic mixing in the melt.

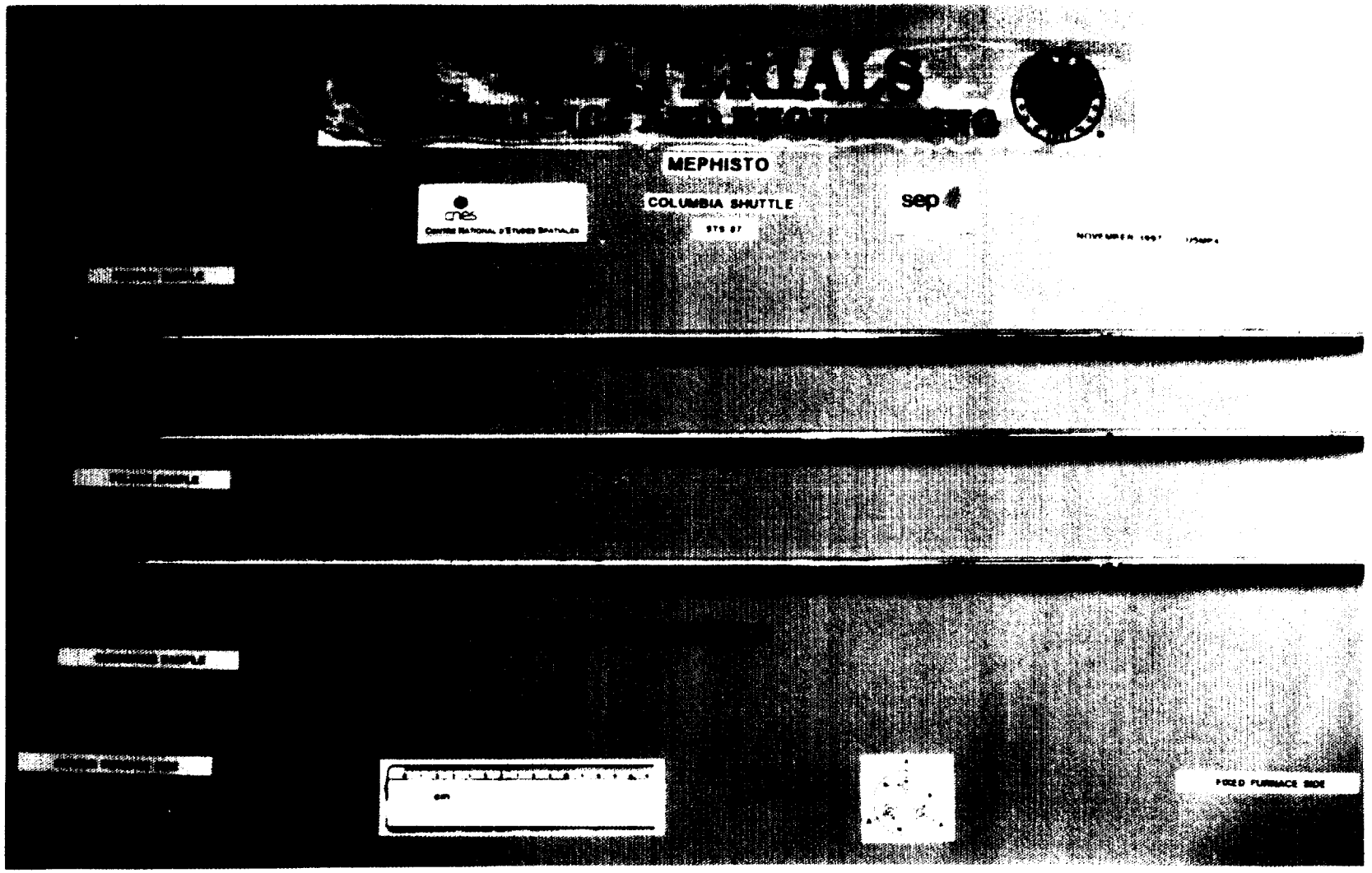

Figure 6. Post-mission photos of Seebeck, Peltier, and Quench samples.

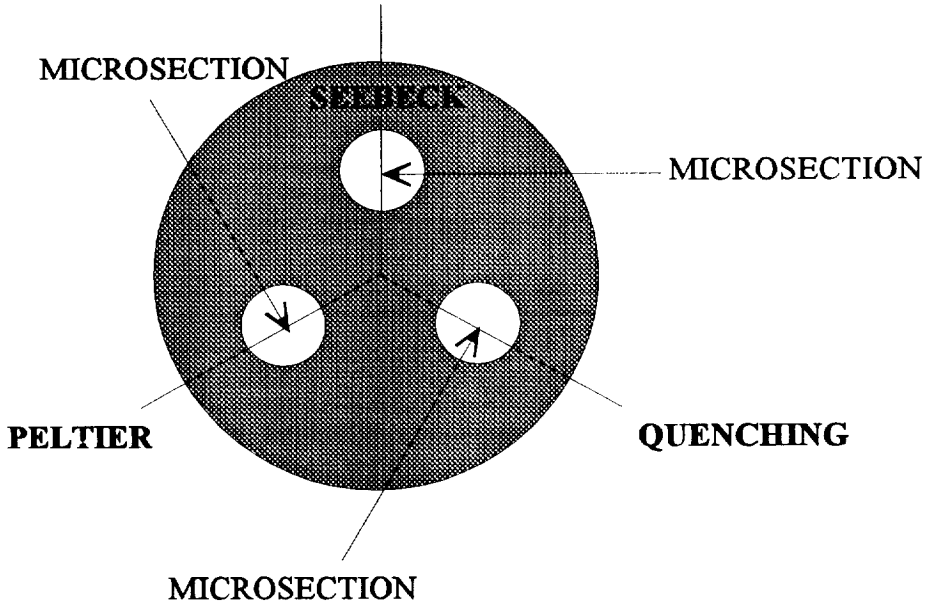

Figure 7. Orientation of microsections of the samples are taken in a direction pointing to the diffuser center and thus thermally equivalent.

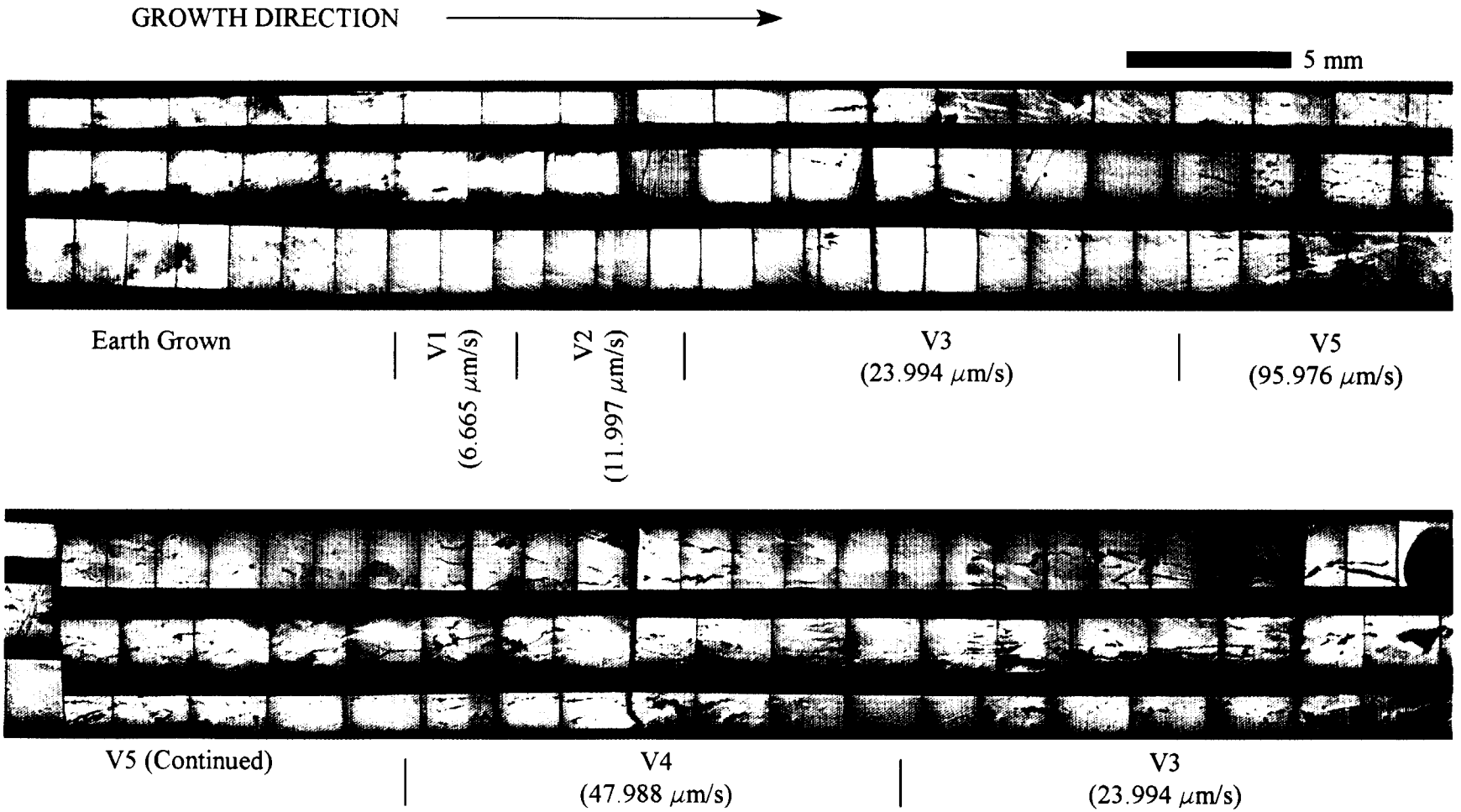

Figure 8a. - Microstructural evolution of the Seebeck sample from the earth grown material to growth in the capillary section.

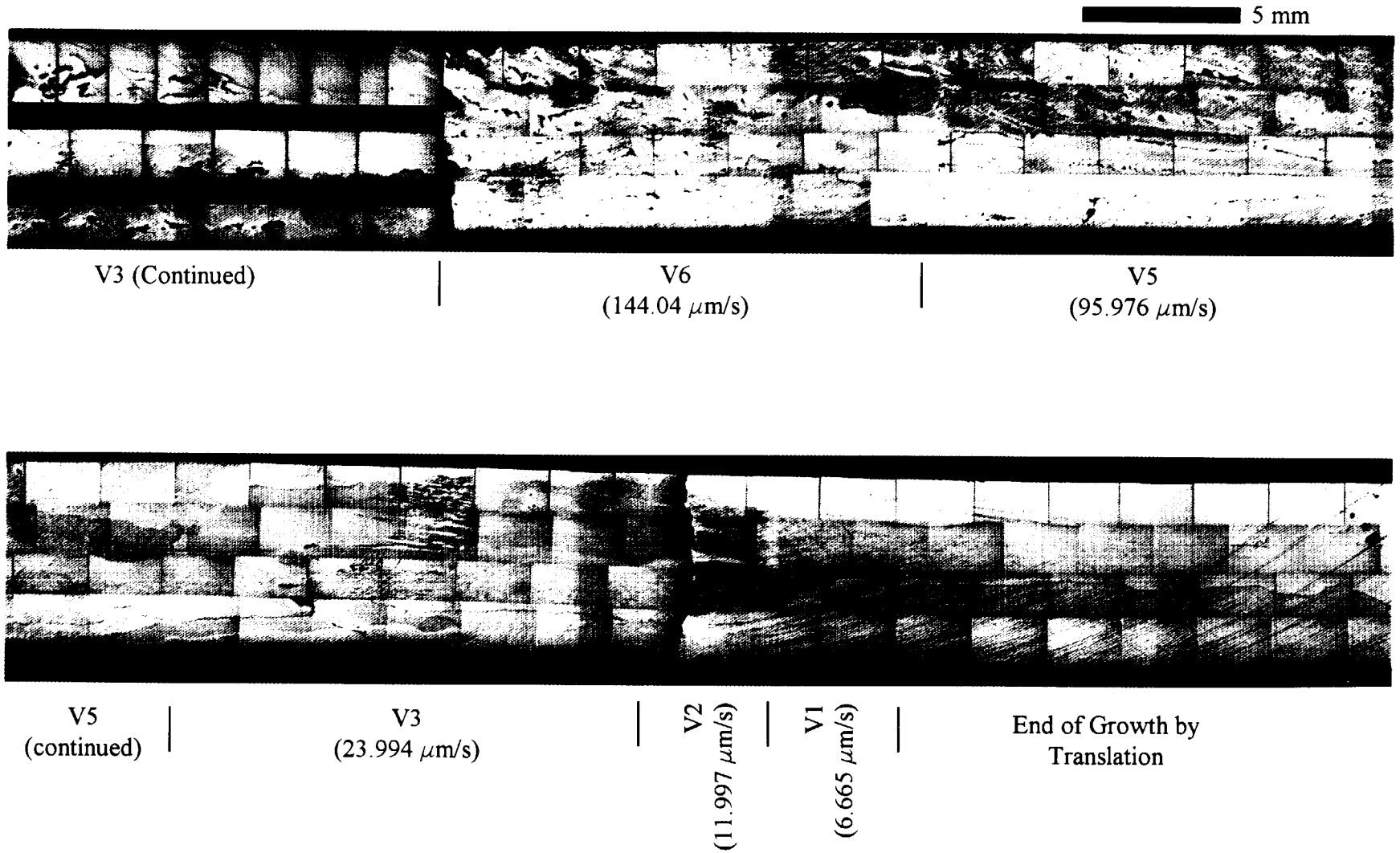

Figure 8b. Continued microstructure of the Seebeck sample extending into the section outside the capillary and finishing in the region where translation finished.

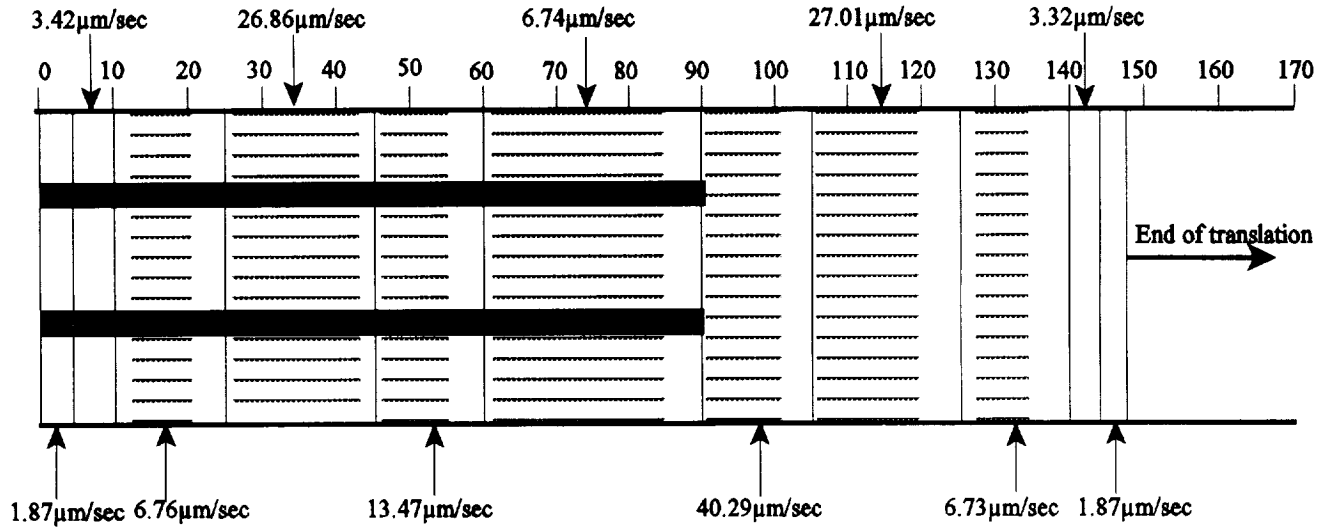

Figure 9: Summary of sample sections preserved during final solidification. Sections with horizontal lines indicate cellular breakdown.

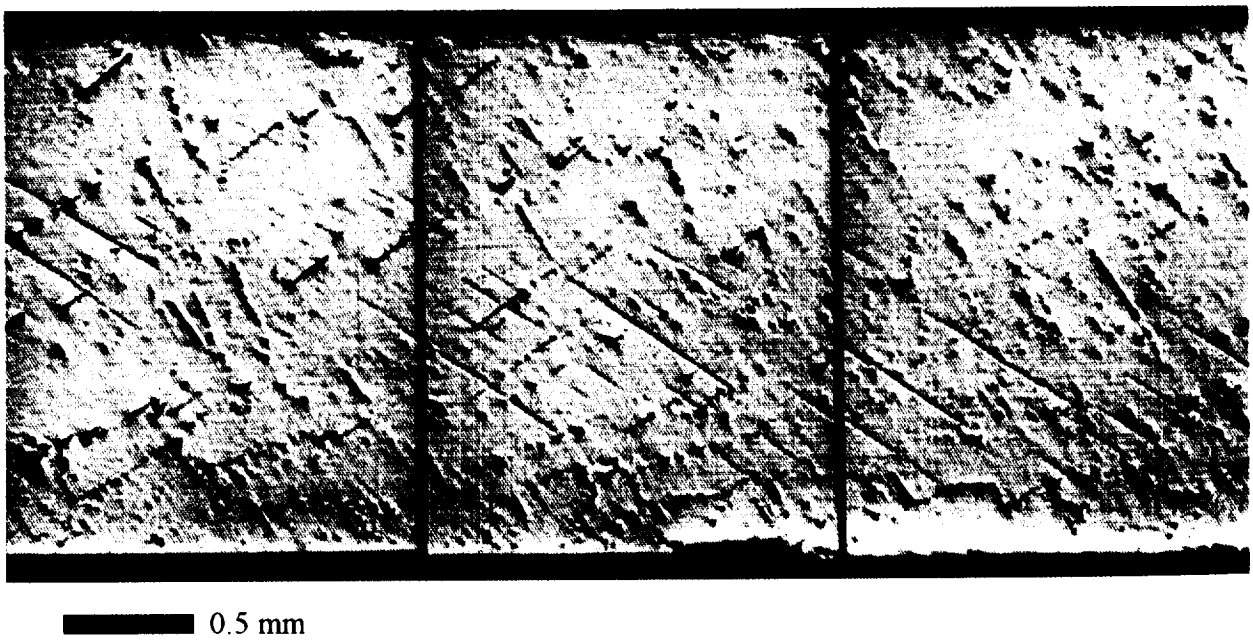

Figure 10. Detail of Earth-grown section showing a faceted cellular/dendritic structure.

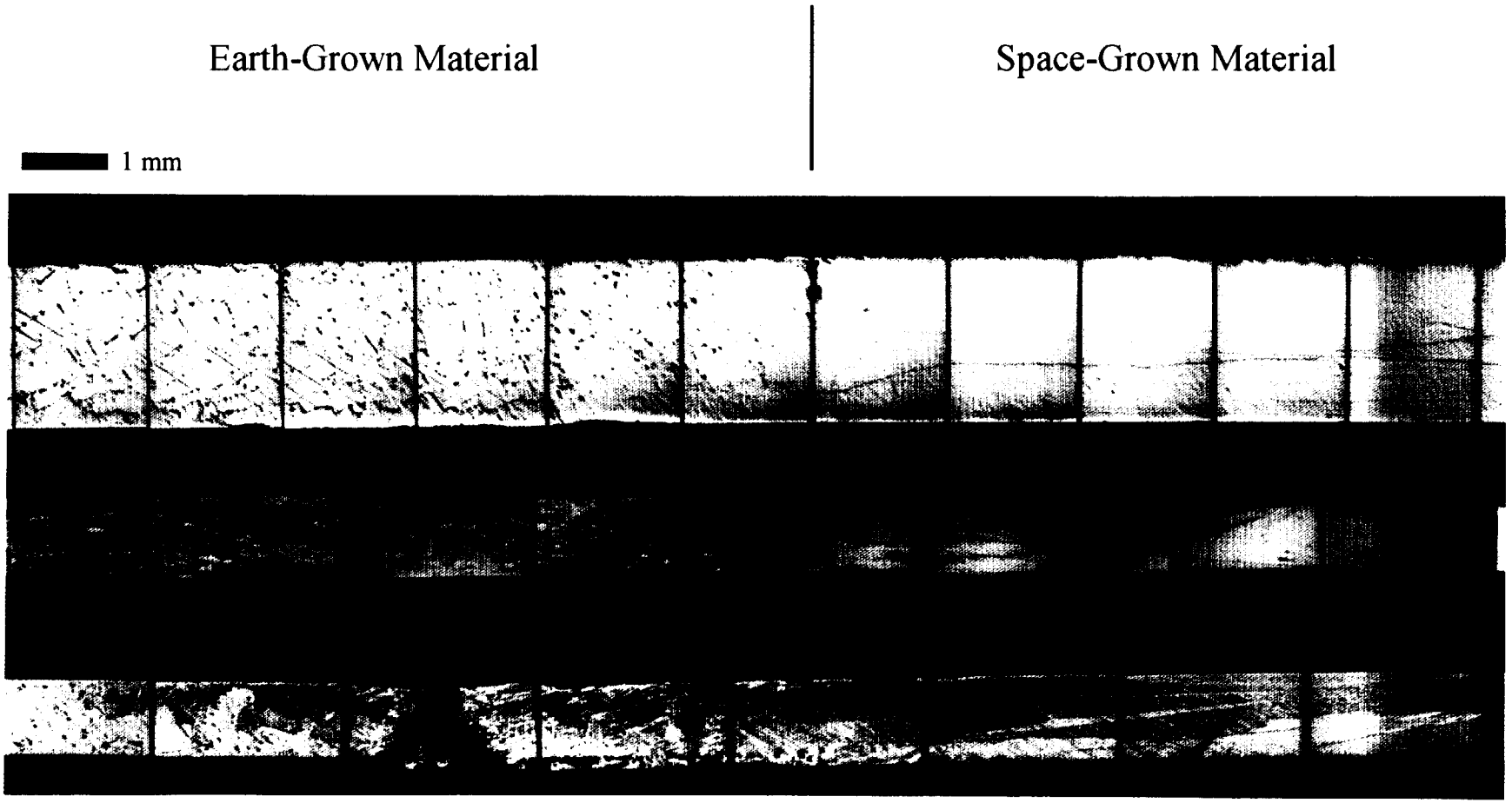

Figure 11a. Composite image of the initial growth of the quench sample. The initial Earth-grown structure on the left hand side shows a faceted cellular/dendritic morphology. The transition to plane-front growth is visible in the space-grown material on the right hand side.

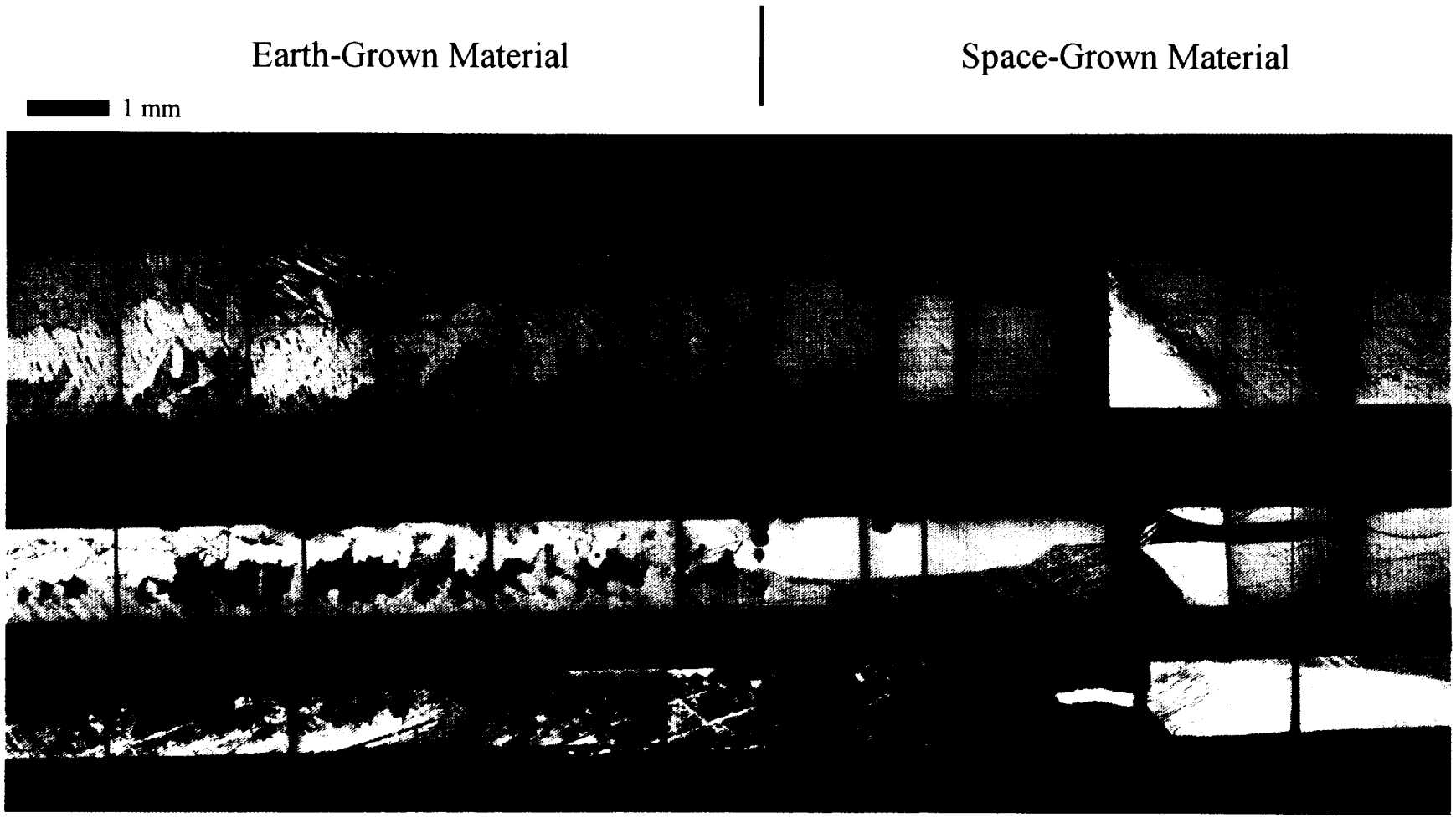

Figure 11b. Composite image of the initial growth of the Peltier sample showing a similar structure to the quench sample. The break in the micrograph is where the sample was cross sectioned.

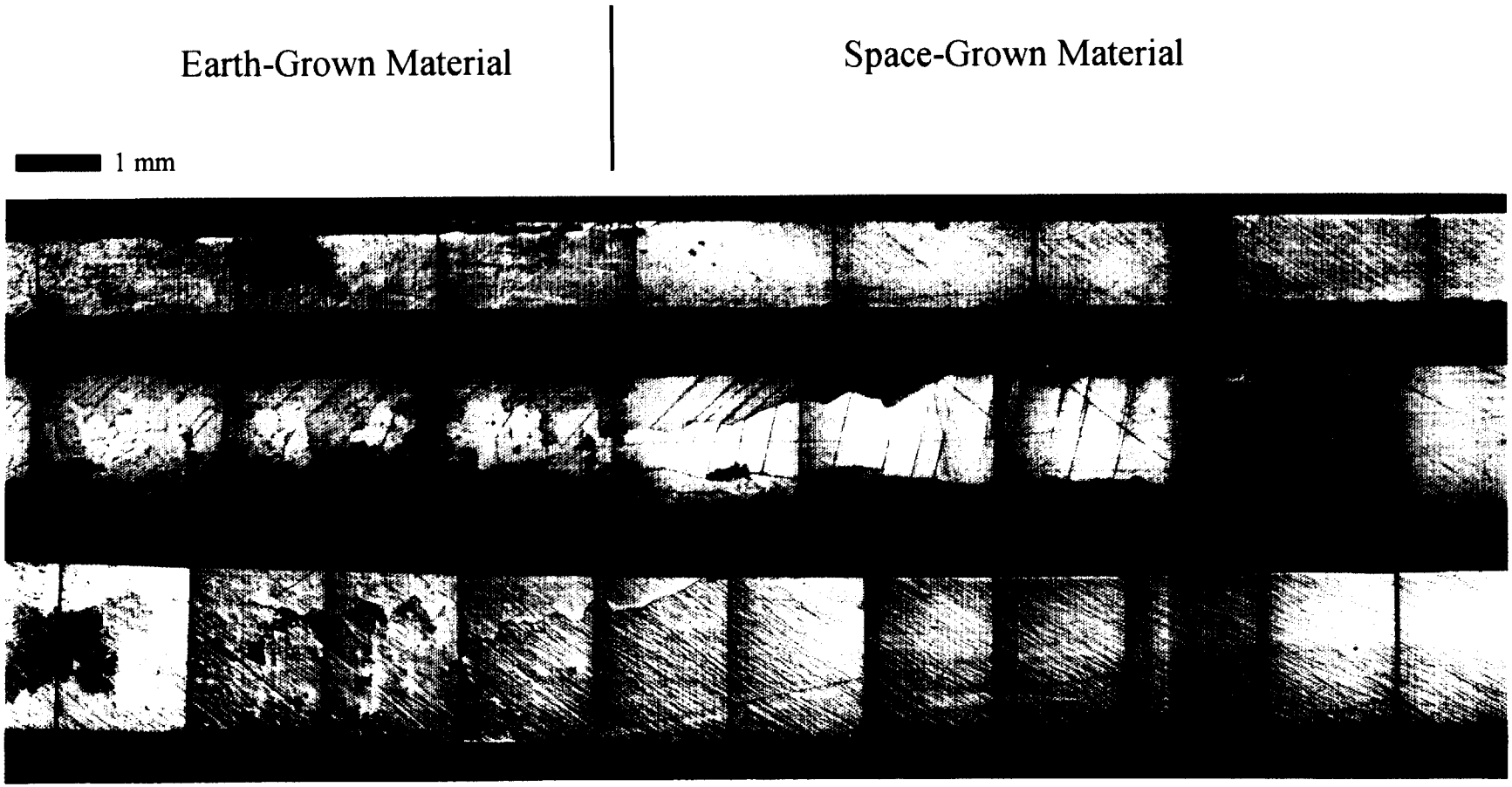

Figure 11c. Composite image of the initial growth of the Seebeck sample showing a similar structure to the previous samples. Twins are visible in the capillary section.

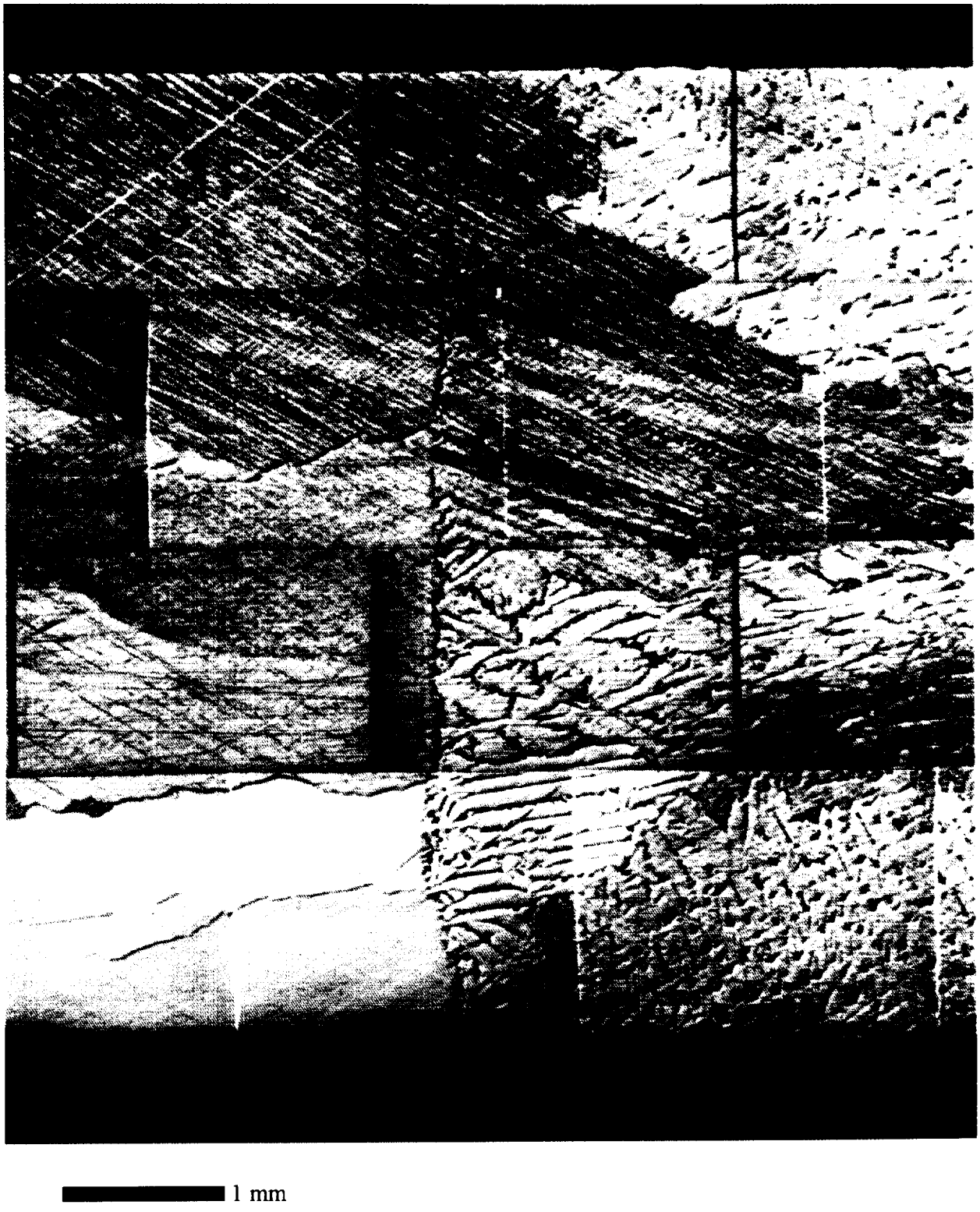

Figure 12. Composite micrograph of quenched section of the quench sample showing the S/L interface shape.

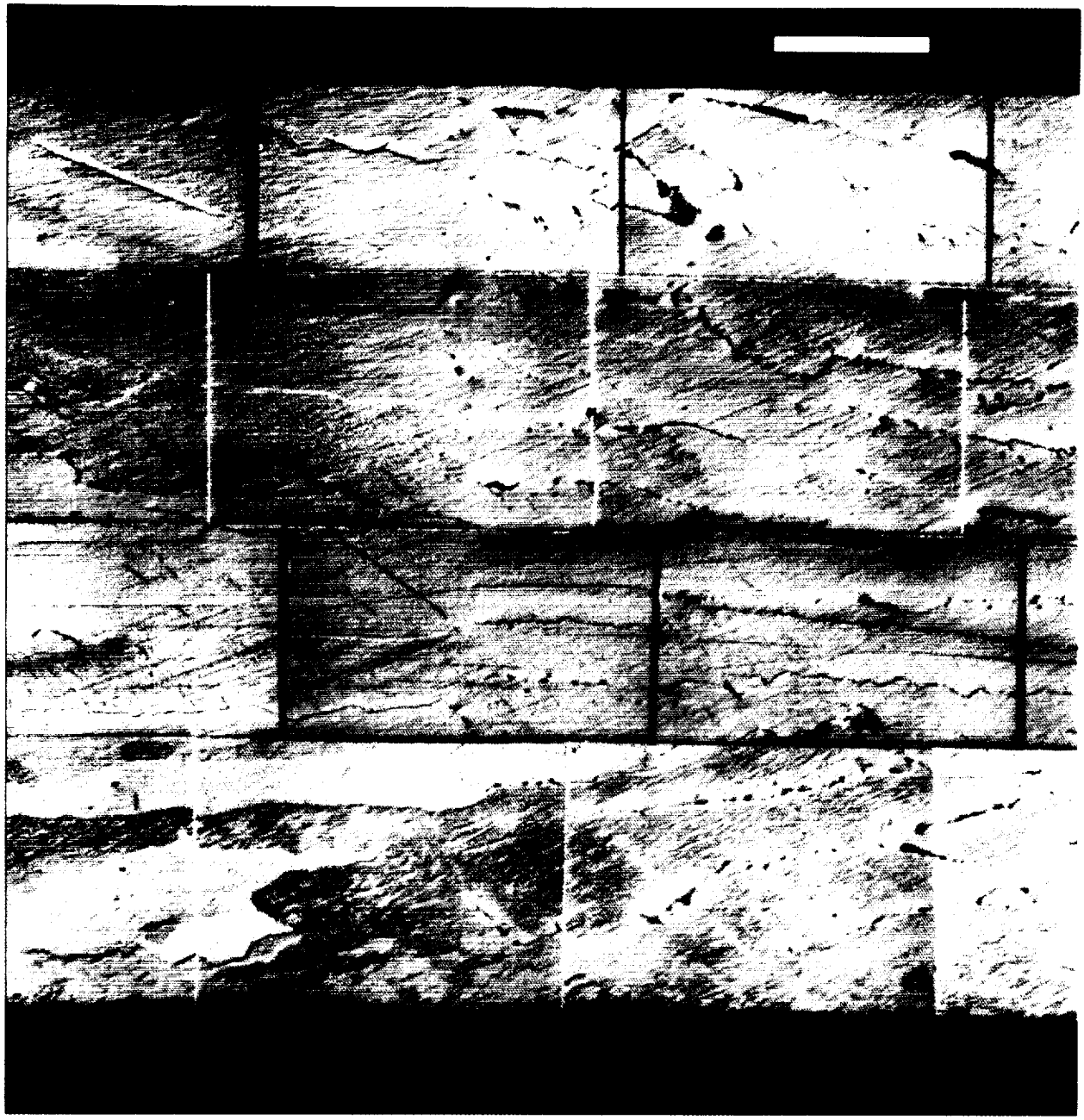

Figure 13. Detail of Peltier sample showing a V5 Breakdown outside of the capillary region.

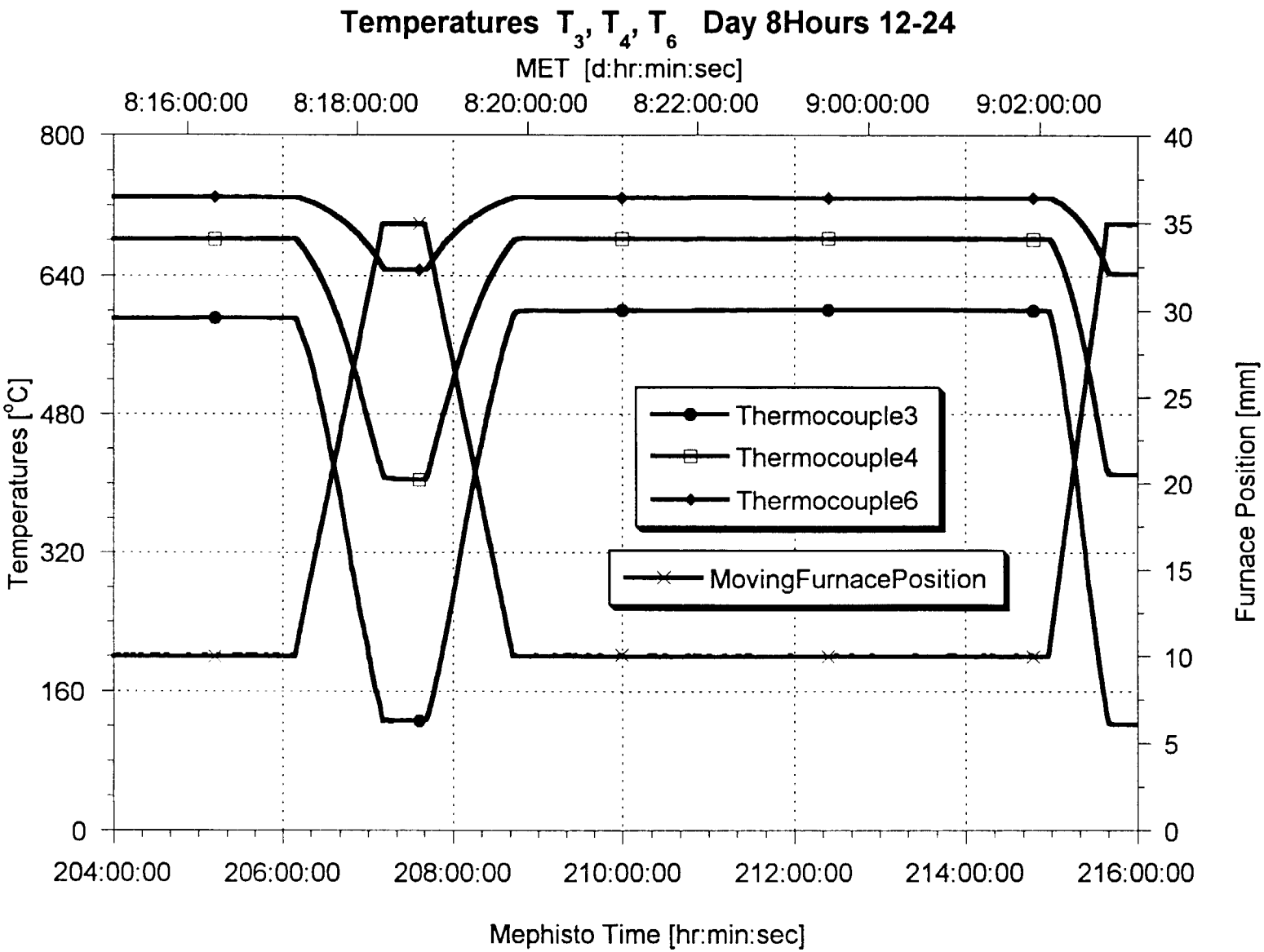

Figure 14. Thermal measurement by the three thermocouples.

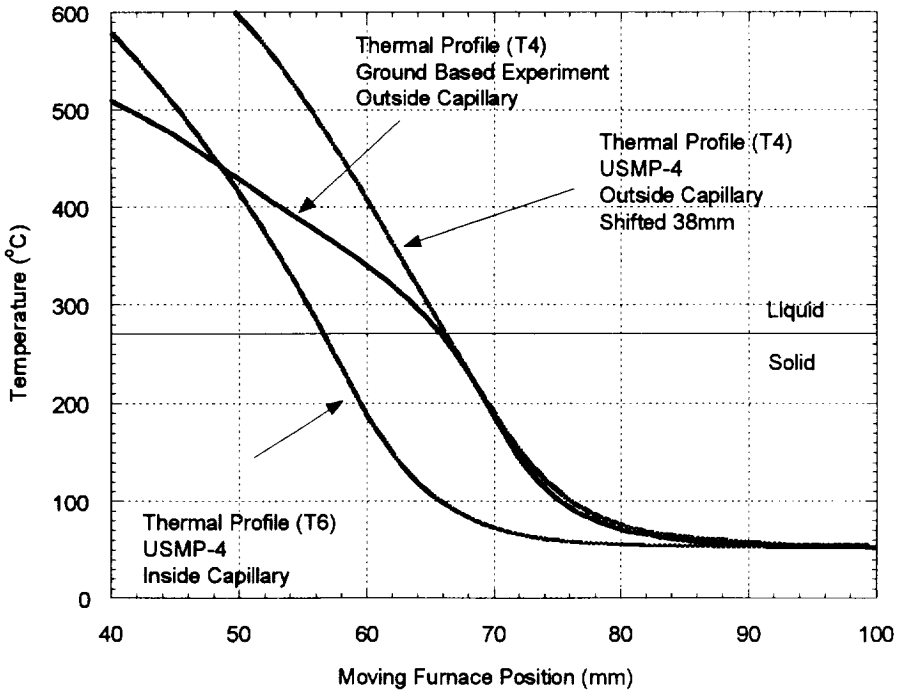

Figure 15: MEPHISTO thermal profile for ground and space based mission. Above the melting point of the liquid the temperature gradient for the ground-based experiments is significantly lower indicating convection. The profile is very similar inside and outside capillary on space-based experiments.

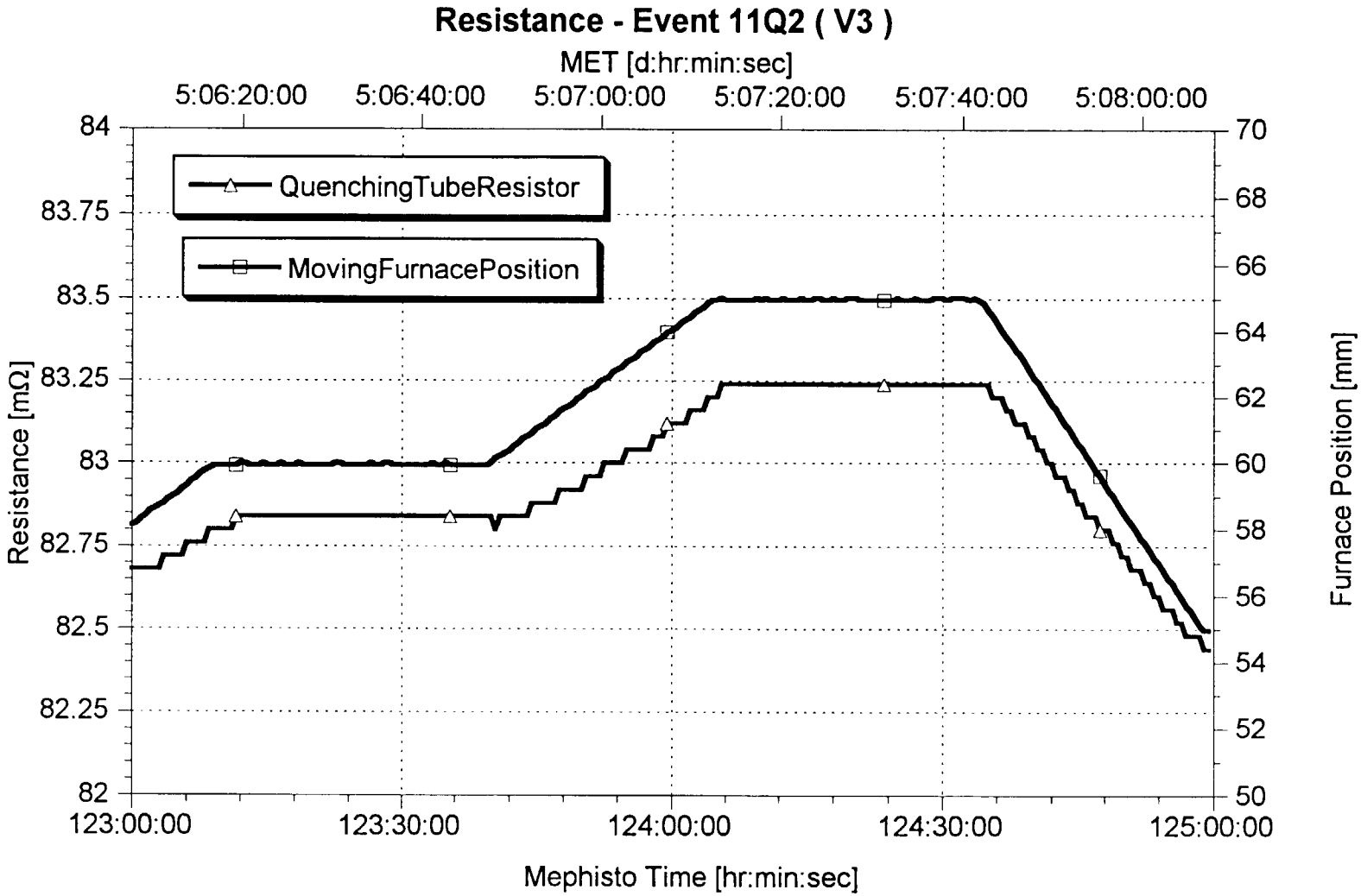

Figure 16. Resistance and furnace position change as a function of processing time during e vent 11Q2 in MEPHISTO experiment.

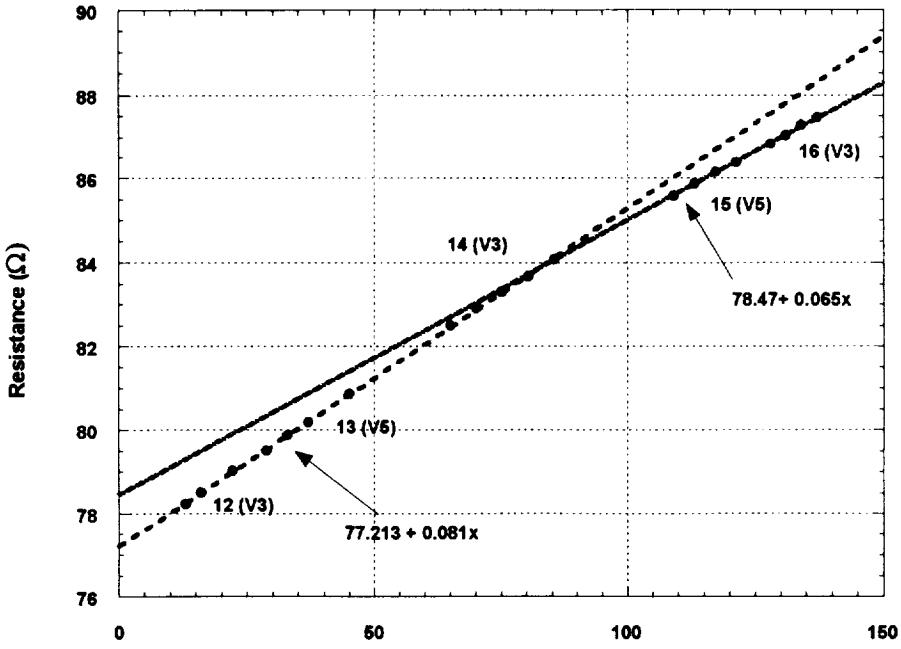

Figure 17: Resistance of Sample versus furnace Position. Crossing of lines is evidence of the end of capillary.

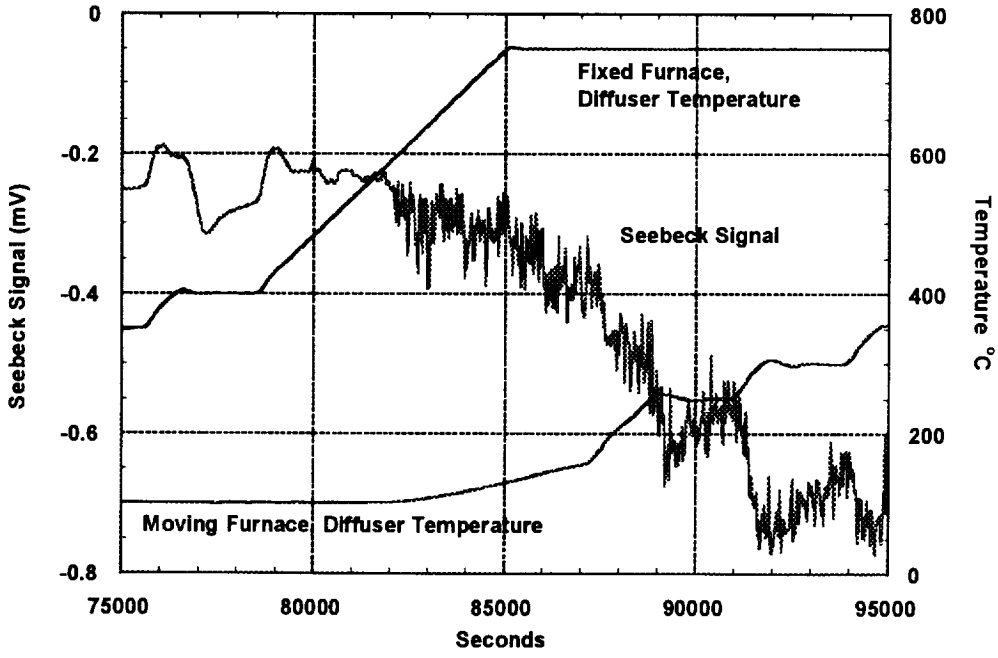

Figure 18: Diffuser temperatures for MEPHISTO furnaces and Seebeck signal during heat-up for ground-based experiments. Fluctuations in the Seebeck signal become apparent as the temperature of the liquid is increased from 400°C to 750°C.

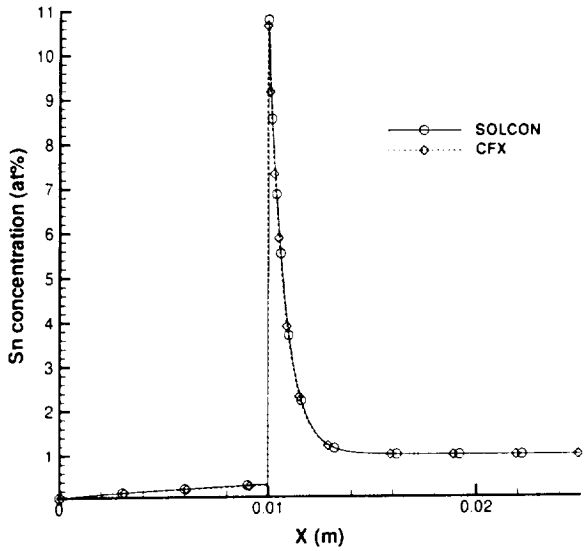

Figure 19. Distribution of solute concentration at the mid-height of the ampoule after 3000 sec of solidification.

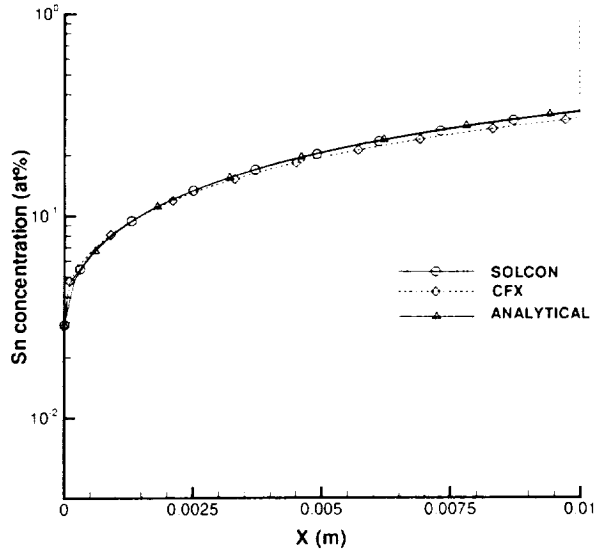

Figure 20. Detailed distribution of solute concentration in the solid part of the sample after 3000 sec of solidification.

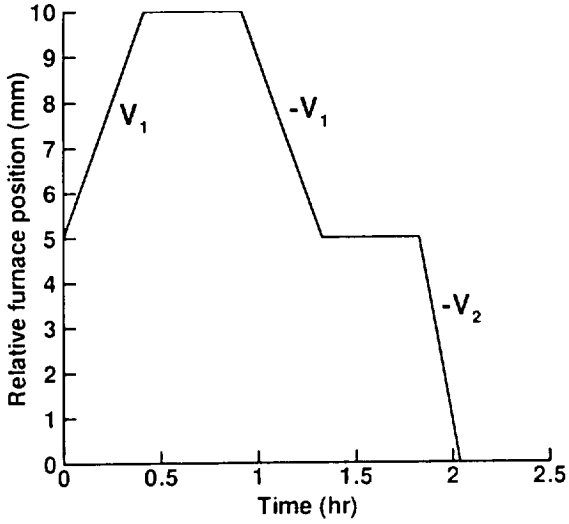

Figure 21. Furnace position as a function of time. V_1 is the furnace velocity during solidification. $-V_1$ and $-V_2$.

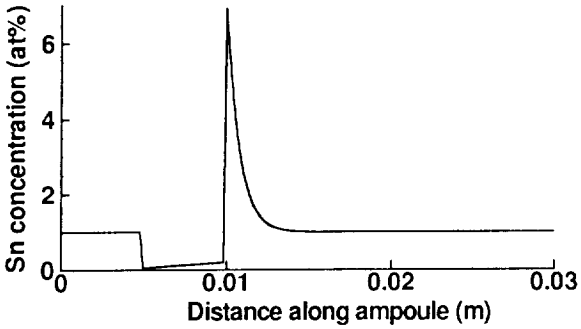

Figure 22. Solute concentration along the mid-height of the ampoule after solidification of 5 mm of liquid at $V_l = 3.34\ \mu m\ s^{-1}$.

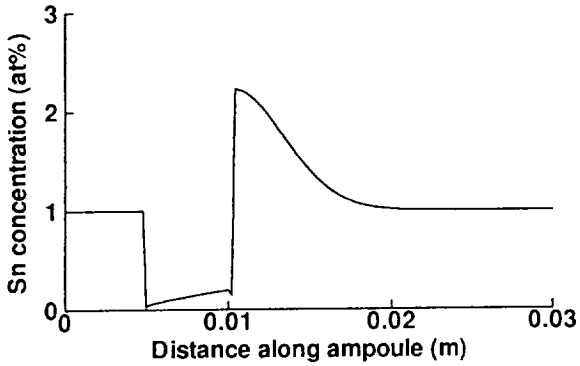

Figure 23. Solute concentration along the mid-height of the ampoule following the first 30 min hold.

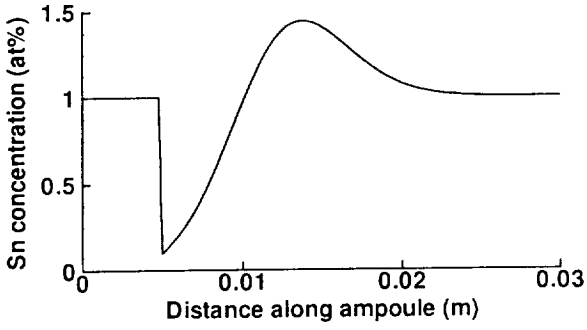

Figure 24. Solute concentration along the mid-height of the ampoule after 5 mm of solid has been melted at $V_l = -3.34\ \mu m\ s^{-1}$.

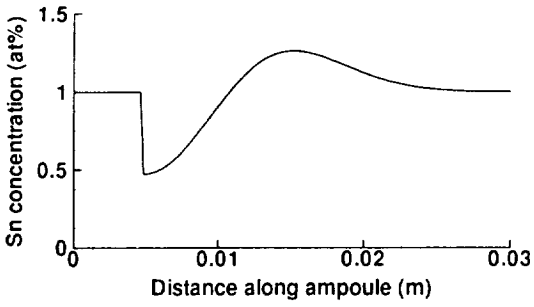

Figure 25. Solute concentration along the mid-height of the ampoule following the second 30 min hold.

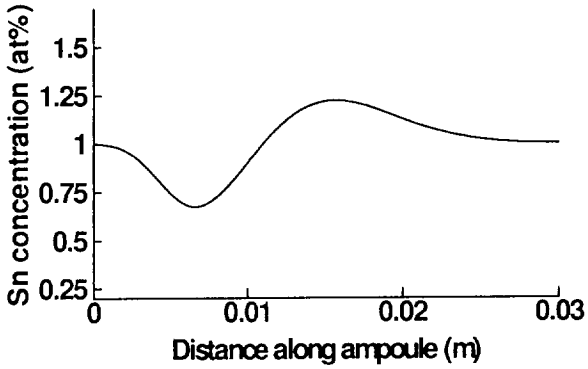

Figure 26. Solute concentration along the mid-height of the ampoule after a further 5 mm of solid has been melted at $V_2 = -6.6\ \mu m\ s^{-1}$.

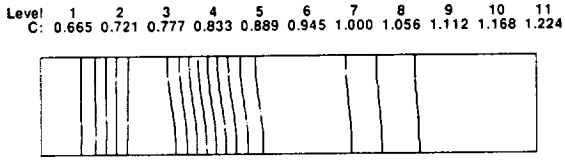

Figure 27. Contours of concentration in the ampoule at the same time as for figure 26, showing evidence of transverse (radial) segregation.

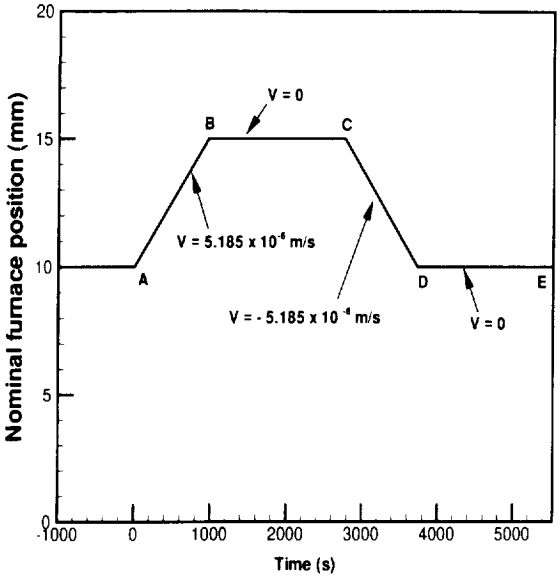

Figure 28. Timeline for the event 9W.

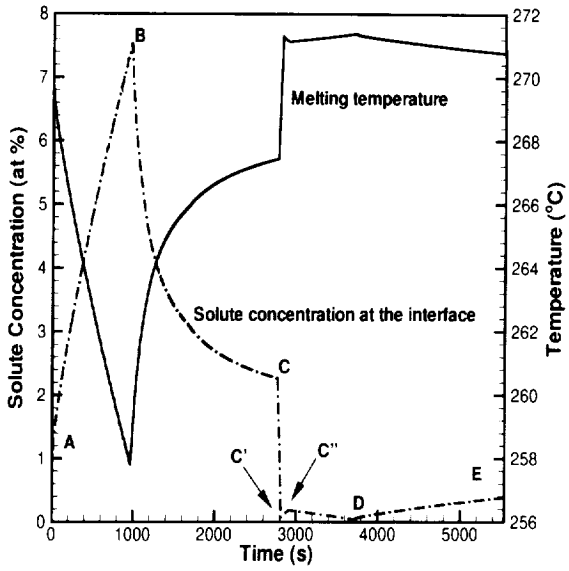

Figure 30. Interface solute concentration ai melting temperature at the mid-height of tl ampoule.

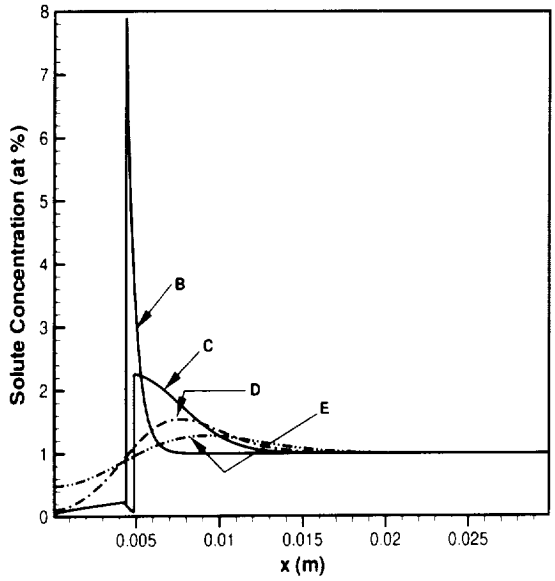

Figure 29. Solute concentration along the horizontal centreline of the ampoule at four different stages of the event.

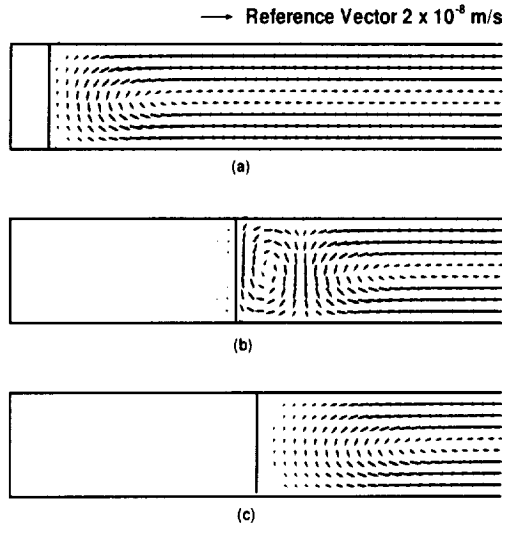

Figure 31. Velocity vectors. (a) early in the solidification; (b) at the end of the solidification; (c) during the first rehomogenization

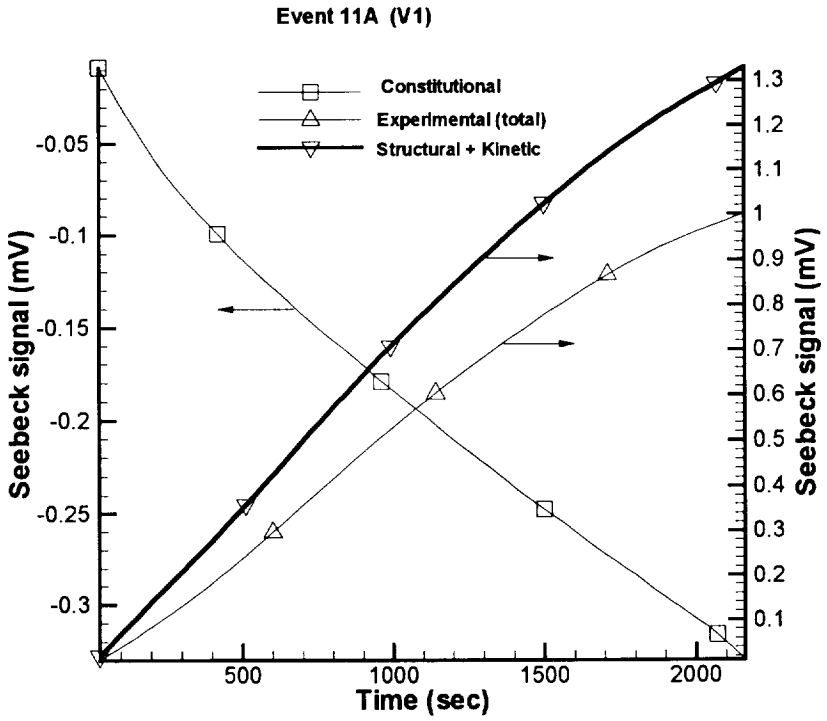

Figure 32. Evaluation on the structural plus kinetic component of the Seebeck signal, for event 11A (pulling velocity V1 = 1.851 μm s^{-1}).

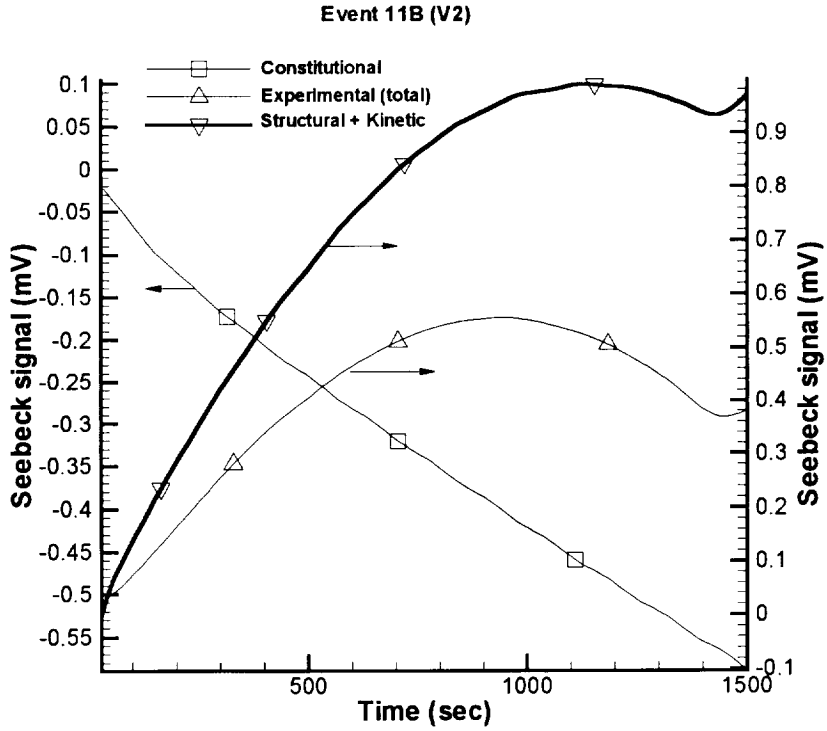

Figure 33. Evaluation on the structural plus kinetic component of the Seebeck signal, for event 11B (pulling velocity V2= 3.34 μm s^{-1})

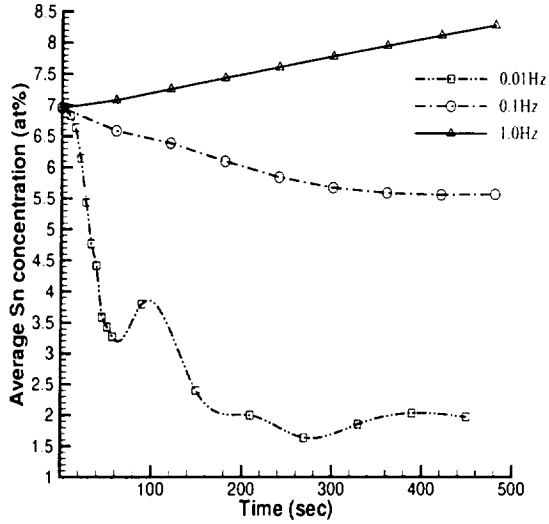

Figure 34. Average concentration at the interface for the disturbances with an amplitude of 10^{-2}g and frequencies of 10^{-2}, 10^{-1} and 1 Hz.

INFLUENCE OF BUOYANT CONVECTION ON THE STABILITY OF ENCLOSED LAMINAR FLAMES

John E. Brooker[1], Kezhong Jia[2], Dennis P. Stocker[1], Lea-Der Chen[2]

[1]NASA Lewis Research Center
Mail Stop 500-115, 21000 Brookpark Road
Cleveland, OH 44135

[2]Department of Mechanical Engineering
The University of Iowa
Iowa City, IA 52242

ABSTRACT

An investigation of the stability limits of Enclosed Laminar Flames (ELF) was conducted in the Middeck Glovebox (MGBX) facility on the STS-87 Space Shuttle mission (November to December 1997). The primary objective of the ELF glovebox investigation is to determine the effect of buoyancy on the stability of round, laminar, gas-jet diffusion flames in a co-flow air duct. Comparison tests were conducted in normal gravity to allow isolation and identification of the influence of buoyancy. The results were used to map the lift-off and blow-out stability limits as a function of the fuel and air velocities for the two buoyancy conditions. Approximately 50 tests were conducted during the Space Shuttle mission, using a 50/50 mixture (volume basis) of methane and nitrogen as the fuel. The experimental results verified the hypothesis that substantially greater velocities are required to destabilize the flame in microgravity. The increase in air velocity required to induce lift off in microgravity (compared to normal gravity) was nearly equal to the increase required to induce blow out. Furthermore, the air velocity increase was relatively independent of the fuel flow, except at low fuel flows. At high fuel flows, it was found that the microgravity flames tend to immediately blow out after lift off. This is in agreement with the free-jet theory of Chung and Lee [1], which suggests that stable lifted flames are not possible for fuels with a Schmidt number of $0.5<Sc<1$, such as the diluted methane used in this study. However, stable lifted flames were observed in microgravity at low fuel flows, and in normal gravity, despite the fuel's low Schmidt number. The discrepancy between the experimental data and the theory of Chung and Lee is presumably due to the differences in the flow condition; namely, the ducted flow versus a free jet, and a non-similar velocity profile versus a self-similar profile.

SECTION I. Introduction

Enclosed diffusion flames are commonly found in practical combustion systems, such as the power-plant combustor, gas turbine combustor, and jet engine after-burner. In these systems, fuel is injected into a duct with a co-flowing or cross-flowing air stream. The diffusion flame is found at the surface where the fuel jet and oxygen meet, react, and consume each other. In combustors, this flame is anchored at the burner (i.e., fuel jet inlet) unless adverse conditions cause the flame to lift off or blow out. Investigations of burner stability study the lift off, reattachment, and blow out of the flame.

Flame stability is strongly dependent on the fuel jet velocity. When the fuel jet velocity is sufficiently low, the diffusion flame anchors at the burner rim. When the fuel jet velocity is increased, the flame base gradually moves downstream. However, when the fuel jet velocity increases beyond a critical value, the flame base abruptly jumps downstream. When this "jump" occurs, the flame is said to have reached its lift-off condition and the critical fuel jet velocity is called the lift-off velocity. While lifted, the flame is not attached to the burner and it appears to float in mid-air. Flow conditions are such that the flame cannot be maintained at the burner rim despite the presence of both fuel and oxygen. When the fuel jet velocity is further increased, the flame will eventually extinguish at its blow-out condition. In contrast, if the fuel jet velocity of a lifted flame is reduced, the flame base moves upstream and abruptly returns to anchor at the burner rim. The fuel jet velocity at reattachment can be much lower than that at lift off, illustrating the hysteresis effect present in flame stability, e.g., previously investigated by Gollahalli et al. [2].

Although there have been numerous studies of flame stability [1-14], the mechanisms controlling it are not well understood. This uncertainty is described by Pitts [3] in his review of various competing theories of lift off and blow out in turbulent jet diffusion flames. There has been some research on the stability of laminar flames [1,4-5], but most studies have focused on turbulent flames [2-3,6-14]. Whatever the jet condition, relatively few studies have investigated the stability of flames with an oxidizer co-flow [6-8], compared with the number of studies on (nearly) free jet diffusion flames [1-5,9-14].

The air flow around the fuel jet can significantly alter the lift off, reattachment and blow out of the jet diffusion flame. The importance of the air velocity on blow out has been clearly demonstrated by Feikema et al. [7-8], both with and without swirl. In normal gravity, however, the effects of the air flow on flame stability are often complicated by the presence of buoyant convection. Buoyant convection is sufficiently strong in normal-gravity flames that it can dominate the flow-field, even at the burner rim. In normal-gravity testing, it is very difficult to delineate the effects of the forced air flow from those of the buoyancy-induced flow. However, a comparison of normal-gravity and microgravity flames provides clear indication of the influence of forced and buoyant flows on the flame stability.

The overall goal of the Enclosed Laminar Flames (ELF) research, described at the following URL site:

http://zeta.lerc.nasa.gov/expr/elf.htm

is to improve our understanding of the effects of buoyant convection on the structure and stability of co-flow diffusion flames. The experiment discussed within this paper investigates the influence of buoyancy on flame stability, and specifically its effect on the velocities at lift off, reattachment, and blow out. The analysis and interpretation of the results is simplified by limiting the study to round,

laminar gas-jet diffusion flames in a co-flow duct. In other words, the cylindrical Burke-Schumann [15] diffusion flame was used as the model flame in this study. Although flames in practical combustors are generally turbulent, they are often laminar at the base. This study is also relevant to practical systems because the momentum-dominated behavior of turbulent flames can be achieved in laminar flames in microgravity.

SECTION II. Experiment

The ELF hardware was designed and built to accommodate microgravity testing within the Middeck Glovebox (MGBX) facility. This facility, described at:

http://liftoff.msfc.nasa.gov/shuttle/usmp4/science/mgbx1.html

has been used to conduct a variety of small and inexpensive experiments on several Space Shuttle missions, and the Russian space station *Mir*. In size, the experiment hardware is limited by the 35-liter volume of the glovebox working area, and the 180x220-mm dimensions of the main door. The MGBX facility provides electrical power (up to 60 Watts), lighting, video photography and recording, air circulation and filtration, containment, and crew access through a pair of gloveports. The hardware constraints are such that the glovebox experiments generally require significant crew involvement, and are sometimes limited to photography for data acquisition.

The space-flown ELF hardware includes an experiment module (described below), 6 interchangeable fuel bottles, and a parts box, containing a control box, 3 electrical cables, ignitors, a camera shroud, etc.

The experiment module, shown in Figure 1, is a miniature, fan-driven wind tunnel, equipped with a gas supply system. The module is 330x180x180 mm and just fits within the glovebox facility. A 1.5-mm diameter nozzle is located on the duct's flow axis. The cross section of the duct is nominally a 76-mm square with rounded corners. The forced air velocity can be varied from about 0.2 to 0.9 m/s, and is measured with a fixed hot-element anemometer. Honeycomb and screens are used to eliminate the fan-induced swirl, which can strongly influence the flame stability [7-8]. The fuel flow is established by a fixed pressure regulator and a mass flow controller. The fuel flow can be set as high as 3 std. cubic centimeter (cc) per second, which corresponds to a nozzle exit velocity of up to 1.70 m/s. The flame is ignited with a replaceable hot-wire ignitor, which is manually rotated to the nozzle exit. The duct is equipped with a manually-positionable rake, instrumented with 5 type-R thermocouples and 25 silicon carbide fibers (not shown in Figure 1). The fuel flow, fan voltage, air velocity, rake position, and two temperatures are displayed on the module front for operator viewing and video recording.

Each fuel bottle consists of a 75-cc bottle, equipped with a diaphragm-type hand valve and a quick-connect for attachment to the ELF module. Multiple bottles are used to limit the amount of fuel within the glovebox. The bottles are filled to 2.5 MPa (or 350 psig) with a 50/50 mixture (volume basis) of methane and nitrogen. Diluted methane is used because (a) the fuel and its combustion products are not toxic, (b) the combustion chemistry is well established, and (c) the flame is (nearly) soot-free. The nitrogen dilution causes a slight decrease in the fuel's Schmidt number compared to that of pure methane. At room temperature and 1 atm, the fuel's Schmidt number is about 0.7, suggesting that the flames may blow out immediately after lift off based on the free-jet study of Chung and Lee [1].

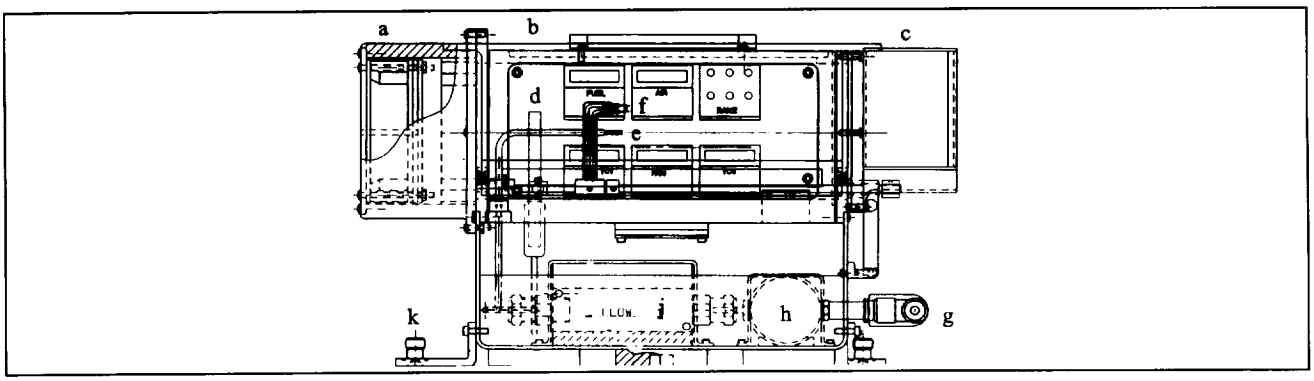

Figure 1. Schematic of ELF Hardware

The primary operational variables are the fuel flow and air velocity. As such, the ELF tests are typically conducted where one velocity is held fixed and the other is varied to determine the velocity at lift off, reattachment, and blow out. Generally, the selected velocity is increased until the flame lifts off, is decreased until it reattaches to the nozzle, and then is increased again until it lifts off and blows out. Both velocities are controlled manually by potentiometers on a control box mounted outside of the glovebox. Therefore, the rate of change for the velocities is directly dependent on the operator. As the "ramp" rate can have a strong effect on the measured stability limits, the astronauts were trained by the ELF Science Team (DPS, JEB, and LDC) on a nearly monthly basis throughout 1997. Despite the training, the results may be somewhat operator dependent. Additional tests were conducted where attached flames were probed with the translating rake, but those temperature results are not reported in this paper.

The microgravity tests were conducted on the STS-87 Space Shuttle mission (November to December 1997). The ELF tests were conducted during two sessions, on flight days 10 and 12 of the 16-day mission. The microgravity results reported in this paper are from the second session only, during which the glovebox was open to the crew cabin via removal of the side doors and airlock port. The cabin pressure was 101.3±0.4 kPa (14.7 ± 0.06 psia), and the oxygen concentration was 21.56 ± 0.23% (with error bars based on instrument resolution).

The normal-gravity comparison tests were conducted without the glovebox, with the module oriented such that the nozzle was pointed upward (i.e., aligned with the gravity vector). The normal-gravity tests were conducted in ambient air, at 98.6±0.3 kPa (14.3 ± 0.05 psia). Although the atmospheric conditions do not match precisely, it is believed that the differences observed between the microgravity and normal-gravity tests are primarily due to buoyant effects. The sensitivity of the stability limits to the atmospheric variations is being investigated numerically and will be reported in a future paper.

SECTION III. Numerical Model

Numerical simulation is performed to study the stability of enclosed laminar flames in microgravity environment. ELF stability results are used to validate the numerical simulation, and numerical simulation results are used to assist the interpretation of the experimental results. The major

assumptions of the mathematical formulation of the numerical model include negligible viscous dissipation, low Mach number, ideal gas, negligible radiative heat transfer, Newtonian fluid and laminar flow. Transport equations for mass, momentum, energy and species in axisymmetric coordinate are considered. The finite-rate chemistry is accounted for by a four-step reduced mechanism, which is based on a 50-step starting mechanism and considers seven species, namely, CH4, H, H2, H2O, CO, CO2 and O2. Steady-state solutions obtained from the flame-sheet model or the one-step reaction model are used as the initial conditions. The flame-sheet model and the one-step reaction calculation assume a still environment and standard state as their initial condition. A symmetric boundary condition is imposed at centerline, and a no-slip, impermeable, and adiabatic condition is applied to the outer wall. At inlet, the fuel and air flow are assumed to be separated by an infinitely-thin wall with Dirichlet boundary conditions. At outflow, a zero second-derivative boundary condition is assigned.

The numerical scheme employs a control-volume discretization method, staggered, non-uniform grids, and semi-implicit fractional step time marching method. The numerical scheme is second-order accurate in spatial discretization and first-order in temporal difference. The first-order time difference scheme has been replaced by a second-order scheme in the recent simulation effort. An explicit scheme is used for the convection and an implicit scheme for the diffusive transport. The flux corrected transport method is applied to convective flux, along with a high-order accurate scheme (Quadratic Upstream Interpolation for Convective Kinematics) to produce monotonic results. The projection method is used to solve the pressure equation.

SECTION IV. Results and Discussion

Analysis of the results has yielded maps of the flame stability under microgravity and normal-gravity conditions, as shown in Figure 2. These maps show the lift-off and blow-out boundaries, as functions of the fuel and air inlet velocities. Discussion of the effects of buoyancy on the flame reattachment and associated hysteresis is left to a future paper. At this time, the stability boundaries were selected based on visual inspection of the video data. Automated image processing and tracking of the flame base position has been attempted to determine the lift-off and reattachment boundaries. However, classical definition of the lift-off condition as an abrupt jump of the flame base is not obvious in the ELF (experimental) video image, or in most of the numerical simulation results. The results thus suggest that the lift-off definition be revisited. The figure's axes are shown with "display" units along with "approximate" speed. The approximate speed is based on the scaling, which is nearly linear and the velocity ranges of the axes are of the order of 0 to 1.70 m/s and 0.15 to 0.60 m/s, for the fuel and air, respectively. It should be noted that during testing the fan was always powered, so there was a minimum air velocity on the order of 0.2 m/s.

The stability maps, Fig. 2, confirmed our hypothesis that higher velocities are required for lift-off and blow-out in microgravity compared to normal gravity. This hypothesis was based on the buoyant contribution to the velocity in normal gravity. In this study, most flames were on the order of 10 mm or less in height, whether in normal gravity or microgravity. As such, it is expected that the buoyant contribution to the axial velocity (in the region of the flame) would be on the order of 0.35 m/s, dependent on the flame size, and based on an estimation method of Glassman [16]. The available data suggests that for a fixed fuel velocity, an increase in air velocity on the order of 0.15 m/s is required to induce lift off in microgravity (compared to normal gravity). As shown on Figure 2, the increase in air

velocity required to induce blow out in microgravity was nearly equal to the increase required to induce lift off. Furthermore, the air velocity increase was relatively independent of the fuel flow, except at low fuel flows where lesser increases were required. Under those conditions, the buoyancy-induced velocity is diminished due to the small flame size.

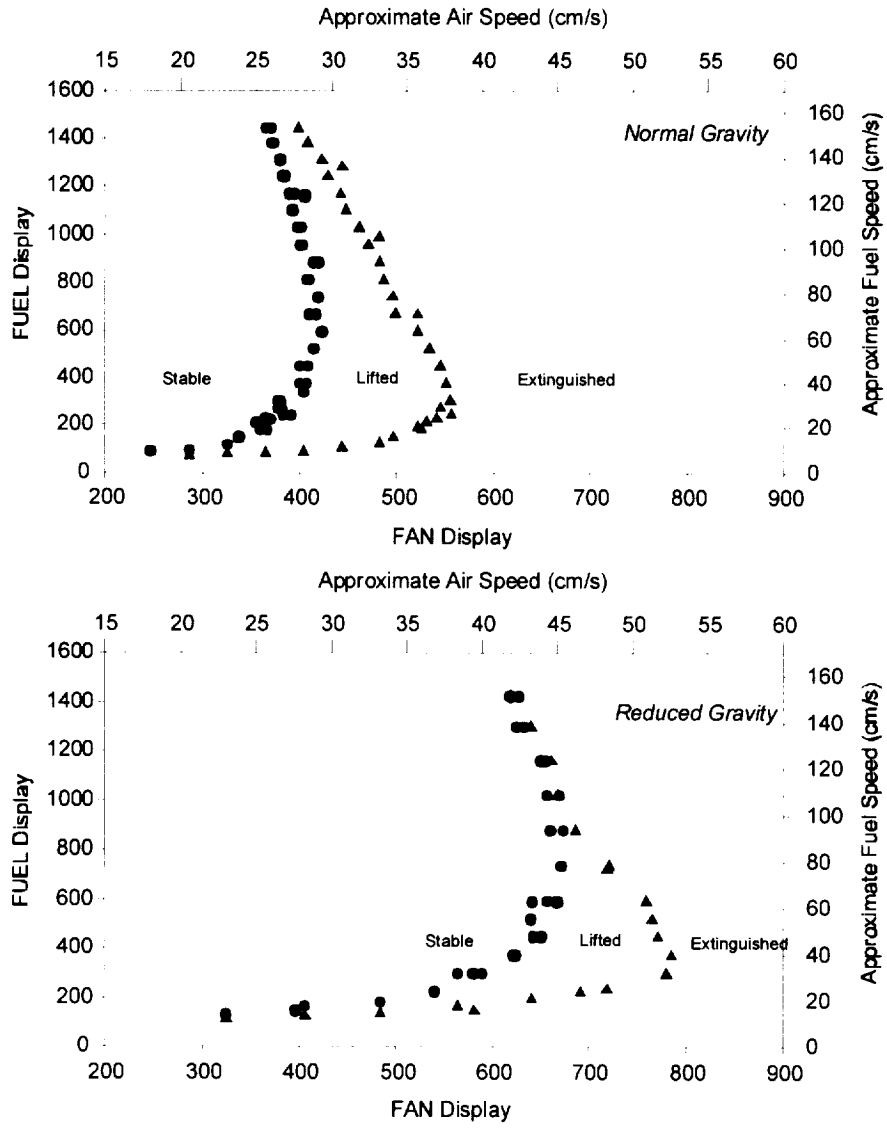

Figure 2. Comparison of Stability Maps in Normal Gravity and Microgravity Environment (circle denotes the lift-off condition and triangle the blow-out condition).

From the stability maps, it can be seen that there is an intermediate "most stable" fuel velocity where the greatest air velocity is required to cause lift off. This observation may have practical application in the design of combustors. There is a similar fuel velocity that is "most stable" in regards to blow out, as previously observed by Feikema et al. [7-8], but it occurs at a lower value (than for lift off) regardless of the buoyancy condition. Comparison of the normal-gravity and microgravity maps reveals that both of these "most stable" fuel velocities occur at higher fuel velocities in microgravity. It is also observed that at low fuel velocities, the microgravity blow-out boundary exhibits a sharp decrease in the extinguishing air velocity with decreasing fuel velocity, whereas the normal-gravity curve shows a more gradual decrease.

At high fuel flows, it was found that the microgravity flames tend to immediately blow out after lift off. This is in agreement with the free-jet theory of Chung and Lee [1], which suggests that stable lifted flames are not possible for fuels with a Schmidt number of $0.5<Sc<1$, such as the diluted methane used in this study. However, stable lifted flames were observed in microgravity at low fuel flows, and in normal gravity, despite the fuel's low Schmidt number. The discrepancy between the experimental data and the theory of Chung and Lee is presumably due to the differences in the flow condition; namely, the ducted flow versus a free jet, and a non-similar velocity profile versus a self-similar profile.

As expected, buoyant convection was found to have a relatively weak effect on the visible appearance of these flames, compared to its effect on their stability. After lifting, the flames generally became shorter and developed an outer, upwardly-turned, fuel-lean rim, essentially becoming hat shaped in appearance. An inner fuel-rich rim (i.e., triple flame structure) was never observed. Ultimately the flames would tend to flatten as shown in Figure 1, becoming disk shaped, but still retaining the fuel-lean outer rim. Similar flame structure behavior has been reported in previous normal-gravity studies [1,4-5,9]. It was noted that the lifted flames had a somewhat tilted base, suggesting that the velocity profile across the duct may not be uniform, possibly due to the rake or another non-uniformity in the hardware. This will be investigated and reported on in a future paper.

Numerical simulation predicts a jump condition of the flame base for the fuel jet velocity at 0.2 m/s when the co-flow air velocity is increased to 0.11 m/s. The experimentally determined lift-off co-flow air velocity is 0.3 m/s when the fuel jet velocity is maintained at 0.2 m/s. It should be noted that in the region near the fuel jet velocity of 0.2 m/s, experiment shows a relatively flat lift-off co-flow air velocity as illustrated in Fig. 2. Hence ramping of the co-flow air velocity can introduce a larger uncertainty level in the determination of the lift-off air velocity. For the fuel jet velocity of 0.2 m/s, the predicted blow-out co-flow air velocity is 0.6 m/s; whereas the experimentally determined value was 0.4 m/s. Numerical simulation did not predict an obvious jump movement of the flame base when the fuel jet velocity is increased above 0.2 m/s. Effort of numerical simulation continues aimed at assessing the lack of the jump movement of the flame base. Numerical simulation predicts blow-out at co-flow air velocity of 0.75 m/s for the fuel jet velocity at 0.4 m/s, and 0.85 m/s at 0.6 m/s. The predicted blow-out conditions are in reasonable agreement with experimental data.

The predicted structure near the flame base is illustrated by local heat release contours superimposed on the axial distance vs. mixture fraction (f) diagram shown in Fig. 3. To the contrary as one may anticipate a triple-flame structure at the flame base, simulation does not suggest existence of the triple flame over the range of conditions reported in Fig. 3. Simulation therefore calls for revisit of the structure in the near flame-base region.

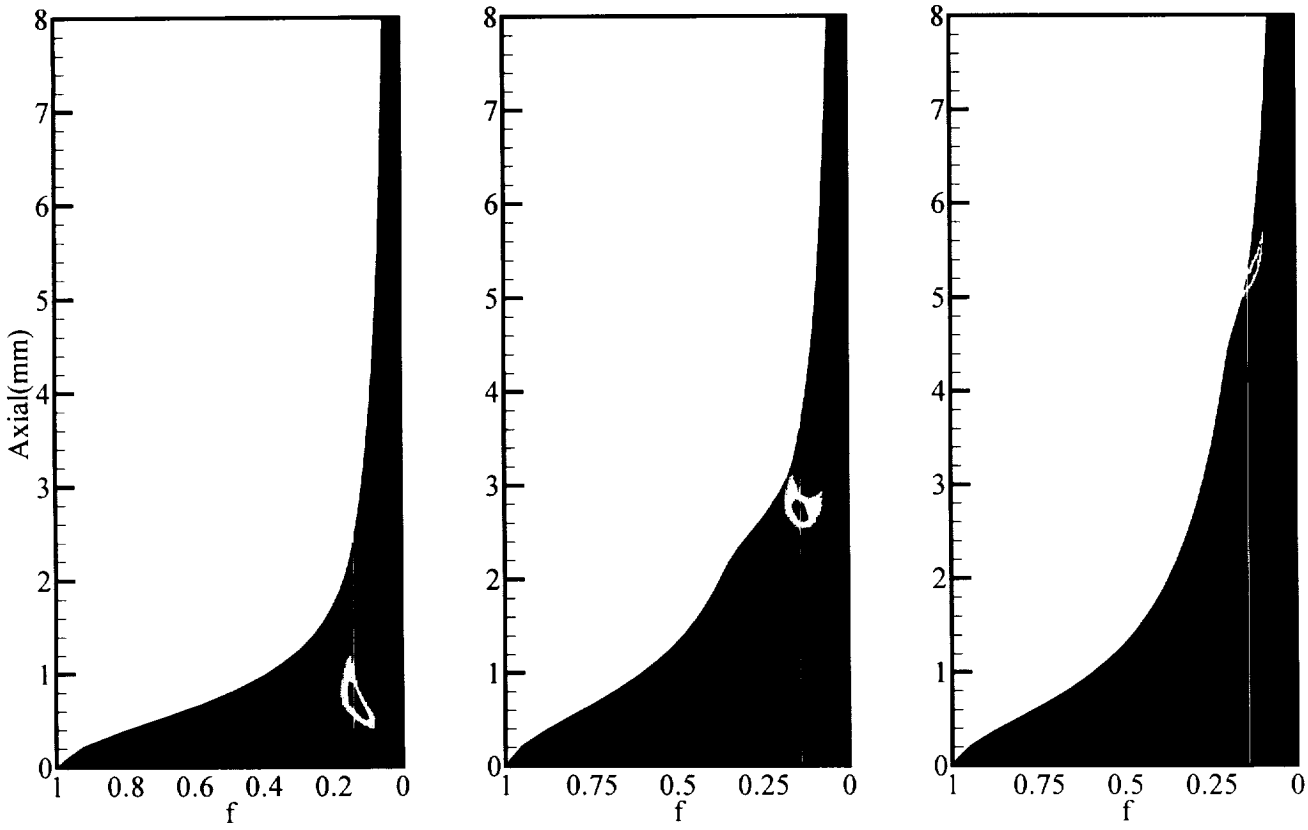

(a) Air Velocity at 0.1 m/s (b) Air Velocity at 0.4 m/s (c) Air Velocity at 0.6 m/s

Figure 3. Contour Plot of Heat Release Superimposed on Axial Distance-Mixture Fraction Plot; Fuel Jet Velocity at 0.2 m/s.

SECTION V. Conclusions

The ELF investigation demonstrated that within a co-flow duct, stable lifted laminar flames can be achieved for a fuel with a Schmidt number of $0.5<Sc<1$, in contrast to the free-jet study of Chung and Lee [1]. It was confirmed that significantly higher forced velocities are required to cause lift off and blow out in a microgravity environment. The increase in air velocity required to induce lift off in microgravity (compared to normal gravity) was found to nearly equal the increase required to induce blow out. Furthermore, that air velocity increase was found to be relatively independent of the fuel flow, except at low fuel flows.

The influence of buoyancy on (a) the temperature field and (b) the hysteresis effect of flame lift off and reattachment will be explored and reported in a future paper.

ACKNOWLEDGEMENTS

The research was supported by the NASA Microgravity Research Division, Code UG, through Grant NAG3-1592 for the effort at The University of Iowa. Special thanks go to Mission Specialists Dr. Kalpana Chawla (NASA) and Dr. Takao Doi (NASDA) for their interest and dedication during training and while conducting the investigation during the STS-87 Space Shuttle mission.

REFERENCES

1. Chung, S.H. and Lee, B.J. Combust. Flame, 86:62-72 (1991).
2. Gollahalli, S.R., Sava , Ö. Huang, R.F., and Rodriquez Azara, J.L. Twenty-First Symposium (International) on Combustion, The Combustion Institute, Pittsburgh, 1986, pp. 1463-1471.
3. Pitts, W.M. Twenty-Second Symposium (International) on Combustion, The Combustion Institute, Pittsburgh, 1989, pp. 809-816.
4. Sava , Ö. and Gollahalli, S.R. J. Fluid Mech., 165:297-318 (1986).
5. Lee, B.J., Cha, M.S., and Chung, S.H. Combust. Sci. and Tech., 127:55-70 (1997).
6. Dahm, W.J.A. and Mayman, A.G., AIAA Journal, 28:7:1157-1162 (1990).
7. Feikema, D., Chen, R.-H. and Driscoll, J.F. Combust. Flame, 80:183-195 (1990).
8. Feikema, D., Chen, R.-H. and Driscoll, J.F. Combust. Flame, 86:347-358 (1991).
9. Whol, K. Kapp, N.M., and Gazley, C. Third Symposium on Combustion and Flame and Explosion Phenomena, The Williams & Wilkins Co., Baltimore, 1949, pp. 3-21.
10. Scholefiled, D.A. and Garside, J.E. Third Symposium on Combustion and Flame and Explosion Phenomena, The Williams & Wilkins Co., Baltimore, 1949, pp. 102-110.
11. Kalghatgi, G.T. Combust. Sci. and Tech., 26:233-239 (1981).
12. Kalghatgi, G.T. Combust. Sci. and Tech., 41:17-29 (1984).
13. Takahashi, F., Mizomoto, M., Ikai, S., and Futaki, N. Twentieth Symposium (International) on Combustion, The Combustion Institute, Pittsburgh, 1984, pp. 295-302.
14. Eickhoff, H., Lenze, B., and Leuckel, W. Twentieth Symposium (International) on Combustion, The Combustion Institute, Pittsburgh, 1984, pp. 311-318.
15. Burke, S.P. and Schumann, T.E.W. Ind. Eng. Chem., 20:998-1004 (1928)
16. Glassman, I. Combustion, 3rd ed., Academic Press, San Diego, 1996, pp. 281-2.

Particle Engulfment and Pushing by Solidifying Interfaces

USMP - 4 One Year Report

D.M.Stefanescu, PI
F.R.Juretzko, Grad.Res.Asst.
A.V.Catalina, Grad.Res.Asst.
University of Alabama, Tuscaloosa

S.Sen, Co-PI *USRA*
P.Curreri *MSFC*

C.Schmitt
S. Gilley
TechMaster

Introduction

The experiment *Particle Pushing and Engulfment by Solidifying Interfaces* (PEP) was conducted during the USMP-4 mission on board the shuttle Columbia in November 1997. This experiment has its place within the framework of a long-term scientific effort to understand the physics of particle pushing. The first flight experiment of this kind was performed with a metal matrix composite on board STS-78 in the summer of 1996. The use of opaque matrices limits the evaluation to pre-and post-flight comparison of particle locations within the sample. By using transparent matrices the interaction of one or multiple particles with an advancing solid/liquid (SL) interface can be studied *in-situ*. If this observation can then directly be transmitted from the orbiter to the scientists by video down-link, a real-time execution of the experiment is possible in a micro-gravity environment.

Part of this experiment was an extensive training of the payload specialists to perform the experiment in orbit. This was further enhanced by the availability of video down-link and direct communication with the astronauts. Even though the PEP experiment is aimed at understanding the interaction of a liquid/solid interface with insoluble particles and thus is fundamental in scope, the prospective applications are not. Possible applications range from improved metal matrix composites to understanding and preventing frost heaving affecting roads[1,2,3].

The physics of particle- SL interface interaction can be described through the different forces acting on the particle and the SL interface as shown in Figure 1. The solid/liquid interface approaches the particle with a velocity V_{SL}. When the particle is pushed by the interface, the flow around the particle results in a drag force, F_D. Additional forces are the buoyancy force, F_g and a repulsive force F_γ, resulting from the differences in surface energy of particle and SL interface. A fourth force originates from the flow, V_L, parallel to the interface. This force, F_L, is a lift force as discussed by Han and Hunt[4]. It has its origin in fluid flow considerations around the

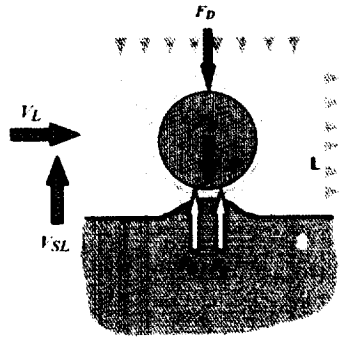

Figure 1 Schematic representation of forces acting on a particle in the vicinity of an approaching SL interface

particle close to the interface. Figure 1 also includes the case of the thermal conductivity of the particle being lower than of the liquid, hence the formation of a bump.

From these acting forces three different regimes of particle-SL interface interaction can be anticipated, which also have been confirmed through experiments[5]:

- no or low melt convection
  $V > V_{cr}$ => engulfment
- no or low melt convection
  $V < V_{cr}$ => pushing
- significant melt convection
  => no particle-SL interface interaction

In order to avoid melt convection a micro-gravity environment is essential. The reduction of melt convection by use of capillary sized samples introduces side wall effects and thus does not facilitate the experiment.

For the PEP experiment on board the microgravity glovebox facility (MGBX) the forces to consider are reduced to a force balance between the repulsive force, F_γ, and the drag force, F_D. This allows the experimental validation of our existing model for prediction of the critical velocity of engulfment.

Experimental Method

Eight samples were processed during the PEP experiment. They included four succinonitrile (SCN) samples with two different particle size distributions and four biphenyl (B) samples with four different particle size distributions. The different samples and particle combinations are listed in Table 1. The two systems chosen exhibit different characteristics. SCN solidifies non-faceted while biphenyl solidifies faceted. The density ratio of the matrix/particle systems is 1.009 for SCN/polystyrene and 0.327 for biphenyl/glass. The ratio of thermal conductivity of particle and matrix is 0.356 for SCN/polystyrene and 9.101 for biphenyl/glass. A compilation of physical data is given in Table 2.

Table 1 Listing of PEP samples used during USMP-4

Sample ID	Matrix-material	Particle-material	Particle size
SCN-1	SCN	polystyrene	0.5 - 25 μm
SCN-2	SCN	polystyrene	1 - 15 μm
SCN-2b	SCN	polystyrene	1 - 15 μm
SCN-3	SCN	polystyrene	1 - 15 μm
B-1	biphenyl	glass beads	2.5/ 5.1/ 8.4/ 10.1 μm
B-2	biphenyl	glass beads	8.4 μm
B-3	biphenyl	glass beads	5.1 μm
B-4	biphenyl	glass beads	2.5 μm

Table 2 Physical data of the sample materials

Parameter	Unit	SCN	Polystyrene	Biphenyl	Glass
T_{Melt}	°C	58.1 [6]	240 [6]	69 [7]	~1600 [7]
ρ_{solid}	g cm^{-3}	1.05	1.04 [6]	0.866 [7]	2.65 [7]
ρ_{liquid}	g cm^{-3}	0.988		@69°C: 0.998[10]	
D	m^2 s^{-1}	10^{-9} [8]		10^{-9} (assumed)	
$K_{particle}$	W m^{-1} K^{-1}		0.0794 [9]		1.256 [7]
K_{liquid}	W m^{-1} K^{-1}	0.223 [8]		0.1316 [7] 0.138 [10]	
ΔH_{fusion}	J m^{-3}	$4.6\ 10^7$ [8]		$1.044\ 10^8$ [7]	
$\gamma_{solid/liquid}$	J m^{-2}	$9\ 10^{-3}$ [8]		$7\ 10^{-4}$ [11]	
a_o	m	$1.27\ 10^{-9}$ (calc)		$8.25\ 10^{-10}$ [5]	
$\Delta\gamma_o$	J m^{-2}	$10.1\ 10^{-3}$ [5]		$14.3\ 10^{-3}$ [5]	
η	kg m^{-1} s^{-1}	$2.59\ 10^{-3}$ [12]		$9.7\ 10^{-4}$ [7]	
contact angle	deg	61.8 (Polyst, air)		58 (glass, air) [a]	

(a) Measured from experiments at Solidification Lab, UA

The samples were produced by repeated zone refining of commercial SCN and biphenyl. The purified SCN was obtained from USRA at the Marshall Space Flight Center and the biphenyl was zone refined at the University of Alabama. Mixing of the matrix and the particles was done in a glass veil. The mixture was transferred into the sample cell. Each filled cell was then remelted under a vacuum to degas the matrix material. A gas bubble had to be present inside the sample cell volume to compensate for volumetric expansion. The backfilling gas was high purity argon gas. Each sample hosted four thermocouples to record the temperature gradients inside the sample. Wiring the sample cell into the holder completed the assembly, as shown in Figure 2.

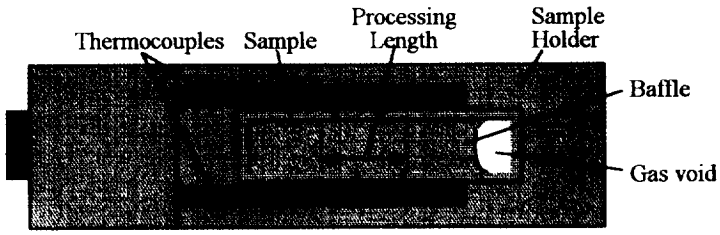

Figure 2 Schematic of the PEP sample cell

In preparation of the PEP experiment a training hardware was used for ground tests and for astronaut training (Figure 3). The table top assembly consisted of a monitor, VCR, controller box, video titler, microscope, thermal chamber, and a laptop computer (PGSC). The PGSC contained the data acquisition- and the command software for the thermal chamber. The thermal chamber was equipped with two heaters and two thermoelectric coolers, Figure 4. The sample was illuminated by a set of light diodes below the cell. The microscope could be focused on the particles through a view port in the top plate. The experimental observations were recorded on video and used for post-experimental evaluation.

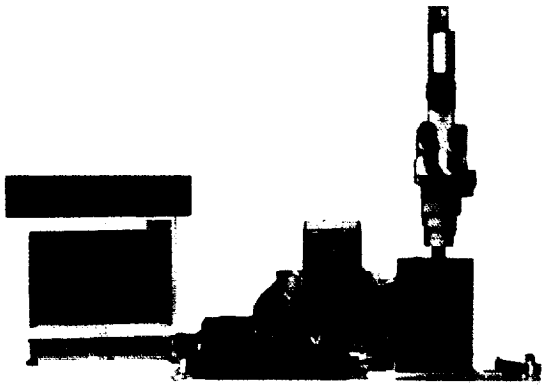

Figure 3 Set-up of the training hardware with closed laptop

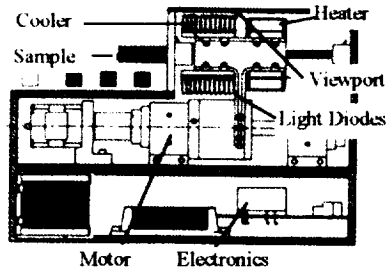

Figure 4 Cross section of the thermal chamber

The temperature settings for the PEP experiment in the MGBX were 100°C (hot) and 20°C (cold) for the SCN samples and 120°C and 20°C for the biphenyl samples.

A number of criteria were followed when determining the critical velocity. Only particles that were pushed were considered. The critical velocity was taken as the lowest velocity above which the particle was engulfed. Only engulfment by a planar interface was considered. When the SL interface became unstable (cellular) the translation velocity was reset to zero.

The on-board video recording and the downlink video were a composite image. It consisted of the actual video recording of the SL interface of the sample and a data overlay. The data displayed were the date, time (Greenwich Mean Time, GMT), sample number, magnification, programmed velocity of the gradient stage (V_{PGSC}), and the temperature recordings of the four thermocouples (Figure 5).

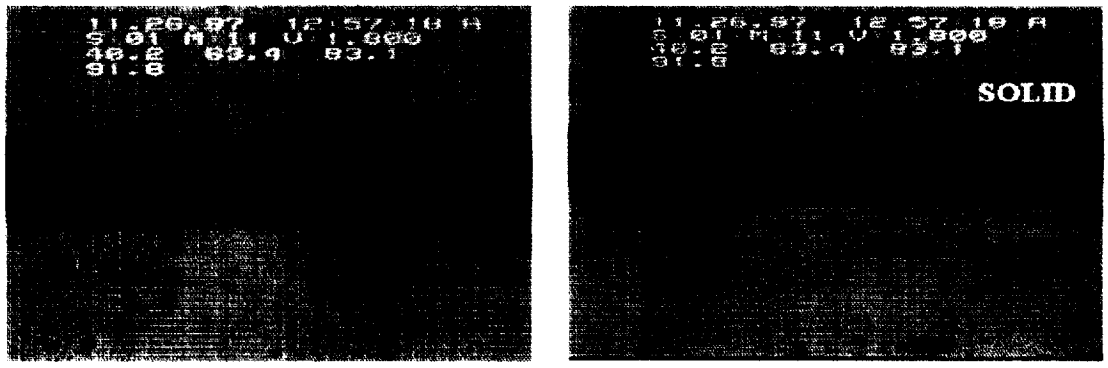

Figure 5 Example of video data screen (left); identified features (right)

Graphs have been obtained based on the PGSC data files for the different experiments. These graphs summarize the progress of the experiments. They show which velocity profile was used, when the experiment was stopped and the direction of the SL interface movement. Positions and the velocities (display and calculated) are plotted versus the total time of the experiment, starting with the initiation of the experiment. The calculated velocity *V(calc)* is based on gradient stage position by time data from the PGSC data file. The data recording was at a rate of 1 per second. It is apparent that the calculated velocity matches the calculated data most of the time. However, when a fast forward command was issued an overshooting in the velocity is apparent.

Furthermore, at 2:24:00 of processing time in SCN-1 a significant discrepancy is visible. This is the result of a STOP command after a short processing segment of V=5 µm/s which led to an interface breakdown, i.e., changing from planar to cellular solidification. The forward movement was paused until a planar SL interface was re-established, Figure 6.

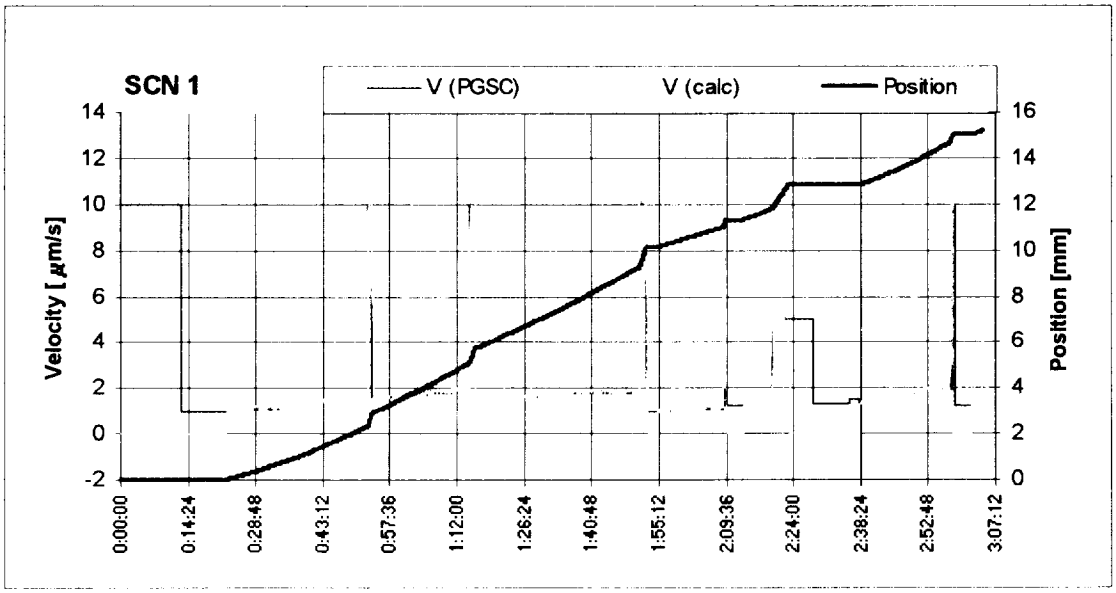

Figure 6 Velocity and position for sample SCN-1.

For SCN-2 a gradually increasing velocity profile was used. At half way the SL interface became loaded with particles. To clean the SL interface a rapid forward movement was used to engulf the accumulated particles. In other instances a rapid backward move left the pushed particles in the liquid for observation (Figure 7).

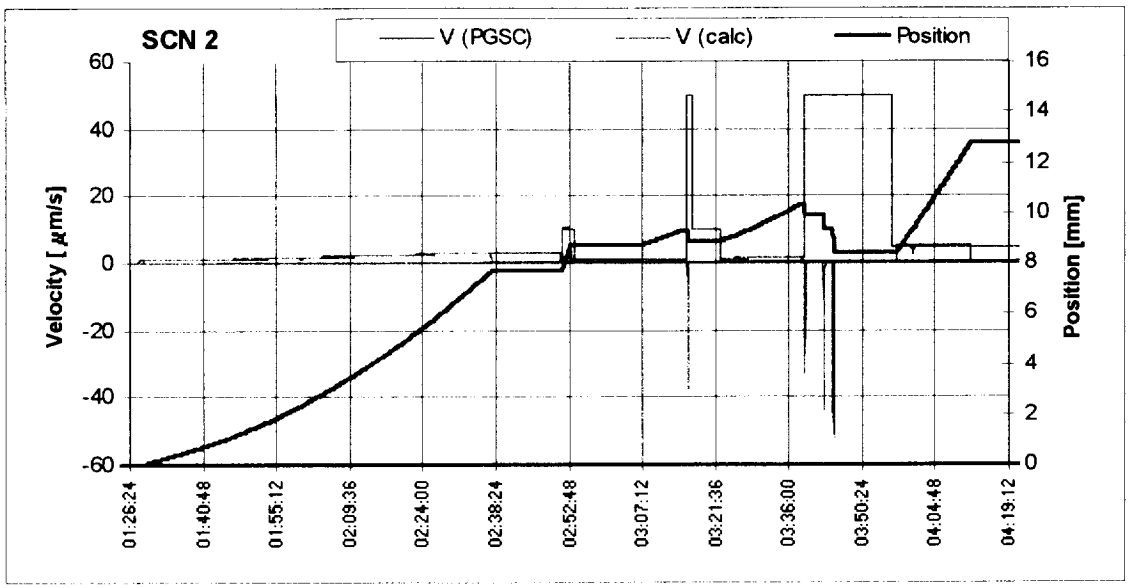

Figure 7 Velocity and position for sample SCN-2.

In sample SCN-2b a similar approach was used as in SCN-2. However, the back and forward motion was used more extensively. From the experience with SCN-2 the velocities used in the fast back and forward mode were not as high but for a longer period of time. This allowed the SL interface to follow the movement of gradient stage more closely, as shown in Figure 8.

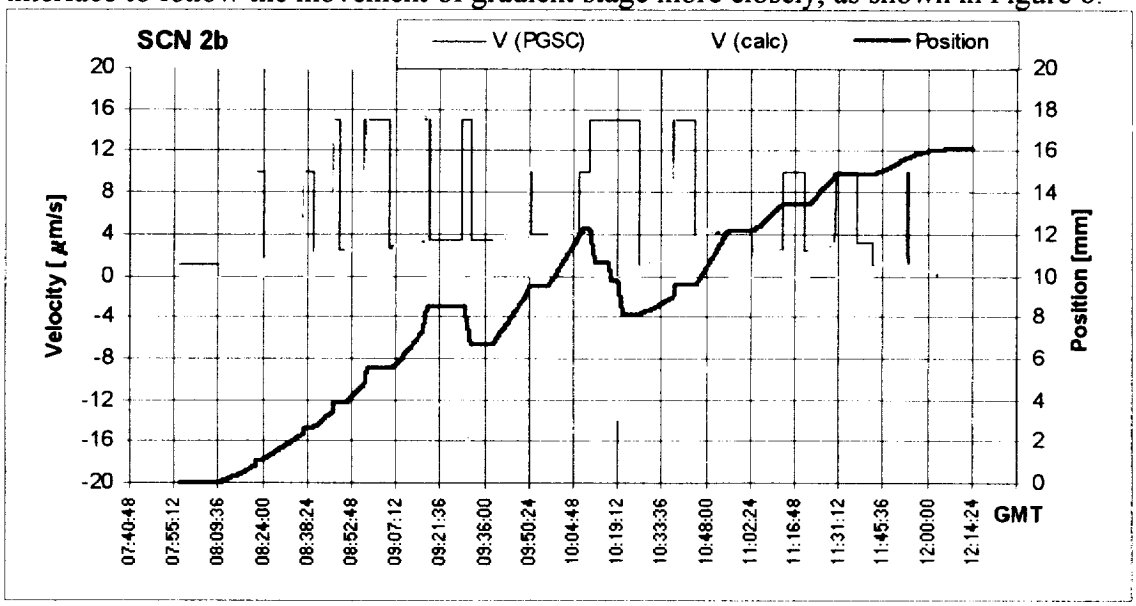

Figure 8 Velocity and position for sample SCN-2b.

In sample SCN-3, which was the last of the SCN samples of the PEP experiment, an inverse start was applied. Starting with a high velocity of 6 µm/s a stepwise decrease in velocity was employed. Again, as the interface became loaded with particles the fast back and forward procedure was executed. Towards the end of the run the velocity was increased to 10 µm/s. This was done to take advantage of the remaining sample length to observe non-planar solidification. It was viewed as an opportunity of additional science for future experiments. When reaching the automatic shut-off point of the gradient stage the experiment was terminated (Figure 9).

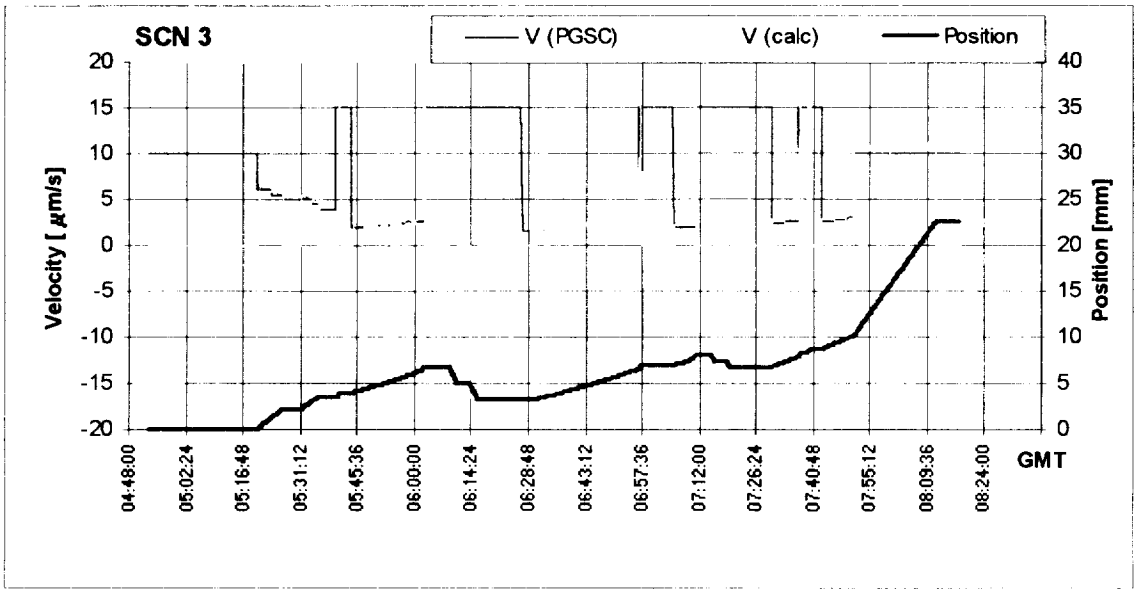

Figure 9 Velocity and position for sample SCN-3.

For the Biphenyl-1 sample, containing four different particle sizes, the reliable procedure of forward and backward movement was applied (Figure 10).

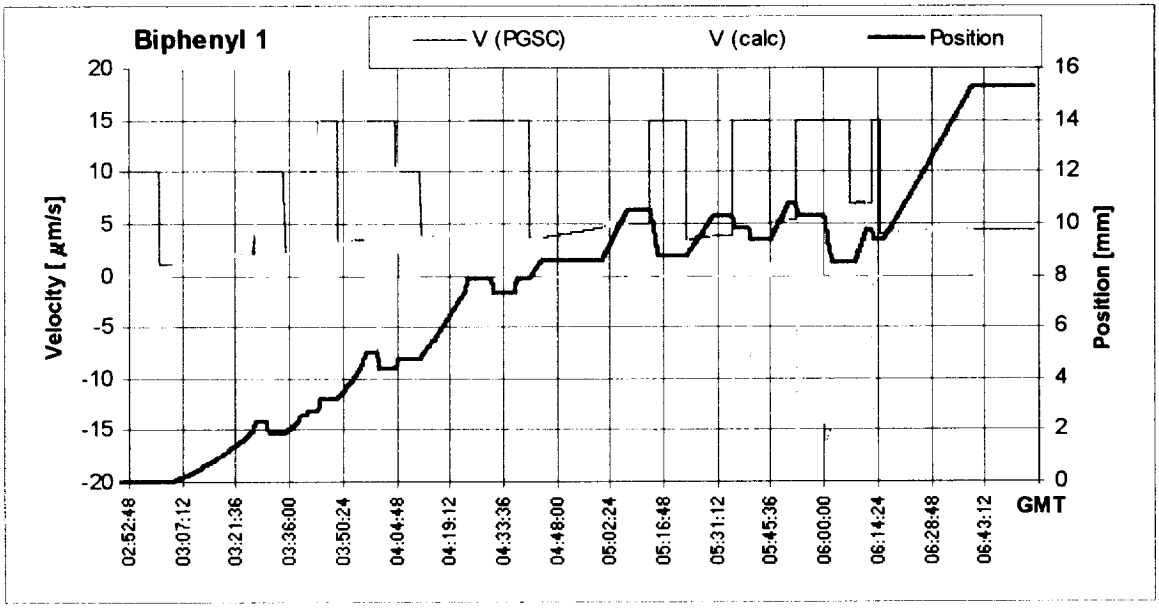

Figure 10 Velocity and position for sample Biphenyl-1.

During the processing of Biphenyl-2, with a nominal particle size of 8.4µm, the only problem during all PEP experiments occurred. Between 08:00:00 and 08:30:00 GMT the GBX facility shut down due to an overheating of the work area (WA). The reasons were twofold: Biphenyl-2 was processed back to back with another PEP experiment, thus not allowing the WA to cool down. Furthermore, the processing temperature of the biphenyl sample was higher than that of the SCN samples. Future problems were avoided by leaving one of the GBX doors open. When the facility shut down the whole experiment support was also affected. Resuming the experiment after sufficient cool down the PGSC had to be restarted. During the shut down the memory of the PGSC was deleted. Therefore, upon restart the position indicated 0.000 mm. The experiment was resumed at the same position where it shut off (Figure 11).

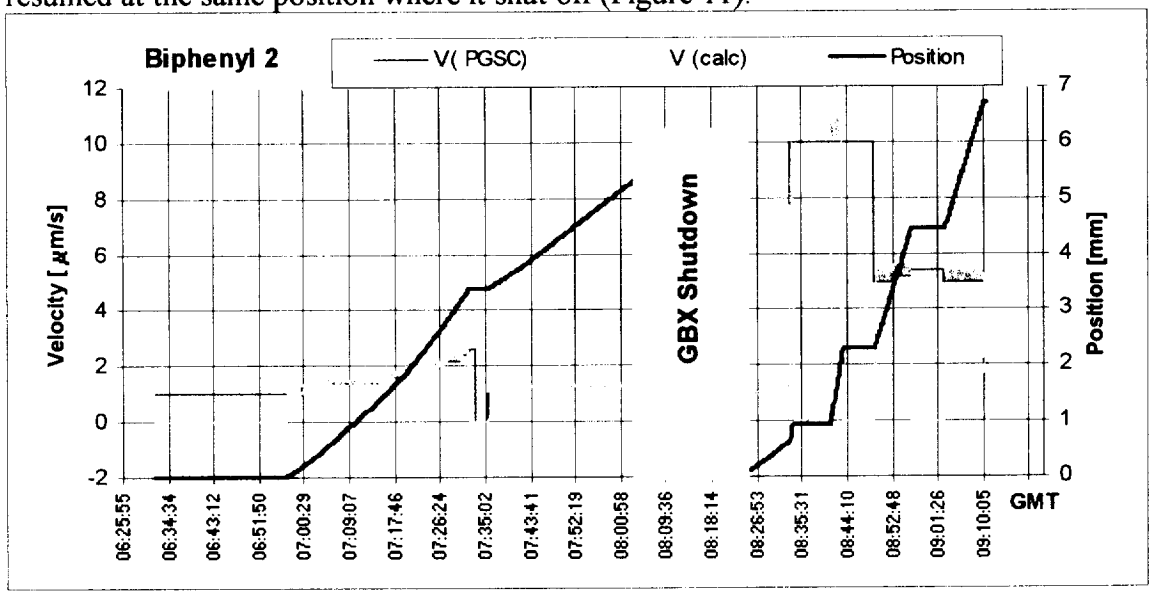

Figure 11 Velocity and position for sample Biphenyl-2.

The particle size in Biphenyl-3 was nominally 5.1 μm which allows for easy identification of the single particles. The experiment was short in duration and was conducted without much back- and forward movements (Figure 12).

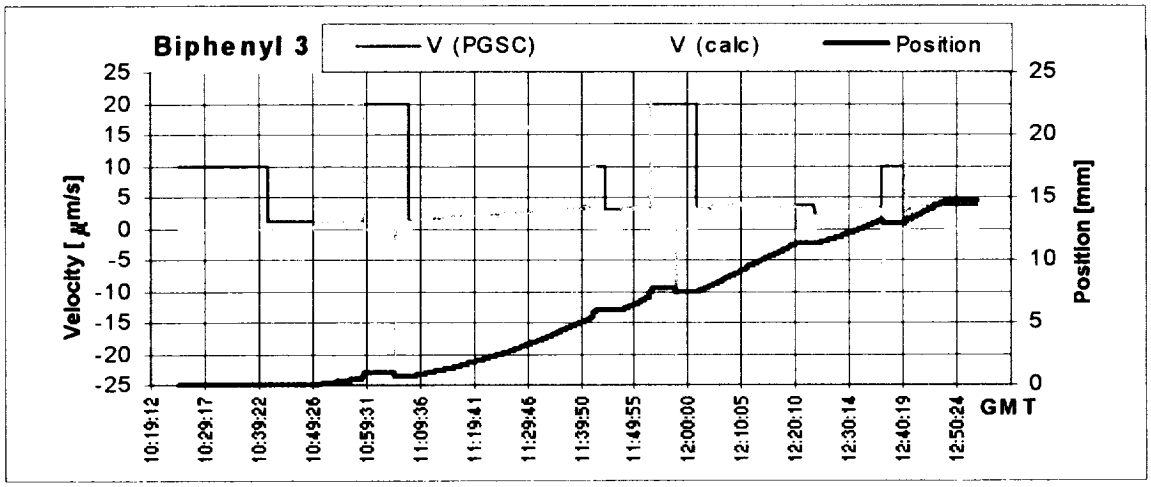

Figure 12 Velocity and position for sample Biphenyl-3.

Biphenyl-4 contained particles of nominally 2.5 μm diameter. These particles are visible under the microscope yet not easily distinguishable in case of little agglomerates. Therefore extensive use was made of the procedure of fast back- and forward movements. Again, comparing the velocity from the PGSC and the calculated one, a discrepancy of 1-2 μm/s is noted (Figure 13). An example of the effect of backward motion and the resulting line of pushed particles is given in Figure 14.

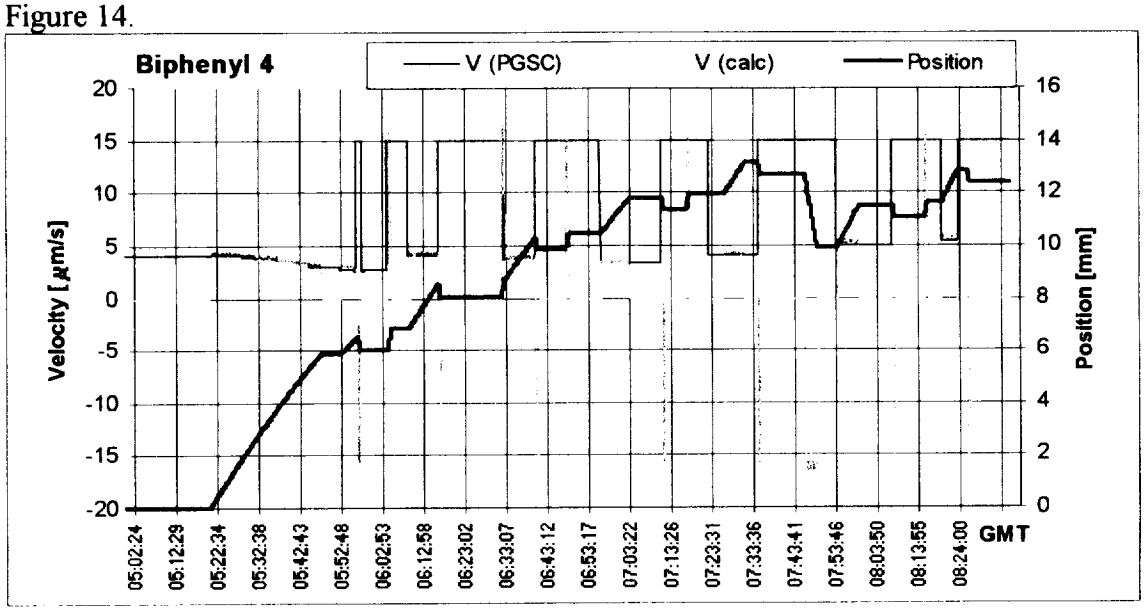

Figure 13 Velocity and position for sample Biphenyl-4.

The evaluation of the critical velocity for the *pushing/engulfment transition* (PET) requires a detailed study of the video recording. The measurements were done on a monitor screen. During the heat-up period of the thermal chamber a calibration slide was inserted and the picture recorded on video. This guaranteed an exact measurement of the particle size and the actual SL interface velocity.

Figure 14 Line of particles ahead of SL interface after *move backward* command

Results

During the review of the video recordings several other observations sparked the interest of the science team, besides the main objective of evaluating the pushing-engulfment transition of particles at a planar SL interface. These observations are the quantifiable observation of solidification shrinkage, which is a net flow of liquid matter towards the growing solid, the behavior of clusters at a planar solidification front, the growth of the faceted biphenyl solid and its interaction with small particles at the SL interface. This became noticeable as vivid motion parallel to the SL interface of these little particles was observed despite the fact that no convection or other outside forces were present in the micro-gravity environment of the space shuttle.

When evaluating the flight video recordings it was observed that the behavior of the particles at the solid-liquid interface changed over time. This can be exemplified by the cleaning procedure employed at several occasions. The cleaning procedure was a fast forward movement of the SL interface to engulf all the accumulated particles. Generally the first fast forward motion did not lead to interface perturbations. In consecutive procedures interface perturbations were observed. They became more pronounced, leading eventually to the formation of a cellular interface towards the end of the experiment. Particle-SL interface interaction was also affected. While being pushed at a given velocity at the beginning of the experiment the same size particles were engulfed towards the end at the same velocity. Two possible reasons for this behavior are the accumulation of solute and a change in thermal gradient. Nuclear Magnetic Resonance (NMR) characterization of the SCN stock material did not disclose any impurities. Further characterization of the flight samples is still pending. The change in thermal gradient originates in the change of the heating area. After sufficient processing time the heating area is positioned at the ceramic baffle and then at the gas bubble. These two possibilities do not confirm with the experimental assumptions of *no solute build-up* at the SL interface and with the demand of a *constant thermal gradient*. Thus to obtain unambiguous data of the pushing-engulfment transition the experimental data are divided into those of the first 5mm of processing length and those from 5mm till the end of the run, Table 3.

Table 3 Compilation of experiment times for 0-5mm and 5-end

Sample	Time *			Sample	Time		
		0-5 mm	5-*15.2* mm**			0-5 mm	5-*15.33* mm
SCN 1	GMT	12:13 - 1:04	1:04 - 2:55	**B 1**	GMT	3:04 - 4:12	4:12 - 6:56
	PT	0:22 - 1:14	1:14 - 3:04		PT	0:23 - 1:31	1:31 - 4:15
		0-5 mm	5-*12.7* mm			0-5 mm	5-*12.01* mm
SCN 2	GMT	1:29 - 2:21	2:21 - 4:21	**B 2**	GMT	6:57 - 7:59	7:59 - 9:10
	PT	0:11 - 1:03	1:03 - 3:04		PT	0:25 - 1:27	1:27 - 2:31
		0-5 mm	5-*16.14* mm			0-5 mm	5-*14.65* mm
SCN 2b	GMT	8:10 - 8:51	8:51 -12:14	**B 3**	GMT	10:49 -11:39	11:39 -12:48
	PT	0:12 - 1:00	1:00 - 4:17		PT	0:25 - 1:15	1:15 - 2:23
		0-5 mm	5-*22.55* mm			0-5 mm	5-*12.83* mm
SCN 3	GMT	5:20 - 5:52	5:52 - 8:11	**B 4**	GMT	5:20 - 5:43	5:43 - 8:23
	PT	0:27 - 0:59	0:59 - 3:18		PT	0:39 - 1:01	1:01 - 3:41

* GMT: Greenwich Mean Time, PT: Processing Time

** end position of thermal chamber in italic

It was not always possible to obtain good data from observed particles. The main reasons were as follows:

- no clear indication of a single particle being engulfed or pushed
- particle out of observation range before behavior is unambiguously observed
- vibration of the video camera stage due to handling, and thus no clear measurement of SL interface velocity
- insufficient time of a steady view to accurately measure SL interface velocity

Uncertain points were not included in this report. Therefore the data presented here are a conservative selection of all the data. As previously stated, only the first 5mm of each run will be considered in the analysis. For completion, the remaining data points are presented in an adjacent plot. These data plots are the complete data set of the PEP experiment for the pushing engulfment transition. They are compiled in Figure 15 through Figure 22.

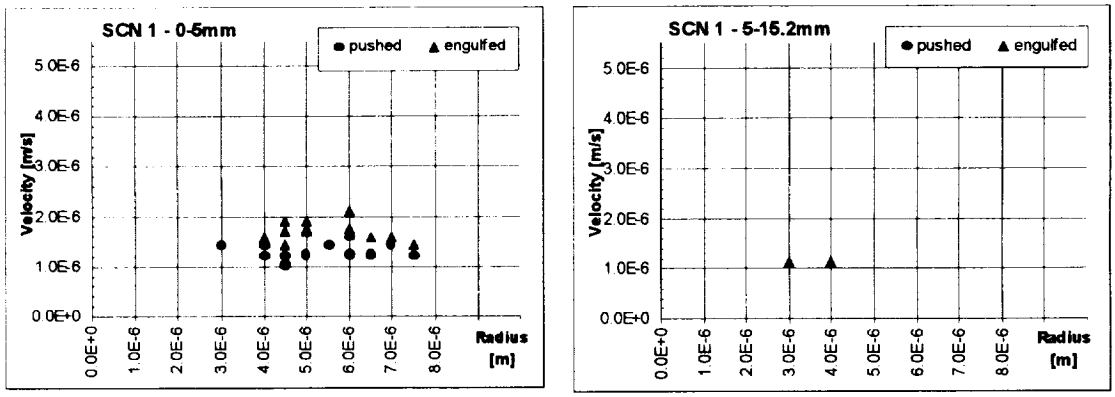

Figure 15 Sample SCN 1 Particle Size: 0.5 - 25 μm Processing Time: 2hr 42min

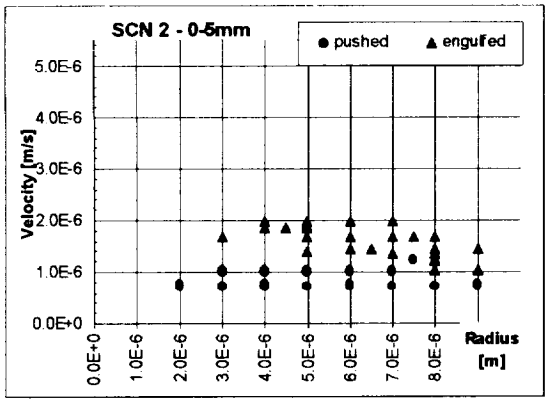

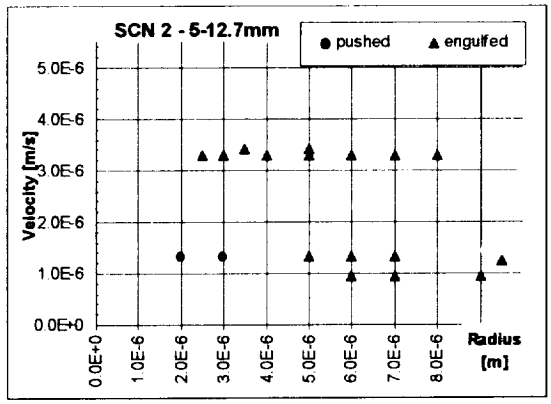

Figure 16 Sample SCN 2 Particle Size: 1-15 μm Processing time: 2hrs 53min

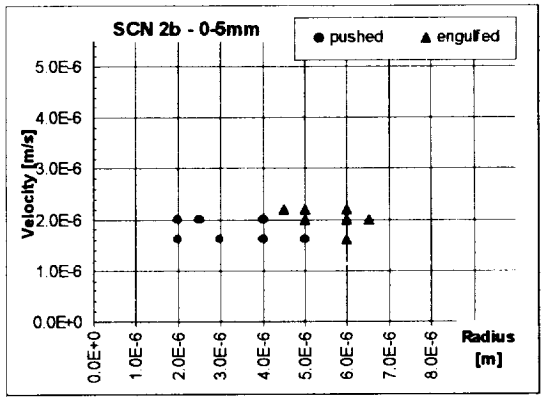

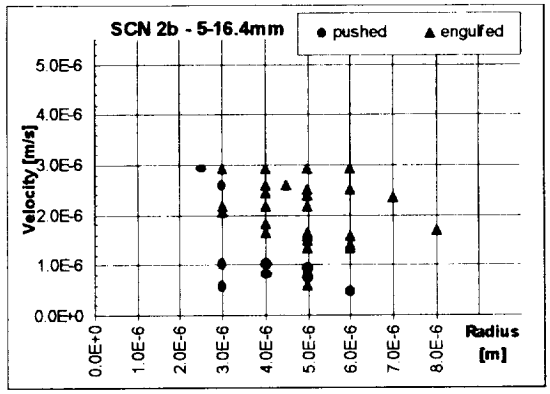

Figure 17 Sample SCN 2b Particle Size: 1-15 μm Processing time: 4hrs 5min

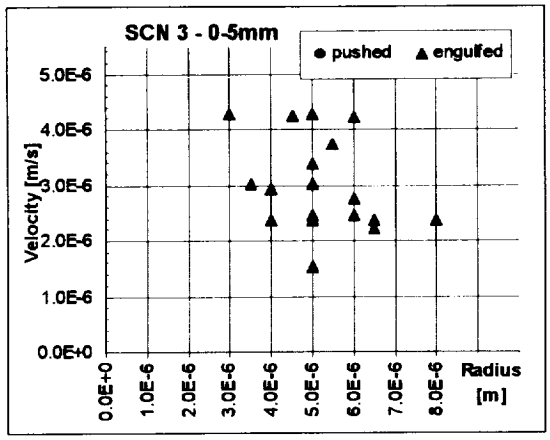

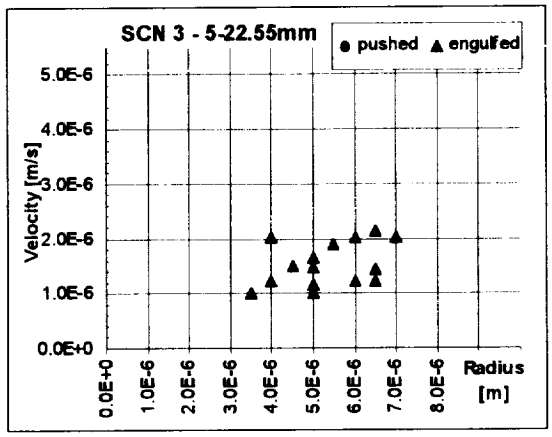

Figure 18 Sample SCN 3 Particle Size: 1-15 μm Processing time: 2hrs 51min

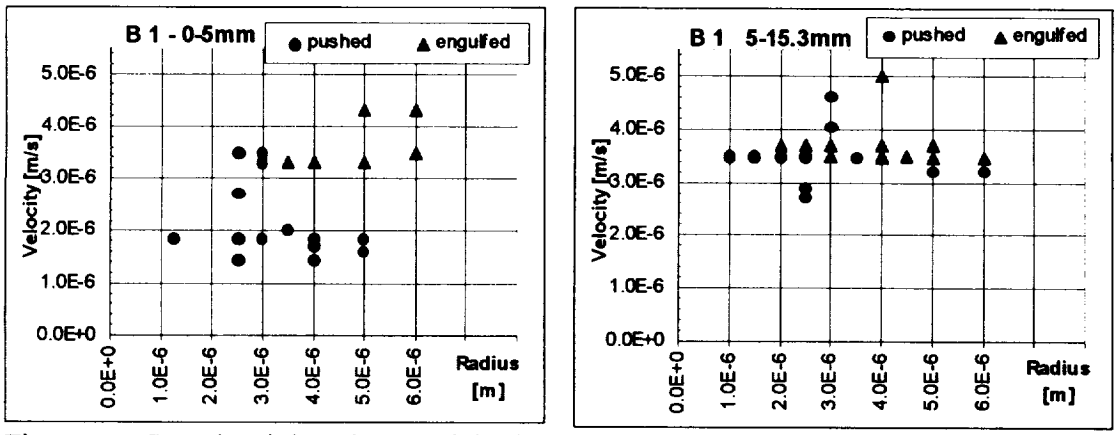

Figure 19 Sample Biphenyl 1 Particle size: 2.5, 5.1, 8.4 and 10.1 µm Proc. time: 3hrs 52min

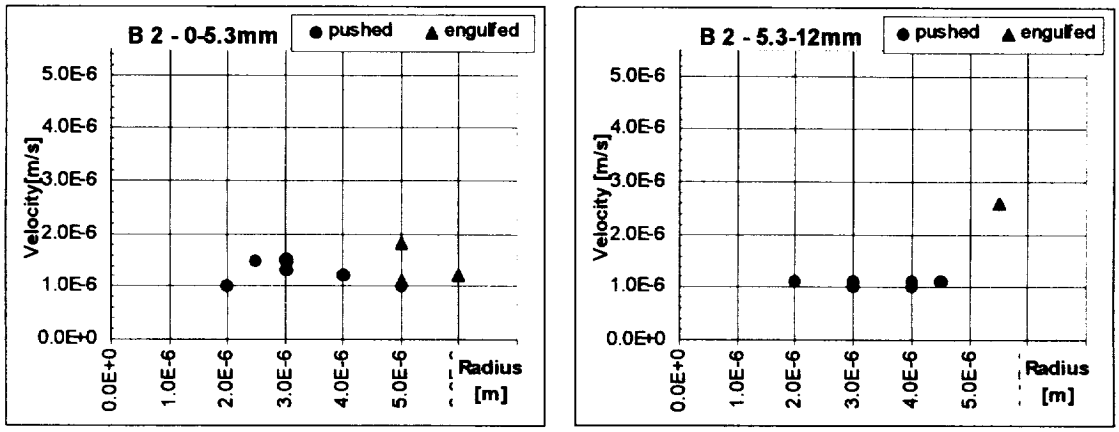

Figure 20 Sample Biphenyl 2 Particle size : 8.4 µm Processing time: 2hrs 6min

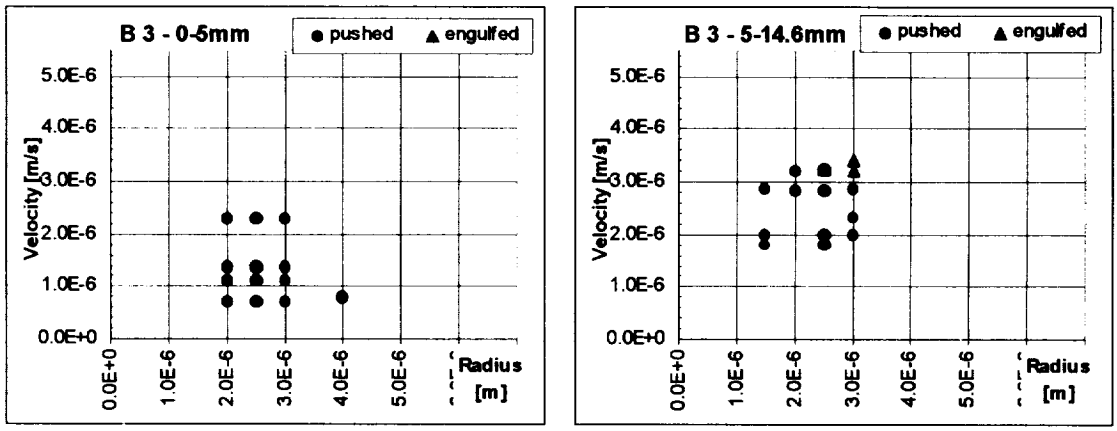

Figure 21 Sample Biphenyl 3 Particle size : 5.1 µm Processing time: 1hr 58min

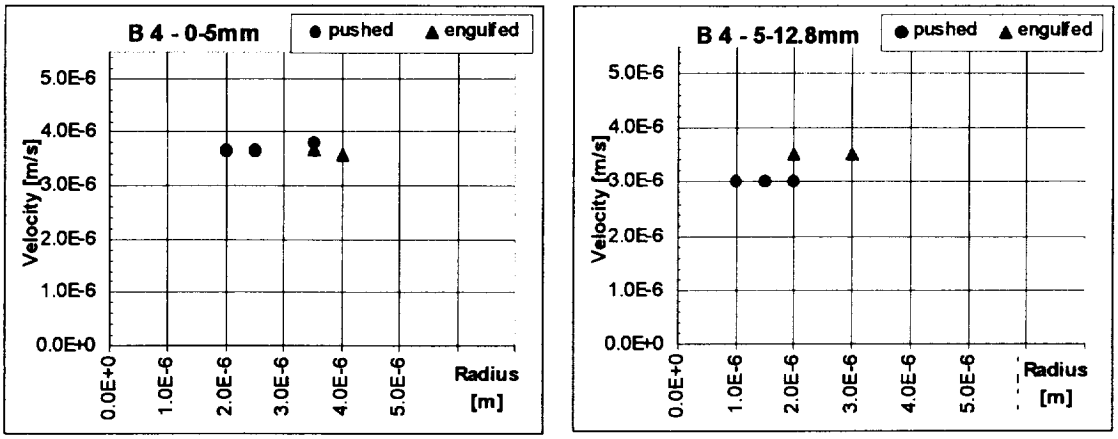

Figure 22 Sample Biphenyl 4 Particle size : 2.5 µm Processing time: 3hrs 2min

Discussion

The exact determination of the PET from these samples is not an easy task. Even with the capability of repetitive examination of the video tapes it is often impossible to pinpoint a certain velocity of the SL interface. Especially during the first experiments there are times when a particle is in the field of view too short a time to make measurements. An additional factor is the attempt of the payload specialist to get the particle under investigation in focus. Even under ground conditions this is not trivial. With the progression of the USMP-4 mission the science team as well as the astronauts became more comfortable with the experiment execution. The experimental procedure was partly modified during flight, for example the employment of the fast back and forward motion.

During the execution of the experiments it has been observed that the SL interface stability decreases with increasing processing time and length. This could be caused by either the accumulation of solute at the SL interface or by a decrease of the thermal gradient ahead of the interface, Figure 23. Therefore, to eliminate any influences of changes in thermal conditions only the first 5mm of each sample are considered.

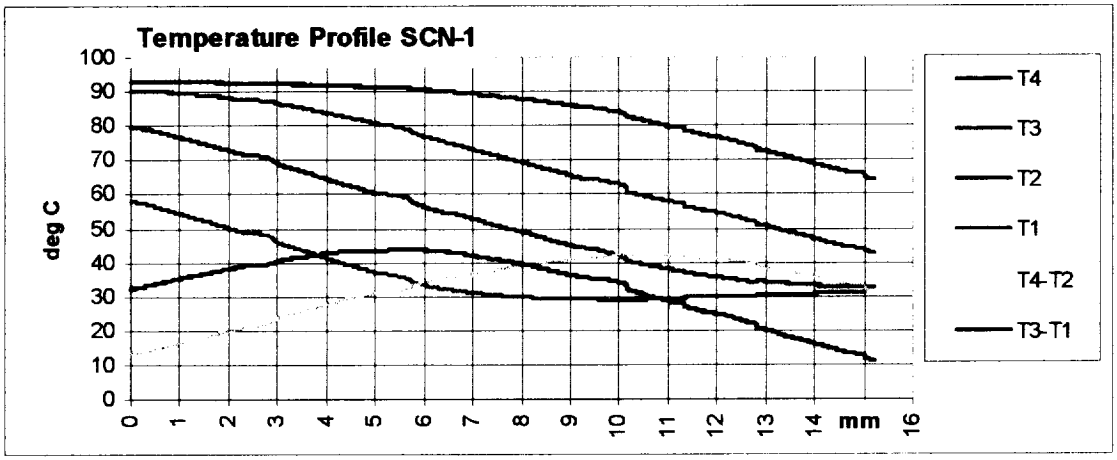

Figure 23 Temperature Profile of SCN-1 over whole processing length

It is typically accepted that the dependency of particle radius and critical velocity can be described by a simple function:

Eq. (1) $V_{cr} = const. * R^a$

The value of the exponent is approximated as $a = -0.5$. For the compiled experimental results an upper and a lower bound were established by applying such a function to the experimental data of SCN/polystyrene (Figure 24) and for biphenyl/glass (Figure 25). These lines separate the data in regions of only pushing, only engulfment, and a transition region. In the SCN/polystyrene system the constant for the lower bound is 2.96 10^{-9} and 3.97 10^{-9} for the upper bound. For biphenyl/glass the constant for the lower bound is 2.79 10^{-9} and 6.98 10^{-9} for the upper bound.

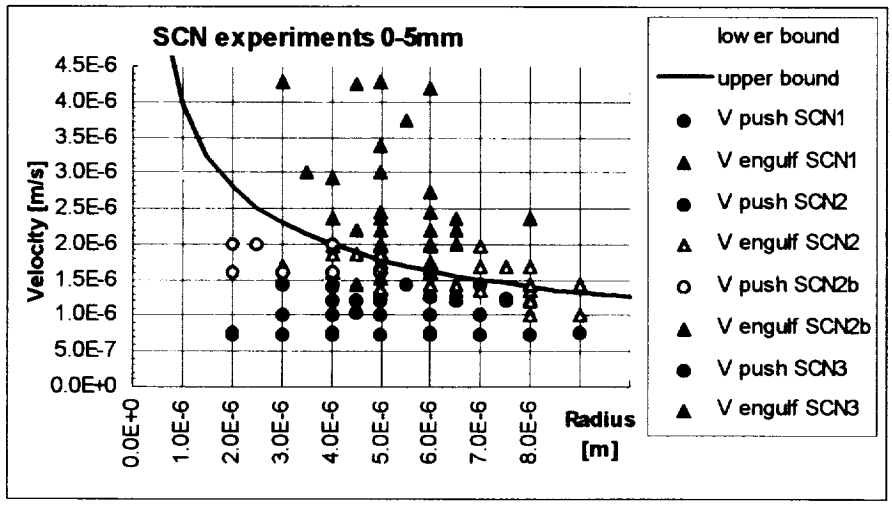

Figure 24 All data points for SCN with lower and upper bound

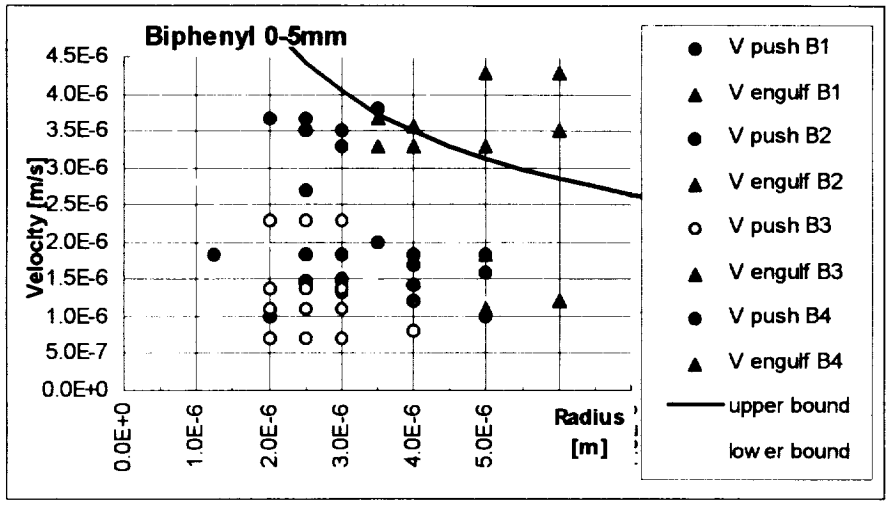

Figure 25 All data points for biphenyl with lower and upper bound

For the SCN data the upper and lower bounds are relatively close together. They are in the range of 0.5 µm/s difference. Considering experimental sources of error, e.g., measurements, magnification, the agreement with the theory is reasonable good. This indicates that the equation for the critical velocity with an exponent of a = -0.5 can be used to describe the experimental data. In contrast, the gap for the biphenyl samples is significantly wider. It is in the range of 2 µm/s. The experimental data can again be described by Eq. (1) with an exponent of a = -0.5. As mentioned previously it has been observed that especially small particles tend to move in a vivid motion parallel to the SL interface at the interface. This could originate from a surface energy

anisotropy due to the faceted nature of biphenyl. However, this behavior has not been observed in 1-g conditions.

USMP-4 data vs. ground data

The comparison of 1-g and μ-g experimental data for SCN is given in Figure 26. The upper and lower bounds are taken from Figure 24. The data points originate from two independent ground experiments at the University of Alabama. The connected data points are values of the critical velocity from [13] while the individual data points are from [14]. The comparison reveals that the critical velocity is higher in 1-g conditions. This is expected as an additional force has to be considered (Figure 1). The convective currents at the SL interface result in the Saffman force which forces the particle away from the SL interface. Thus for the interface to engulf the particle a higher SL interface velocity is needed. The positions of the data points suggest that the upper bound in 0-g can also be viewed as the lower bound for the 1-g experiments.

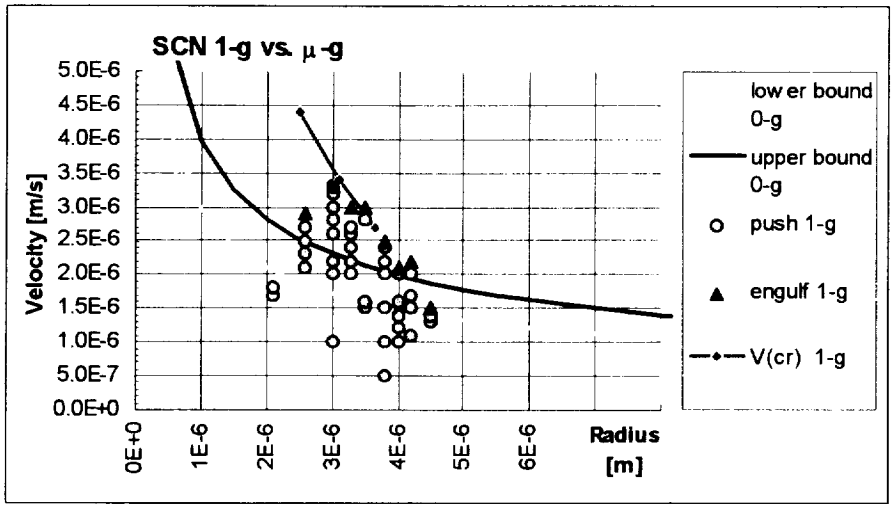

Figure 26 SCN 1-g versus μ-g results

The experimental data for 1-g experiments with biphenyl/glass are shown in Figure 27. The lines for upper and lower bound are from Figure 25. The 1-g data points are obtained from a PEP experiment done by Dr. Doi during the training phase. The discrepancy between the 1-g and 0-g

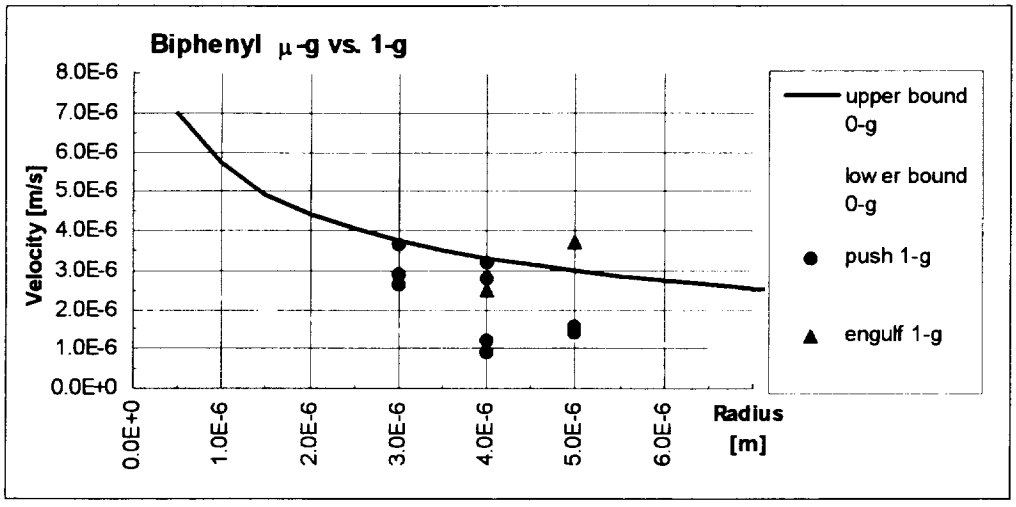

Figure 27 Biphenyl 1-g versus μ-g results

data is not very pronounced. From this limited set of data no clear statement can yet be made regarding the position of an upper or lower bound for 1-g conditions. Further experiments have to be done with this system. While SCN/polystyrene is an almost isodense system, biphenyl/glass is not. It can thus be anticipated that the density difference will significantly influence the ground data.

Model validation

The theoretical model to be tested is a further development of our earlier analytical model[15]. It is still based on the force balance between the repulsive interface interaction force, F_γ, and the drag force, F_D. The criterion for the critical velocity is though different[16]. The final equation for the critical velocity is given as:

Eq. 2 $$V_{cr} = \left(\frac{\Delta\gamma_o \, a_o^2}{3\eta K^* R} \right)^{\frac{1}{2}}$$

where $\Delta\gamma_o$ is the difference in surface energies of particle/liquid and particle/solid, a_o the atomic distance, η the kinematic viscosity, K^* the ratio of the thermal conductivities of the particle and the liquid, and R the particle radius.

It has been demonstrated that this equation describes well the behavior of zirconia particles in an aluminum melt in a μ-gravity environment[17]. However, for these transparent organic matrices the use of the atomic distance is not suitable. The molecular structure has to be considered and is reflected in the value of a_o.

SCN samples

The base for model comparison are the upper and lower bounds as established in Figure 24. The data used for the model are : $\Delta\gamma_o$=1.01 10^{-2} J m^{-2}, η = 2.59 10^{-3} kg m^{-1} s^{-1}, K_p=7.94 10^{-2} W m^{-1} K^{-1} and K_l = 2.23 10^{-1} W m^{-1} K^{-1}. The value of a_o was calculated to be 1.27 10^{-9} m. The calculation was based on the molar volume and consideration of the acentricity factor of the SCN molecule. The theoretical calculation is compared with the experimental results in Figure 28.

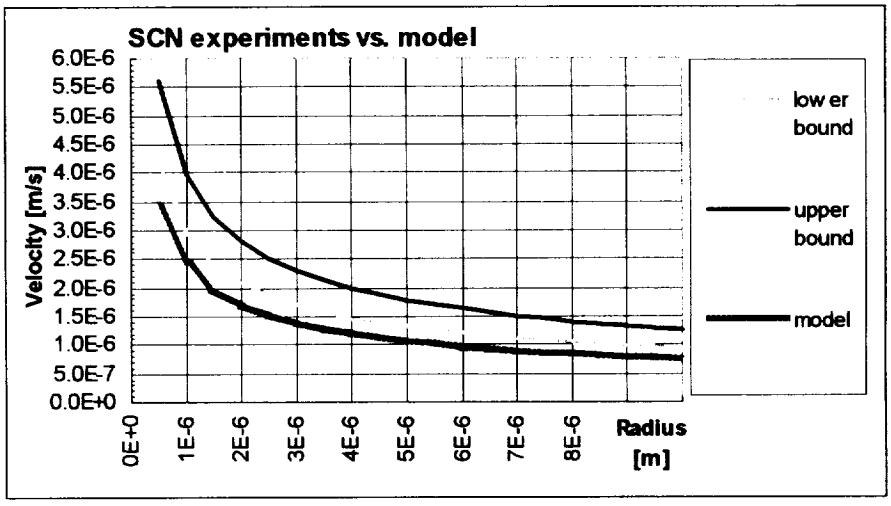

Figure 28 Comparison of experimental data with model prediction for SCN.

The model predicts a critical velocity which is closely matched by the lower bound. The deviation ranges between 0.2 - 0.3 μm. This deviation is well within the range of experimental error of the data points.

Biphenyl samples

The established upper and lower bounds for biphenyl (Figure 25) are compared with the model in Figure 29. The values used for calculation were: $\Delta\gamma_o = 1.43\ 10^{-2}$ J m^{-2}, $\eta = 9.7\ 10^{-4}$ kg m^{-1} s^{-1}, $K_p = 1.256$ W m^{-1} K^{-1}, $K_l = 1.38\ 10^{-1}$ W m^{-1} K^{-1}, and the value for a_o was $8.25\ 10^{-9}$m.

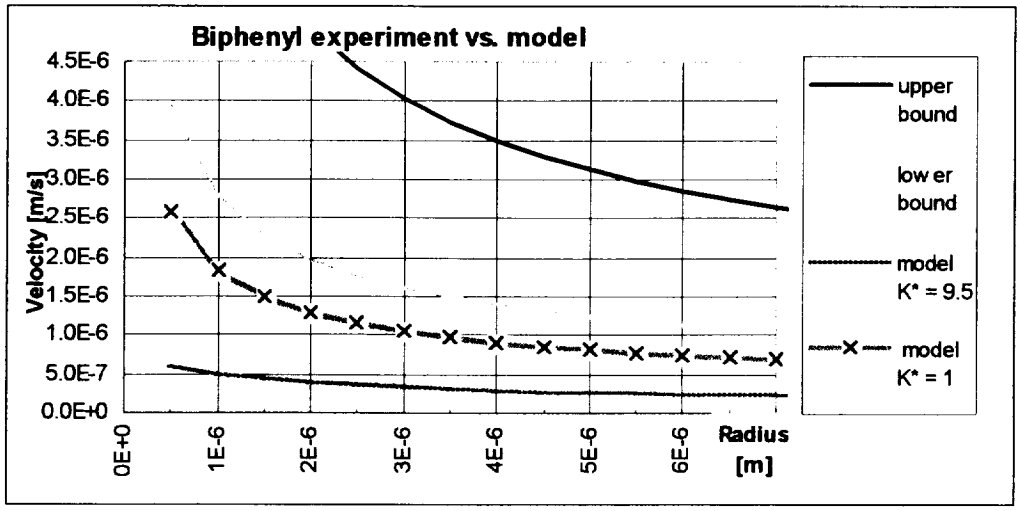

Figure 29 Comparison of experimental results with model predictions for biphenyl

The experimental data for biphenyl are significantly different in comparison to SCN. While still a clear distinction can be made between a pushing and engulfment region, the prediction by the model is significantly lower.

One possible explanation of this discrepancy could be that the biphenyl is a faceted material. Consequently local deformation of the SL interface is more difficult. Thus, according to Eq. 2, the value of K^* should be decreased, and thus V_{cr} should increase. Furthermore, particle motion at the SL interface, especially for small particles, will induce an additional force, which will increase the critical velocity of engulfment and thus shift the calculated velocity upward. As a minimum value of K^* an additional line is shown in Figure 29. It represents the upper limit of the theoretical calculation with $K^* = 1$. This decreases the difference between lower bound and theoretical calculation within 0.5 μm/s. It can thus be hypothesized that for systems like biphenyl/glass, which solidify faceted and exhibit a large value for K^*, a value of 1 for K^* is required to describe the experimental data.

The constants for each system and the constant calculated for the model, as used in Eq. (1), are listed in Table 4. For SCN the calculated constant is relatively close to the value of the lower bound. For biphenyl with a K*=9.5 the calculated value is about an order of magnitude smaller than the experimental data. However, for the case of K*=1 the value approaches the lower bound.

Table 4 Comparison of constants as used in Eq. (1)

System	*const.* from experimental data		*const.* from theoretical model
	lower bound	upper bound	
SCN/polystyrene	$2.96\ 10^{-9}$	$3.97\ 10^{-9}$	$2.43\ 10^{-9}$
biphenyl/glass	$2.79\ 10^{-9}$	$6.98\ 10^{-9}$	$6.06\ 10^{-10}$ with $K^*= 9.54$ $1.38\ 10^{-9}$ with $K^*= 1$

Conclusions

A series of eight PEP experiments have successfully been conducted in a microgravity environment. The transparent organic matrix materials allowed the *in-situ* observation of pushing and engulfment in real-time. For the evaluation of the critical velocity only the first 5mm of processing length were considered. This was done to avoid the effects of possible accumulation of solute and changes in the thermal gradient during processing. These experimental results present a bench mark set of data for the validation of models describing the engulfment/pushing transition of inert particles. For each system upper and lower bounds were established which confine a transition region. For the SCN samples this region is about 0.5 μm/s wide. For the biphenyl samples this range is about 2 μm/s.

The model proposed to predict the critical velocity of engulfment has been validated for the system SCN/polystyrene where a reasonable agreement between model predictions and the lower bound is achieved. The deviation of lower bound and the model is in the range of 0.2-0.3 μm/s. For the system biphenyl/glass the model predicts significantly lower values for the critical velocity then experimentally determined. It is suggested that the faceted solidification mode significantly contributes to this discrepancy. In addition to the data on V_{cr} other observations include the behavior of agglomerates at the solid/liquid interface and the behavior of small particles at a faceted planar solidification front. The evaluation of these data is still underway.

Acknowledgments

The PEP team would like to thank the crew and especially the payload specialists Dr.Kalpana Chawla, Dr.Takao Doi and Cpt. Winston Scott of STS-87 for their patience during the training phase and for their good work in orbit. Thanks to Z.Hester, J.Brunson, T.Hernandez, T.Broach, A.Dorries, A.Johnston at Marshall Space Flight Center in Huntsville, AL for their relentless support during the preparation and flight phase. Thanks also to G.Smith and L.Adcock at the University of Alabama in Huntsville for their help with the experimental hardware. This project was sponsored by NASA grant no.NAS 8 - 39715.

---

[1] D.M.Stefanescu, B.K.Dhindaw, S.A.Kacar, A.Moitra: *Met.Trans.* A, vol.19A, 1988, pp. 2847
[2] Y.Wu, H.Liu, E.J.Lavernia: *Acta Metall.Mater.*, vol.42, no.3, 1994, pp. 825
[3] K.A.Jackson, B.Chalmers: *J.Appl.Phys.*, vol.29, no.8, 1958, pp.1178
[4] Q.Han, J.D.Hunt: *ISIJ Intl.*, vol.35, no.6, 1995, pp.693
[5] S.Sen et al: *J.Crystal Growth* , 173, 1997, pp.574
[6] Polymer Handbook 3rd edition, J.Brandrup, E.H.Immergut
[7] R.C. Weast editor, CRC Handbook of Chemistry and Physics, 67th ed., CRC Press Inc., Boca Raton, Florida (1986)
[8] W.Kurz and D.J.Fisher, Fundamentals of Solidification, Trans.Tech Pub.,Switzerland (1989)
[9] W.Y.Lalland and C.M.Burns: *J.Polymer Sci. Polymer Phys.*, 12, 1974. pp.431
[10] Kirk-Othmer: Encyclopedia of Chemical Technology, 4th edition, Vol.4, Wiley&Sons, 1992
[11] S.N. Omenyi, A.W. Neumann: *J.Appl. Phys.*, 47, 9, 1976, pp.3956
[12] J.Timmermans, in: Physico-Chemical Constants of Pure Organic Compounds (Elsevier, Amsterdam, 1950), p.549
[13] H.Pang, D.M.Stefanescu, BK.Dhindaw: in 2nd Intl.Conf. Cast MMC's, Tuscaloosa, AL, 1993, pp.57
[14] R.S.Bhamidipati: M.S. Thesis, 1998, University of Alabama
[15] D.Shangguan, S.Ahuja, D.M.Stefafnescu: *Met.Trans.*, vol.23A, 1992, pp.669
[16] D.M.Stefanescu, A.V.Catalina: *ISIJ Intl.*, vol.38, no.5, 1998, pp.503
[17] D.M.Stefanescu et al: *Met.Trans.*, vol.29A, 1998, pp.1697

WETTING CHARACTERISTICS OF IMMISCIBLES

J.B. Andrews and L.J. Little
Department of Materials and Mechanical Engineering
University of Alabama at Birmingham

ABSTRACT

Early microgravity experiments with immiscible alloys were usually carried out with the intent of forming dispersed microstructures. By processing under microgravity conditions, the main mechanism leading to gross phase separation could be eliminated. However, analysis of flight samples revealed a separated structure where the minor phase was present along the outer surface, while the major phase was present in the center. The Wetting Characteristics of Immiscibles (WCI) project, which flew aboard the USMP-4 mission in November of 1997, was designed to gain insight into the mechanisms causing segregation of these alloys. This investigation utilized an immiscible transparent organic alloy system and a transparent container in order to facilitate direct observation of the separation process. A range of immiscible alloy compositions was utilized in order to obtain variations in the minor and major phases present and observe the influence on the segregation processes. A small composition range was found where the minor liquid phase perfectly wet the cell gasket. Unexplained observations were made at the extremes of the composition range.

INTRODUCTION

Binary immiscible alloys are made of two components which, on melting, form two separated liquids that exist over a temperature and composition range. Many desirable characteristics and uses have been proposed for these immiscible alloys (1-4). For example, some immiscible alloys show promise for use in medical applications, including use as filters for sub-micron particulates. Other alloys are expected to exhibit Type II superconductivity or high coercive magnetic field strengths. In order to obtain these desirable characteristics, it is necessary to prevent the normal segregation problems that hinder the ability to form desired microstructures in immiscible alloy systems.

The most common segregation mechanism in immiscible alloys is gravity-driven sedimentation of the higher density immiscible liquid phase. This difficulty usually occurs during normal processing in an attempt to form a dispersed microstructure. Sedimentation can also occur during directional solidification to form an aligned structure if interface stability is not maintained. Microgravity processing should provide a solution to this problem. However, segregation has also been observed in low gravity processed immiscible alloys (5-10). There are obviously some critically important, but less studied, factors that influence segregation during microgravity processing. These factors include the interfacial energies between the phases (11),

alloy/ampoule reactions (12), droplet migration due to gradients in surface tension brought about by temperature and compositional inhomogeneities (10), the relative volume fractions of the immiscible phases (7), and alloy/ampoule wetting characteristics (7, 12-14).

In this investigation, transparent immiscible metal analog samples were used in order to study how the wetting behavior between the immiscible phases in hypermonotectic samples and the ampoule influence segregation. The succinonitrile-glycerin alloy system, which has been used by several researchers in past studies, was selected because the segregation process could be directly observed. This alloy system also exhibits a reasonable monotectic ($L_1 \rightarrow S_1 + L_2$) temperature. (See Figure 1).

The alloy compositions used covered the composition range of the miscibility gap. Using this approach allows the investigation of combinations where the minor phase wets the ampoule and where the minor phase does not wet the ampoule. In addition, it should be possible to study the influence of the volume fraction of the two immiscible phases on the segregation process.

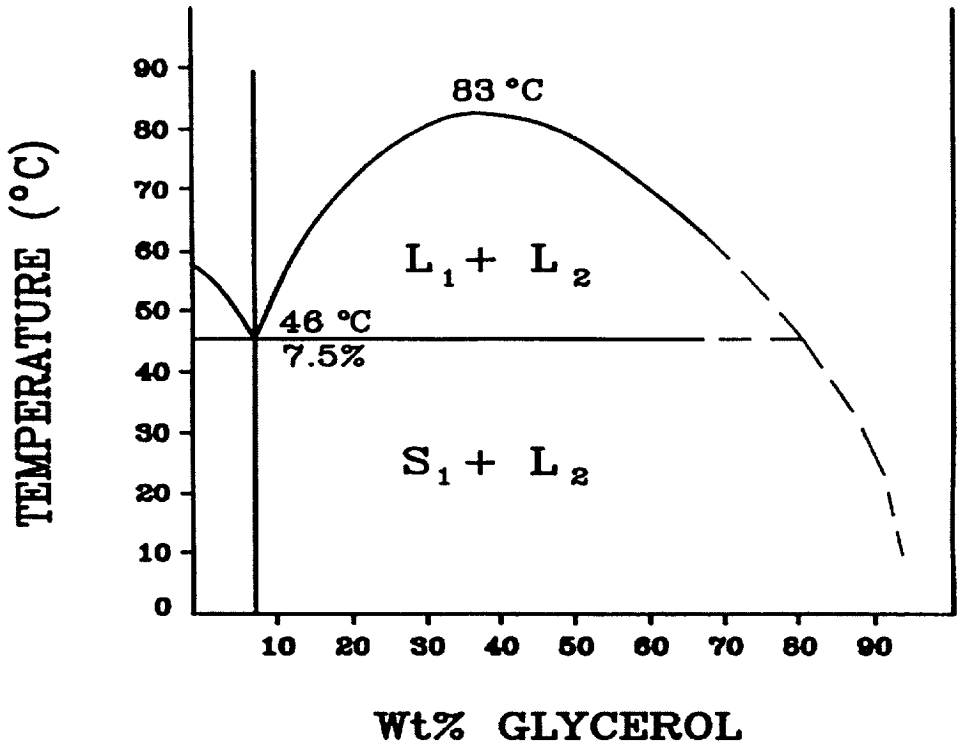

Figure 1. Partial succinonitrile-glycerin phase diagram as proposed by Kaukler (15)

BACKGROUND

While, there are several operative segregation mechanisms in immiscible systems, one of the most important of these mechanisms appears to involve the wetting characteristics between the immiscible phases and the ampoule (7, 12-14). When an immiscible (i.e. hypermonotectic) alloy is cooled into the miscibility gap, droplets of one of the liquid phases will form in the other. One theory postulates that if the lower volume fraction immiscible liquid phase perfectly wets the ampoule, segregation will occur. Droplets that touch the ampoule will immediately wet the wall and spread along it. The flow produced in the adjacent liquid by this spreading action brings additional immiscible liquid droplets to the wall where the process is repeated. This usually results in massive segregation where the low volume fraction immiscible liquid phase is found along the ampoule wall surrounding a core of the high volume fraction phase. Figure 2 depicts this series of events.

There is also speculation that nucleation events may be strongly affected when the minor phase perfectly wets the container wall. For perfect wetting, the surface energy of the system is actually reduced once nucleation has taken place. This results in no surface energy barrier to heterogeneous nucleation of perfectly wetting droplets on the ampoule wall. This heterogeneous nucleation could also result in the minor phase being found along the ampoule wall.

Another factor that has an influence on the segregation process is the volume fraction of the minor phase. Alloys in which the minor phase is present at a higher volume fraction may be expected to exhibit more rapid coalescence and different wetting characteristics than low volume fraction alloys (12).

Cahn's analysis of wetting in immiscible systems indicates perfect wetting is anticipated between one of the immiscible liquid phases and a solid surface for compositions near the center of the miscibility gap (16). The range over which this perfect wetting occurs varies with the alloy systems and with the solid surface.

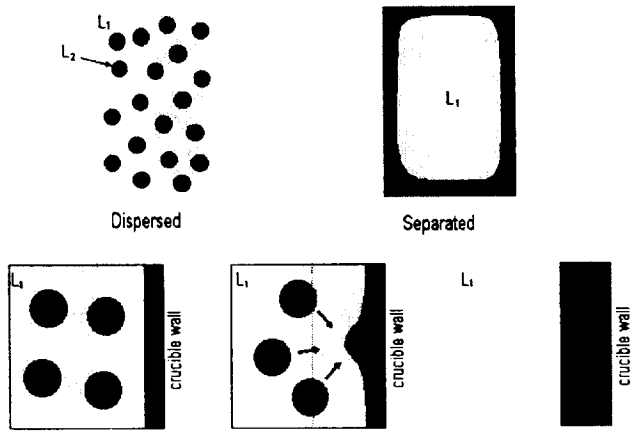

Figure 2. Series of events that lead to segregation of phases in an immiscible alloy due to wetting.

EXPERIMENTAL APPROACH

In this investigation, it was important that nucleation events, droplet coalescence and droplet migration were directly observable. This requirement dictated the use of a transparent analog sample (succinonitrile-glycerin) and a transparent cell assembly of a suitable aspect ratio for experimentation. Cells were constructed from standard 25mm x 75mm x 1mm microscope slides, separated by a Teflon® gasket (See Figure 3). The microscope slides were cleaned using boiling ethanol and then distilled water. It was not necessary to provide a non-wetting coating for the glass slides. Several gasket thicknesses were initially tried with the final design using a relatively small wall-to-wall spacing (0.13mm) in order to optimize optical characteristics. Nucleation on or droplet migration to the Teflon® gasket surface was monitored during the investigation. Fine gauge thermocouples (0.051mm) were embedded in the gasket material on each edge of the cells to monitor nucleation temperatures and verify the thermal history of the cells during processing.

Special care was necessary in filling these thin cells with the alloy. It was necessary to carry out sample mixing and filling with the solutions and cells heated to 90°C. In addition, all work was done within a glovebox filled with an argon atmosphere. The sample cells were filled by a modified vacuum backfill method. The filling procedure was performed using a vacuum desiccator, which was contained in the glovebox. The empty cells were placed on a copper plate, which was fixed to the bottom of the desiccator and maintained at a temperature of 90°C. The heated succinonitrile-glycerol mixture was pipetted onto the opening of the heated sample cell. After this step, the vacuum desiccator was closed, and evacuated using a roughing pump. Once the assembly had been evacuated, argon was bled into the desiccator and served to push the solution into the evacuated cells. A Teflon® plug was then used to close the cells and this plug was sealed using a silicone sealant.

The sample cells were processed aboard NASA's STS-87 USMP-4 mission, during the fall of 1997. The sample cells, containing the succinonitrile-glycerol mixtures, were first heated to 90°C using a thermal chamber. The cells were held at this temperature for times ranging from 15 to 25 minutes in order to allow homogenization. Once homogenized, the crew removed the cells from the thermal chamber and placed them on a backlit holder for observation using a stereo microscope during cooling. The microscope was outfitted with a video camera. The camera image was displayed on a lap top computer screen within the shuttle middeck area and was both recorded and downlinked to the ground to permit real time observation by the investigators. Figure 4 shows a schematic of the equipment setup of the experiment. Twelve sample cells, with varying compositions were processed. Table 1 lists the target and actual compositions along with the sample number. Samples with high percentages of glycerin were processed first because of their limited shelf lives.

With the particular immiscible alloy system used in this investigation, it was expected that as samples on the glycerol-rich side of the miscibility gap cooled, the succinonitrile-rich droplets which formed may have wet the ampoule gasket and formed a segregated structure. For compositions near the midpoint of the miscibility gap, perfect wetting was expected to occur. The perfect wetting would result in a succinonitrile-rich layer that coated the ampoule gasket and surrounded a core of glycerol-rich liquid. For samples on the succinonitrile-rich side of the

miscibility gap, as the sample cooled glycerol-rich droplets were expected to form. The minor glycerol-rich liquid phase should not wet the ampoule gasket; while the succinonitrile-rich phase should. As a result, a dispersion of glycerol-rich liquid droplets in a succinonitrile-rich liquid matrix was anticipated.

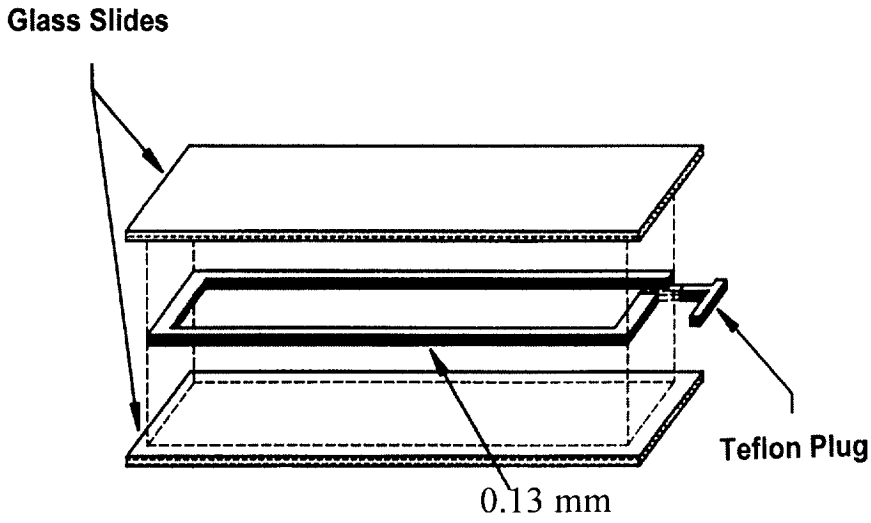

Figure 3. Sample cell assembly

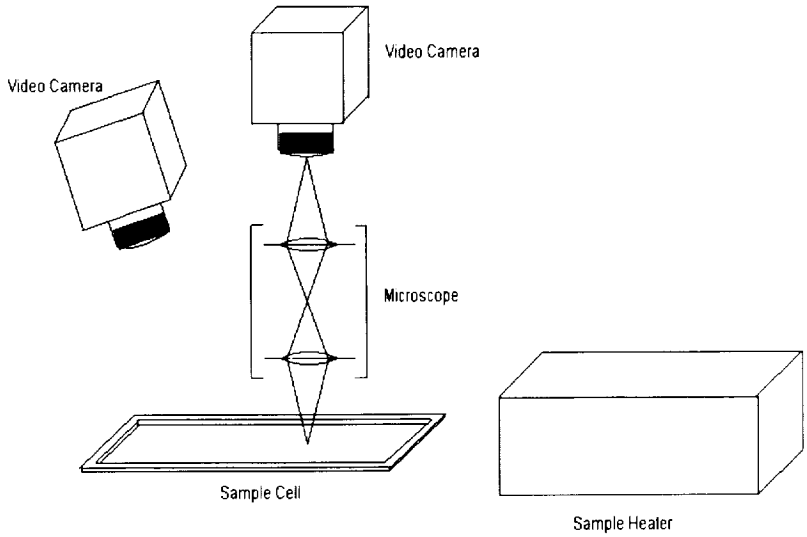

Figure 4. Experimental setup

Table I. Desired and actual compositions used for the experiment.

Sample Number	Target Composition (Wt % GLY)	Actual Composition (Wt % GLY)
1	70	70.03
2	65	65.03
3	60	60.08
4	55	55.03
5	50	50.07
6	45	45.02
7	40	39.99
8	35	35.00
9	30	29.99
10	25	25.05
11	20	20.06
12	15	15.04

RESULTS AND DISCUSSIONS

The first cells processed were those which were high in glycerol content. This composition range resulted in the formation of succinonitrile-rich droplets in a glycerol-rich liquid when cooling from the single-phase liquid region. The magnification of the microscope was initially set so that the width of the video frame was approximately 1mm. In addition, the field of view was set such that events at the gasket edge could be observed. A location adjacent to one of the cell thermocouples was selected so that accurate temperature information could be gathered. Real time video downlink during the cooling phase for each sample permitted observation of the results and facilitated crew/investigator interaction during processing.

The first four samples (70, 65, 60, and 55 wt% GLY) behaved in a manner consistent with what was anticipated. In these samples succinonitrile-rich droplets appeared to nucleate more or less uniformly throughout the cell without preferential nucleation on the gasket. While droplets were found at the gasket surface, the approximate contact angles were relatively high. During the early stages of a typical experiment, low velocity flow was usually apparent in the liquid. However, droplet movement appears to occur in several different directions. Coalescence of droplets was also apparent during the processing of these samples. Later in the run after the samples had solidified, the image was scanned along the gasket. Contact angles between the succinonitrile-rich droplets and the gasket were seen to range from approximately 30 to 80 degrees. An image obtained from a 55 wt% GLY sample during this late stage of a processing run is shown in Figure 5.

Figure 5. Image obtained from a 55 wt% GLY sample during processing. The gasket material is seen at the bottom of the image and the succinonitrile-glycerol mixture is at the top.

The behavior of the 50 wt% GLY sample during cooling was quite different. At the beginning of processing, nucleation and rapid coalescence were observed; however, there was no apparent migration of the droplets. As the field of view was moved along the gasket surface, several regions with relatively low contact angles ($\approx 10°$) were seen. Further movement along the gasket surface revealed an extended region that was covered by a continuous film indicating perfect wetting. This is shown in Figure 6.

Figure 6. Image obtained from a 50 wt% GLY sample. Note the continuous succinotrile-rich liquid film along the gasket surface near the bottom of the frame.

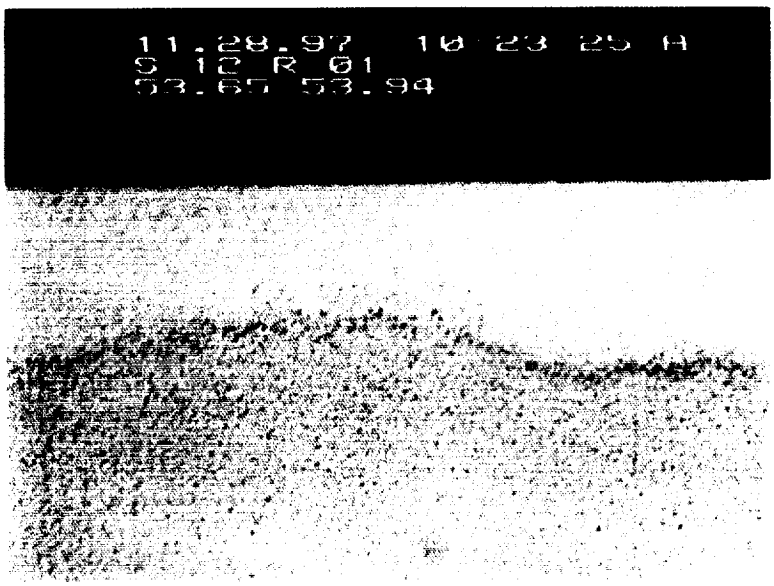

Figure 7. Image of a microgravity processed 15 wt% GLY sample. Note the region adjacent to the gasket surface is free of glycerol-rich droplets.

Unfortunately, the nucleation events at or adjacent to the gasket surface took place outside the field of view of the microscope in the 50 wt% GLY sample. It would have been most informative to observe if preferential nucleation took place at the gasket surface or if the film formed due to droplet migration alone. The dramatic difference in behavior between the 55 wt% GLY and the 50 wt% GLY samples is of great significance. The fact that perfect wetting occurred in some areas of the 50 wt% GLY sample but was not observed for the 55 wt% GLY sample indicates that the perfect wetting transition occurred somewhere between 50 and 55 weight percent glycerol.

The non-uniformity of the film in the 50 wt% GLY sample raised questions about whether the 15 minute homogenization time was sufficient. As a result, the time was increased to 20 minutes in the remaining samples. The next sample processed (45 wt% GLY) exhibited similar behavior to the 50 wt% GLY sample. Unfortunately, this sample had started to degrade before processing. This was due to an unusually high cabin temperature during a portion of the mission and a limited shelf life of the samples. As a result, there are too many unknowns to permit a sound analysis of this sample.

The remaining samples (most of which had a longer shelf life) were on the succinonitrile-rich side of the miscibility gap. Therefore, during cooling these samples all formed a succinonitrile-rich liquid containing droplets of the glycerol-rich liquid. In all cases the glycerin did not perfectly wet the Teflon® gasket. This, nonwetting behavior permitted the formation of a uniform dispersion in most samples.

The last sample processed contained the least amount of glycerol (15 wt% GLY) and exhibited unanticipated behavior. Samples of this composition had always produced a fairly uniform structure when processed on the ground. However as can be seen in Figure 7 during microgravity processing, droplets of the glycerol-rich liquid appeared to move away from the gasket surface yielding a small droplet free region. It is assumed this behavior resulted because the glycerol-rich droplets did not wet the gasket surface and, in fact, were in some manners repelled from it. The

the glycerol-rich droplets did not wet the gasket surface and, in fact, were in some manners repelled from it. The fact that this behavior had not been observed during ground processing was most likely due to the drag of droplets along the cell surface due to sedimentation. Further work is being done to determine the origin of this anomaly.

SUMMARY

Twelve samples in the transparent model system, succinonitrile-glycerol, were processed during the USMP-4 mission in the fall of 1997. A transparent cell assembly was utilized to permit direct observation of the events taking place. Sample compositions covered the majority of the composition range of the miscibility gap.

Perfect wetting was observed in the 45 and 50 weight percent glycerol samples. This perfect wetting led to the formation of a film of the minor phase around the perimeter of the cell. This behavior may explain difficulties encountered by some investigators in producing a uniform dispersion in microgravity processed immiscible alloy systems. An unexplained observation was made at one of the composition extremes where droplets were found to move away from the gasket surface leaving a depleted region during processing.

ACKNOWLEDGMENTS

The authors wish to acknowledge the support of the National Aeronautics and Space Administration for this research under contract NAS8-39717.

REFERENCES

1. J. L. Reger: Interim Report, contract NAS8-28267 NASA Marshall Space Flight Center, TRW System Group, Redondo Beach, CA (1973).

2. A.J. Markworth, W. Oldfield, J. Duga, S. H. Gelles, "Investigation of Immiscible Systems and Potential Application," NASA CR-120667, 1975.

3. R. A. Parr and M. H. Johnston, "Growth Parameters for Aligned Microstructures in Directionally Solidified Aluminum-Bismuth Monotectics," Metal. Trans. 9A, 1978, 1825-1828.

4. J. Markworth, S. H. Gelles, J. J. Duga, W. Oldfield, "Immiscible Materials and Alloys," Proceedings of the 3rd Space Processing Symposium, NASA Report 74-5, June 1974.

5. S. H. Gelles and A. J. Markworth: AIAA Journal, 1978, vol 16, no. 5, 431-438.

6. T. Carlburg and H. Fredriksson: "Microgravity Studies in the Liquid-Phase Immiscible System: Aluminum-Indium," Metal. Trans., 1980, vol 11A, 1665-1676.

7. J. B. Andrews, A. C. Sandlin, P. A. Curreri, "Influence of Gravity Level and Interfacial Energies on Dispersion-Forming Tendencies in Hypermonotectic Cu-Pb-Al Alloys, Metal. Trans., 19A, 1988, 2645-2650.

8. H. C. deGroh III, H. B. Probst, "Effects of Crucible Wetting During Solidification of Immiscible Pb-Zn," NASA Technical Memorandum 101872, 1988.

9. Deruyterre, L. Froyen, "Melting and Solidification of Metallic Composites," Proceedings for the Workshop on Effect of Gravity of Solidification of Immiscible Alloys, Stockholm, ESAS, SP-219, 1984, 65-67.

10. L. Ratke, W. K. Thieringer, H. Fishchmiester, "Coarsening of Immiscible Liquid Alloys by Ostwald Ripening," Proceedings of the Norderney Symposium on Scientific Results of the German Spacelab Mission D1, 1986, 332-341.

11. P. A. Curreri, J. M. Van Alstine, D. E. Brooks, S. Bamberger, R. N. Snyder: Marshall Space Flight Center Preprint Series No. 85-0156, 1985, Marshall Space Flight Center, Huntsville, Alabama.

12. A.B. Cheney, J. B. Andrews, "The Evaluation of Ampoule Materials for Low-g Processing of Immiscible Alloys," Proceedings of the 6th International Symposium on Experimental Methods for Microgravity Materials Science, San Francisco, CA, Feb 28 - March 2, 1994, TMS, 191-198.

13. S. H. Gelles: NAS8-32952, Final Post Flight Report, MEA A1 Experiments, 1984, S. H. Gelles Associates, Columbus, OH.

14. Potard, Materials Processing in the Reduced Gravity Environment of Space, Elsevier Science Publishing Co., New York, NY, 1982, 543-551.

15. W. F. Kaukler: University of Alabama in Huntsville, private communication, January 1990.

16. J.W. Cahn, "Critical Point Wetting," Journal of Chemical Physics, 66, 1977, 3667-3672.

ACCELERATION MEASUREMENT AND CHARACTERIZATION IN SUPPORT OF THE USMP-4 PAYLOADS

M.J.B. Rogers,
National Center for Microgravity Research on Fluids and Combustion

K. Hrovat,
Tal-Cut Company

K. McPherson, R. DeLombard,
NASA Lewis Research Center

T. Reckart
Tal-Cut Company

21000 Brookpark Road
Cleveland, Ohio 44135

INTRODUCTION

One common characteristic of the USMP-4 experiments is that various effects of gravity make it difficult, if not impossible, to achieve usable results when performing the experiments on Earth's surface. Therefore, the investigators took advantage of the microgravity environment afforded by being in low-Earth orbit to perform their research. Interpretation of the experiment results both during the mission and upon post-mission analyses of data and samples required an understanding of the microgravity environment in which the experiments were conducted. To achieve that understanding, data were collected using the Orbital Acceleration Research Experiment (OARE) and two Space Acceleration Measurement Systems (SAMS). Data from those systems, combined with an assessment of mission and experiment activities, were used to characterize the microgravity environment that existed on Columbia during the mission. The text herein gives details about some characteristics of the environment that were noted during the mission and during post-mission data analysis. The disturbances studied include the Ku-band antenna 17 Hz dither; the effect of changing the Orbiter attitude deadband limits; the effects of different bicycle ergometer configurations; and the effect of IDGE experiment fans and SAMS computer hard drives. Additional information about the microgravity environment is provided in [1] and [2]. Reference [1] and supplementary data plots representing the environment throughout the majority of the mission are available at the Uniform Resource Locator (URL) cited in Table 1. Data files for both SAMS and OARE are accessible via anonymous file transfer protocol from the file server cited in Table 1.

The AADSF, CHeX, IDGE, MEPHISTO, and SAMS USMP-4 experiments were located in the payload bay of Columbia on two Mission Peculiar Experiment Support Structures (MPESS). Figure 1 is a schematic of the payload bay which gives an indication of the approximate locations of the USMP-4 experiments. The OARE was attached to the keel bridge of Columbia, underneath the other USMP-4

experiments, see Figure 2. In addition to USMP-4, several other payloads were included on the STS-87 flight. The Extravehicular Activity Demonstration Flight Test (EDFT) and the Spartan satellite deploy and retrieval were of particular interest to the USMP-4 investigators. The Spartan satellite and the equipment for the EDFT were also located in the payload bay, as were several experiments on a Hitchhiker platform.

During the STS-87 mission, primary microgravity time started at approximately MET 005/12:00. During the designated microgravity period, the crew and Orbiter control teams attempted to maintain a quiet microgravity environment. Prior to that time, the Spartan satellite deploy and retrieval and EDFT activities occurred. The Spartan satellite was deployed using the Orbiter Remote Manipulator System, with initial grapple of the satellite at MET 001/23:46. A deploy situation resulting in an uncontrolled tumbling of the satellite resulted in replanning of the mission timeline. The satellite was captured and returned to the payload bay by two crew members during an extravehicular activity (EVA) at about MET 005/07:40. A portion of the EDFT was run following the satellite stow until about MET 005/11. A redeployment of the Spartan and additional EDFT activities occurred late in the mission. Times for several activities that were of interest to the microgravity scientists are listed in Table 2. A general overview of the mission timeline is provided in Figure 3.

ACCELERATION MEASUREMENT PROGRAM SUPPORT OF USMP-4

The Microgravity Research Program's Acceleration Measurement Program is based at the NASA Lewis Research Center, providing microgravity investigators with accelerometer systems, acceleration data analysis, and carrier microgravity environment characterization.

Two types of accelerometer systems were included in the USMP-4 contingent to provide the experiments with a characterization of the microgravity environment of Columbia during the STS-87 mission. Two SAMS units were located on the MPESS. These units recorded and downlinked in near real-time acceleration data in the 0.01 Hz to 100 Hz range in support of the AADSF, MEPHISTO, CHeX, and IDGE experiments. This frequency range is mostly affected by vibrations due to the operation of Orbiter and experiment apparatus and by crew activity. More information about the SAMS is available in the literature [3-7] and details about the specific configuration of the two SAMS units on STS-87 are provided in Table 3. SAMS Unit G, Triaxial Sensor Head (TSH) C was activated during the mission, but set to a scientifically insignificant data sampling rate because of data downlink restrictions. The SAMS data are reported here in terms of the Orbiter structural coordinate system (X_o, Y_o, Z_o) and the reference frame used is such that a forward thrust of the Orbiter is recorded as a negative X_o-acceleration.

During post-mission analyses for MEPHISTO in which long series of SAMS Unit F, TSH A data were processed, it became evident that this TSH's acceleration data erroneously tracked the sensor temperature data. This problem is most evident in the lowest frequency regime of the data. Throughout the mission, the Orbiter was commanded to a number of different attitudes, which resulted in different temperature profiles. For those with large temperature variations (over the course of an orbit), the acceleration data manifests this problem most noticeably. For other periods of relatively small temperature swings, the problem is less obvious. The analyses performed for this report were done

before this problem was noticed, but the analysis results were subsequently examined to assure that this problem was properly accounted for.

The OARE measures the quasi-steady acceleration environment of the Orbiter Columbia. The OARE was mounted to the floor of Columbia's payload bay on a keel bridge, close to the Orbiter center of mass in the Orbiter X_o- and Y_o-axes. The location and orientation of the sensor with respect to the Orbiter structural coordinate system are given in Table 4. The quasi-steady microgravity environment is affected by aerodynamic drag on the Orbiter, gravity gradient effects, rotational motion of the Orbiter about its center of mass, maneuvering of the Orbiter, venting of water and air from the Orbiter, and crew activity. The OARE was designed to measure quasi-steady accelerations from below $1x10^{-8}$ g up to $2.5x10^{-3}$ g. In support of USMP-4 experiments, the sensor output acceleration signal was filtered with a Bessel filter with a lowpass cutoff frequency of 1 Hz. The output signal was digitized at 10 samples per second and was processed and digitally filtered with an adaptive trimmean filter prior to electronic storage. More information about OARE is available in references [7-10].

On STS-87, the OARE was configured such that data were recorded on-board the Orbiter and sent down to the ground periodically. The data are reported in terms of the Orbiter body coordinate system (X_b, Y_b, Z_b) with a frame of reference fixed to the Orbiter, such that a forward thrust of the Orbiter is recorded as a negative X_b-axis acceleration because a free particle would appear to translate in the negative X_b-axis direction relative to the Orbiter. OARE data are available from MET 00/00:11 through sensor saturation at MET 015/14:34 during Orbiter re-entry.

The PIMS team is tasked to characterize the microgravity environment of spacecraft and other carriers used by NASA Microgravity Research Program investigators. Real-time support of the science teams was accomplished exclusively using SAMS data. Throughout the mission, PIMS received real-time downlink data from both SAMS units, converted the raw SAMS telemetry frame to engineering unit data, and generated data plots in the format requested pre-mission by the USMP-4 principal investigators. Periodic updates to the plotted images were made available approximately every two minutes through the PIMS USMP-4 World Wide Web (WWW) page. Prior to flight, PIMS talked to USMP-4 project scientists and principal investigators in an effort to understand the nature of acceleration data support required for real-time, near real-time, and post-mission analysis. These inquiries resulted in identification of the accelerometer systems, the frequency characteristics of the SAMS sensor heads, the real-time plot formats, and near real-time plot formats to be used in support of the USMP-4 experiments.

The plot types developed by PIMS for Unit G, TSH B real-time data were driven specifically by the CHeX experiment team. Throughout the entire USMP-4 segment of the mission, the CHeX team requested plots of real-time acceleration versus time, interval maximum absolute value acceleration versus time, power spectral density, color spectrograms, and g_{RMS} versus time (for three frequency bands specified by CHeX). The plot types displayed using the Unit F, TSH A real-time data were acceleration versus time and color spectrograms. PIMS selected these plots as a compromise among varied plot type requests for the Unit F, TSH A data.

The unprocessed OARE data were recorded on the Orbiter payload tape recorder and telemetered to the ground approximately eight to ten hours after the measurement. Because the OARE data on USMP-4 were not available in real-time, payload recorder dumps containing the OARE data

were processed by Marshall Space Flight Center's Data Reduction group for subsequent processing by PIMS computers located at the NASA Lewis Research Center Telescience Support Center. The results of OARE data analysis were made available to the USMP-4 teams via the PIMS WWW page approximately ten to twelve hours after the actual measurement time had transpired. The plot types developed by PIMS using OARE data were limited to trimmean filtered acceleration versus time as measured at the OARE location and mathematically mapped to the following locations within the Orbiter: Orbiter center of mass, AADSF experiment location, and IDGE experiment location.

The AADSF experiment team requested processing of an additional set of data depicting the quasi-steady acceleration environment. This data set was from the Microgravity Analysis Workstation (MAWS). The MAWS model is used to predict the quasi-steady acceleration environment at any point in the Orbiter. The AADSF experiment team requested comparison plots of the MAWS predictions of the quasi-steady acceleration environment at the AADSF experiment location with the OARE data mapped to the AADSF experiment location. Note that the MAWS model does not include the effects of venting forces such as those resulting from water dumps and cabin pressure changes. These comparison plots were generated in support of the three AADSF experiment runs.

In addition to the real-time accelerometer data displays that PIMS provided during the mission, the PIMS team also provided data analysis and interpretation during the mission in an "off-line" fashion. When experiment team members needed information about the STS-87 microgravity environment some time after a particular event, the PIMS team used archived data to fulfill the request. During the mission, the PIMS team received approximately 100 different requests.

MICROGRAVITY ENVIRONMENT OF COLUMBIA ON STS-87

This section provides details on the effects that specific events had on the microgravity environment of Columbia.

Orbiter Systems—Ku-band Antenna

The Ku-band antenna is located on the forward starboard sill of the Orbiter's payload bay. On orbit, this antenna is used primarily for communications between the Orbiter and the ground via the Tracking and Data Relay Satellite System. In order to maintain line-of-sight, the Ku-band antenna must slew to compensate for motion of the Orbiter with respect to these communications satellites. The Ku-band antenna is mounted on gimbals, which allow for this tracking; however, the antenna must be dithered at 17 Hz to prevent stiction of the gimbal mechanism. Reaction torque forces at the base of this assembly introduce a strong 17 Hz oscillatory disturbance into the acceleration environment of the Orbiter, along with various contributions from its second through at least its sixth harmonics. Focusing analysis on a narrow spectral region (0.2 Hz wide) centered on the dither frequency, we can track the root-mean-square (RMS) acceleration for the frequency band from 16.93 to 17.13 Hz. Figures 4 and 5 depict 56-hour periods for this type of analysis performed on SAMS Unit F, TSH B data for the USMP-3 and USMP-4 payloads, respectively. For both of these missions, SAMS Unit F, TSH B was mounted on the forward MPESS at the Orbiter structural coordinates shown in Table 5.

The vertical dashed lines at the 47-hour mark in Figures 4 and 5 indicate the Ku-band antenna stowage time, which brings antenna dithering to an end. Table 6 aims to quantify the measured disparity between "dither on" and "dither off" periods. The values given represent the average RMS acceleration values for the times shown.

While the ambient Orbiter environment for this small frequency range was measured to be under 10 μg_{RMS}, the antenna dithering added over 100 μg_{RMS} for both USMP-3 and USMP-4 missions. The Euclidean distance between the two Orbiter cargo bay positions enumerated in Table 5 is approximately five feet, but transmission of the dither frequency vibrations for the different structural paths to these locations is uncertain. Table 6 suggests a couple of possibilities: the USMP-3 location was less responsive to the 17 Hz disturbance than the USMP-4 location, and/or the dithering intensity was somewhat greater on the latter mission. Note that acceleration measurements recorded in the Spacelab module during STS-65/IML-2 averaged around 100 μg_{RMS} for this same 0.2 Hz wide frequency band. This would suggest, not surprisingly, that transmission of the Ku-band dither excitation is damped by the structure of the Spacelab module. Speculation that a Spacelab module structural mode exists around 17 Hz is not supported by these observations.

While the dither intensity does typically vary with time throughout most missions, there are certain times when the intensity decreases or the dither is turned off altogether. Expected off times take place during gimbal flips. When the Ku-band antenna is actively tracking a satellite and the line-of-sight causes one of its two gimbals to reach their physical limit, the system will do what is commonly called a gimbal flip [4]. During the gimbal flip, the antenna will quickly slew (20°/sec) until the dish is again pointing in the correct direction on the other side of the physical stop. During fast slew operations, the 17 Hz dither is disabled. Analyses of SAMS Unit F, TSH B data and data for the Ku-band antenna's alpha gimbal angle indicate that when the antenna is slewing quickly, the dither disturbance is non-existent [1].

Prior to de-orbit, the Ku-band antenna must be moved into its stowed position so that the payload bay doors can be closed for re-entry. Table 7 details timing of the events for this stow procedure. Analysis of SAMS Unit F, TSH B data for this period indicates the spectral peak at the dither frequency and its second and third harmonics (34 and 51 Hz) cease just before stowage [1]. It is also evident in the data that the crew forced a gimbal flip prior to stowing the antenna [11]. This is seen around the 4-minute mark in Figure 6. The dither stop time, as seen on this plot just before the 8-minute mark, occurred at MET 014/20:17:52. Mean acceleration magnitude for the dither-on times in Figure 6 was 264 µg, compared to about 83 µg for the dither-off times. The highest acceleration magnitudes recorded in the time frame of Figure 6 were in excess of 1×10^{-6} g, and occurred over a span of about 8 seconds just before dithering ceased. When the crew takes the "KU ANT" switch to the "STOW" position, the system moves to prescribed stow angles. Next, the system drives the locking pins, and then performs a "wiggle" test to verify that the pins are seated properly and that the antenna is in a locked position. This would account for the large accelerations observed just before the 8-minute mark of Figure 6 [12].

Orbiter Systems—Vehicle Structural Modes

Vehicle structural modes constitute some primary components of the Orbiter's vibratory environment in the oscillatory region of the acceleration spectrum. In the absence of substantial

transient acceleration events or crew exercise, these resonant frequencies dominate the spectrum below about 10 Hz. They establish the ambient oscillatory acceleration environment in this spectral region in that they are always present with varying degrees of intensity. Crew exercise and Orbiter thruster firings tend to excite these resonances, causing heightened acceleration levels which persist for a short period of time before damping down towards some baseline.

Columbia's thrusters imparted numerous impulsive accelerations in an attempt to track the wayward Spartan satellite from about MET 002/01:20 to about MET 002/12:00. Like sporadic pinging of a tuning fork, these firings excited the Orbiter's natural frequencies and provided the opportunity for examining the heightened response of these vehicle structural modes. Toward that end, spectral averaging was performed on Hanning-windowed power spectral density (PSD) calculations using the parameters shown in Table 8 for the period from MET 002/02:30 to MET 002/07:30. Note that the last column shows the aggregate span of the spectral average. This does not total five hours, as suggested by the MET span, because any candidate PSD period containing a substantial impulsive transient (like would be the case for a thruster firing) was ignored. The intent here was to examine the resonant ringing after these impulsive accelerations. Figures 7, 8, and 9 show the resultant PSDs. Once these were computed, the RMS accelerations were then derived from them via Parseval's relation to yield the results shown in Table 9.

The resonance at 3.5 Hz represents an Orbiter fuselage torsion mode and expectedly imparts most energy in the Y_o Z_o-plane. The strongest structural mode resides at about 4.7 Hz and aligns primarily with the Z_o-axis. Note that structural modes can be hard to identify on plots of short periods of time, but are readily apparent when examining a long-duration spectrogram.

The spectrogram of Figure 10 represents an arbitrary 6-hour time frame where the structural modes quantified in Table 9 are indicated by the long horizontal ticks shown on the frequency axis. Of these, the mode at 3.2 Hz is the most obscure, while again we see that the 4.7 Hz mode is the most intense. The RMS accelerations shown in Table 9 were computed from a time span of repeated impulsive battering. In order to investigate the nominal behavior of the 4.7 Hz mode measured over a longer time frame, the RMS acceleration contributed by this mode was computed every 81 seconds for SAMS Unit F, TSH A data, and every 66 seconds for TSH B data from both SAMS Units F and G. This RMS acceleration tracking was performed for the 24-hour period starting at MET 010/00:00. The results for SAMS Unit F, TSH B are shown in Figure 11. The salient features of this plot are as follows:

- the sample rate, f_s, shown in small text in the upper left portion of the figure represents how often the RMS acceleration value was computed (one sample every 66 seconds at 0.02 samples per second),

- the alignment of this structural mode is reinforced by comparing the Z_o-axis data to those of the other two axes; essentially, the X_o- and Y_o-axes' data represent ambient or background accelerations in this spectral region,

- the transition to crew wake occurs just before the 4-hour mark as seen by heightening of the Z_o-axis data (see also Appendix page C-44 in [1]) and the transition to crew

sleep occurs just before the 22-hour mark as seen by quieting of the Z_o-axis (see also Appendix page C-47 in [1]); as expected, crew movement tends to excite this mode,

- crew exercise periods (at around hours 4 to 6 and again at around hour 18) result in the highest measured RMS accelerations for this mode in this 24-hour period; in fact, when the third harmonic of the shoulder-sway frequency approaches 4.7 Hz (as seen at about MET 010/05:20 on Appendix page C-44 and at about MET 010/17:30 on Appendix page C-46 in [1]), the resonant RMS acceleration level contributed by this mode alone approaches that of Vernier Reaction Control System (VRCS) thruster firings.

Results from similar RMS acceleration versus time plots for SAMS Unit F, TSH A and Unit G, TSH B mimic those gleaned from Figure 11. Table 10 summarizes the results for all three plots. Comparing the shaded cells in Tables 9 and 10, note that the 4.7 Hz mode was somewhat higher in amplitude in the aftermath of the repeated thruster firings required for satellite-tracking maneuvers. In contrast to the steady, albeit nebulous, mode at 4.7 Hz, the apparent structural mode at about 3.2 Hz has been observed to shift in frequency. Most notable are the spectral shifts seen in Reference [1] on the spectrogram of Appendix page B-50 at about MET 011/12:35, 011/13:53, 011/14:39, and 011/16:43. The cause of these frequency shifts is unknown at this time.

Orbiter Systems—Deadband Collapse

The Orbiter's attitude with respect to its orbital path plays an important role in a number of operational concerns. Maintaining suitable orientation for links with communications satellites, minimizing damage by space debris, and keeping proper alignment to account for the orbital mechanics that dictate quasi-steady acceleration levels are three motivating factors for defining an attitude. Deadband is a term used to specify the allowable deviations (number of degrees and rotational rate of the Orbiter) from a desired attitude. The Orbiter's Reaction Control System is used to maintain a desired attitude, ensuring that the chosen deadband criteria are met. The Reaction Control System consists of the Primary Reaction Control System (PRCS) and the VRCS. The PRCS is typically used on orbit for pitch, roll, and yaw maneuvers, while the VRCS is used for fine adjustments of vehicle attitude. The Digital Auto Pilot (DAP) constantly monitors the Orbiter's orientation and governs the VRCS (or PRCS), commanding the proper sequence and direction of thruster firings required to return to attitude when a specified deadband limit is exceeded.

On occasion, the deadband is changed as more (or less) stringent pointing needs arise or as vehicle health issues evolve. When the deadband is changed from a higher value to a lower one, the allowable deviation from the nominal attitude decreases. This is referred to as a deadband collapse. There were numerous deadband collapses during the STS-87 mission, many of them imposed for jet temperature maintenance [13]. Table 11 is a partial list of deadband collapse times from this mission as recorded in the PIMS logbook or as indicated by examination of the acceleration data. For these times, the DAP was changing between the A3 (0.07° deadband) and the A12 (1.0° deadband) settings. Note that most of these collapsed deadbands lasted for just a few minutes. However, there were some that lasted for nearly ten minutes.

Table 12 gives a rudimentary accounting of VRCS thruster firing activity during time frames before and during two of the longer deadband collapses. The values shown in the "Number of VRCS Firings" column were retrieved from the operational downlink database maintained by the Johnson Space Center: the Mission Evaluation Workstation (MEWS). The values shown in this column were tallied such that simultaneous firings were counted as a single firing and, because the database is incomplete, these numbers represent a minimum value. For example, during the period MET 008/07:00:00–008/07:29:00, there were no fewer than 22 VRCS thruster firings.

Note from the shaded rows in Table 12 that, during the two periods of deadband collapse, the VRCS firing rate was a couple of orders of magnitude greater than during nominal periods. Qualitative examination of data plots for the times indicated in Table 11 reveals that the increased firing frequency of the VRCS during deadband collapse tends to have broadband spectral effects. Most noticeably, it excites the vehicle structural modes below about 10 Hz, and somewhat heightens the spectrum around the Ku-band antenna dither frequency (17 Hz) and its harmonics. Figure 12 provides a quantitative measure of the effects of the deadband collapse that started at about MET 008/07:29:48. The data for each of the four subplots in this figure start at MET 008/07:00. Note that the ordinate scales for the four plots shown in this figure are different. Table 13 summarizes the acceleration magnitude disparity between a portion of the deadband collapse period (MET 008/07:31 to 008/07:37) and a period preceding this (MET 008/07:00 to 008/07:29).

The values of acceleration magnitude shown in the rightmost column of Table 13 represent the average for the time frame indicated. As expected, for each sensor the acceleration magnitude was greater during the deadband collapse period. The difference was more extreme for the lower frequency sensors (TSH A for both SAMS Units F and G). This is because below 10 Hz the acceleration spectrum of the Orbiter is dominated by vehicle structural modes, which are highly excitable by impulsive events such as thruster firings. While this is still a factor for the higher frequency sensors, the effect of the firings is overshadowed by vehicle subsystems and experimental equipment vibrations above 10 Hz. For these sensors, the measured acceleration magnitude difference mentioned above is smaller because vibrations caused by experimental equipment and vehicle subsystems (except for RCS) are not driven by these firings.

Orbiter Systems—Water Dump Operations

The Orbiter Food, Water, and Waste Management Subsystem provides storage and dumping capabilities for potable and waste water [14]. Supply and waste water dumps are performed using nozzles on the port side of the Orbiter. Water dumps from these nozzles are expected to cause a steady acceleration of about 5×10^{-7} g in the Y_b-axis [15]. Figures 13 and 14 show the effect of a simultaneous supply water and waste water dump and of a supply water dump on the quasi-steady acceleration environment, as represented by OARE data. These water dump plots show contributions to the Y_b-axis and to the Z_b-axis. While the anticipated effects on the acceleration environment from water dumps is exclusively in the Y_b-axis, effects have been routinely observed in the Z_b-axis since STS-73/USML-2.

Orbiter Systems—Radiator Deployment

Radiator panels attached to the forward payload bay doors are part of the Active Thermal Control System which provides Orbiter heat rejection during a mission. The port and starboard side radiators can be deployed independently to accommodate the heat rejection requirements for a particular

Orbiter attitude or mission. An electromechanical actuation system on the door unlatches and deploys the radiators when open and latches and stows the radiators when closed [16]. In deploying each radiator, six motor driven latches are unlocked and the deploy motor moves the radiator to the desired position.

The deployment or stowage of either the port or starboard side radiator results in a general excitation of the Orbiter structural modes. In particular, the 6.3 Hz structural mode and its second and third harmonics are excited. Figure 15 is an acceleration vector magnitude versus time plot during deployment of the port side radiator. The increased magnitude around the 150-second mark of this plot illustrates the impact of the radiator deployment on the environment.

On-board Activities—Crew Sleep Cycle

Table 14 shows the MET start and stop times of crew sleep taken from the mission replanned timeline. This table shows that the nominal scheduled sleep duration was eight hours, and sleep start times shifted forward in time as the mission progressed as dictated by landing and Spartan deployment constraints. As human nature has it, the start time for sleep can be planned, but the transition is certainly not instantaneous. On the other hand, the sleep stop time can be enforced with an alarm, which in this case was a daily wake-up song that was broadcast up to the crew. These facts are evidenced by examining SAMS and OARE data.

Analyses show that an obvious quieting occurs below about 13 Hz when the crew transitions from wake to sleep. In an attempt to quantify this quieting, the RMS acceleration level contributed by the spectrum below 13 Hz was calculated approximately every 66 seconds for a 96-hour span (MET 009/12:00 to 013/12:00) for SAMS TSH B on both Units F and G. Figure 16 shows the results of these calculations for Unit F. The four pairs of consecutive vertical dashed/solid lines indicate scheduled crew sleep start/stop times, respectively, for this 4-day time frame. Note again that actual reduction in acceleration levels typically lags scheduled sleep start times by at least several minutes, while increased excitation of the environment is coincident with the scheduled wake times owing to the daily wake-up song. For the plot shown in Figure 16, the mean RMS acceleration during the non-sleep times was 62 μg_{RMS}, while the mean RMS acceleration during the four sleep periods was 23 μg_{RMS}. Calculations for Unit G yield a mean RMS acceleration during non-sleep times of 55 μg_{RMS}, and a mean RMS acceleration during sleep periods of 29 μg_{RMS}.

As might be expected, the crew may have to wake during a sleep period for one reason or another. It is quite possible that this is what happened at around MET 003/17:20 when there were 5 to 10 minutes of heightened spectral response, particularly below 10 Hz. This period coincides with an entry in the PIMS mission logbook, which notes that the IDGE science team observed "their crystal rotate and move" at that time. The correlation implied here is not a definitive cause-and-effect identification, it is merely conjecture. The IDGE team's concern about their crystal motion prompted an unsuccessful search (by Marshall Space Flight Center and Johnson Space Center controllers) for specific disturbance sources.

A summary plot of the OARE data for the entire STS-87 mission is provided in acceleration versus time format in Figure 17. This figure clearly illustrates the sleep cycles of the crew through the periodic quieting of the data on all three axes. Peak-to-peak variations are on the order of 1×10^{-6} g for

crew active periods and $0.2x10^{-6}$ g for crew sleep periods. Additional quasi-steady acceleration plots shown in [1] more clearly illustrate that multiple attitudes were flown in support of separate USMP-4 payloads and the non-microgravity payloads, including Spartan.

On-board Activities—Public Affair Office Events

While crew sleep clearly provides a certain measure of quieting as detailed earlier, there are other non-sleep times during a mission that afford similar effects on the acceleration environment. Most notably, Public Affair Office (PAO) events offer at least a brief respite for the crew. During a typical PAO event, the crew is relatively motionless and gathered in front of a camera for audio and video communications with interested parties on the ground. This period of minimal movement mimics that of sleep from an acceleration disturbance perspective, albeit for a much shorter time span. PAO events normally last around 15 to 20 minutes, compared to the 8-hour sleep periods. For this mission, the crew participated in more than a half dozen PAO events; Table 15 lists those that show up prominently in the SAMS data.

The longer-than-normal PAO event that takes place starting at about MET 012/14:49 exemplifies the quietude, especially below about 13 Hz, which can be achieved by minimizing crew movement. For person-intensive tasks, this restriction might be impractical or unfeasible, but situational awareness and planning may facilitate maximum usage of desirable acceleration environmental conditions at some time in the future of microgravity research.

The quasi-steady environment measured by OARE also exhibits a noticeable quieting during PAO events. Figure 18 shows the effect of the fifth PAO event listed in Table 15 on the quasi-steady acceleration environment. With the reduced crew activity, the quasi-steady acceleration environment variations are more pronounced, much like the effects observed for crew sleep periods. The variations in the OARE data during PAO events is typically $0.2x10^{-6}$ g peak-to-peak. Non-PAO time intervals demonstrate a peak-to-peak variation of $1x10^{-6}$ g.

On-board Activities—Bicycle Ergometer Isolation

While crew sleep periods and PAO events provide quiet microgravity conditions, other crew activity is routinely observed to have a negative effect on the microgravity environment. Crew members are expected to exercise to maintain physical conditioning. On STS-87, aerobic exercise was achieved using a bicycle ergometer. During the first few days of the mission, the ergometer was mounted to the Orbiter with each of three configurations of an ergometer vibration isolation system called the Passive Cycle Isolation System (PCIS). During mission planning, the mission management team requested that the PIMS team provide analysis of the SAMS Unit F, TSH A data collected during these initial days of crew exercise to assist them in assessing the vibration isolation performance of the PCIS. Two types of analysis were employed to quantify the differences measured by the SAMS among the three PCIS configurations and a hardmount configuration: (1) Δg_{RMS} derived from interval RMS acceleration versus time, and (2) cumulative RMS acceleration versus frequency.

The first type of analysis was aimed at quantifying the change in the RMS acceleration level for two distinct periods: a non-exercise baseline period and the exercise period of interest. Care was taken to ensure that no strong, non-exercise related disturbances below 10 Hz were present for one period and not for the other. Following the selection of appropriate baseline and exercise periods, a 0.5-second

interval RMS acceleration versus time curve was used to ascertain the difference in the median of the RMS acceleration values of the baseline and exercise periods. This was done for the three orthogonal Orbiter structural axes and for the overall RMS acceleration calculated from the root-sum-of-squares (RSS) of the axial RMS acceleration values. The results were compiled in near real-time in tabular form on a PIMS WWW page.

After the Δg_{RMS} values were calculated, the cumulative RMS acceleration versus frequency curves for both the baseline and exercise periods were plotted. These served to quantify the contributions of spectral components at and below a given frequency to the overall RMS acceleration level for the periods of interest.

Commander Kevin Kregel was the only crew member to exercise in all of the ergometer configurations. Configuration #1 used stiff PCIS mounts on the front of the ergometer and stiff mounts at the seat connection; #2 used soft front and stiff seat connections; and #3 used stiff front and soft seat mounts. Based on analyses of Kregel's early exercise, several observations were made. Overall, PCIS configuration #3 was better than either of the first two configurations. For the X_o-axis only, PCIS configuration #2 was the best. For the Y_o-axis only, PCIS configuration #1 was the best. For the Z_o-axis, the hardmount was the best. The differences among the three PCIS configurations were marginal.

Based on the analysis provided by PIMS, the following decision was uplinked to the crew as part of the Flight Day 5 Payload Summary,

> RECOMMENDED PCIS CONFIGURATION: It appears that the differences among the three configurations are marginal. However, after analyzing the $\bullet g_{RMS}$ (g_{RMS}exercise–g_{RMS}background) values for the three configurations, the final configuration was found to have the overall lowest value. Therefore, the Mission Scientist recommends the final configuration #3 as the optimum PCIS configuration for [Flight Days] 5-14.

The real-time PCIS data analysis relied exclusively on the SAMS Unit F, TSH A data which had the temperature/acceleration data problem mentioned earlier. This analysis, however, was done in a differential fashion, whereby the $\bullet g_{RMS}$ between baseline and exercise periods was the decisive quantity. Assuming that the anomalous low-frequency component varied only slightly over the span of the baseline and exercise periods, then this analysis should not have been significantly affected.

Payload Operations—IDGE-Related Disturbances

Early in the mission, following activation of the USMP-4 experiments, a set of acceleration disturbances clustered around 56 Hz was noticed in the real-time spectrogram displays of SAMS Unit G, TSH B. See, for example, the pronounced red horizontal streaks at this frequency in the spectrograms of Appendix D [1]. The CHeX team expressed concern about these disturbances because of their experiment susceptibility to vibrations around 55 Hz. During the first few days of the mission, an investigation was conducted by consulting with the various experiment teams, Spacelab-MPESS support staff, and Orbiter subsystem personnel to ascertain the source of these disturbances. In discussions with IDGE personnel, it was discovered that there were seven cooling fans within the IDGE apparatus. One of the fans had its speed controlled according to a measured internal IDGE temperature.

The 56 Hz traces, a variable frequency trace between 35 and 40 Hz, and a 74 Hz disturbance ceased at the time of the IDGE power-off at about MET 015/09:45. When the IDGE and SAMS units were returned to NASA Lewis Research Center after de-integration from the Orbiter, a vibration assessment was performed with the IDGE flight apparatus and SAMS Unit G, TSH B. This test confirmed that the variable 35 to 40 Hz trace, the traces around 56 Hz, and the 74 Hz disturbance were all related to IDGE fans.

During the ground testing of the IDGE hardware, another disturbance evident in the SAMS data was potentially assigned to IDGE. This disturbance was manifested as a persistent spectral peak at 21 Hz (1260 rpm if a rotational source) and was seen to start and stop in the bench test SAMS data. A similar disturbance was seen in the mission data. It was tightly controlled in frequency and spanned the time frame from approximately MET 000/20:39 to MET 014/15:30 with only two brief pauses. The first intermission started at about MET 001/05:19 and lasted just under seven minutes. The second started at about MET 013/09:58 and lasted just over fifteen minutes. To quantify this disturbance, its RMS acceleration was computed every 33 seconds for the 24-hour period starting at MET 004/00:00 for TSH B on both SAMS Units F and G. Figure 19 shows the RMS acceleration versus time for the frequency range from 20.8 to 21.1 Hz for SAMS Unit F, TSH B measurements. As seen, the intensity of this disturbance is somewhat variable; similar analyses of SAMS Unit G, TSH B data led to the results summarized in Table 16. The RMS values indicate that this disturbance is relatively close in intensity at the two different sensor locations.

Payload Operations—SAMS Hard Drive Disturbance

While studying the SAMS Unit G, TSH B data between the filter cutoff frequency of 100 Hz and the highest obtainable frequency limit of 125 Hz, a strong, persistent 120 Hz disturbance was noticed. Subsequent discussions with the SAMS engineering team and evaluation of ground test data led to the determination that the 120 Hz disturbance was caused by the 7200 rpm rotation of the SAMS computer hard disk drives used to record data on orbit.

Payload Operations—Orbiter Cabin and Airlock Depressurization

In preparation for the two EVAs conducted during the STS-87 mission, the crew cabin and the airlock had to be depressurized to various degrees. In preparation for both EVAs, the cabin was depressurized from a nominal 14.7 psi to 10.2 psi. Prior to egress, the airlock was depressurized from 10.2 psi to the vacuum of space. This airlock depressurization was performed in two steps, from 10.2 psi to 5.5 psi and from 5.5 psi to vacuum. The air removed from the Orbiter during depressurization was vented through a relief valve located on the port side of the Orbiter. This relief valve is located very near the valves used for conducting supply water and waste water dumps. This was the first mission where the effects of cabin depressurization and airlock depressurization on the microgravity acceleration environment were measured and recorded.

The effects of cabin depressurization and airlock depressurization are most evident in the quasi-steady acceleration environment. The OARE Y_b-axis and the OARE Z_b-axis data shown in Figures 20 and 21 indicate that the magnitude of the cabin depressurization can be as large as 10 μg. The OARE Y_b-axis and the OARE Z_b-axis data shown in Figures 22 and 23 indicate the magnitude of the airlock depressurization can be as large as 5 μg.

Figure 24 illustrates the two step process involved in performing the airlock depressurization. The dashed line shows the differential pressure between the airlock and the payload bay as indicated by data retrieved from the MEWS system. The change in the differential pressure approximately 23 minutes into the plot causes a corresponding change in the quasi-steady acceleration environment of about 5 μg. When 5.5 psi is reached, the venting is stopped for about 5 minutes. The next change in pressure results in further venting that also affects the quasi-steady acceleration environment.

Payload Operations—EVA Operations

As NASA prepares to build the International Space Station in collaboration with its international partners, successful completion of EVA missions becomes critical. Designers and mission planners are developing the equipment and procedures for constructing the space station and, while a good deal of testing can be done on the ground, certain tests must be performed on orbit. Lessons learned from a series of EVA tests will serve to increase the experience base of hardware developers, flight controllers, and the astronauts doing the spacewalks [17]. During the STS-87 mission, astronauts Winston Scott and Takao Doi performed two EVAs. Grappling and berthing of the wayward Spartan satellite consumed much of the time on the first of these. The second was focused on evaluation of equipment and procedures that will be used during construction and maintenance of the International Space Station. This spacewalk was intended to accomplish all of the primary objectives originally planned as part of the STS-80 mission in November 1996 that were not achieved due to a stuck airlock hatch [18].

For convenience, the first EVA, which took place from about MET 005/04:30 to 005/11:50 will be referred to as EVA #1, and the one that took place from about MET 013/13:20 to 013/18:15 will be referred to as EVA #2. A cursory examination of the SAMS data collected during these times shows that these EVAs tended to excite the acceleration spectrum below about 50 Hz. In order to quantify this comparison and to gain a better understanding of the effects that an EVA activity has on the Orbiter's acceleration environment, the RMS accelerations for a number of frequency bands were calculated as a function of time.

The RMS acceleration for each of the frequency bands shown in Table 17 was computed every 32.768 seconds from the SAMS Unit G, TSH B data for the period MET 005/06:30 to 005/15:30, which spans most of EVA #1 and a few hours thereafter; and for the period MET 013/13:00 to 013/22:00, which spans most of EVA #2 and a few hours following. The RMS levels shown in the "During EVA" columns represent the median values during part of the EVA (MET 005/07:30 to 005/10:30 for EVA #1, and MET 013/13:20 to 013/16:20 for EVA #2), while the "After EVA" columns show the median values after the EVA (MET 005/12:30 to 005/15:30 for EVA #1, and MET 013/19:00 to 013/22:00 for EVA #2). Note that for each band the levels during the EVAs were higher, although only marginally so above about 50 Hz. The RMS acceleration levels for the 0-10, 10-20, and 30-40 Hz bands for this sensor are appreciably lower after the EVAs.

SAMS Unit F, TSH A and B data were analyzed as described above, with the exception that the analysis was limited by the lowpass filter cutoff frequencies of these heads (10 Hz for TSH A, and 25 Hz for TSH B). The results shown in Tables 18 and 19 for Unit F are similar to those obtained for Unit G. For example, a plot of the RMS acceleration versus time for the first band (0 to 10 Hz) is shown in Figure 25. The plot is annotated to indicate the "During EVA #1" and "After EVA #1" time frames

considered for Table 18. Note from the figure the obvious disparity in RMS levels for this frequency band.

To further investigate the sources of disturbance that may have contributed to the measured accelerations during the two EVAs, Orbiter thruster firing activity was analyzed. The MEWS software enabled access to a record, albeit incomplete, of Columbia's Reaction Control System thruster firing times. The firing count shown in the right-hand column of Table 20 gives the minimum number of times that the VRCS jets were fired. Simultaneous firings were counted as one. The PRCS thrusters were not fired during either EVA according to the MEWS data.

For EVA #1, these data indicate that the increased excitation observed during the spacewalk is not attributable to thruster firings. The same implication cannot be gleaned from the firing count numbers for EVA #2 taken alone, however, when considered in conjunction with those of EVA #1, we infer that the thruster firings did not play a defining role in heightening the acceleration spectra in some preferential manner during the EVAs. The nature of the work being done during these spacewalks may help to explain the increased acceleration levels. It stands to reason that cumbersome space suits and "construction" work requires greater forces be exerted by the astronauts than nominal crew compartment activities. Also, during the EVAs the astronauts were closer to the SAMS sensors; spacewalk disturbances originated in the Orbiter's payload bay, where the SAMS heads were mounted, instead of the middeck or flight deck, where the crew was the remainder of the mission.

Unknown Disturbance Sources—Distinct 8.5 Hz Disturbance

An disturbance with a characteristic signature at 8.5 Hz was noticed in the SAMS Unit F, TSH A spectrograms during the mission. On the spectrograms, this signal would appear suddenly as a very distinct horizontal line and last for several minutes, see Figure 26. Numerous occurrences of the disturbance were noted in the PIMS logbook, including the similarity to 8.5 Hz disturbances seen in SAMS and Quasi-Steady Acceleration Measurement system data on STS-65 (on the Orbiter Columbia) [19, 20]. Attempts made following the STS-65 mission and during and after the STS-87 mission to identify the source of this disturbance were unsuccessful. During post-mission analysis of the STS-87 SAMS Unit F, TSH A data, a second manifestation of the 8.5 Hz signal was noticed. At times, a reduced magnitude 8.5 Hz signal appears in the spectrograms, see Figure 27. These weaker 8.5 Hz signals last longer temporally than the stronger occurrences. Table 21 is a list of times that an 8.5 Hz signal was noticeable in the SAMS Unit F, TSH A data.

Unknown Disturbance Sources—11.35 Hz Disturbance

An unidentified disturbance at 11.35 Hz, along with its second harmonic at 22.7 Hz, is visible occasionally in the Reference [1] Appendix B spectrograms. The first occurrence of this disturbance was at approximately MET 009/14:30:00 and the last occurrence was at approximately MET 010/09:00:00. There exist eleven occurrences of this disturbance, the maximum duration being about fifteen minutes. Typical durations seem to be approximately five minutes in length.

Figure 28 is a plot of RMS acceleration versus time for the narrow frequency band 11.25 Hz to 11.45 Hz. The intent of this analysis was to compare the signal in this frequency band when the 11.35 Hz signal was active versus when it was inactive. The elevated levels from the 0 to 10 minute mark and

from the 90 to 100 minute mark represent intervals when the 11.35 Hz signal was present and clearly illustrate the change in signal.

Unknown Disturbance Sources—Twin Disturbances at 12 to 15 Hz

An unidentified pair of disturbances shows up as two closely spaced spectral peaks, most clearly seen in the spectrograms of Appendix B of [1]. These twin disturbances tend to track each other in the frequency domain, and gradually increase in frequency from around 12 Hz early in the mission to over 15 Hz on MET day 11. They exhibit sharp spectral transitions on occasion. For example, in Reference [1] see Appendix pages B-31 and B-32 until about MET 007/01:30, Appendix pages B-35 and B-36 until about MET 008/01:40, and Appendix page B-47 at about MET 010/22:50. These disturbances are hard to discern from about MET 008/06:30 to about MET 008/18:00, and apparently cease sometime around MET 011/04:30.

SUMMARY

The OARE and two SAMS units were used to measure and record the microgravity environment of the Orbiter Columbia during the STS-87 mission in November-December 1997. Data from the two SAMS units were telemetered to the ground during the mission and data plots were displayed for USMP-4 investigators in near real-time using the World Wide Web. During SAMS data processing after the mission, it was determined that there was a problem with temperature / acceleration signals on SAMS Unit F, TSH A. The effects of this problem can be removed from the data in some types of analyses. Plots generated using OARE data telemetered to the ground were provided to the investigators approximately twelve hours after data recording using the World Wide Web.

Disturbances in the microgravity environment as recorded by these instruments are grouped by source type in this report: Orbiter systems, on-board activities, payload operations, and unknown sources. The environment related to the Ku-band antenna dither, Orbiter structural modes, attitude deadband collapses, water dump operations, crew sleep, and crew exercise was comparable to the effects of these sources on previous Orbiter missions. RMS acceleration levels for the Ku-band dither disturbance (16.93 to 17.13 Hz) were about 1.9×10^{-4} g_{RMS} during USMP-4. Average RMS acceleration levels for the 4.7 Hz Orbiter structural mode ranged from 2×10^{-6} g_{RMS} for the least affected X_O-axis to 3×10^{-5} g_{RMS} for the most affected Z_O-axis. Attitude deadband collapses necessitated by VRCS jet conditions tended to increase the VRCS jet firing rate from approximately one firing per minute for the standard deadband (1.0°) to greater than 100 firings per minute for the collapsed deadband (0.07°). Disturbances related to operations of the IDGE fans and SAMS hard drives that were not observed on previous missions are detailed in the text.

The effects of EVAs and related Orbiter cabin depressurization on the microgravity environment are reported. The exact cause of heightened SAMS-recorded acceleration spectral levels during EVAs is not known, although the nature and location of the work being done during the STS-87 spacewalks may help to explain the increased levels. The effects of the cabin depressurizations performed to prepare the spacewalking astronauts for their EVAs were best seen in the OARE data as excursions from the background acceleration levels of as much as 1×10^{-5} g. Sources for disturbances at 8.5 Hz, 11.35 Hz, and twin excitations varying between 12 and 15 Hz have not been identified.

REFERENCES

[1] Rogers, M. J. B., K. Hrovat, K. McPherson, R. DeLombard, and T. Reckart, Summary Report of Mission Acceleration Measurements for STS-87. NASA Technical Memorandum 98-208647.

[2] Rogers, M. J. B., K. Hrovat, and M. E. Moskowitz, Effects of Exercise Equipment on the Microgravity Environment, to be published in Advances in Space Research as part of the proceedings of the 32nd COSPAR Scientific Assembly, Nagoya, Japan, July 1998.

[3] Rogers, M. J. B. and R. DeLombard, Summary Report of Mission Acceleration Measurements for STS-62. NASA Technical Memorandum 106773, November 1994.

[4] Rogers, M. J. B., K. Hrovat, M. Moskowitz, K. McPherson, and R. DeLombard, Summary Report of Mission Acceleration Measurements for STS-75. NASA Technical Memorandum 107359, November 1996.

[5] DeLombard, R. and B. D. Finley, Space Acceleration Measurement System Description and Operations on the First Spacelab Life Sciences Mission. NASA Technical Memorandum 105301, November 1991.

[6] Baugher, C. R., G. L. Martin, and R. DeLombard, Low-frequency Vibration Environment for Five Shuttle Missions. NASA Technical Memorandum 106059, March 1993.

[7] Rogers, M. J. B., C. R. Baugher, R. C. Blanchard, R. DeLombard, W. W. Durgin, D. H. Matthiesen, W. Neupert, and P. Roussel, A Comparison of Low-gravity Measurements On-board Columbia During STS-40. Microgravity Science and Technology VI/3 (1993) 207.

[8] Blanchard, R. C., M. K. Hendrix, J. C. Fox, D. J. Thomas, and J. Y. Nicholson, Orbital Acceleration Research Experiment. J. Spacecraft and Rockets 24 (1987) 504.

[9] Blanchard, R. C., J. Y. Nicholson, and J. R. Ritter, STS-40 Orbital Acceleration Research Experiment Flight Results During a Typical Sleep Period. NASA Technical Memorandum 104209, January 1992.

[10] Blanchard, R. C., J. Y. Nicholson, and J. R. Ritter, Preliminary OARE Absolute Acceleration Measurements on STS-50. NASA Technical Memorandum 107724, February 1993.

[11] Personal communication with Martin O'Hare, Ku-Band Subsystem Engineer, Boeing North American, Johnson Space Center.

[12] Personal communication with Richard LaBrode, Instrumentation and Communication Officer (INCO), United Space Alliance, Johnson Space Center.

[13] STS-87 Space Shuttle Mission Report, NSTS-37418, Johnson Space Center, Houston, TX, February 1998.

[14] Shuttle Operational Data Book, Volume 1, JSC-08934, Rev. E, Johnson Space Center, Houston, TX, January 1988.

[15] Rogers, M. J. B., B. P. Matisak, and J. I. Alexander, Venting Force Contributions—Quasi-steady Accelerations on STS-50. Microgravity Science and Technology VII/4 (1995) 293.

[16] http://shuttle.nasa.gov/reference/shutref/structure/baydoors.html

[17] http://shuttle.nasa.gov/sts-80/orbit/eva/edftov.html

[18] http://shuttle.nasa.gov/sts-87/orbit/payloads/#EVA

[19] Rogers, M. J. B. and R. DeLombard, Summary Report of Mission Acceleration Measurements for STS-65. NASA Technical Memorandum 106871, March 1995.

[20] Personal communication with Jan Kruder and Hans Hamacher, Institute of Space Simulation of the German Aerospace Research Establishment (DLR), 1995.

Table 1. Internet access to STS-87 acceleration data products.

Acceleration Data Product	Access Information
STS-87 Acceleration Mission Summary Report [1]	http://www.lerc.nasa.gov/WWW/MMAP/PIMS/HTMLS/reportlist.html
STS-87 SAMS Data	ftp://beech.lerc.nasa.gov/pub/
STS-87 OARE Data	ftp://beech.lerc.nasa.gov/pub/
SAMS URL	http://zeta.lerc.nasa.gov/expr/sams.htm
OARE URL	http://zeta.lerc.nasa.gov/expr/oare.htm
PIMS URL	http://www.lerc.nasa.gov/WWW/MMAP/PIMS/

Table 2. STS-87 Mission Events List. The official JSC Mission Event List is a product of the Johnson Space Center Mission Evaluation Room. Any questions should be addressed to MV3/V. Hill (281) 483-3334 or MV3/R. Fricke (281) 483-3313.

Event	Mission Elapsed Time	Greenwich Mean Time
Payload Bay Doors Open		
Right	000/01:29:42	323/21:15:42
Left	000/01:31:02	323/21:17:02
Spartan Grapple in Payload Bay	001/23:46:13	325/19:32:13
Spartan Unberth Indicated	002/00:19:45	325/20:05:45
Spartan Release	002/01:18:37	325/21:04:37
Spartan Re-grapple	002/01:24:37	325/21:10:37
Starboard Radiator Deploy	003/09:51:42	327/05:37:42
Cabin De-pressurization End	004/09:34:42	328/05:20:42
Starboard Radiator Stow	005/00:54:28	328/20:40:28
Orbital Maneuvering System 3 Ignition	005/01:33:33	328/21:19:33
Orbital Maneuvering System 3 Cutoff	005/01:33:48	328/21:19:48
Orbital Maneuvering System Ignition	005/03:04:38	328/22:50:38
Orbital Maneuvering System Cutoff	005/03:04:50	328/22:50:49
Airlock De-pressurization End	005/03:56:25	328/23:42:25
Cabin Re-pressurization Start	005/04:15:54	329/00:01:54
Spartan Grapple	005/06:52:50	329/02:38:50
Spartan Berth	005/07:37:09	329/03:23:09
Spartan Latch	005/07:39:09	329/03:23:09
Spartan Ungrapple	005/0:40:24	329/03:26:24
Airlock Re-pressurization Start	005/11:59:40	329/07:45:40
Port Radiator Deploy	007/03:43:57	330/23:29:57
Port Radiator Stow	010/07:48:56	334/03:34:56
Starboard Radiator Deploy	010/20:38:42	334/16:24:42
Port Radiator Deploy	012/14:35:06	336/10:21:06
Cabin De-pressurization End	012/19:31:30	336/15:17:30
Starboard Radiator Stow	012/19:44:18	336/15:30:18
Port Radiator Stow	012/19:44:55	336/15:30:55
Spartan Grapple	013/08:56:53	337/04:42:53
Spartan Unberth Indicated	013/09:10:19	337/04:56:19
Spartan Berth	013/13:25:27	337/09:11:27
Spartan Latch	013/13:26:02	337/09:12:02
Spartan Ungrapple	013/13:28:54	337/09:14:54
Cabin Re-pressurization Start	013/13:24:49	337/09:10:49
Airlock De-pressurization End	013/13:25:05	337/09:11:05
Airlock Re-pressurization Start	013/18:22:24	337/14:08:24
Flight Control System Check Out Auxiliary Power Unit Start	014/14:05:24	338/09:51:23.940
Auxiliary Power Unit Stop	014/14:17:21	338/10:03:21.243
Payload Bay Doors Closed		
Left	015/12:53:10	339/08:39:10
Right	015/12:56/16	339/08:42:16
Auxiliary Power Unit Activation		
APU-2	015/15:30:35	339/11:16:35.381
APU-1	015/15:49:26	339/11:35:26.423
APU-3	015/15:49:33	339/11:35:33.133
Deorbit Burn Start	015/15:35:28	339/11:21:28.2
Deorbit Burn End	015/15:38:00	339/11:24:00.4

Table 3. STS-87 SAMS Sensor Head Configuration

Unit F, TSH A	Sample Rate: 50 samples / second
Forward MPESS	Frequency Cutoff: 10 Hz

Orientation		**Location**
Orbiter Structural Axis	**Sensor Axis**	**Orbital Structural Coordinate (in.)**
X_O	$-Y_H$	X_O = 987.69
Y_O	$+Z_H$	Y_O = 3.94
Z_O	$-X_H$	Z_O = 416.76

Unit F, TSH B	Sample Rate: 125 samples / second
Forward MPESS	Frequency Cutoff: 25 Hz

Orientation		**Location**
Orbiter Structural Axis	**Sensor Axis**	**Orbital Structural Coordinate (in.)**
X_O	$-Y_H$	X_O = 987.69
Y_O	$+Z_H$	Y_O = -4.31
Z_O	$-X_H$	Z_O = 416.76

Unit G, TSH A	Sample Rate: 50 samples / second
Rear MPESS, inside IDGE	Frequency Cutoff: 5 Hz

Orientation		**Location**
Orbiter Structural Axis	**Sensor Axis**	**Orbital Structural Coordinate (in.)**
X_O	$+Z_H$	X_O = 1083.77
Y_O	$-.7071X_H + .0107Y_H$	Y_O = -37.08
Z_O	$-.7071X_H - .0107Y_H$	Z_O = 442.82

Unit F, TSH B	Sample Rate: 250 samples / second
Rear MPESS, inside CHeX	Frequency Cutoff: 100 Hz

Orientation		**Location**
Orbiter Structural Axis	**Sensor Axis**	**Orbital Structural Coordinate (in.)**
X_O	$.5446X_H + .8387Z_H$	X_O = 1069.52
Y_O	$+Y_H$	Y_O = 29.52
Z_O	$-.8387X_H + .5446Z_H$	Z_O = 442.51

Table 4. STS-87 OARE Sensor Configuration

OARE Sensor Orbiter Keel Bridge		Sample Rate: 10 samples / second Frequency Cutoff: 1 Hz
Orientation		**Location**
Orbiter Structural Axis	**Sensor Axis**	**Orbital Structural Coordinate (in.)**
X_O	$-X_{OARE}$	X_O= 1153.3
Y_O	$+Z_{OARE}$	Y_O= -1.3
Z_O	$+Y_{OARE}$	Z_O= 317.8

Table 5. SAMS Unit F, TSH B Sensor Locations for USMP-3 and USMP-4 with respect to the Orbiter Structural Coordinate System

Mission	**Sensor Location (inches)**		
	X_O	Y_O	Z_O
STS-75 / USMP-3	1048.37	-4.37	418.13
STS-87 / USMP-4	987.69	-4.31	416.76

Table 6. Ku-band Antenna Dither RMS Acceleration Levels (16.93 < f < 17.13 Hz)

Mission Elapsed Time	**Mission**	**Dither Condition**	**RMS Acceleration (μg_{RMS})**
012/00:00–013/00:00	STS-75/USMP-3	On	143
014/00:00–014/08:00	STS-75/USMP-3	Off	9
012/21:20–013/21:20	STS-87/USMP-4	On	197
014/21:20–015/05:20	STS-87/USMP-4	Off	8

Table 7. Timeline for Ku-band Antenna Stow Procedure

Time Relative to MET 014/20:10:00 (mm:ss)	**Mission Event**
00:00	Start of STOW event
02:36	Ku-band in RADAR mode
02:55	Start slew to antenna azimuth=0, elevation=0
03:15	At azimuth=0, elevation=0 (alpha=0, beta=0)
03:25	Slew up for 14 seconds, cable positioning procedure
03:39	Cable positioning complete
04:08	Slew to azimuth=-123, elevation=-27 (alpha=124.4, beta=-30.7)
04:35	At azimuth=-123, elevation=-27 (alpha=124.4, beta=-30.7)
07:22	Stow switch to STOW, azimuth=-125.1, elevation=-29.6 (alpha=124.3, beta=-27.5)
07:43	Alpha and beta gimbals are locked
07:58	Wiggle test complete—system ready for STOW
08:40	Antenna Deployed Assembly begins to move to its stowed position
09:02	Antenna Deployed Assembly is STOWED
09:20	Ku-band system is powered OFF

Table 8. Power Spectral Density Parameters for Satellite-tracking Period

SAMS Sensor Head			Number of Points per PSD	Number of PSDs per Spectral Average	Effective Span (hours)
Unit	TSH	Sample Rate (samples / second)			
F	A	50	1024	660	3.75
F	B	125	4096	344	3.13
G	B	250	8192	346	3.15

Table 9. Structural Mode RMS Accelerations Resulting from Satellite-tracking Maneuvers

Frequency (Hz)	RMS Acceleration (μg_{RMS})								
	Unit F, TSH A			Unit F, TSH B			Unit G, TSH B		
	X_o	Y_o	Z_o	X_o	Y_o	Z_o	X_o	Y_o	Z_o
3.2	4.6	11.4	7.3	1.4	7.1	3.5	6.7	3.5	3.6
3.5	2.9	25.6	5.5	2.0	25.7	7.0	3.7	19.5	3.3
4.7	6.4	18.3	**39.1**	3.9	13.4	**35.6**	1.7	4.0	**24.2**
6.3	3.3	5.0	7.2	1.4	2.2	5.0	1.5	1.2	3.0

Table 10. 4.7 Hz Structural Mode Mean RMS Accelerations for MET 010/00:00–011/00:00

Frequency (Hz)	RMS Acceleration (μg_{RMS})								
	Unit F, TSH A			Unit F, TSH B			Unit G, TSH B		
	X_o	Y_o	Z_o	X_o	Y_o	Z_o	X_o	Y_o	Z_o
4.7	2.8	8.2	**29.3**	2.6	7.2	**26.4**	1.9	5.7	**21.9**

Table 11. Deadband Collapse Times

Approximate MET Start	Approximate Duration (minutes)
006/08:20:14	1.8
007/06:01/29	0.5
008/07:29:48	9.3
008/11:47:48	1.6
008/20:06:03	3.2
009/21:53:58	1.1
009/22:55:03	1.4
009/23:30:52	1.9

Table 12. Deadband Collapse VRCS Firing Comparisons

MET	Duration (minutes)	Number of VRCS Firings	VRCS Firing Rate (firings per minute)
008/07:00:00–008/07:29:00	29.0	22	0.8
008/07:29:48–008/07:39:08	9.3	953	102.1
008/19:30:00–008/20:00:55	30.9	25	0.8
008/20:06:03–008/20:15:57	9.9	1699	171.6

Table 13. Acceleration Magnitude Comparison for Deadband Collapse

SAMS Unit	TSH	Sensor Cutoff Frequency (Hz)	MET	Acceleration Magnitude (μg)
F	A	10	before deadband collapse 008/07:00–008/07:29	35
			during deadband collapse 008/07:30–008/07:37	201
F	B	25	before deadband collapse 008/07:00–008/07:29	156
			during deadband collapse 008/07:30–008/07:37	627
G	A	5	before deadband collapse 008/07:00–008/07:29	26
			during deadband collapse 008/07:30–008/07:37	133
G	B	100	before deadband collapse 008/07:00–008/07:29	781
			during deadband collapse 008/07:30–008/07:37	809

Table 14. USMP-4 Replanned Timeline Crew Sleep Times

Start Sleep Period (MET)	End Sleep Period (MET)
000/11:00	000/19:00
001/12:00	001/20:00
002/12:00	002/20:00
003/14:00	003/22:00
004:15:00	004/23:00
005/16:00	006/00:00
006/17:00	007/01:00
007/18:00	008/02:00
008/19:00	009/03:00
009/20:00	010/04:00
010/21:00	011/05:00
011/22:00	012/06:00
012/22:00	013/06:00
013/22:00	014/06:00
014/22:00	015/07:00

Table 15. Public Affairs Office Events

Approximate MET Start	Duration (minutes)	Appendix Pages [1]
003/07:44	19	B-, C-, D-, E-17
006/13:03	8	B-, C-, D-, E-30
007/14:53	15	B-, C-, D-, E-34
011/08:32	19	B-, C-, D-, E-49
012/14:49	34	B-, C-, D-, E-54
014/17:15	15	B-, C-, D-, E-62

Table 16. RMS Accelerations from a 21 Hz Disturbance for MET 004/00:00–005/00:00

	RMS Acceleration (μg_{RMS})	
	Unit F, TSH B	Unit G, TSH B
Minimum	3.1	3.9
Mean	12.4	14.6
Maximum	48.8	68.2

Table 17. EVA RMS Acceleration Comparison (SAMS Unit G, TSH B)

Frequency Range (Hz)	RMS Acceleration (μg_{RMS})			
	During EVA #1	After EVA #1	During EVA #2	After EVA #2
0–10	110	45	98	41
10–20	259	156	295	163
20–30	110	68	138	58
30–40	202	122	197	98
40–50	108	69	97	62
50–60	138	137	213	195
60–70	91	89	99	95
70–80	84	83	90	87
80–90	102	98	88	81
90–100	77	71	90	85

Table 18. EVA #1 RMS Acceleration Comparison (SAMS Unit F, TSH A and B)

Frequency Range (Hz)	RMS Acceleration (μg_{RMS})			
	Unit F, TSH A		Unit F, TSH B	
	During EVA	After EVA	During EVA	After EVA
0–10	116	48	121	51
10–20			267	105

Table 19. EVA #2 RMS Acceleration Comparison (SAMS Unit F, TSH A and B)

Frequency Range (Hz)	RMS Acceleration (μg_{RMS})			
	Unit F, TSH A		Unit F, TSH B	
	During EVA	After EVA	During EVA	After EVA
0–10	116	52	121	55
10–20			318	185

Table 20. Orbiter VRCS Thruster Firing Activity during EVAs

MET	VRCS Thruster Firing Count
005/08:00–005/11:00 (during EVA #1)	154
005/12:00–005/15:00 (after EVA #1)	640
013/13:40–013/16:40 (during EVA #2)	414
013/19:00–013/22:00 (after EVA #2)	66

Table 21. USMP-4 8.5 Hz Disturbance Times, Estimated from Spectrograms [1]

MET Start	Duration (minutes)	MET Start	Duration (minutes)
000/12:50:40.212	3.7	006/23:23:13.604	1.8
000/15:04:39.786	4.1	007/01:00:12.332	0.9
002/13:26:36.629	1.8	007/01:02:51.527	0.6
002/15:00:04.771	2.2	010/01:23:22.142	5.0
003/19:02:55.255	3.4	010/06:15:04.499	30.5
003/20:38:50.979	2.3	010/07:21:39.365	7.2
004/03:37:03.855	2.2	010/08:08:51.306	2.2
004/05:14:41.043	1.5	010/10:17:51.479	6.6
004/11:32:45.361	13.5	010/18:23:41.355	2.7
004/17:27:41.328	3.7	010/19:22:00.901	2.7
004/19:02:55.255	3.5	010/20:07:35.931	1.8
004/20:04:43.270	0.9	011/03:05:52.673	1.7
004/20:37:55.636	2.9	011/04:08:52.408	1.2
005/18:30:40.212	1.2	011/04:16:32.416	2.4
005/18:33:32.576	1.0	011/16:49:41.675	2.0
005/18:43:11.229	3.5	011/17:13:13.000	1.0
005/20:00:08.136	1.4	011/18:45:59.733	2.9
005/20:03:25.124	0.8	011/20:12:51.247	1.2
005/21:31:48.322	2.9	011/20:17:37.188	7.4
005/21:49:51.756	3.5	012/01:46:46.697	4.1
005/23:00:26.999	1.0	012/15:08:51.135	2.0
005/23:03:56.299	0.4	012/18:36:59.461	1.8
005/23:25:16.721	2.5	013/09:15:04.499	1.8
006/00:59:01.391	2.3	013/10:24:10.115	2.0
006/01:01:53.676	2.9	013/10:46:57.630	1.6
006/02:39:42.146	2.3	013/10:57:22.165	3.8
006/04:15:41.150	3.7	013/12:23:28.264	2.1
006/05:51:23.151	4.1	014/03:45:12.611	4.5
006/07:25:03.169	5.0	014/10:58:15.997	5.5
006/18:22:18.880	0.9	014/12:19:41.612	10.4
006/18:27:22.544	1.2	014/12:44:01.815	1.8
006/18:44:10.155	1.6	014/12:53:38.211	13.8
006/19:57:33.276	6.4	014/13:57:31.243	1.6
006/20:09:17.223	1.4	014/17:01:53.815	2.0
006/21:51:17.939	2.3	014/18:33:50.153	2.2
		014/20:04:41.488	2.3

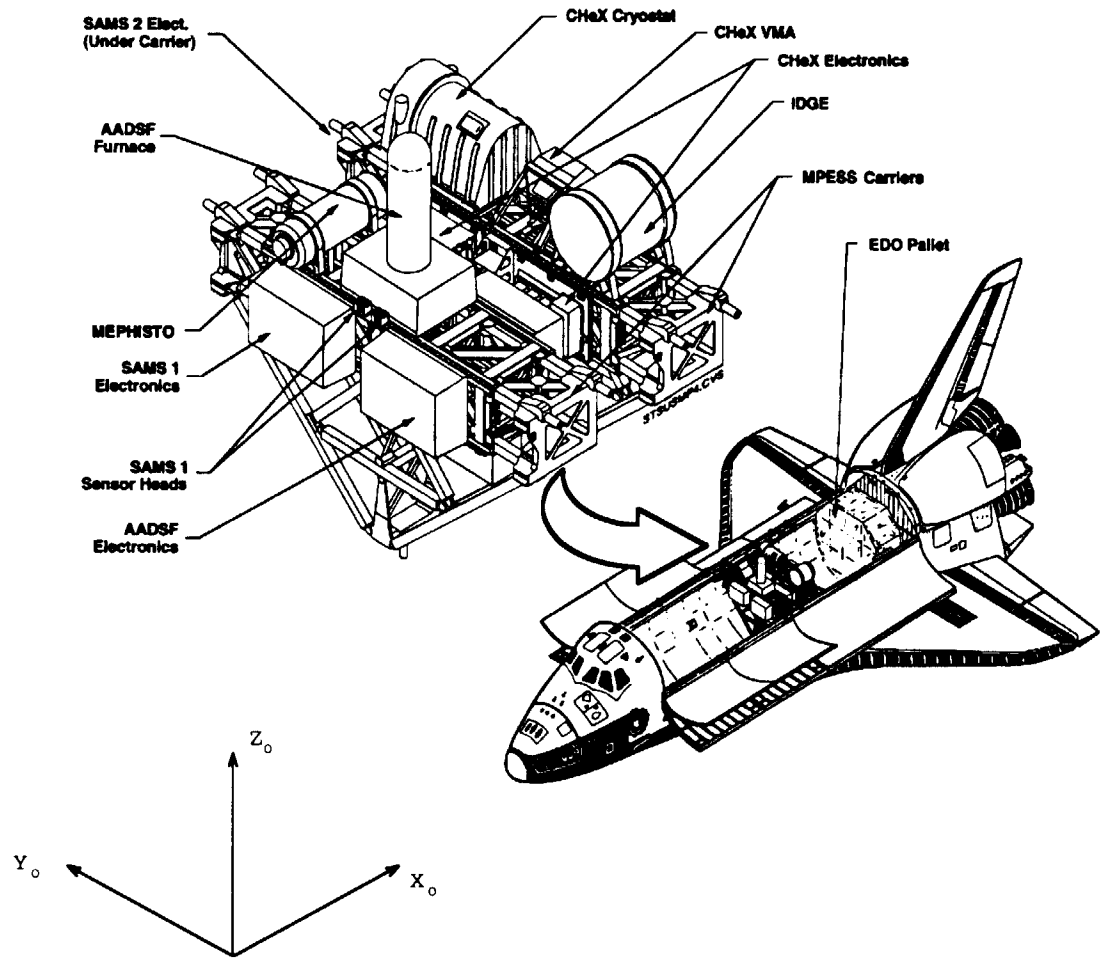

Figure 1. Approximate payload bay location of USMP-4 and orientation of the Orbiter Structural Coordinate System.

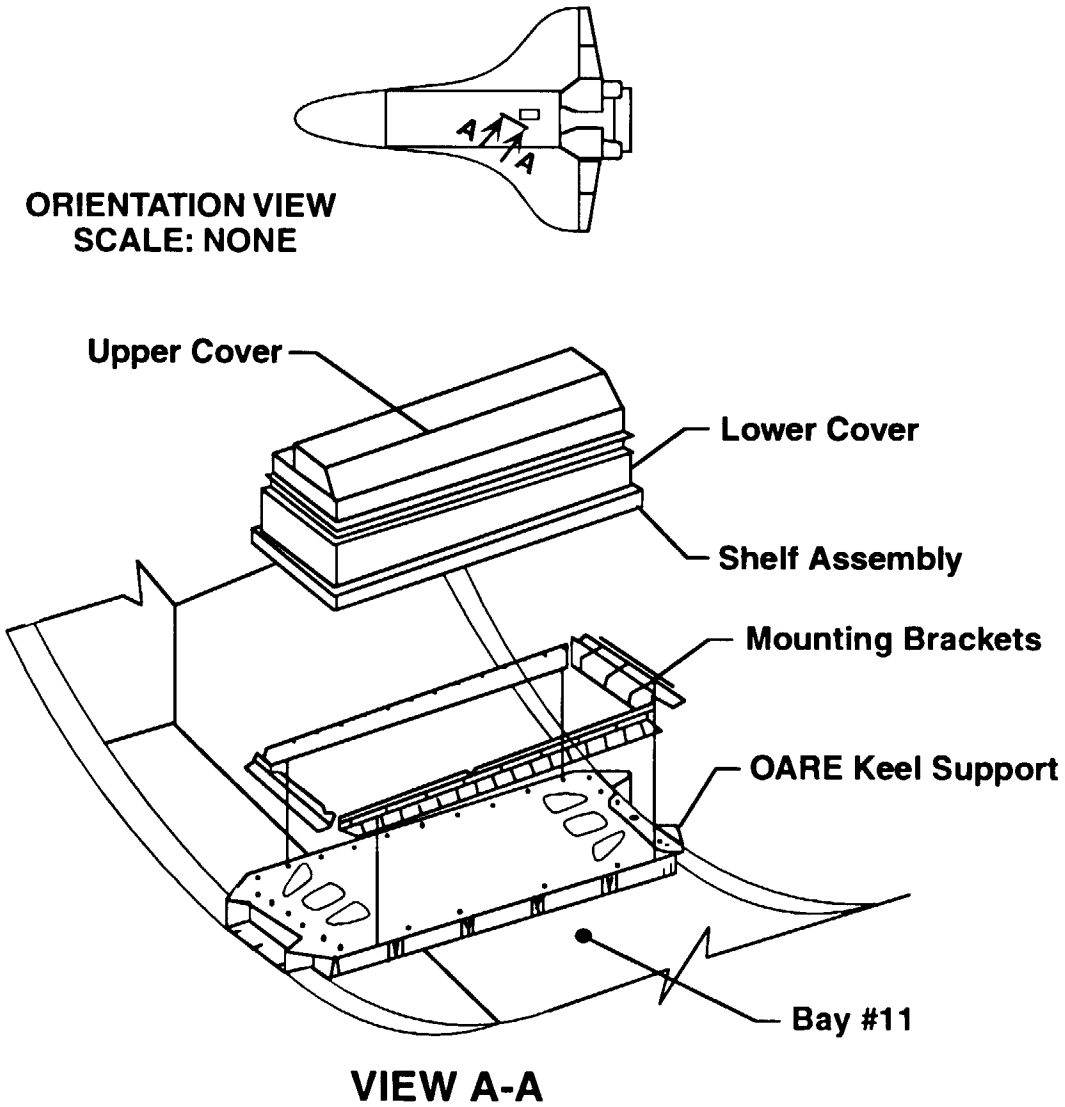

Figure 2. Approximate OARE instrument location on STS-87.

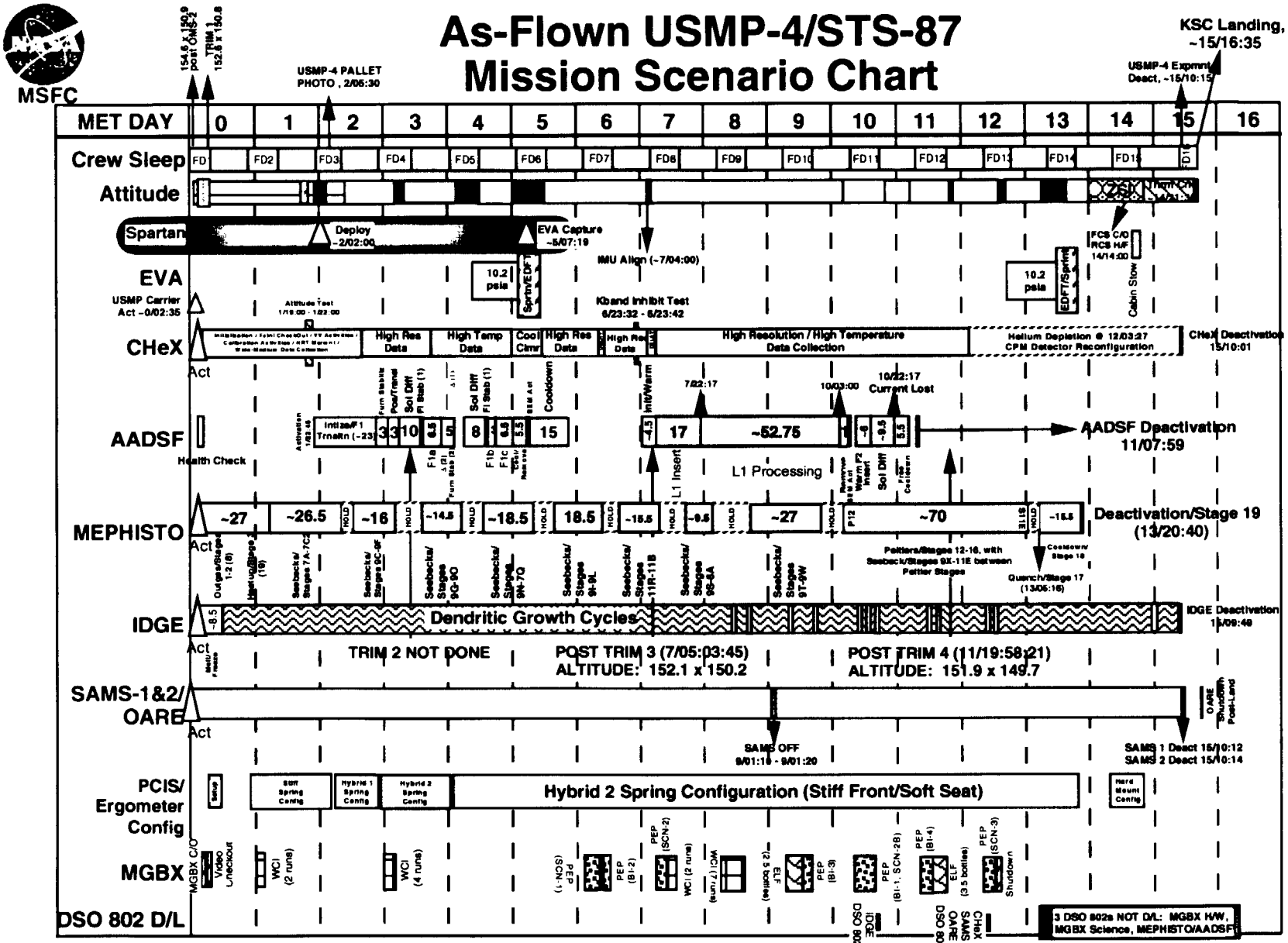

Figure 3. As-flown mission scenario [1].

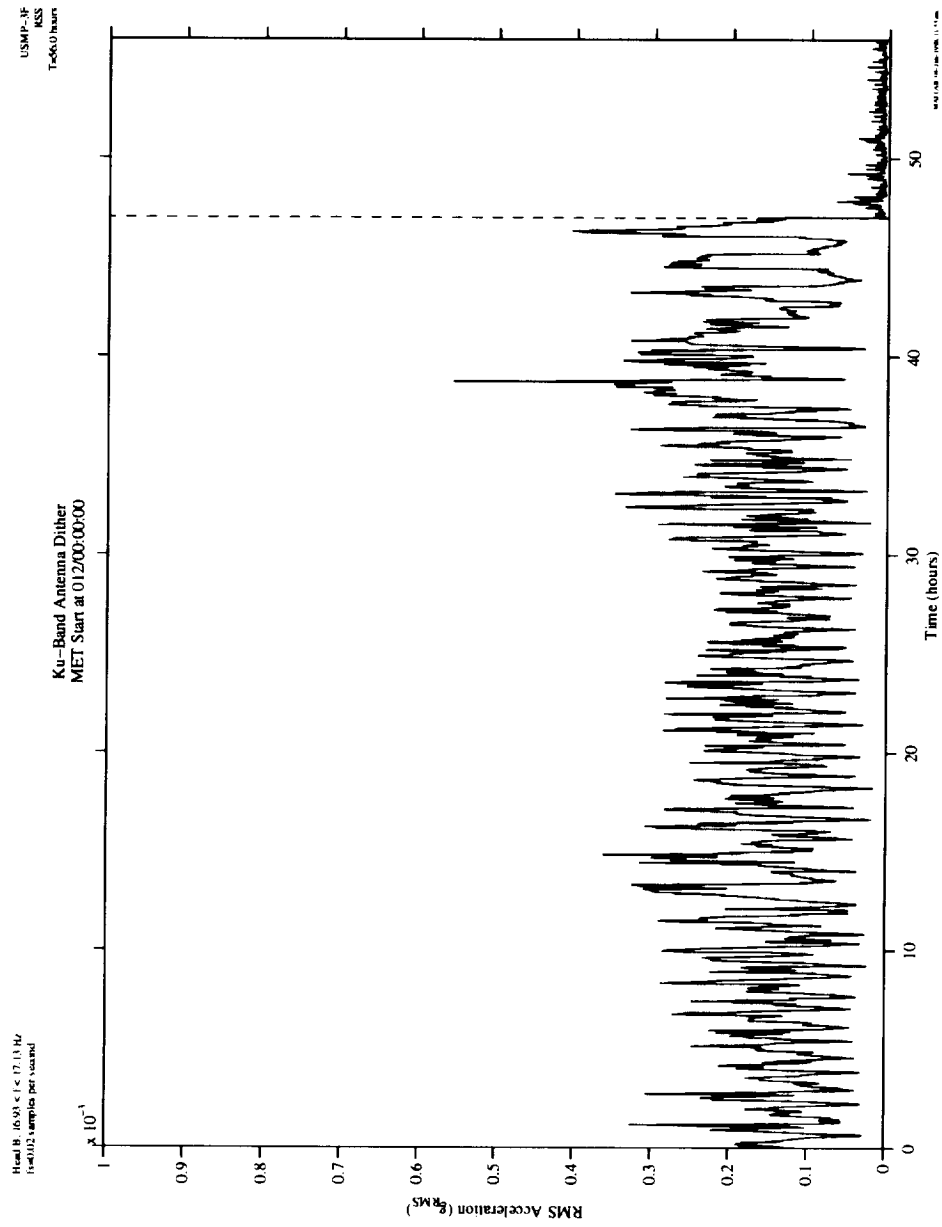

Figure 4. Ku-band antenna dither cessation (USMP-3).

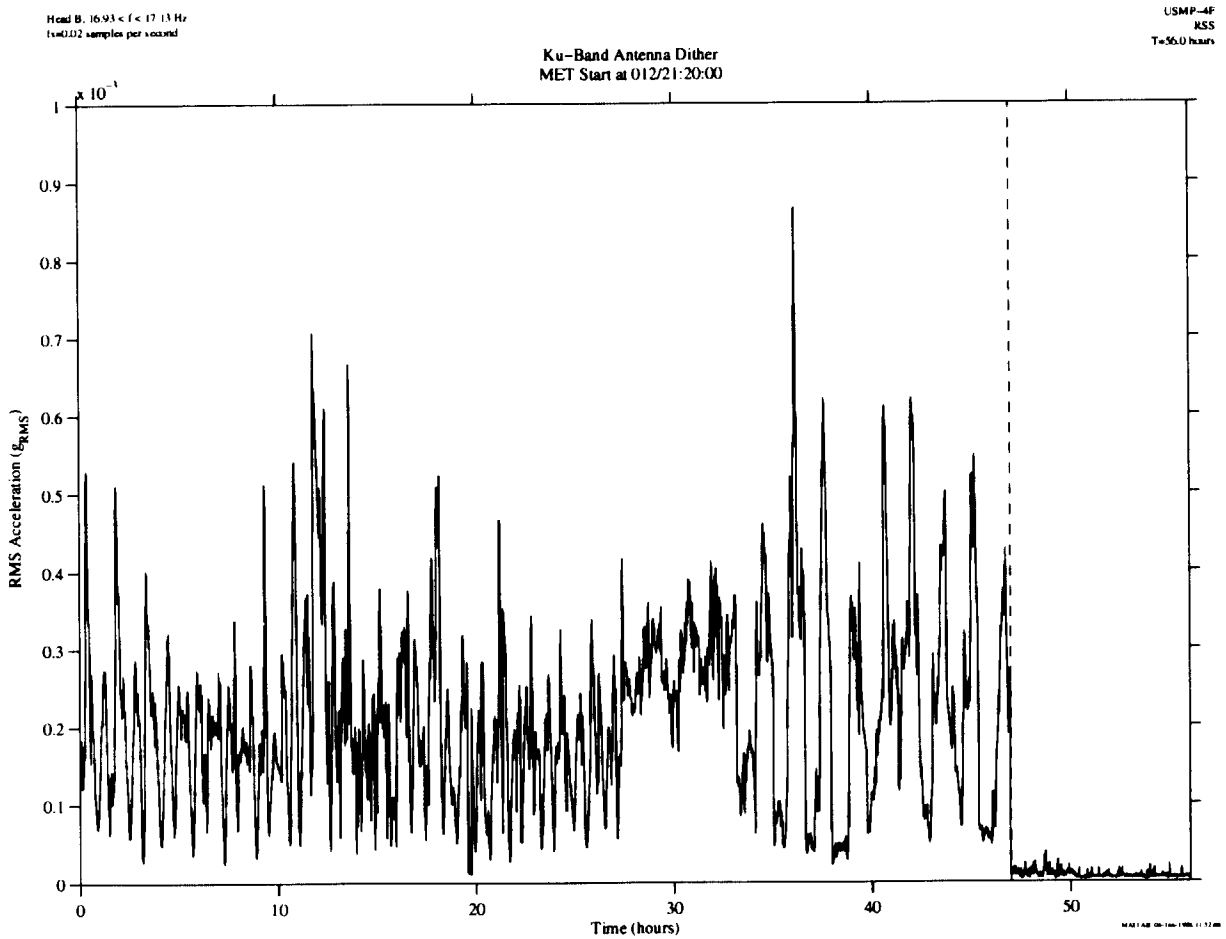

Figure 5. Ku-band antenna dither cessation (USMP-4).

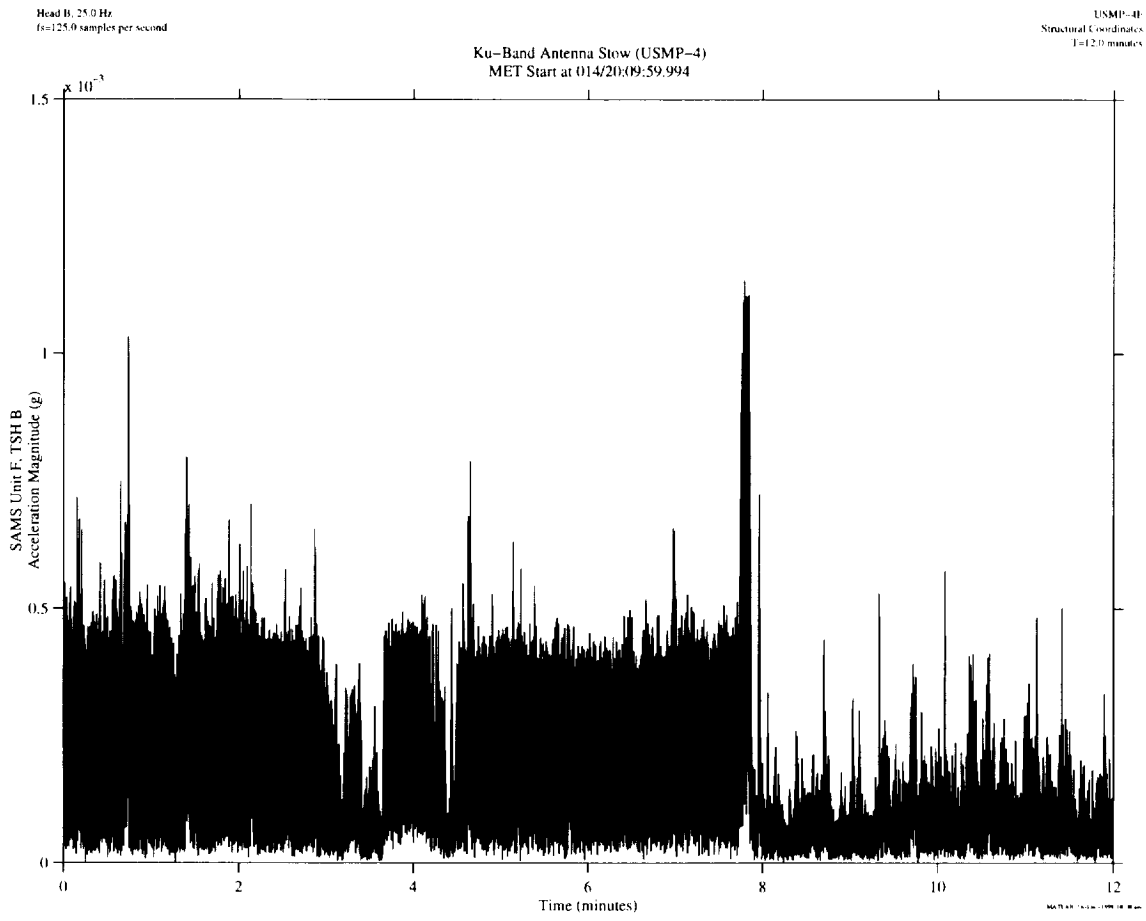

Figure 6. Ku-band antenna stow.

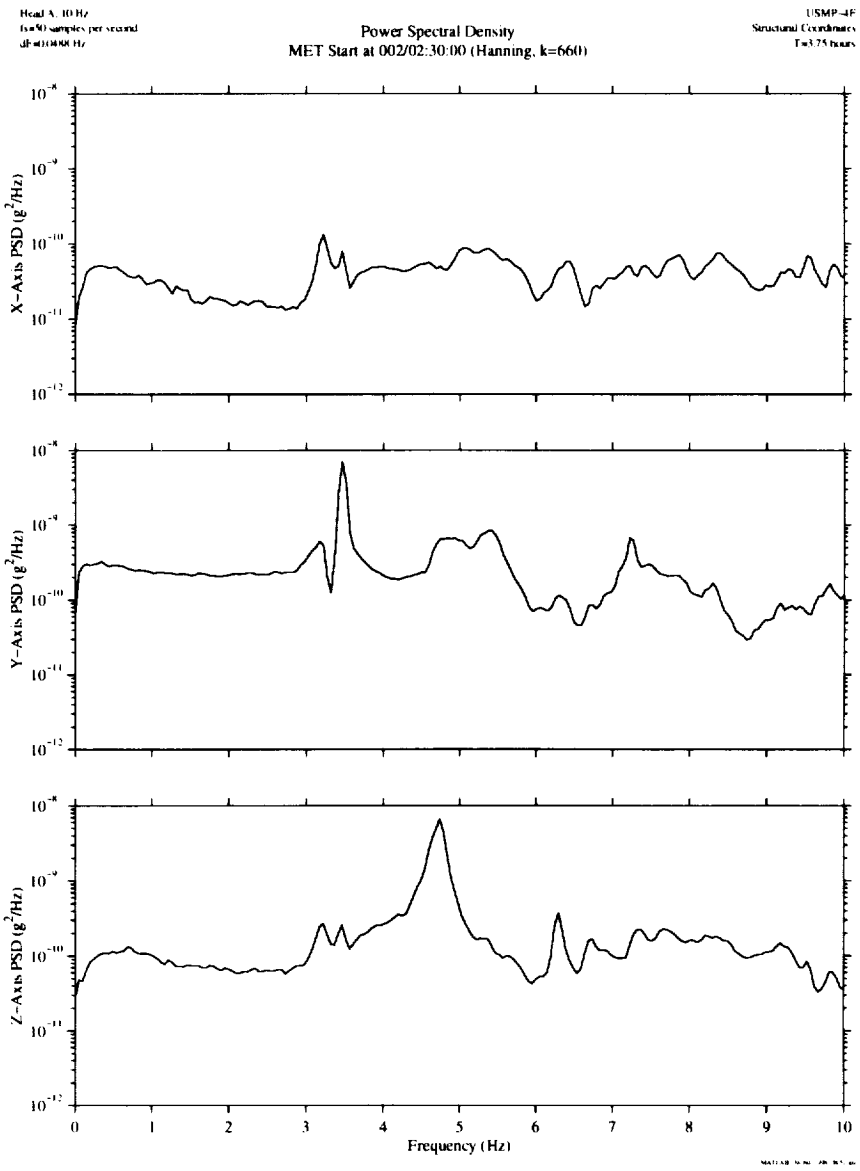

Figure 7. Structural response to satellite tracking maneuvers (SAMS Unit F, TSH A).

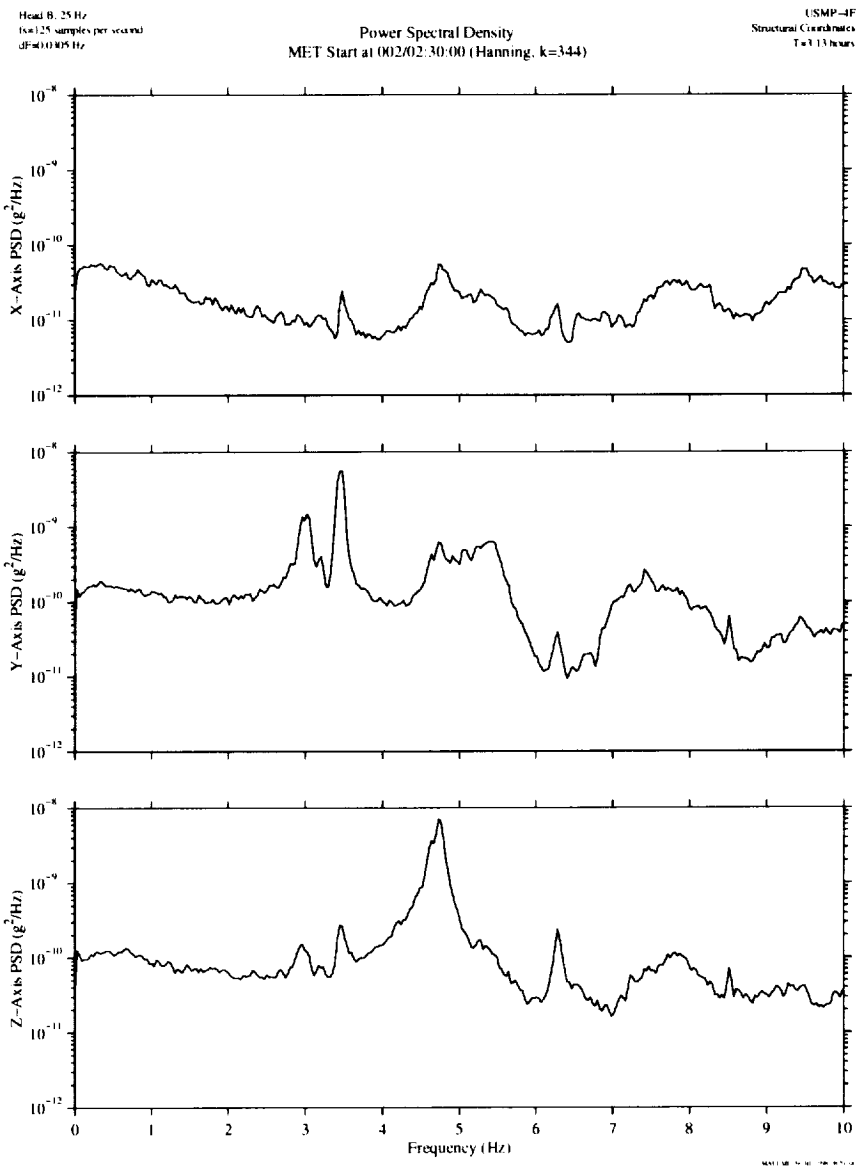

Figure 8. Structural response to satellite tracking maneuvers (SAMS Unit F, TSH B).

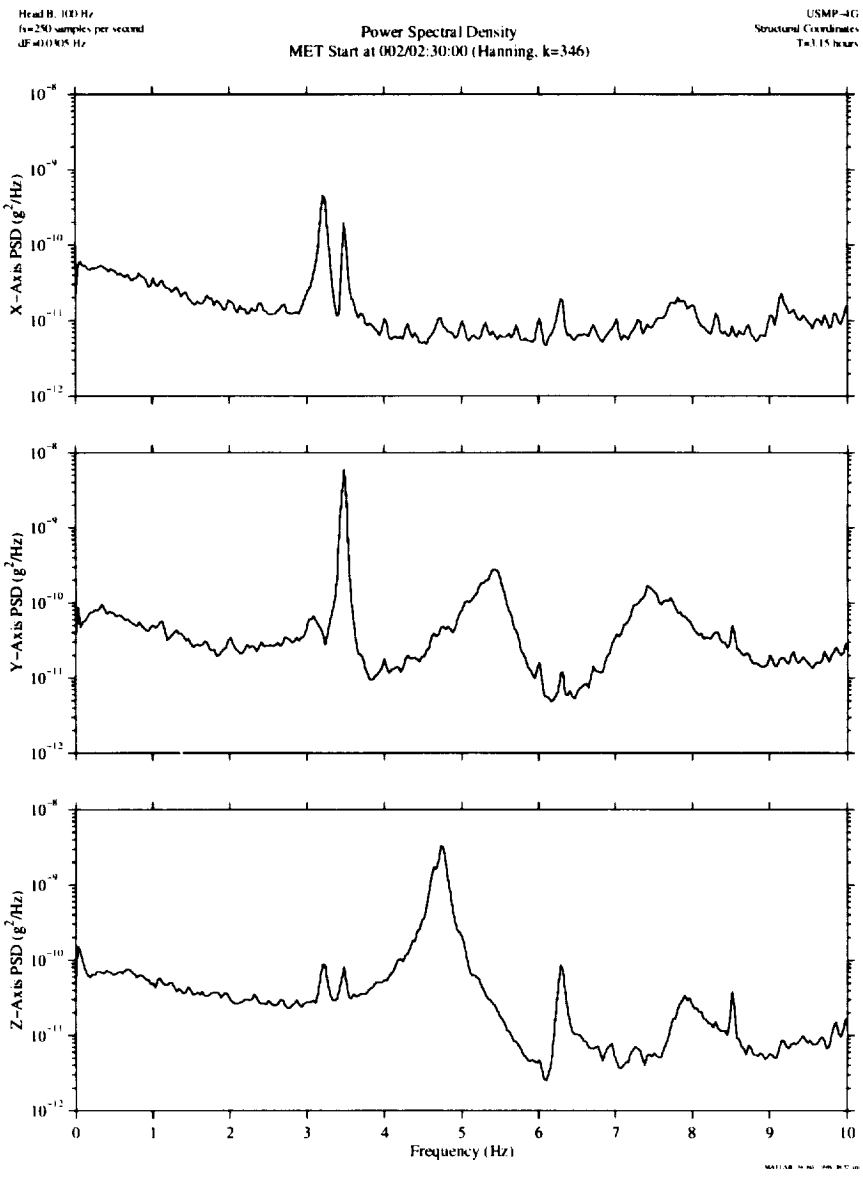

Figure 9. Structural response to satellite tracking maneuvers (SAMS Unit G, TSH B).

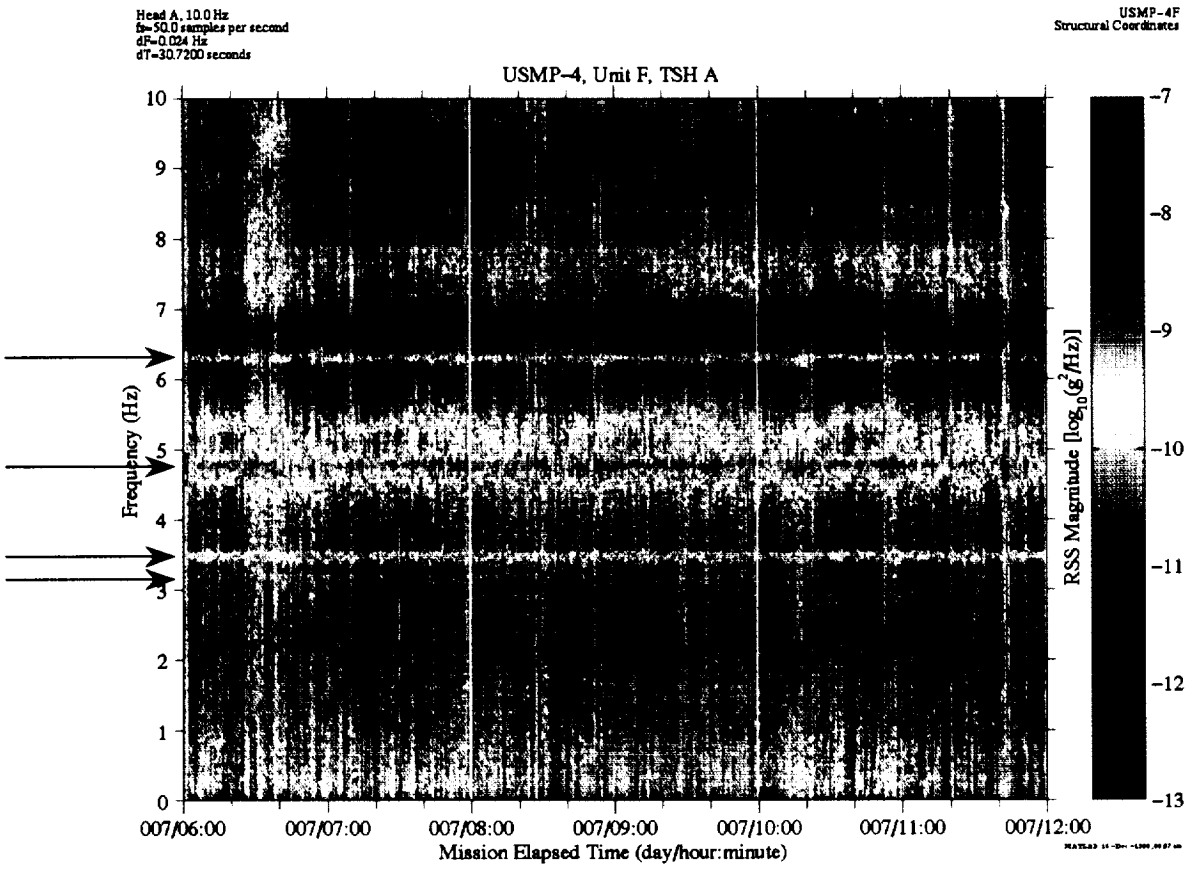

Figure 10. Structural modes spectrogram. Note that modes at 3.2, 3.5, 4.7, and 6.3 Hz are indicated by arrows at the left of the plot.

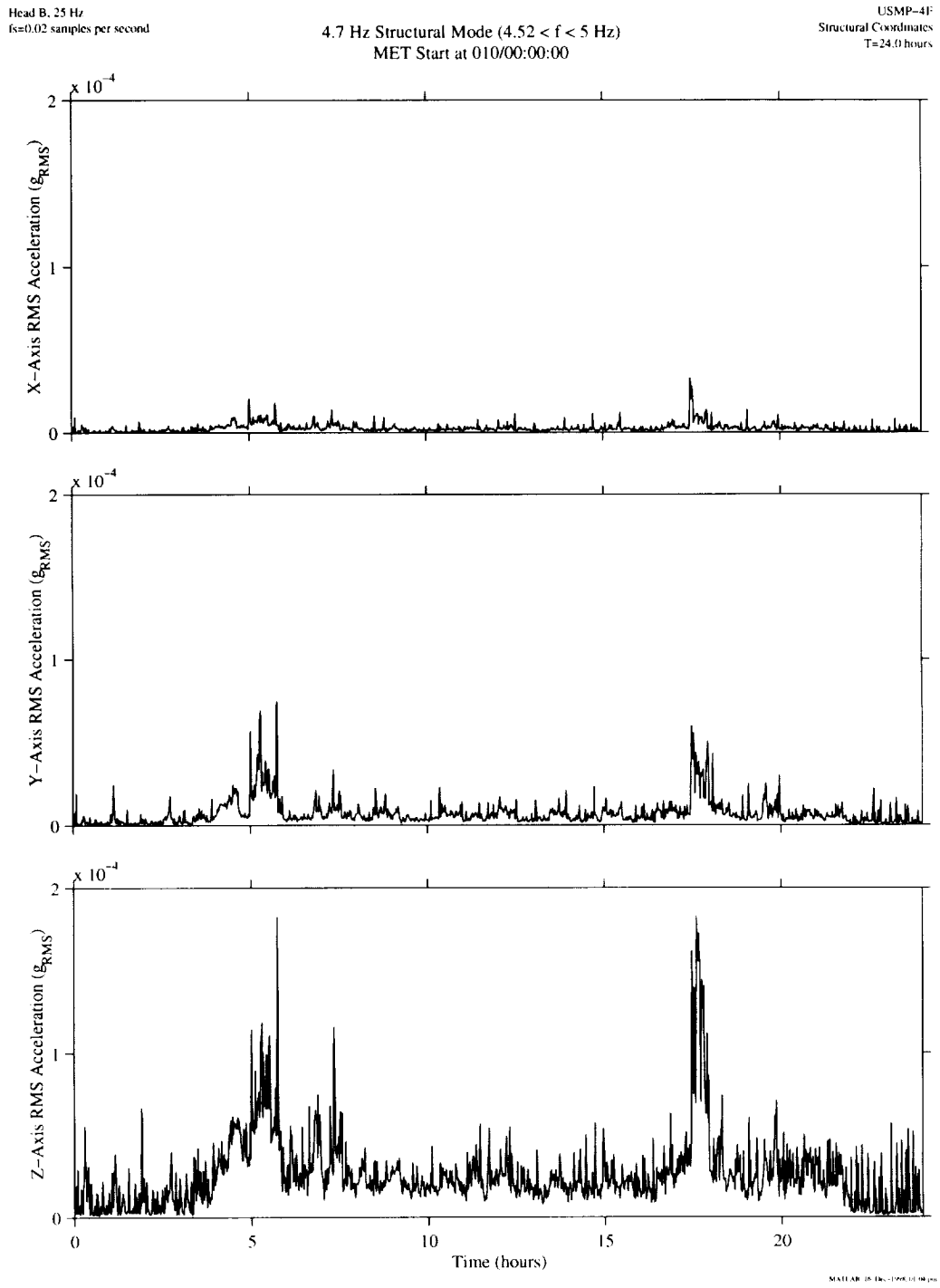

Figure 11. 4.7 Hz structural mode acceleration versus time with respect to the Orbiter Structural Coordinate System.

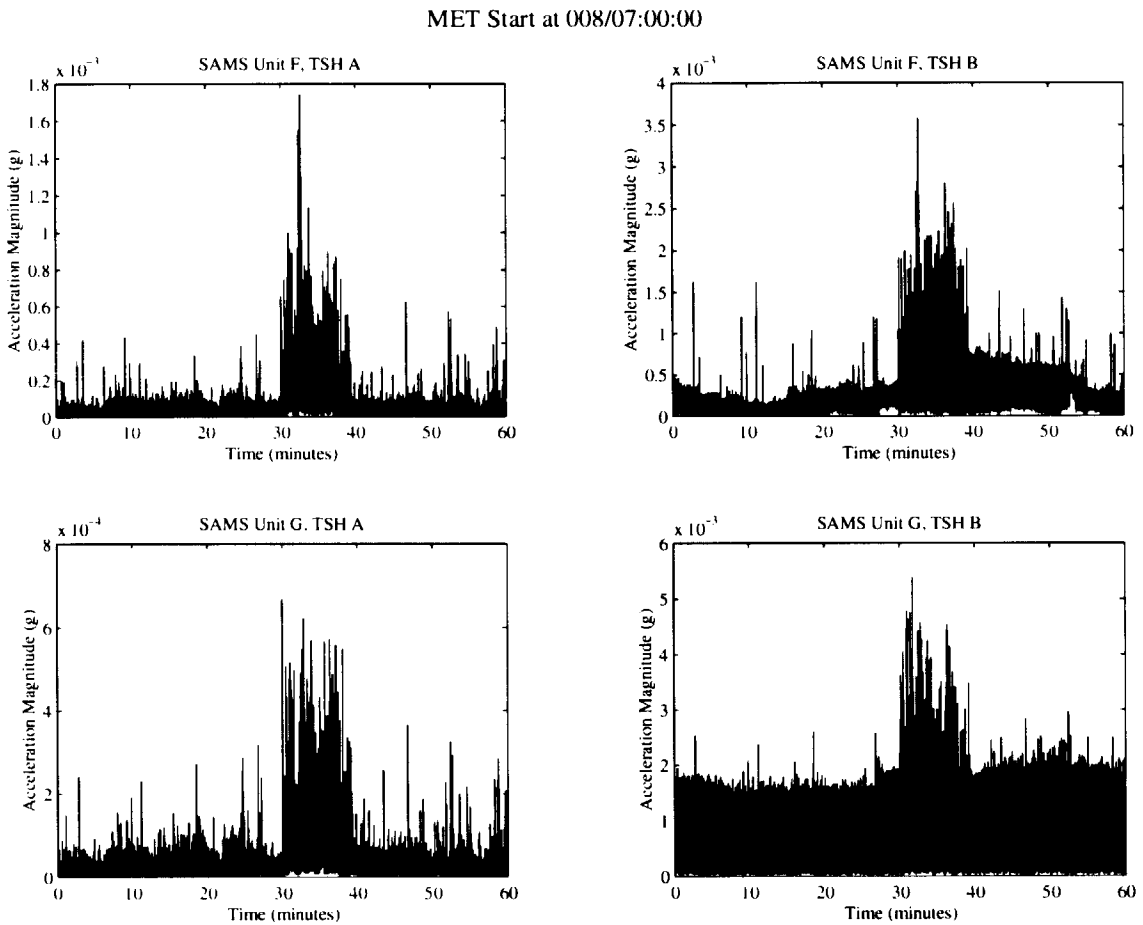

Figure 12. Heightened acceleration magnitude during deadband collapse.

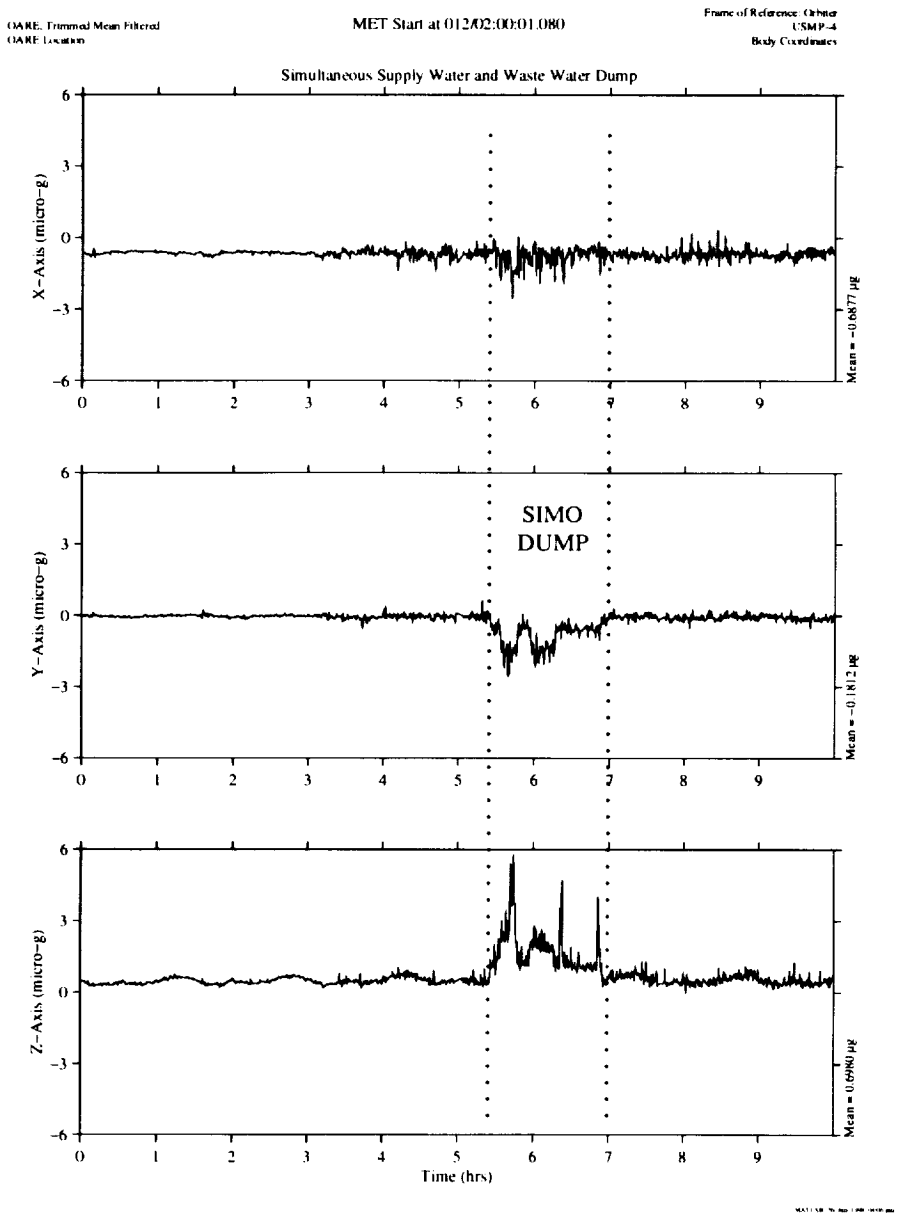

Figure 13. OARE data collected during a simultaneous supply and waste water dump.

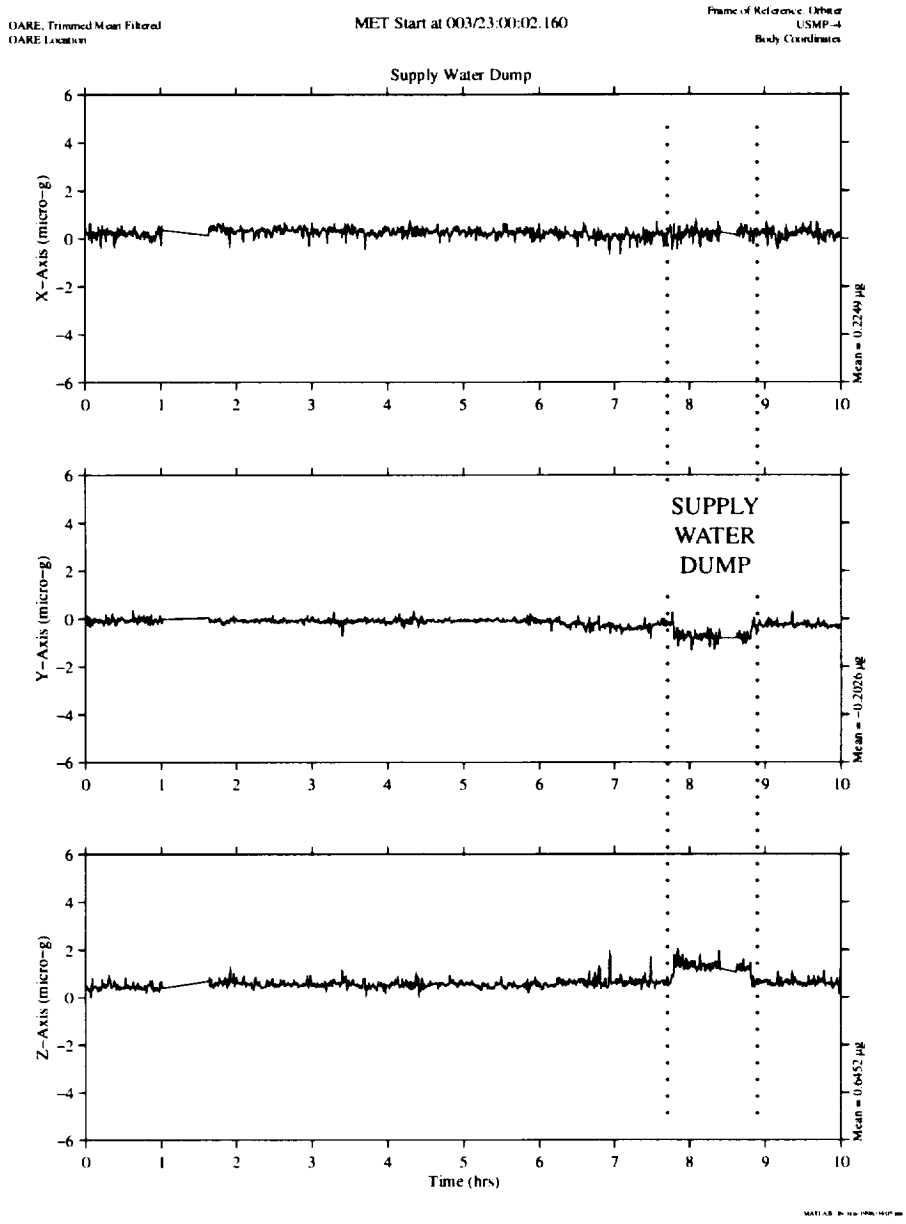

Figure 14. OARE data collected during a supply water dump starting at approximately MET 004/07:00.

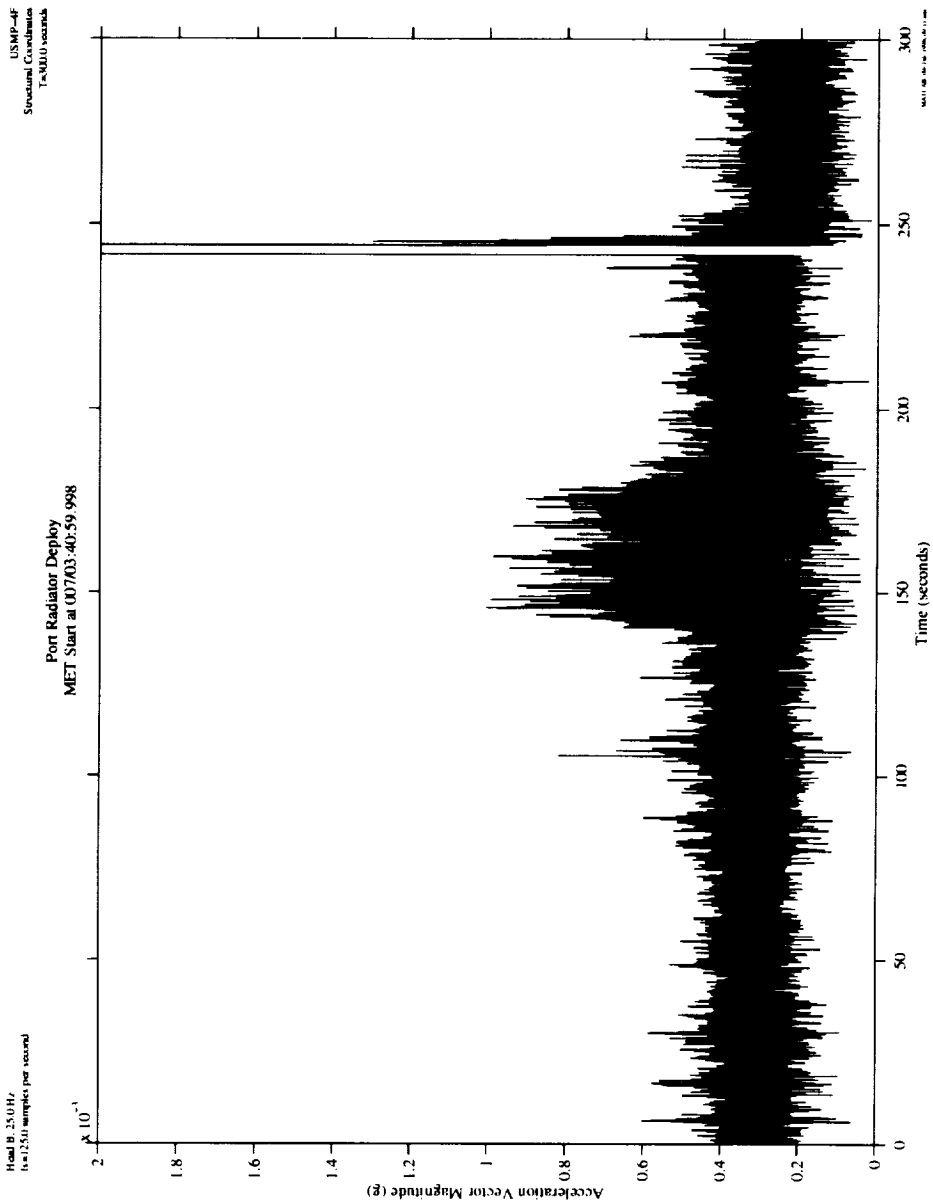

Figure 15. Port radiator deploy; plot start at MET 007/03:41.

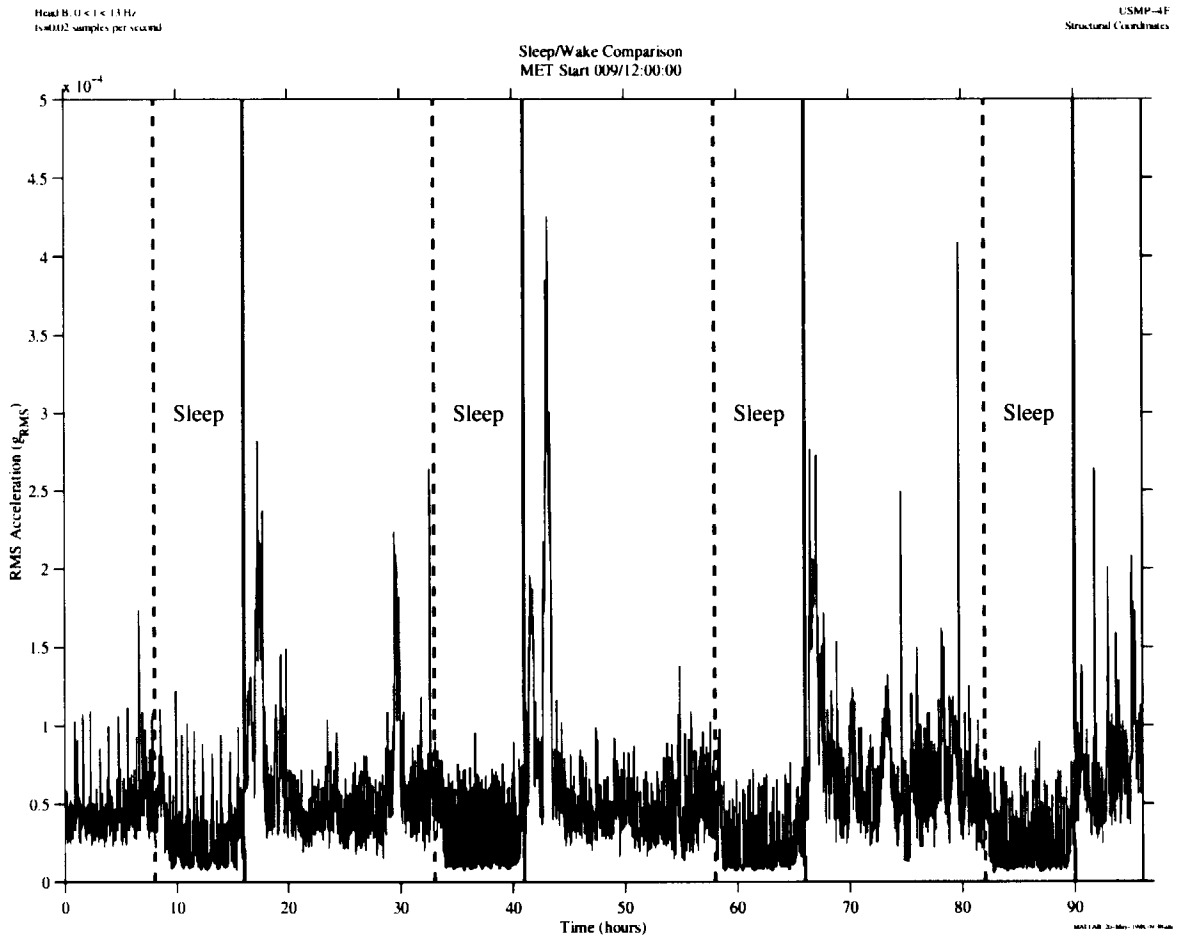

Figure 16. Sleep/wake RMS acceleration comparison.

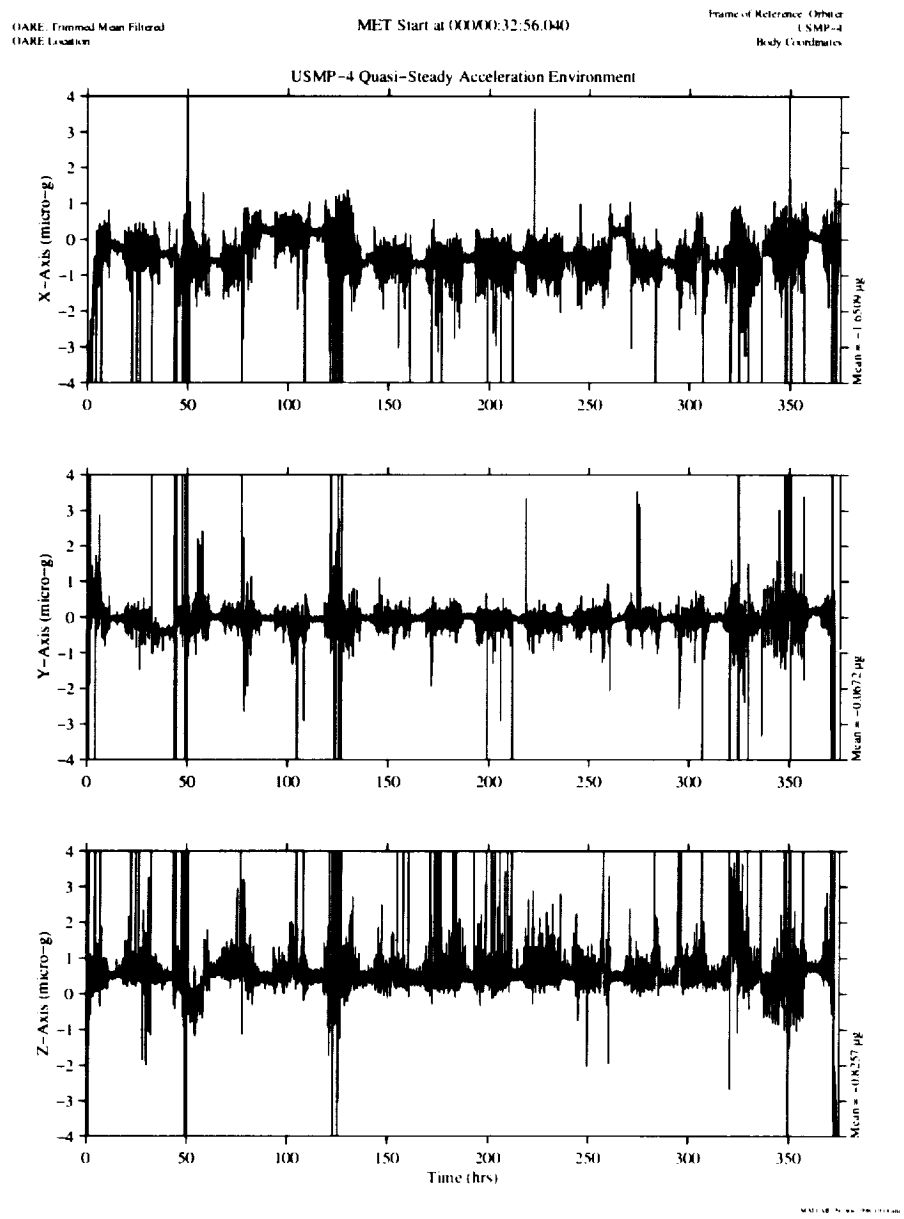

Figure 17. Trimmean filtered OARE data versus time for the STS-87 mission.

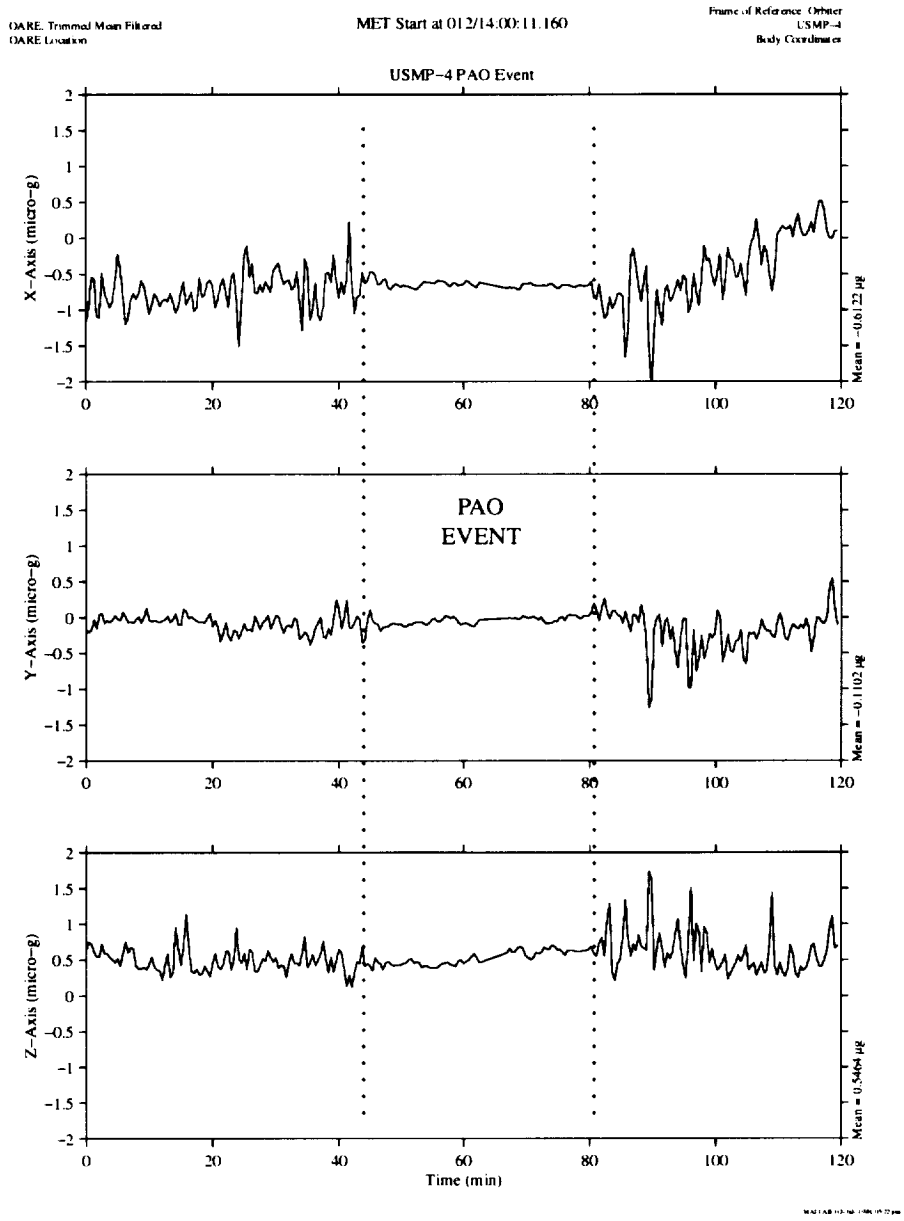

Figure 18. Trimmean filter OARE data during an STS-87 PAO event.

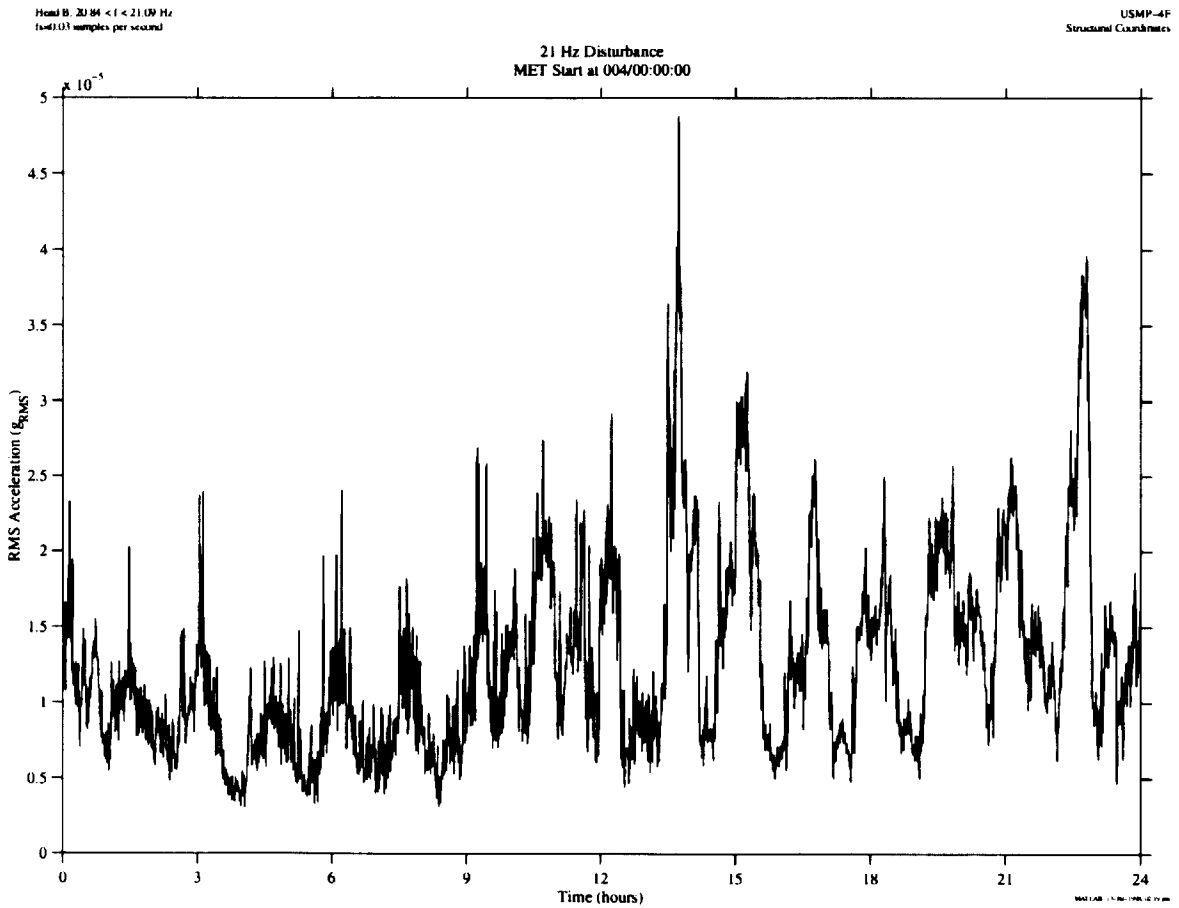

Figure 19. RMS acceleration versus time for the 21 Hz disturbance.

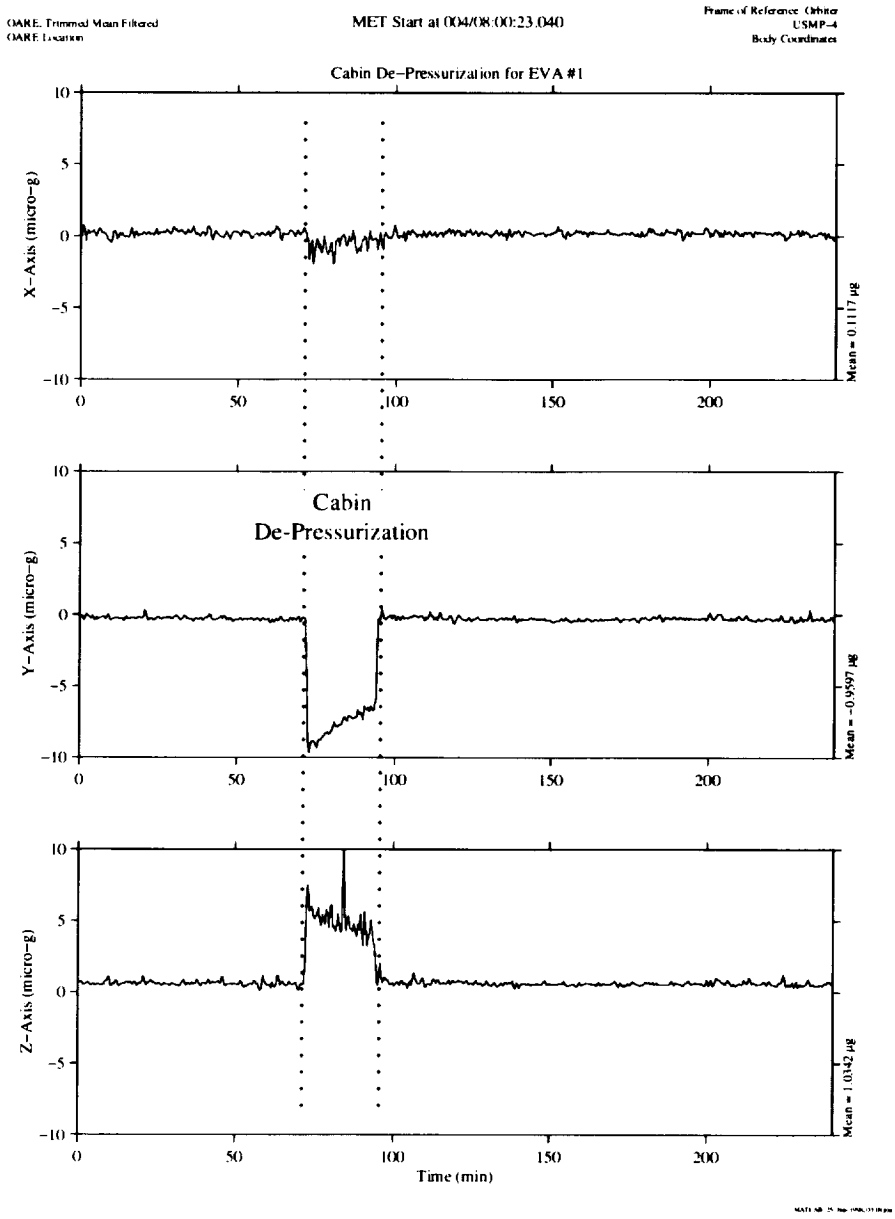

Figure 20. Cabin de-pressurization in preparation for EVA #1.

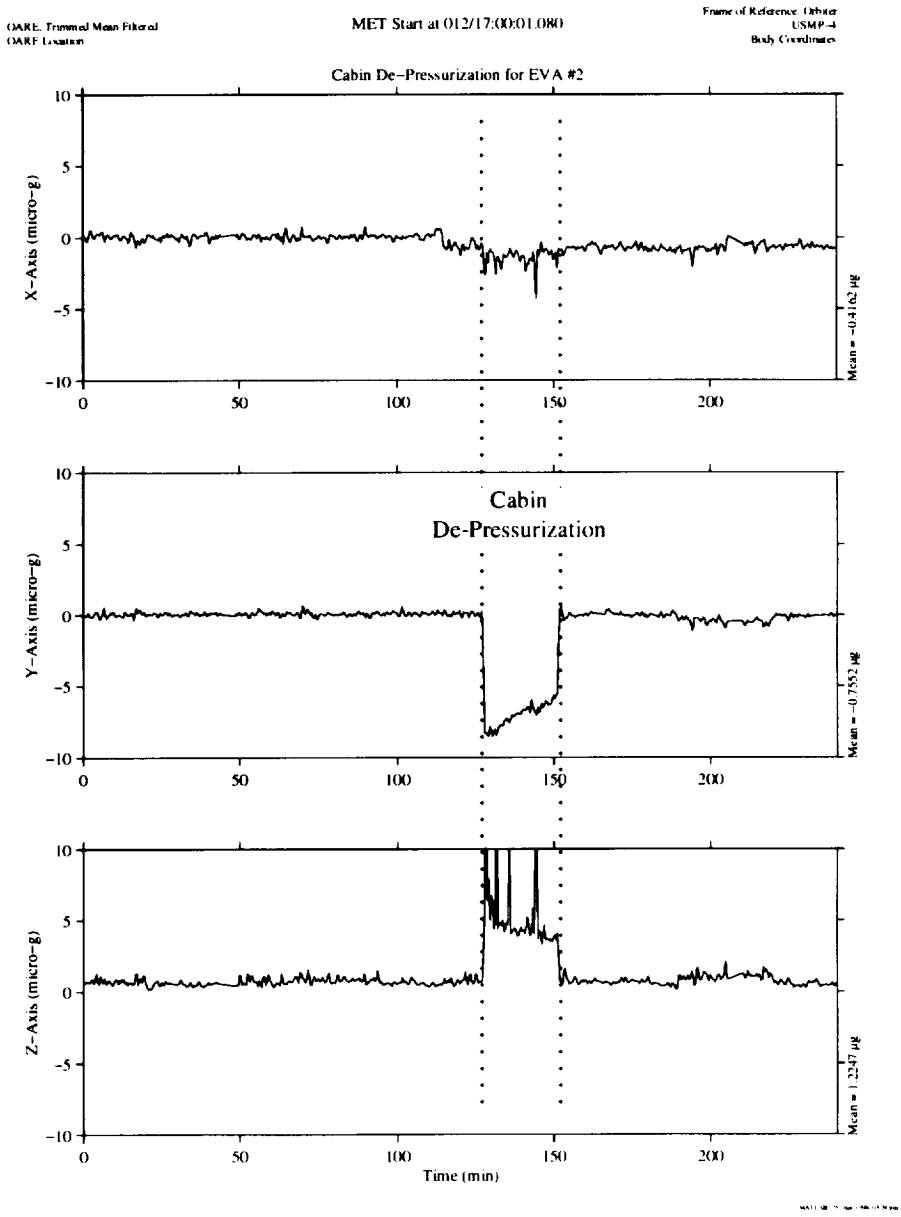

Figure 21. Cabin de-pressurization in preparation for EVA #2.

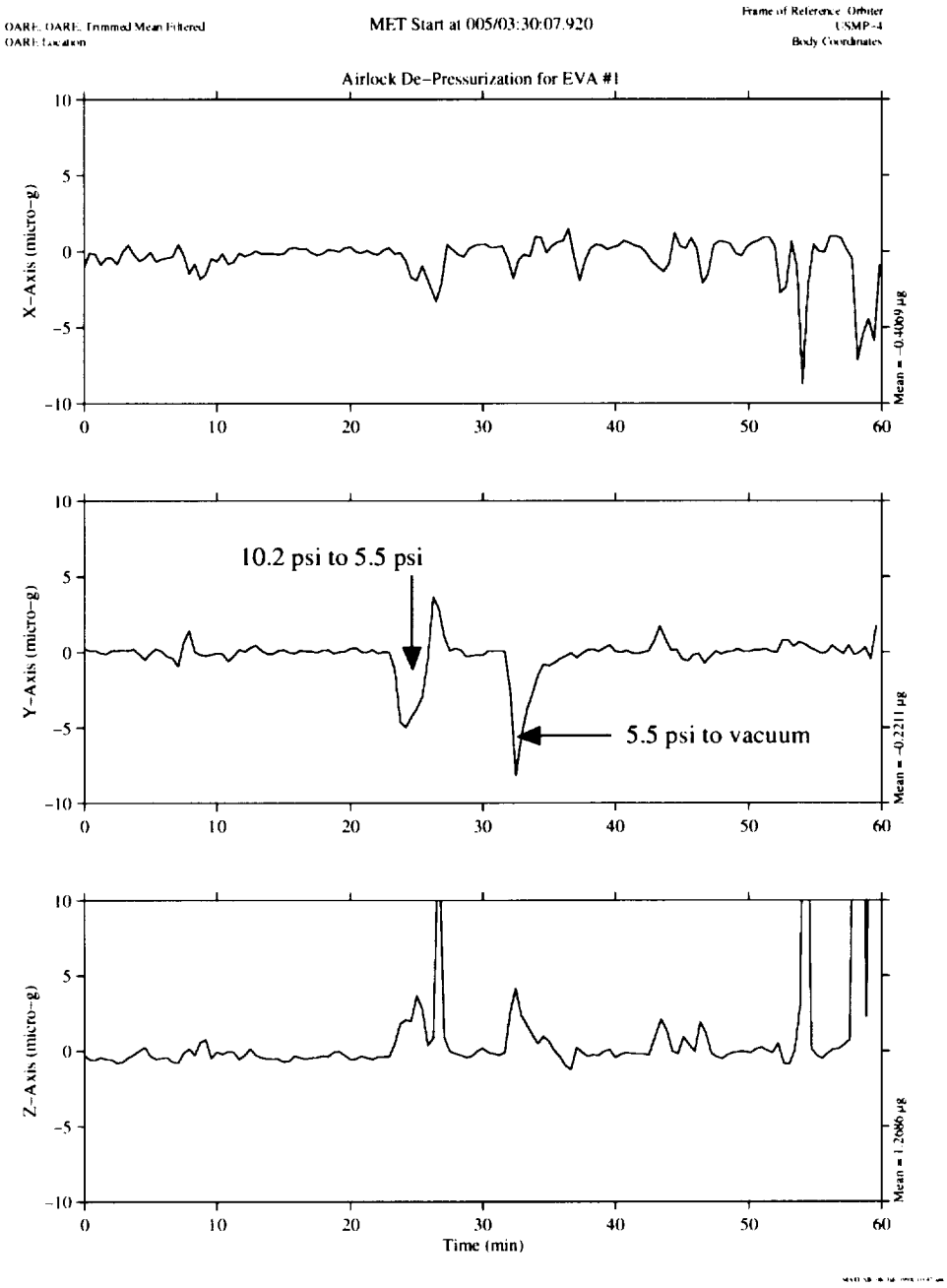

Figure 22. Airlock de-pressurization in preparation for EVA #1.

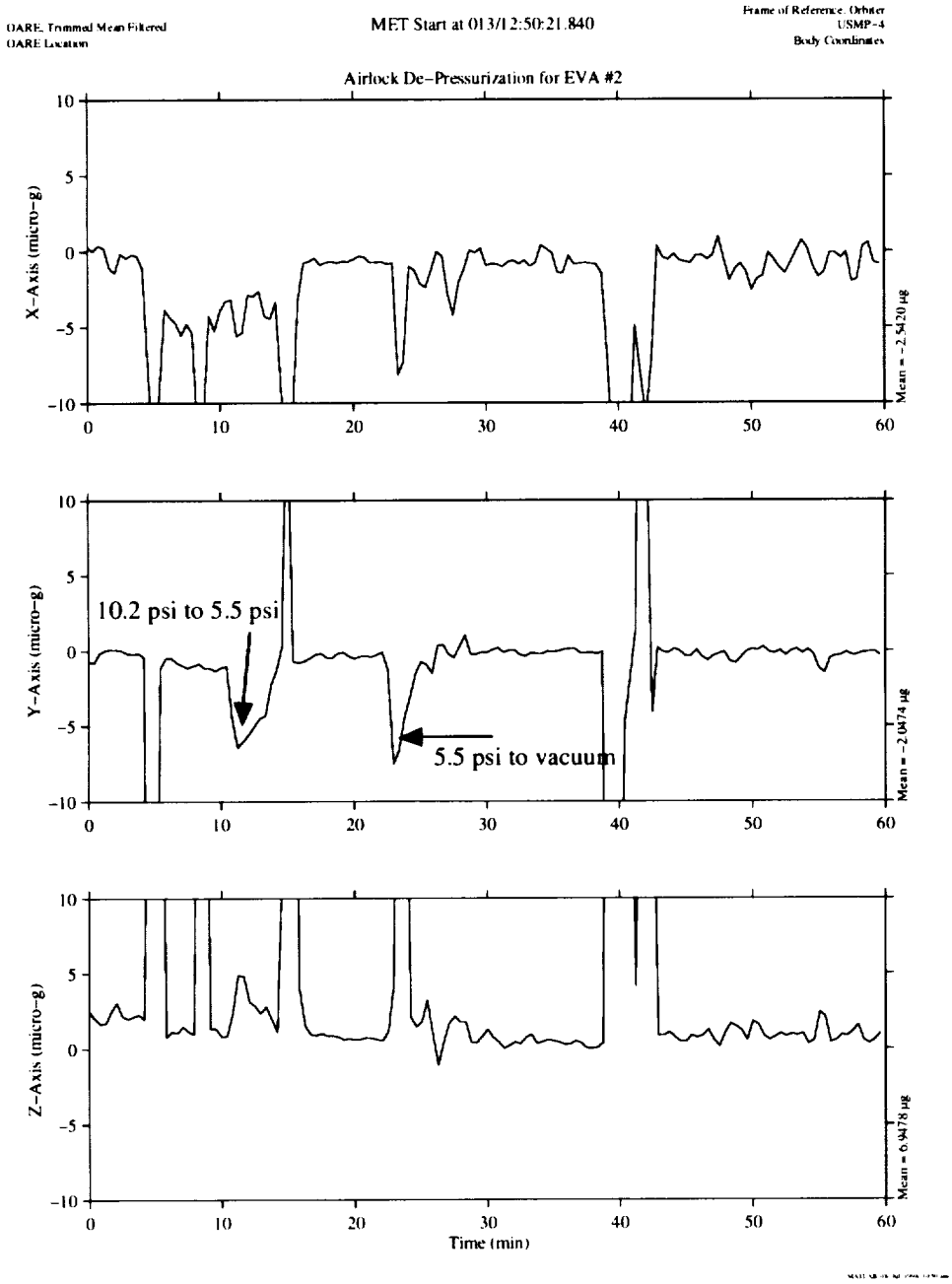

Figure 23. Airlock de-pressurization in preparation for EVA #2.

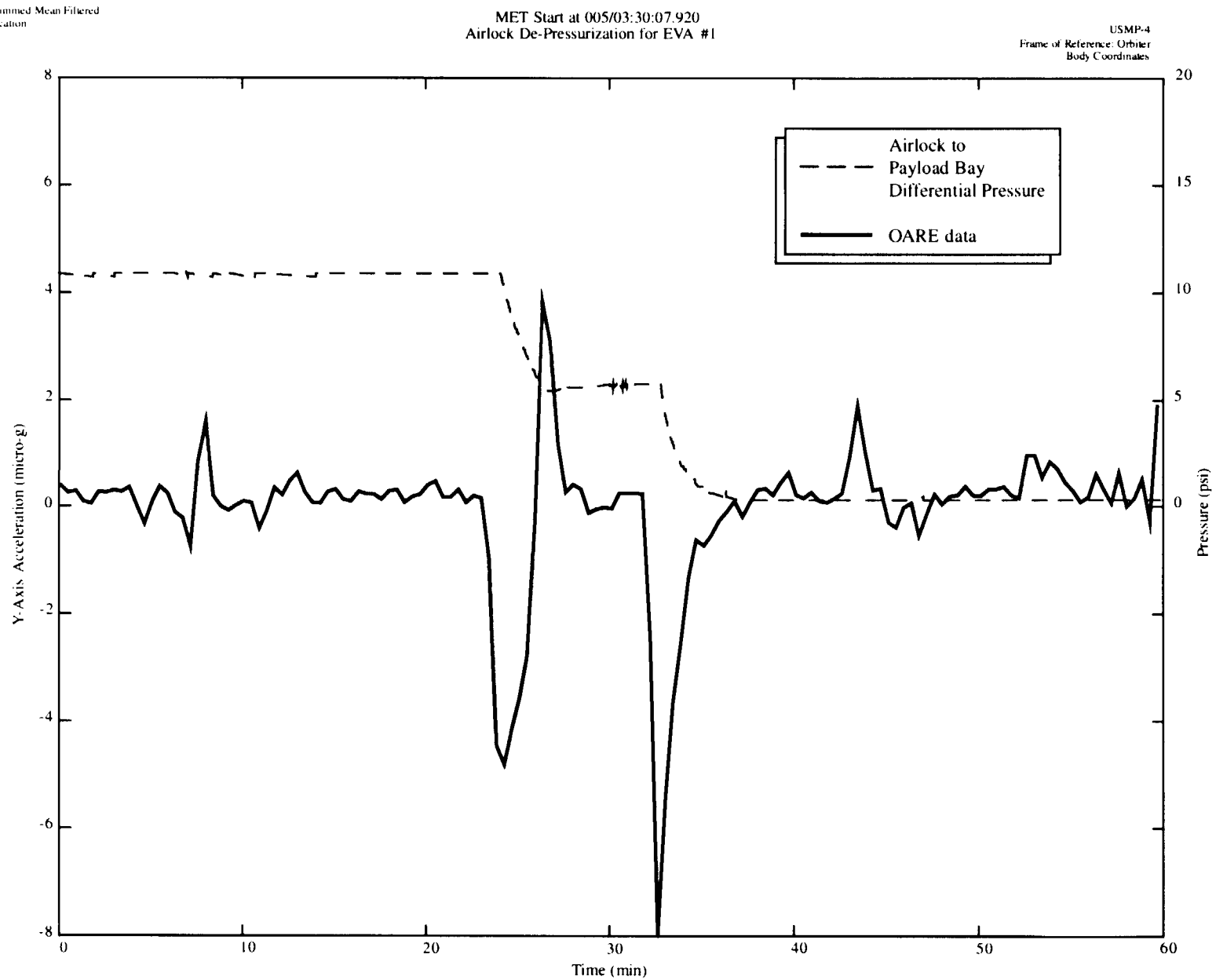

Figure 24. Airlock de-pressurization for EVA #1 on STS-87.

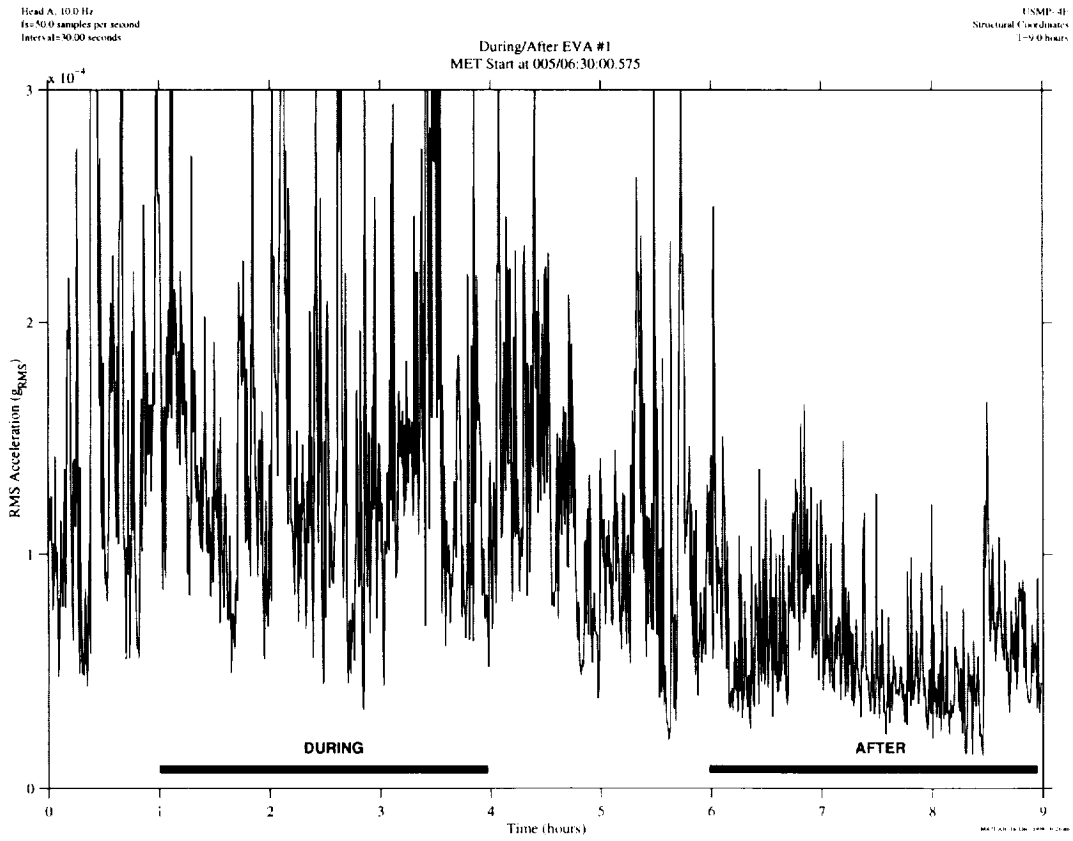

Figure 25. RMS acceleration versus time during and after EVA #1.

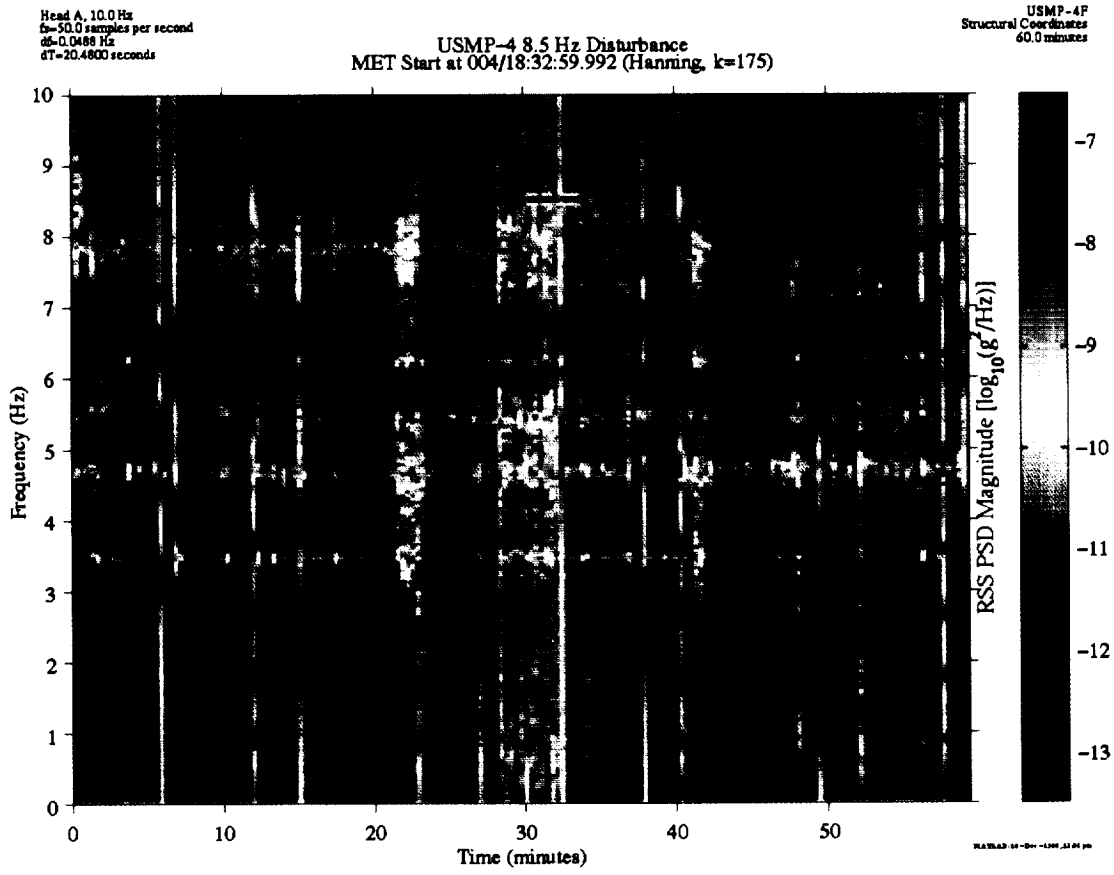

Figure 26. Typical short duration, high magnitude 8.5 Hz disturbance as seen in STS-87 SAMS spectrograms.

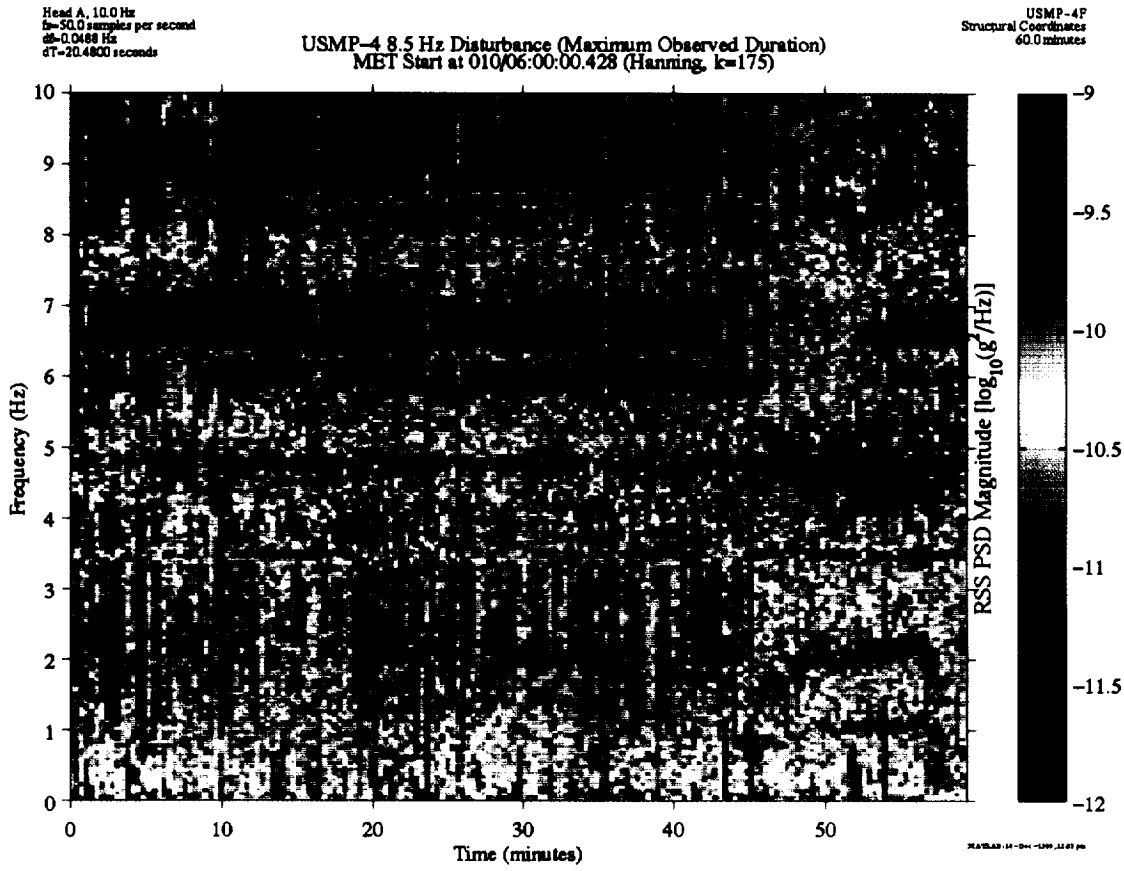

Figure 27. SAMS Unit F, TSH A spectrogram showing an occurrence of a lower magnitude, longer duration 8.5 Hz signal. Note that the PSD magnitude scale is different than that for Figure 26.

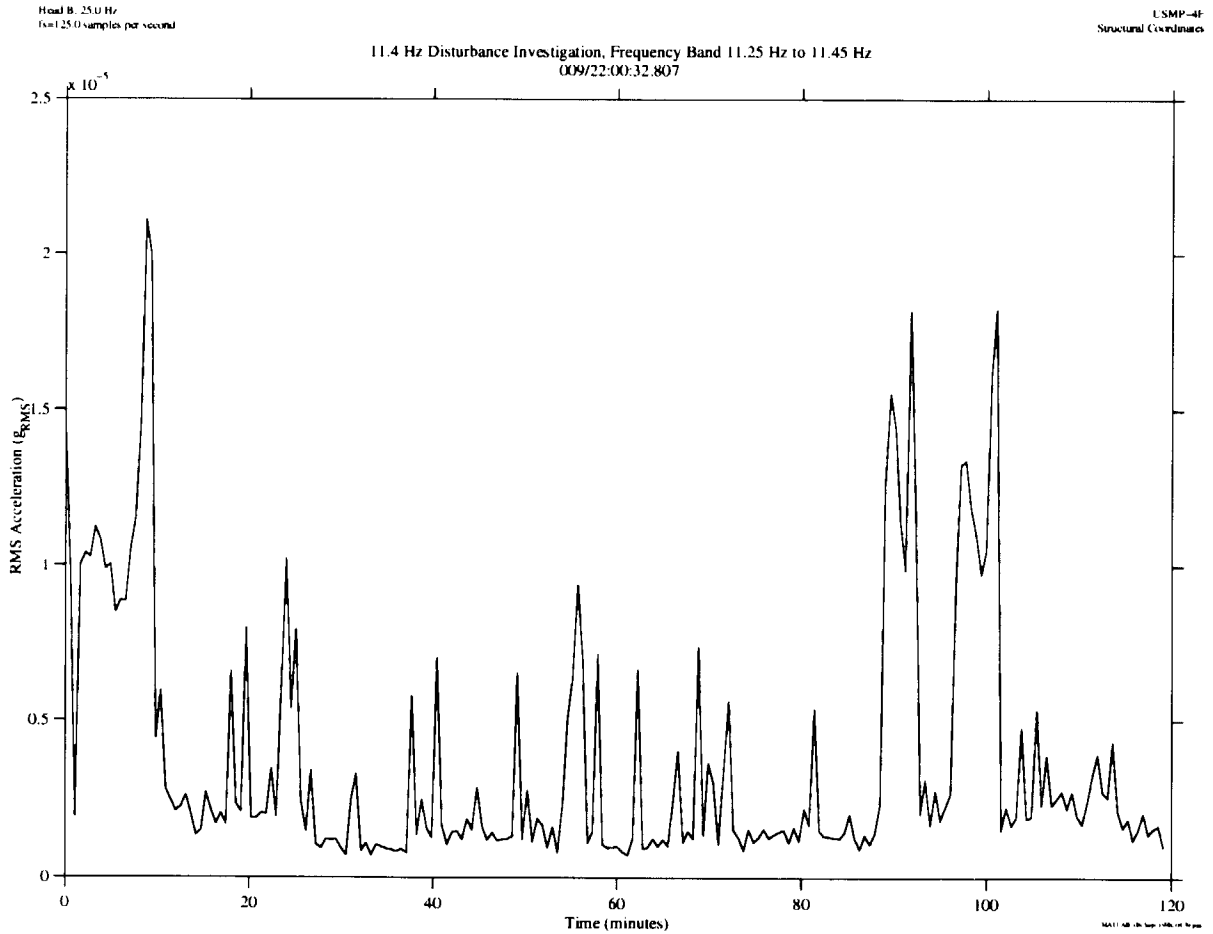

Figure 28. 11.35 Hz disturbance investigation, frequency band 11.25 Hz to 11.45 Hz.

REPORT DOCUMENTATION PAGE

Form Approved
OMB No. 0704-0188

1. AGENCY USE ONLY *(Leave Blank)*	2. REPORT DATE	3. REPORT TYPE AND DATES COVERED
	September 1999	Conference Publication

4. TITLE AND SUBTITLE
Fourth United States Microgravity Payload: One Year Report

5. FUNDING NUMBERS

6. AUTHORS
E.C. Ethridge, P.A. Curreri, and D.E. McCauley,* Compilers

7. PERFORMING ORGANIZATION NAMES(S) AND ADDRESS(ES)
George C. Marshall Space Flight Center
Marshall Space Flight Center, Alabama 35812

8. PERFORMING ORGANIZATION REPORT NUMBER
M–939

9. SPONSORING/MONITORING AGENCY NAME(S) AND ADDRESS(ES)
National Aeronautics and Space Administration
Washington, DC 20546–0001

10. SPONSORING/MONITORING AGENCY REPORT NUMBER
NASA/CP—1999–209628

11. SUPPLEMENTARY NOTES
Proceedings of a conference held at Marshall Space Flight Center, January 22, 1999. Prepared for Microgravity Sciences & Applications Department, Science Directorate.
*University of Alabama in Huntsville, Huntsville, Alabama

12a. DISTRIBUTION/AVAILABILITY STATEMENT
Unclassified-Unlimited
Subject Category 88
Standard Distribution

12b. DISTRIBUTION CODE

13. ABSTRACT *(Maximum 200 words)*

This document reports the one year science results for the Fourth United States Microgravity Payload (USMP–4). The USMP–4 major experiments were on a support structure in the Space Shuttle's payload bay and operated almost completely by the Principal Investigators through telescience. The mission included a Glovebox where the crew performed additional experiments for the investigators. Together about eight major scientific experiments were performed, advancing the state of knowledge in fields such as low temperature physics, solidification, and combustion. The results demonstrate the range of quality science that can be conducted utilizing orbital laboratories in microgravity and provide a look forward to a highly productive Space Station era.

14. SUBJECT TERMS
USMP–4, microgravity research, materials science, combustion science, low temperature physics, solidification, telescience, crystal growth

15. NUMBER OF PAGES
248

16. PRICE CODE
A11

17. SECURITY CLASSIFICATION OF REPORT	18. SECURITY CLASSIFICATION OF THIS PAGE	19. SECURITY CLASSIFICATION OF ABSTRACT	20. LIMITATION OF ABSTRACT
Unclassified	Unclassified	Unclassified	Unlimited